VELOCITY, COUPLING COMBUSTION INSTABILITY

Merrill W. Beckstead, et al

Hercules, Incorporated

Prepared for:

Air Force Rocket Propulsion Laboratory

September 1973

AFRPL - TR-73-73

VELOCITY COUPLING COMBUSTION INSTABILITY

FINAL TECHNICAL REPORT, AFRPL-TR-73-73

SEPTEMBER 1973

HERCULES INCORPORATED
SYSTEMS GROUP
Bacchus Works • Magna, Utah

AIR FORCE ROCKET PROPULSION LABORATORY
DIRECTOR OF SCIENCE AND TECHNOLOGY
AIR FORCE SYSTEMS COMMAND
UNITED STATES AIR FORCE
EDWARDS, CALIFORNIA 93523

FOREWORD

This is the final report to be issued under Contract F04611-72-C-0003, "A Study of the Influence of Velocity Coupling on Solid Rocket Motor Combustion Instability", and covers the time period of August 1971 through July 1973. The technical work was performed by Hercules Incorporated (HI), Bacchus Works, Magna, Utah, and the Chemical Engineering Department of Brigham Young University (BYU), Provo, Utah.

Preparation of this report is authorized under Contract F04611-72-C-0003 in accordance with Item B003, Exhibit B, Contract Data Requirements List. This contract is sponsored by the Air Force Rocket Propulsion Laboratory, Director of Laboratories, Edwards, California, Air Force Systems Command, United States Air Force, under Project Officer Mr. R. J. Schoner.

Publication of this report does not constitute Air Force approval of the reports findings or conclusions. It is published only for the exchange and stimulation of ideas.

This report has been reviewed and is approved.

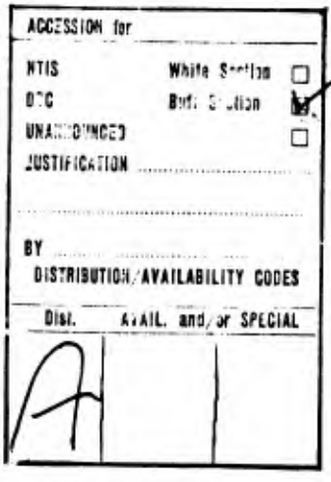

Paul J. Daily, Colonel, USAF
Chief, Technology Division

NOTICES

When U. S. Government drawings, specifications, or other data are used for any purpose other than a definitely related Government procurement operation, the Government thereby incurs no responsibility nor any obligation whatsoever, and the fact that the Government may have formulated, furnished, or in any way supplied the said drawings, specifications, or other data, is not to be regarded by implication or otherwise, or in any manner licensing the holder or any other person or corporation, or conveying any rights or permission to manufacture, use, or sell any patented invention that may in any way be related thereto.

Unclassified

SECURITY CLASSIFICATION OF THIS PAGE (When Data Entered)

REPORT DOCUMENTATION PAGE		READ INSTRUCTIONS BEFORE COMPLETING FORM
1. REPORT NUMBER AFRPL-TR-73-73	2. GOVT ACCESSION NO.	3. RECIPIENT'S CATALOG NUMBER
4. TITLE (and Subtitle) Velocity Coupling Combustion Instability		5. TYPE OF REPORT & PERIOD COVERED Final Aug 71 thru Jul 73
		6. PERFORMING ORG. REPORT NUMBER
7. AUTHOR(s) Merrill W. Beckstead, M. Duane Horton, Maurice Krashin, A. Garn Butcher		8. CONTRACT OR GRANT NUMBER(s) F04611-72-C-0003
9. PERFORMING ORGANIZATION NAME AND ADDRESS Hercules Incorporated Bacchus Works, Magna, Utah		10. PROGRAM ELEMENT, PROJECT, TASK AREA & WORK UNIT NUMBERS 62302F, 5730, 10, EL
11. CONTROLLING OFFICE NAME AND ADDRESS AFRPL (DYSC) Edwards CA 93523		12. REPORT DATE September 1973
		13. NUMBER OF PAGES ~~204~~ 207
14. MONITORING AGENCY NAME & ADDRESS (if different from Controlling Office) Same		15. SECURITY CLASS. (of this report) Unclassified
		15a. DECLASSIFICATION/DOWNGRADING SCHEDULE

16. DISTRIBUTION STATEMENT (of this Report)

Approved for Public Release; Distribution Unlimited.

17. DISTRIBUTION STATEMENT (of the abstract entered in Block 20, if different from Report)

Same

18. SUPPLEMENTARY NOTES

19. KEY WORDS (Continue on reverse side if necessary and identify by block number)

Combustion Instability, Solid Rockets, Solid Propellant Combustion

20. ABSTRACT (Continue on reverse side if necessary and identify by block number)

The program was conducted as a joint effort between Hercules Incorporated and Brigham Young University. The objectives of the program were: To develop an understanding of the role of velocity-coupled combustion response in solid propellant combustion instability, to evaluate various methods for quantitatively measuring this response, and to select the most appropriate method for future development and evaluation. The study was divided into three phases: Supporting analyses to provide direction for the experimental phases; a

DD FORM 1 JAN 73 1473 EDITION OF 1 NOV 65 IS OBSOLETE

Unclassified

SECURITY CLASSIFICATION OF THIS PAGE (When Data Entered)

phenomenological study to determine relative effects of propellant combustion in an oscillatory environment; and the evaluation of test techniques to find a quantitative tool for characterizing velocity coupling. Parametric calculations were made on the Minuteman II Stage III motor examining various effects of velocity coupling, and for a T-burner modified to include four propellant samples. The latter calculations showed that discrete samples located a quarter length from the T-burner end would provide maximum velocity-coupled driving (the configuration has been named the velocity-coupled T-burner). High speed movies were taken of propellant combustion subjected to large acoustic velocities varying the propellant compositions and test conditions. The net results indicated that CYH propellant at approximately 300 psi and 500 Hz appeared to be optimum test conditions for exhibiting velocity coupling.

As part of the technique evaluation, test results are presented for the velocity-coupled T-burner and an end-vented burner. The conclusions reached were that the velocity-coupled T-burner gave more quantitative data and overall was more practical to operate. Additional tests showed that CYH propellant has a velocity-coupled response of approximately 13, almost an order of magnitude greater than the pressure-coupled response. Testing with different lots of CYH propellant and with ANB-3066 propellant show that the velocity-coupled T-burner technique can differentiate between different propellants and propellant lots. The results from the test technique appear to be sensitive to frequency changes but not to changes in the size of the driver sample. Nonlinear interpretation of the data indicates a stronger nonlinear mechanism than is normally observed in pressure-coupled testing. The final conclusion reached is that velocity coupling is a significant mechanism in solid propellant rocket motors and the velocity-coupled T-burner appears capable of providing quantitative data on the velocity-coupled response.

TABLE OF CONTENTS

TABLE OF CONTENTS (Cont)

TABLE OF CONTENTS (Cont)

LIST OF FIGURES

LIST OF FIGURES (Cont)

LIST OF FIGURES (Cont)

LIST OF FIGURES (Cont)

LIST OF FIGURES (Cont)

LIST OF TABLES

NOMENCLATURE

A	Nondimensional acoustic admittance
A_ℓ	Wave function coefficient defined by Equation 4-66
A_n	Nondimensional nozzle acoustic admittance
A_b	Propellant acoustic admittance
a	Speed of sound in gas
a_m	Speed of sound in gas-particle mixture
B_e	Wave function coefficient defined by Equation 4-67
B_s	Pressure coupling response coefficient equal to $R_b^r + \frac{1}{\gamma}\left(A_b^r/\bar{M}_b + 1 - R_b^r\right)$
C_h/C_{ho}	Stanton coefficient
C_ℓ^e	Wave function coefficient defined by Equations 4-71 and 4-73
C_ℓ^o	Wave function coefficient defined by Equations 4-70 and 4-72
$\mathcal{C}_{\ell 1}$	Pressure coupling coefficient defined by Equation 4-84
$\mathcal{C}_{\ell v}$	Velocity coupling coefficient defined by Equation 4-85
D_c	Inside diameter of burning cylindrical propellant sample
D_{co}	Inside diameter of T-burner tube
D_e	Wave function coefficient defined by Equation 4-68
E	$\left(\frac{a}{\gamma}\right) R_{vi}/R_b^r$
E_ℓ^2	Dimensional energy term equal to $\int_o^L p^2\, dz$
$\mathcal{E}_\ell^2$	Nondimensional energy term equal to $E_\ell^2/(L\, S_{co})$
F	Parameter defined by Equation 4-23
F_ℓ	Wave function coefficient defined by Equation 4-69
f	T-burner oscillation frequency
G	Second order nonlinear coefficient

$g_{\ell 1}$	Mean flow coefficient for pressure coupling cylindrical grain defined by Equation 4-80
$g_{\ell v}$	Mean flow coefficient for velocity coupling cylindrical grain defined by Equation 4-81
h	Gas film heat transfer coefficient
$\frac{h_{es} - h_{wg}}{\Delta h}$	Enthalpy change after vaporization divided by enthalpy of evaporation
J_o	Bessel function of first kind and order zero
K_i	i = 1, 2, 3, 4, 5, 6 constants defined by containing equations
K_ℓ	Nondimensional wave number defined by Equation 4-60(e)
k	Complex wave number of perturbed oscillations equal to $(\omega - i\alpha)/\bar{a}$
k_g	Thermal conductivity of combustion products
k_ℓ	Complex wave number of unperturbed acoustic oscillation equal to $\omega_\ell/\bar{a}$
k_v	Erosive burning constant
L	Total inside length of T-burner
L_i	i = 0, 1, 2, 3, v See Figure 4-9 and Equation 4-60
M	Mach number
m	Mass burn rate per unit burning surface
n	Propellant burn rate exponent
$P_{\ell 1}$	Velocity coupling coefficient defined by Equation 4-87
$P_{\ell v}$	Velocity coupling coefficient defined by Equation 4-88
Pr	Prandtl number
p	Pressure

Q	Acoustic amplitude factor
q	Circumferential distance around inner surface of propellant sample
R	Radius of resonance tube in Equation 4-15
R_b	Acoustic pressure coupling response of burning propellant
R_v	Acoustic velocity coupling response of burning propellant
R_{vi}	Velocity coupling response function equal to the imaginary part of R_v
r	Burn rate in Equations 4-1 and 4-2 Radial distance from centerline of resonance tube in Equation 4-15
S	Surface area
S_b	Total burning surface area
S_{be}	End burning surface area
S_{bs}	Cylindrical burning surface area
S_c	Cylindrical propellant cross sectional area
S_{co}	T-burner cross-sectional area
U	Equivalent sinusoidal velocity amplitude
u	Axial flow velocity
u_e	Steady erosive velocity
u'_e	Erosive component of acoustic velocity
u_t	Threshold velocity for erosive burning
u_w	Wall velocity
VCTB	Velocity coupled T-burner
VF	Vent parameter for flow turning
VFG	Grain parameter for flow turning
Y	Acoustic admittance function

y	Nondimensional distance along T-burner axis defined by Equation 4-27
z	Distance along T-burner axis
α	Acoustic growth or decay rate
α_d	Basic acoustic decay rate for nonburning condition
α_{mf}	Mean flow acoustic decay rate
α_{pc}	Pressure coupling acoustic growth rate
α_{pd}	Particle damping acoustic decay rate
α_{tot}	Total acoustic growth or decay rate
α_v	Volume damping coefficient
α_{vc}	Velocity coupling acoustic growth rate
β_i	i = 0, 1, 2, 3, v See Figure 4-9 and Equation 4-60
γ	Ratio of specific heats
Δ	Incremental difference operator
θ	Parameter defined by Equation 4-24
λ	Thermal conductivity
μ	Viscosity
ξ	Nondimension axial distance along T-burner defined by Equation 4-60(f)
π	Nonlinear correlating parameter, $2\frac{\Delta P_L}{\alpha}\frac{f}{\bar{p}}$
ρ	Gas density
τ	Particle relaxation time
ω	Angular frequency of oscillations

Subscript	Designation
$( )_b$	Burning surface value
$( )_\ell$	ℓth mode
$( )_n$	Nozzle
$(\underset{\sim}{\ })$	Vector

Superscript	Designation
$( )^i$	Imaginary part
$( )^r$	Real part
$( )'$	Acoustic value
$(\hat{\ })$	Amplitude
$(\bar{\ })$	Steady value

SECTION I

INTRODUCTION

A. INTRODUCTION

Combustion instability is a phenomenon that has occurred repeatedly under a wide variety of conditions throughout the history of rocketry. The occurrence can be manifested as a mild vibration, a severe vibration, or (in the extreme) as a catastrophic motor failure. The instability usually couples with an acoustic mode of the rocket chamber and exhibits itself as a pressure oscillation. Velocity coupling is usually (but not always) associated with the axial (i.e., longitudinal) mode of the combustion chamber. Actually, this phenomenon has been referred to by several names including axial mode instability, intermediate frequency instability, acoustic erosivity, or nonlinear longitudinal instability. These names probably refer to two velocity dependent phenomena which have occurred at different pressures, frequencies, and motor conditions.

One case, usually referred to as acoustic erosivity, occurs when the scrubbing action of the acoustic wave increases the mean burning rate of propellant, probably due to enhanced heat transfer at the propellant surface. The second case occurs when the phasing of the propellant combustion is such that it couples with the acoustic velocity wave either to drive or attenuate the wave. The latter is the velocity coupling phenomenon which provides the basis of the current program. (In a severe form it can also lead to acoustic erosivity.)

Despite the potential adverse effects velocity coupled instability has on missiles, the present state of knowledge is not adequate to permit the design engineer to minimize occurrence. Often the problem is not even considered until its presence is inferred from firings of the rocket motor. Attempts to "fix" the problem after the fact are usually expensive, inefficient, and do not contribute significantly to fundamental understanding of the basic problem. This lack of understanding has been perpetuated to a large measure by the fact that a suitable laboratory test device has not existed which permitted quantitative, reliable measurements to be made of the combustion response to velocity waves. The lack of such a test device provided the motivation for the current program.

B. PROGRAM OBJECTIVE

The objectives of this program were:

- To develop an understanding of the role of velocity coupled combustion response in solid propellant combustion instability
- To evaluate various methods for quantitatively measuring this response
- To select the most appropriate method for future development and evaluation.

C. APPROACH

The program was conducted as a joint effort between Hercules and Brigham Young University (BYU) over a 2-year period. The program was divided into three sequential phases. Hercules and BYU shared the responsibility of Phase I, Supporting Analyses. BYU performed Phase II, a Phenomenological Investigation, with Hercules providing a small coordinating effort. Phase III, Technique Evaluation, was performed by Hercules with BYU providing consulting services.

1. Phase I - Supporting Analyses

The objective of Phase I was to provide analytical support and direction for the later experimental phases of the program. This was accomplished by making parametric studies of the effects and manifestations of velocity coupling in a motor environment and in a test environment. Phase I was subdivided into three studies that were pursued concurrently. The first portion was a study of the fundamental interaction between an acoustic velocity and the propellant combustion. The second portion was the generalization of an existing BYU computer program describing instability in a T-burner, which ultimately led to the development of a computer program describing the velocity coupled T-burner. The third portion was the generalization of the existing Hercules motor stability analysis program to include the effects of flow reversal and a threshold velocity on velocity-coupled acoustic driving.

These analyses (and the resultant computer programs) were used in both Phase II and Phase III to aid in the technique screening task, and to provide guidance as to what data should be obtained and how it should be applied.

2. Phase II - Phenomenological Investigation

The phenomenological investigation was directed towards determining relative effects of propellant combustion in an oscillatory environment for a wide range of test conditions. The primary test apparatus was the T-burner modified as discussed in Section V. The principal modification permitted high speed photographic coverage of a test sample located at the acoustic velocity antinode. Over 100 tests were performed at a wide range of test conditions varying pressure, propellant driving area, burner length, and propellant formulations. The data were analyzed to determine under which conditions the greatest changes in behavior were observed. These results were compared and correlated with the analyses from Phase I. The results of Phase II were analyzed with the objective of helping to determine the test conditions for Phase III testing.

3. Phase III - Technique Evaluation

In the evaluation of test techniques, several techniques were considered for possible application based on the results of Phases I and II. These included modifications of the T-burner and a small end vented device adapted for measuring velocity coupling. The techniques were evaluated on the basis of the ability to produce oscillations, the type of data obtained, and the practicality of operating the device.

The velocity-coupled T-burner and an end vented device were selected for actual screening tests. A limited number of tests (~30) were performed, analyzed, and evaluated to determine which device appeared to be most sensitive, and the extent that the data from the device could be applied and incorporated into motor analyses.

Based on the results and interpretation of the screening tests, the velocity-coupled T-burner was chosen for further evaluation. Approximately 60 characterization tests were performed varying frequency, oscillation amplitude, and propellant formulation.

The purpose of these tests was to determine the sensitivity of the velocity-coupled T-burner to typical variations in test conditions, and particularly to determine if the velocity-coupled T-burner could differentiate between propellant formulations.

SECTION II

SUMMARY

A. PHASE I - SUPPORTING ANALYSES

An examination of various possible forms of interaction between oscillating velocity effects on propellant burning rate and oscillating pressure effects on propellant burning rate was carried out. A more complex interaction between the two effects than is indicated by additive or multiplicative interaction was recommended for use until more accurate experimental data are available.

An analysis of the McClure-Hart-Cantrell and Culick theoretical derivations of acoustic driving was carried out showing the two derivations lead to identical results except for the term describing the convection of kinetic energy. This term is negligibly small for end-nozzle motors but strongly influences the calculations for center vented T-burners. Parametric calculations showed that the position halfway between the T-burner end and center vent would produce the maximum velocity coupling for a discrete test sample.

The Hercules velocity-coupled acoustic driving computer program was modified to include the effects of flow reversal and a threshold velocity in the calculations. In the Minuteman II stage III motor, a 50 ft/sec threshold velocity decreases the velocity-coupled driving by 50 percent at acoustic amplitudes that are 10 percent of the operating pressure. At acoustic amplitudes that are 1 percent of the operating pressure, a 50 ft/sec threshold velocity decreases the acoustic driving by only 4 percent.

B. PHASE II - A PHENOMENOLOGICAL STUDY

During the phenomenological phase of the program, it was observed that the standing wave in the T-burner did not have a simple sine or cosine form when the nozzle was displaced from the center of the burner or when dissimilar amounts of propellant were used in the two ends of the burner.

With all of the propellants tested in Phase II it was found that large velocity oscillations (about 70 ft/sec) would cause an abrupt, reversible, order-of-magnitude change in flame luminosity. At increased velocities, the propellant continued to burn with little or no visible flame. With aluminized propellants, this change was relatively insensitive to the aluminum ignition and combustion.

Differences attributed to propellant composition were difficult to quantitize. Although somewhat different velocity amplitudes were required to produce the dark combustion, most of the propellants required an amplitude of about 70 ft/sec. However, the magnitude of the luminosity during the dark combustion differed greatly from propellant to propellant. The CYH flame had the lowest luminosity level of all the propellants, indicating a possibly high susceptibility to velocity coupling.

A principal objective of this phase of the program was to define optimized test conditions for the quantitative testing to be performed as the final phase of the program. The results indicated that using CYH propellant at 300 psi and 500 Hz should provide a combination of conditions exhibiting significant velocity coupling.

C. PHASE III - TECHNIQUE EVALUATION

Several devices were initially considered for evaluation of velocity coupling. The velocity-coupled T-burner and an end vented burner were selected for experimental evaluation. Both used established variable area T-burner techniques, instrumentation, and hardware. Propellant samples were symmetrically located in the ends of the burner and one quarter length from the ends. Approximately 30 screening tests were performed with the two configurations.

Tests in the velocity-coupled T-burner resulted in quantitative data. Most test conditions yielded spontaneous oscillations with little evidence of wave distortion or harmonic content. The oscillations limited at relatively low amplitudes indicating larger than normal nonlinear limiting mechanisms (apparently indicative of velocity coupling).

Tests in the end vented burner resulted in much poorer quality data than the velocity-coupled T-burner. Most of the tests had to be pulsed. The resultant oscillations decayed very rapidly and exhibited significant harmonic content introducing excessive data scatter. Data interpretation is complicated due to the necessity of determining the damping of the end vent. Due to these problems, quantitative results were not obtained from the end vented burner.

Based on the screening tests, the velocity-coupled T-burner was selected as the technique for further evaluation, and a variety of additional tests were performed. The data from these tests indicate that the velocity-coupled T-burner can yield quantitative data. The velocity-coupled response of CYH propellant was determined to be approximately 13 (at 300 psi and 450 Hz) which is an order of magnitude greater than the pressure-coupled response at these conditions. These data indicate that velocity coupling is a very significant mechanism relative to acoustics in solid propellant rocket motors.

Data were obtained with ANB-3066 propellant and with CYH lot SR-28 propellant both of which showed different characteristics than the CYH lot 1-14 propellant. Thus, the technique appears able to differentiate between different types of propellant (composite versus CMDB) and between different lots of propellant with differing motor characteristics*. The data indicate that CYH lot 1-14 is much more susceptible to velocity coupling than lot SR-28 which in agreement with actual motor firings.

*CYH lot 1-14 exhibits significantly more severe oscillations in the Minuteman II stage III motor than CYH lot SR-28.

The test technique also showed a sensitivity to frequency. Tests fired with the CYH lot 1-14 propellant at 800 Hz gave a lower response and differing test characteristics than the baseline data at 450 Hz.

The measured growth constant versus test sample area ratio plot as a straight line for the basic test technique (both the SR-28 and the 800 Hz data were exceptions to this observation). This simplifies data interpretation. A very large effect due to either T-burner volume or sample/wall lip was observed. As a sample burned out, increasing volume and changing the propellant-to-wall lip configuration, changes in the measured growth constant on the order of 50 sec^{-1} were observed (for corresponding conditions in the pressure-coupled T-burner changes of approximately 15 sec^{-1} are observed).

No significant difference in the response was observed in the data when the driver sample was varied. Thus, it appears that the technique gives consistent results independent of mean flow and acoustic pressure amplitude.

Considerable uncertainty remains in quantitative interpretation of the data obtained due to the acoustic/flow interaction terms, VF and VFG. Until the magnitude of these terms has been defined there will be uncertainty in the value of the velocity-coupled response (the same holds true for pressure-coupled data also). A series of tests were fired with the purpose of evaluating these terms. The results indicate that the net sum of VF-VFG is an acoustic loss with a value of -3. Actually, the data could be indicating that the formulation of the acoustic equations is not adequate to describe the T-burner; possibly a two-dimensional description is required.

Nonlinear interpretation of the data indicate that the nonlinearities are greater than those observed in a pressure-coupled T-burner.

The net result from the current contract has shown that velocity coupling is significant and is quantitatively measurable. The results further show the velocity-coupled T-burner to be extremely promising as a quantitative tool for measuring velocity coupling. However, the results are somewhat preliminary in nature and considerable future work needs to be performed to develop the technique and velocity-coupling technology in general.

SECTION III

VELOCITY COUPLING BACKGROUND

At the onset of the present study a literature review was conducted to determine the state of knowledge for velocity coupling. The review was conducted with the objectives of helping to develop an understanding of the role of velocity coupling and to help identify and evaluate potential methods for quantitatively measuring velocity coupling.

A. INTRODUCTION

Velocity coupled combustion instability has been referred to by several names in the literature including axial mode instability, intermediate frequency instability, acoustic erosivity, and nonlinear longitudinal instability. These names probably refer to two velocity dependent phenomena which have occurred at different pressures, frequencies, and motor conditions. These two phenomena which Price[1] referred to in 1964 as "mild" or "severe" forms will be discussed here as "linear velocity coupling" and "acoustic erosivity." Acoustic erosivity occurs when the scrubbing action of the acoustic wave increases the mean burning rate of propellant, probably due to enhanced heat transfer at the propellant surface. It is apparently caused by the same mechanism that leads to erosive burning in rockets having large magnitude velocities. In the present case, however, the large velocity is caused by an acoustic oscillation which can be driven by either pressure or velocity coupled combustion instability. It has been studied extensively over the years with the earliest paper directed specifically at acoustic erosivity by Hart, Bird and McClure in 1960.[2] Several theoretical papers have been published since then considering the interaction of an erosive burning mechanism and acoustics.[3-6] As a result, the basic equations describing an assumed propellant response to a velocity wave, interacting with the acoustics of a rocket motor, are well defined.

There are a large number of occurrences of acoustic erosivity documented in the literature. Price has published two review papers on occurrences of combustion instability in rocket motors covering the period of time up to 1964.[7,8] He documents over 20 cases of "intermediate frequency instability," in development or operational motors, the majority of which exhibited acoustic erosivity (i.e., a significant mean pressure shift due to the acoustic oscillations). In only one of these cases did the motor actually fail (i.e., blew up) due to acoustic oscillations. However, in most cases performance deviated sufficiently from design conditions that the acoustic problem had to be solved before the motor was acceptable.

Price[9] and Brownlee[10] have performed extensive laboratory testing with small scale hardware in both end vented and center vented configurations. A principal measurement in both studies was the ballistic mean pressure shift indicating onset of acoustic erosivity. These studies and the cases quoted above include composite propellants (all types of binders), double-base propellants, and CMDB propellants both with and without aluminum; in short, all types of solid propellants and a wide range of burn rates.

The second form of velocity coupling, referred to here as linear velocity coupling, occurs when the phasing of the propellant combustion is such that combustion couples with the acoustic velocity wave to either drive or attenuate the acoustic wave. It is directly analogous to pressure coupled combustion instability in that it is the response of the solid propellant combustion to a transient velocity wave over the propellant surface. Examples of this linear velocity coupling are not as readily available as for acoustic erosivity. This is due to the fact that in a motor or a T-burner, oscillations driven by linear velocity coupling cannot easily be distinguished from pressure coupled oscillations. Actually, linear acoustic oscillations will normally occur as a result of a sum of the driving from both pressure-coupled and velocity-coupled sources, except in special cases.

The identification of linear velocity coupling is closely related to theoretical analyses of acoustic chambers for velocity coupling. Theory indicates that for a symmetrical end vented motor, velocity coupling in one end cancels that in the other end leaving a net value of zero. Conversely, in a center vented motor there is virtually no way to eliminate velocity coupling (except, of course, for end burning grains). Thus, to verify the existence of linear velocity coupling, the established acoustic analyses must be carefully applied to particular cases where test variables have been varied to emphasize velocity coupling effects. Price observed a "mild form" or sinusoidal oscillation in his testing, usually preceding the more severe form of oscillation. This mild form is interpreted here as being linear velocity coupling. Probably the most emphatic evidence for linear velocity coupling has been generated on the current program.

Historically, Price reports "Acoustic instability in the axial mode of solid propellant rocket motors was relatively uncommon prior to 1958." However, as is evident from the literature of the early 1960's, axial mode combustion instability became of increasing concern. This was due in part to the development of larger motors and to the extensive use of aluminized propellants (which appear to be more susceptible to this mode of instability). Also, the general increased level of funding in rocketry resulted in many studies relating to combustion instability of all types.

In the early 1960's, a pulse test technique was developed[9-11] which permitted the qualitative evaluation of this form of instability. This pulse technique has been used extensively since then in various studies of combustion instability (see discussion in paragraph C.). At very nearly the same time a mathematical treatment of axial mode instability for a solid rocket motor was published.[3] These initial studies relating to velocity coupled instability provided added impetus to the field and many related studies have continued since then.

In spite of the many programs and the progress that was made, virtually no progress was made in developing a small scale laboratory tool for evaluating velocity coupling. The lack of such a laboratory tool capable of quantitative evaluation of velocity coupled instability has hampered progress considerably. However, one laboratory tool has been developed that is worthy of mention at this time. The modified T-burner was developed by Stepp,[12] specifically to measure velocity coupled instability. The mathematical development of the concept is basically sound and initial testing appeared to be very promising. However, cost, reproducibility, and the apparent lack of sensitivity seemed to have hampered extensive acceptance of the device.

In the following paragraphs, both the analyses and experimental studies that have been performed will be discussed and evaluated in more detail.

B. ANALYSES OF VELOCITY COUPLED INSTABILITY

1. Basic Theory

Acoustic oscillations in a rocket motor are driven by an interaction between the combustion process and the acoustic oscillations. The burning propellant adds energy to the acoustic wave when the mass flux from the surface increases during the wave compression half cycle and decreases during the wave rarefaction half cycle. The mass flux from the burning propellant may, of course, have any phase relationship to the acoustic wave but only that component of the fluctuating mass flux that is in phase with the acoustic wave (in the sense described above) will add energy to the wave and thereby drive the wave to larger amplitudes.

The acoustic wave is postulated to interact with the combustion process in two ways: (1) The combustion is affected by pressure oscillations normal to the burning surface, and (2) the combustion is affected by oscillations in the gas velocity tangent to the burning surface. The first type of interaction is known as pressure-coupled response while the second type of interaction is known as velocity-coupled response. In general, both of these interactions can and will exist simultaneously. The development of governing equations describing pressure-coupled and velocity-coupled acoustic driving must assume a relationship between the fluctuation of mass flux and the acoustic oscillations. This relationship (the velocity coupled response) can be defined as

$$R_v \equiv \frac{m_b'/\bar{m}_b}{\left[\,|u' + \bar{u}| - |\bar{u}|\,\right]/a}$$

The most extensive analysis of combustion instability in solid propellant rocket motors has been carried out by Hart, McClure, and co-workers in the Applied Physics Laboratory. This group published four papers and reports[2-5] during the period 1960 to 1965 which are particularly important to this subject. In these articles the concept of velocity coupled combustion instability is explored in considerable detail. Subsequent work by Culick,[13] Hopkins,[14] and Flandro[15] has somewhat expanded the work of Hart and McClure, but has not altered their fundamental conclusions.

The Hart-McClure analysis leads to the following basic equation for the experimental growth constant for acoustic oscillations in a motor or burner:

$$\alpha = -(1/2) \frac{\left\langle \int \left[p' \underline{u}' + \frac{u(p')^2}{a^2} + \rho (\underline{u} \cdot \underline{u}') \underline{u}' \right] \cdot dS \right\rangle}{\left\langle \int_V \rho (u')^2 dV \right\rangle} + \alpha_v \qquad (3\text{-}1)$$

where $\langle\ \rangle$ indicates the time average, and α_d the damping constant associated with volume losses, and the other quantities are defined in the List of Nomenclature.

Subsequent analysis (See Section IV and Reference 16) leads to the equation:

$$\alpha_{vc} = \frac{\gamma \bar{u}_b}{2} \frac{\int_{S_b} (\tilde{p}_b^{\,2}/\tilde{\epsilon}_b)\ \mathrm{Re} \left\{ \left(R_v(\omega) \right) \overbrace{\left[|u_e| - |\bar{u}_e| \right]} \right\} dS_b}{\int_V \tilde{p}_b^{\,2}\ dV} \qquad (3\text{-}2)$$

where α_{vc} is the contribution to the growth constant from velocity coupling. Culick[13] postulates that there is an additional flow turning term which will be discussed in more detail in Sections IV and VII. The important conclusions reached when the above equation is applied to various test conditions are as follows:

(a) Velocity coupling can either amplify or attenuate oscillations.[2,3]

(b) Velocity coupling is dependent on the comparative amplitudes of the mean and acoustic velocities.[2,3,13]

(c) The grain geometry, the nozzle placement, and the chamber configuration critically affect the velocity coupling.[2,13]

(d) Velocity coupling can cause coupling between various modes.[4]

(e) Axial modes will ordinarily be those subject to velocity coupling.[3] (i.e., Velocity coupling is proportional to the product of mean flow and acoustic velocity vectors. Transverse modes will generally be perpendicular to the mean flow; therefore, their contribution to velocity coupling is ~ zero.)

(f) Velocity coupling nonlinearities may cause a motor that is stable to small amplitude pulses to be unstable to large amplitude pulses. For example, consider a motor where velocity coupling is stabilizing and the motor is stable, if a pulse large enough to cause flow reversal is introduced, the rectifying effect of flow reversal will reduce the contribution of velocity coupling. A situation is readily conceived where the effect could be large enough to result in an unstable condition.

Equation (3-2) has been applied to specific combustors[17] and will be discussed in the following paragraphs.

2. Analysis Emphasizing Combustion

Analyses have been performed by Povinelli,[18] Price and Dehority,[19] and Marxman and Wooldridge.[20] Each of these analyses emphasizes the combustion aspects of the instability more than a general motor stability analysis. Povinelli utilized an analysis basically similar to liquid rocket motor treatment. His results are couched in terms of an "erosive burning factor" which makes his results rather heuristic as far as interpretation is concerned. However, he does emphasize a significant point; that instability is strongly enhanced at low Mach numbers. This effect also becomes evident from several other studies discussed below.

Price and Dehority have undertaken to simplify the extremely complex combustion-flow situation into a simpler phenomenological representation, described by simplified mathematics utilizing time lags for key, but unknown effects. In this manner, the effects of aluminum burning at a considerable distance from the surface and of surface agglomeration are simulated. Similar relationships are developed accounting for the fact that the head and aft end of the motor simultaneously experience different acoustic and flow fields, and that a particular phasing relationship must exist between them to drive acoustic oscillations. For the present discussion, the relationship between the combustion of the aluminum and that of the propellant surface is significant. Before drawing a specific conclusion here, it is best to examine the work of Marxman.

Marxman and Wooldridge make use of a pressure coupled model to describe the onset of axial mode instability and claim success for their model. Judging from the discrepancies in data from pulsed motors (see Section C), their optimism seems at best, premature. However, their approach of utilizing knowledge of pressure coupled instability can be very informative, at least until more knowledge is gained about velocity coupled response.

The peak of the pressure-coupled response curve generally lies in the frequency range of interest for velocity coupled instability (e.g., 300 to 800 Hz for typical parameters). However, the phase of the pressure response goes through zero, from positive to negative with increasing frequency, at very nearly the same frequency as the peak.[21-23] Reasoning that the velocity response is similar to the pressure response phase (i.e., the acoustic velocity is 90^{o} out of phase with the acoustic pressure) one should anticipate both positive and negative values of the velocity-coupled response. Positive values would appear to be more probable at low frequencies while negative values would be more probable with increasing frequencies. It would appear that one could expect to find positive, zero, and negative values of velocity coupling all for a given propellant but at various conditions.

3. Application to Motor Analysis

A computer program has been developed at Hercules for performing acoustic stability analysis following the approaches of References 13 and 15 and is described in Reference 14. The program is a motor stability analysis which computes both pressure coupling and velocity-coupled driving.

This computer program was used to calculate the velocity-coupled acoustic driving in the Minuteman II, stage III rocket motor,[17] using a velocity-coupled response parameter as measured in modified T-burner tests. This program provided the basis for the velocity coupling calculations discussed in Section IV.D.

C. EXPERIMENTAL WORK

1. Small Motor Testing

a. CARDE Work

In the early 1960's an experimental test technique for pulsing a subscale rocket motor into unstable combustion was developed at CARDE. Since that time a very large amount of testing has been performed at CARDE using this technique.[24-32] The basic technique involved motors typically 4 to 5 in. in diameter by 30 to 80 in. long that usually burned with a slightly progressive pressure history. At various times during burning, a charge of black powder is fired into the motor to create the

pulse. Figure 3-1 was taken from Ref. 10 showing typical results for a range of test conditions. The bottom trace shows a configuration that was stable. However, decreasing the throat diameter (increasing the pressure and the port to throat ratio) resulted in a wide range of unstable conditions. The instability was evident in the DC pressure shift and in a very distorted oscillatory wave form (somewhat analogous to a shock front). The data indicate that the instability is more prone to occur at higher pressures or smaller values of J.* Additional data obtained for neutral burning motors show that at constant pressure, a motor may be stable early in the burn time but become unstable at a later time.[30] Thus, pressure is not the only factor influencing the conditions for instability. From these later results, two factors could possibly be important. As the propellant burns, opening up the port, the mean velocity of the gases drops considerably. This could be an important factor. At the same time, the nozzle losses α_N should be decreasing significantly[33] (i.e., $\alpha_N \sim J$).* On the basis of nozzle losses alone, one would expect the motor be be more unstable late in firing as J becomes small.

A second factor that was observed in the CARDE work was that for a given propellant and pressure, a shorter motor (higher frequency) was much more prone to instability.[30,24] Examining the two motors at a given value of pressure, the nozzle damping is a factor of ~5 greater for the short motor and the mean gas velocity is a factor of 2 greater. Based on the other results, both of these trends should have a stabilizing influence. Assuming all of these observations are correct, the frequency must have a very significant effect on velocity-coupled instability. The frequencies of these two motors correspond to ~100 and 250 Hz.

A considerable amount of work was done varying formulation parameters for CTPB and polyurethane systems. For each system studied, well-defined trends were observed for systematic formulation changes with the given system. However, general trends encompassing both binder systems seem to be somewhat confusing. One general trend that seems to hold in the majority of cases is that a higher burning rate propellant tends to be more stable than a lower burning rate propellant.

Some testing was done in a motor modified for taking movies through windows.[26,34,35] There seemed to be a degree of success in obtaining high speed movies as well as continuous Schlieren photographs of shock-type waves.

The very extensive testing that has been performed, yielding only qualitative data which are quite difficult to interpret quantitatively, points up the great need for a quantitative laboratory tool.

---

*J is the ratio of the nozzle throat area to propellant port area.

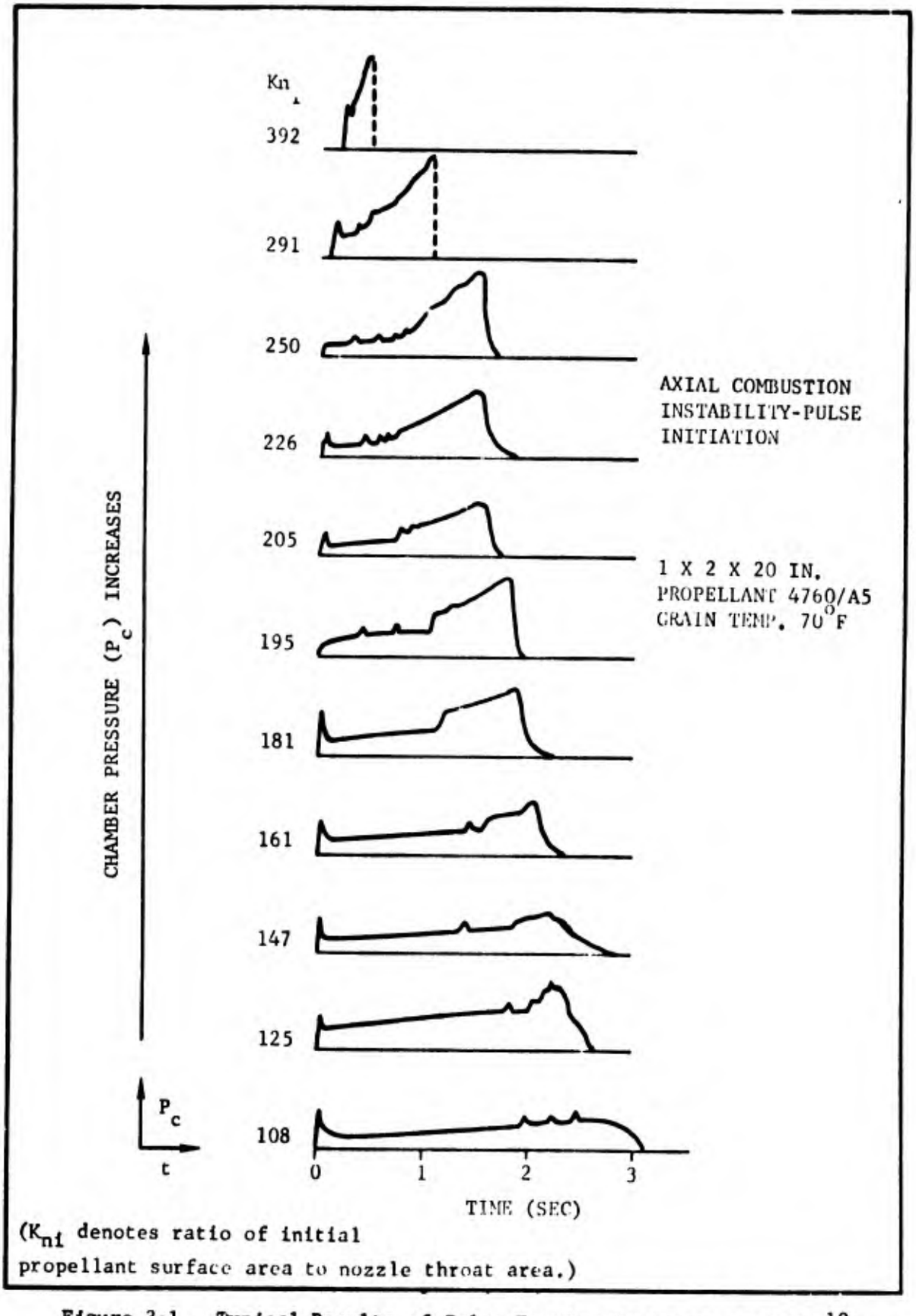

Figure 3-1. Typical Results of Pulse Testing Performed at CARDE[10]

b. SRI Work

Pulse testing has also been conducted at Stanford Research Institute,[36] but the testing there has not been nearly as extensive as the work at CARDE. Data were obtained using several different oxidizers in rubber base binders. The data were interpreted in terms of a threshold burning rate and a threshold pressure at which instability would occur. This concept seems to be directly contradictory with the CARDE results where at a constant pressure, motors were observed to be stable (to a pulse) until late in firing. The most recent CARDE publication[24] also contradicts the general observations of the SRI group. It again appears that there has been a significant amount of data generated in this work that cannot be adequately explained on the basis of the existing state of knowledge.

c. NWC Work

Price[9] reports work done at NWC using a center-vented motor (an "ARPA" motor). In his testing the nozzle losses were eliminated (with the nozzle at a pressure node) thus reducing the complexity of an extra variable. He found that the enhanced stability of the center-vented configuration permitted oscillations to grow spontaneously rather than be induced by pulsing (however, both pulsed and nonpulsed tests were run). The oscillations generally grew sinusoidally at first but with a transition to a very nonlinear (but cyclic) form. It appeared that the nonlinear form accompanied the DC shift in pressure. Price also observed the stabilizing effect of lower pressure that others have observed. For the polyurethane composite propellant that was tested, medium sized aluminum in the propellant formulation seemed more prone to instability than either coarser or finer aluminum particle sizes.

2. Laboratory Scale Testing

The first quantitative measurements of velocity coupling were made by Stepp[12] who developed what has come to be known as the modified T-burner. The basis of the modified T-burner approach is illustrated in Figure 3-2 where the velocity and pressure waves are plotted for a conventional T-burner. Although the velocity wave has a maximum at precise locations, propellant at these locations cannot drive acoustic pressure oscillations because the pressure amplitude is zero (i.e., a nodal point). Therefore, in order for the velocity wave to couple with the combustion and actually feed or amplify a pressure oscillation, the propellant surface must be located at a position where neither the pressure nor the velocity wave is zero. Figure 3-3 shows the configuration used by Stepp where the growth constants due to pressure coupling and velocity coupling have been

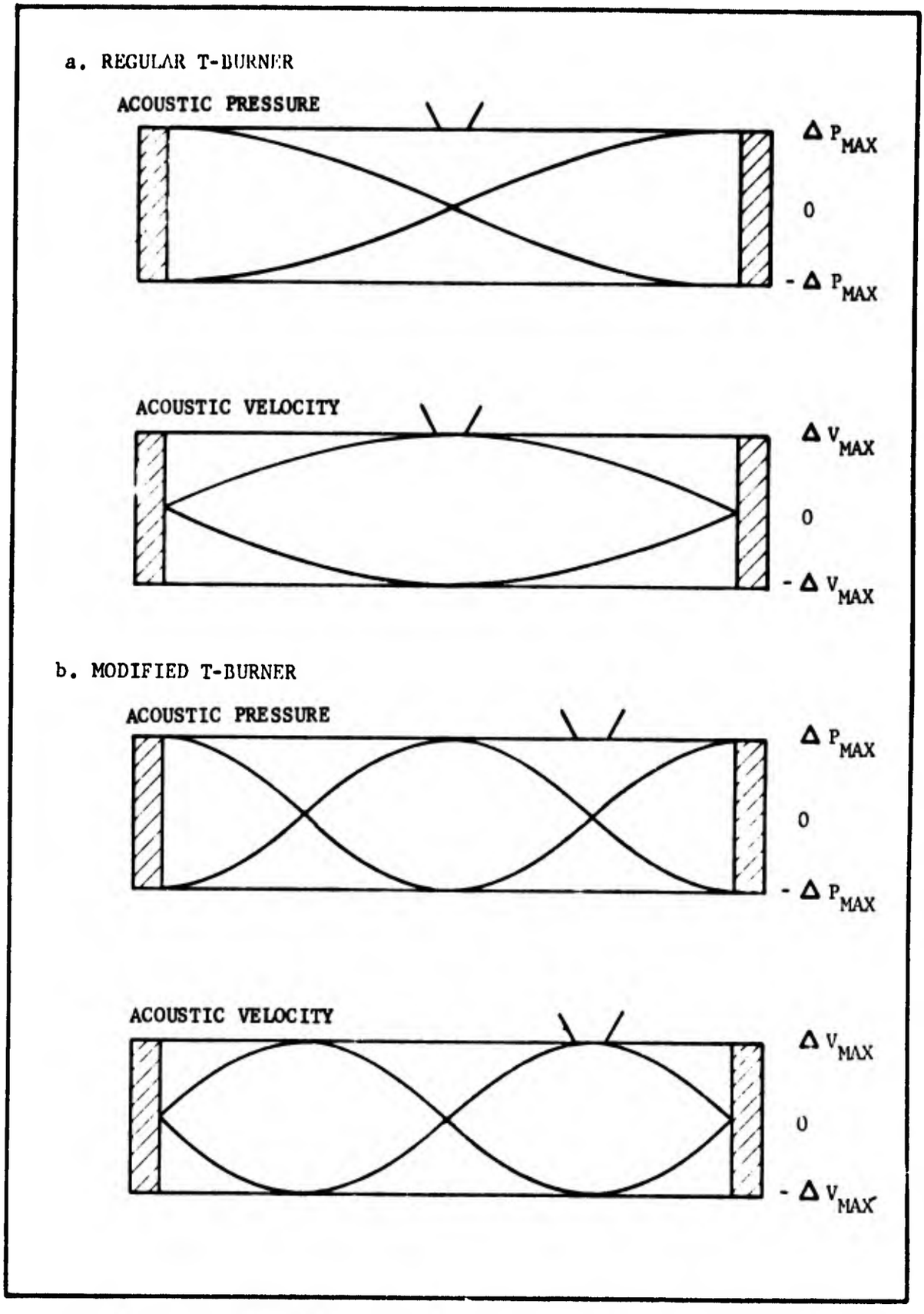

Figure 3-2. Comparison of Acoustics of Regular and Modified T-Burner

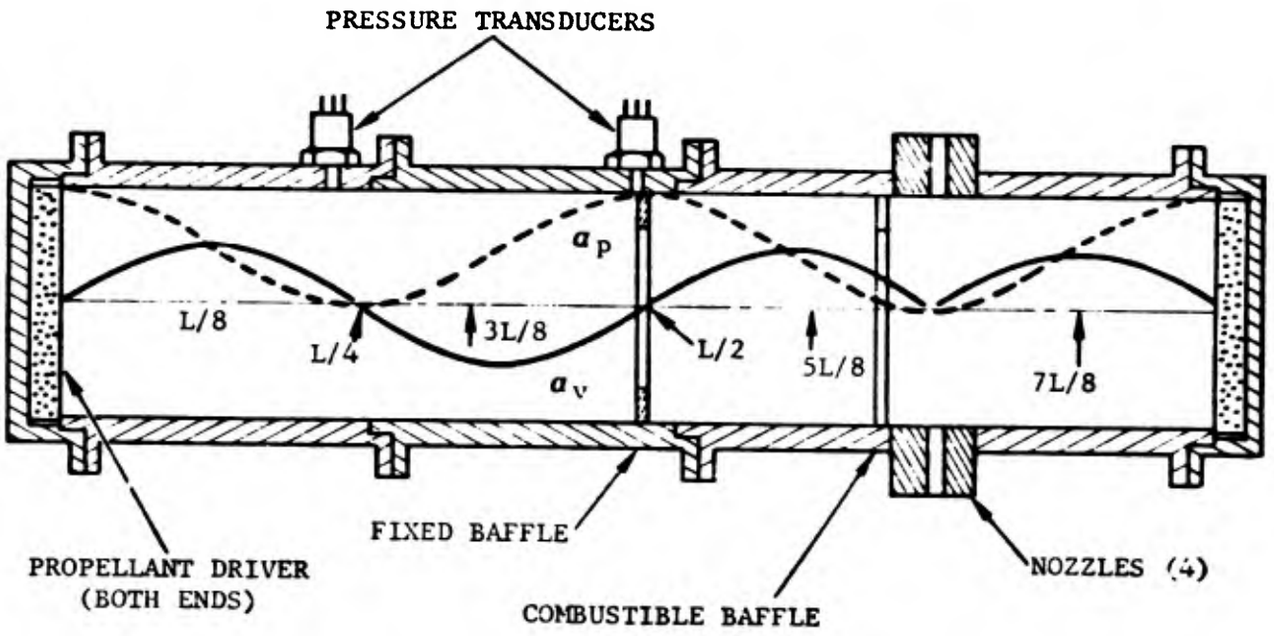

Figure 3-3. Modified 8.5-Inch T-Burner Showing Variation of α_p and α_v with Chamber Position

plotted. Stepp's procedure was to test at the L/8 and 3L/8 position where α_v is maximum. From the figure it can be seen that

$$\alpha_{L/8} - \alpha_{3L/8} = 2\alpha_v \quad . \tag{3-3}$$

A small number of tests were performed with unmetalized propellant. The results showed the potential importance of velocity coupling. The measured values of velocity coupling were on the same order as pressure coupling for the propellants tested. Two of the three propellants actually indicated negative values for the velocity coupled response.

A later program[37] utilized the same burner in an attempt to measure the velocity coupling of two aluminized propellants, but the results were inconclusive. The reasons why can be seen from an examination of the test conditions. Assuming a value of 10 for the velocity coupling response and rearranging Equation (3-3) yields:

$$\alpha_{L/8} - \alpha_{3L/8} = \frac{S_b f^2 L \rho_s \gamma r}{\gamma \bar{P} S_{co}} \; \text{Im}\left[cR_v(\omega)\right] \tag{3-4}$$

if the corrective term for particle damping is neglected. Using the appropriate values for the parameters, we find that

$$\alpha_{L/8} - \alpha_{3L/8} = 14.$$

For typical growth constants of about 50 sec^{-1} and typical scatter obtained in T-burner experiments of ~10 to 15 percent, it is clear that such a difference would be difficult to identify in the data scatter for the test conditions.

Practical disadvantages of the modified T-burner were principally that (1) the test sample was mounted in the center of the burner and thus was subjected to abnormal flow conditions, and (2) there was an undesirable mixing of the unmetalized driver gases and the metalized test sample gases. These disadvantages, coupled with the insensitivity described above, have kept the modified T-burner concept from wide acceptance.

3. Miscellaneous Burners and Concepts

Two other small scale burners should be mentioned here. These are the pancake burner, developed and tested by Povinelli[38,39] and a "velocity coupling" burner tested by Eisel.[40] Both of these burners

were developed to obtain qualitative information on a smaller scale than the motors discussed above.

The pancake burner consisted of a flat center vented burner with a center perforated propellant grain. A gas generator fed gases tangentially into the main chamber causing transverse mode instability. The burner represents a rather novel approach in that suppressive additives could be injected independently to the main chamber from the gas generator. However, the data obtained were very qualitative and there appears to be little prospect of adapting it to obtain quantitative data.

The burner developed by Eisel consisted of two opposed, burning slabs of propellant with rotating vented discs at either end of the burner. The discs were aligned so that when one exposed an open vent, the other was closed. By rotating the discs, flow could be reversed at a desired frequency across the propellant surfaces. The combustion was monitored by a pressure gage and visually through transparent side walls. Again, the burner did not provide quantitative data and the problem of providing a seal between the moving disc and the burner proved to be virtually insurmountable.

An approach to measuring velocity coupling that was considered early in the present study was the use of a propellant sample mounted on a spinning disc and placed in a hot gas flow field. (See Figure 3-4.) A varying velocity would be achieved by moving the propellant relative to the gas rather than acoustically moving the gas with respect to the propellant surface. However, to achieve frequencies of 1000 Hz would require 60,000 rpm disc rotation speed. Even at speeds (and corresponding frequencies) much lower than this, centrifugal forces would probably be important enough to obscure effects produced by the alternating velocities. Hence, this approach was abandoned.

Before proceeding, it seems worthwhile to review some of the many devices (other than the T-burner) that were proposed, evaluated, and rejected as laboratory tools for measuring pressure-coupled instability.

Price[41] developed a system called the Helmholtz burner that consisted of two coupled Helmholtz resonators that were self-excited by propellant grains inside the resonators. This system was abandoned because the oscillations were erratic and not reproducible.

Efforts were made at Rocketdyne[42,43] to study instability by the use of a weak shock imposed on the burning propellant. This method, which depended on comparing the impinging and reflecting shocks, was extremely attractive because of the wealth that theoretically could be obtained from one test. However, it was found impossible to achieve the very high precision required for successful operation.

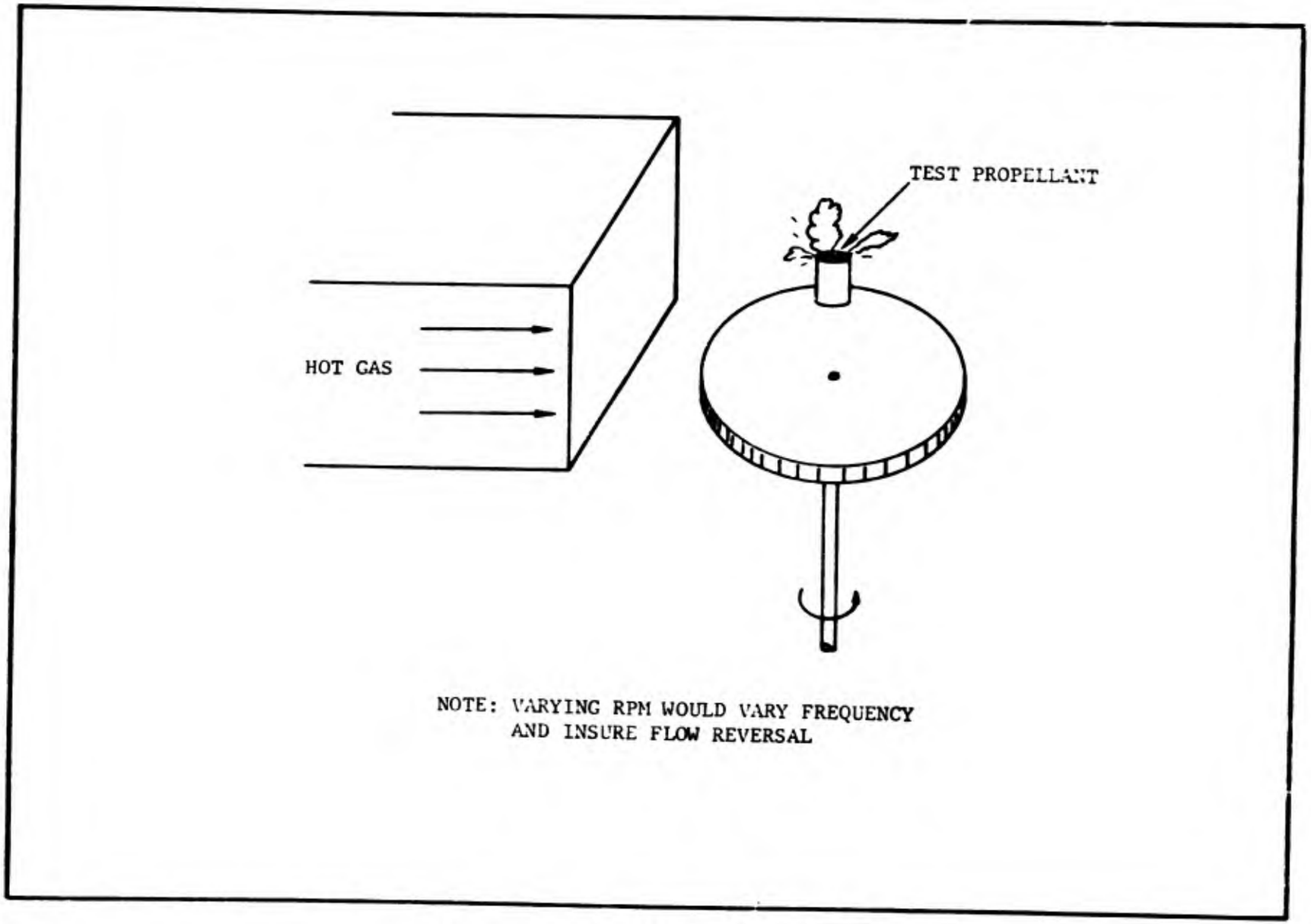

Figure 3-4. Possible Test System

To avoid the restrictions imposed by the self-excited T-burner, several attempts[44-47] were made to use driven systems for providing the acoustic field. In all cases, it was found that some measurement, usually varying light emission, definitely indicated an interaction between the combustion and the pressure oscillations. However, it was not possible to use the measurements and analytically calculate the values for pressure-coupled instability.

D. SUMMARY OF PAST EXPERIENCES AND RECOMMENDATIONS

The acoustic analyses that have been performed by various investigators (e.g., McClure et al, Culick, Hopkins, etc) of rocket motors are very similar in many respects and provide a solid foundation for further work. The combustion related analyses of Price and Dehority or Marxman and Wooldridge (as discussed above) also contribute to the fundamental understanding of velocity-coupled instability.

The experimental work performed at CARDE, NWC, and SRI is very extensive, but a comprehensive understanding of causes and effects is lacking. The SRI conclusion that some propellants or motor lengths (i.e., frequencies) are inherently stable seems to be contradicted directly by the CARDE work. Also, from the above discussion it appears logical that even though a propellant is stable at one set of conditions, there is ample evidence to suspect that there are conditions at which it will exhibit instability. The trends that do seem to be consistent can be summarized mainly as high pressure and lower mean burning rate both promote instability. Both are related to a low gas velocity. With all of the other observed trends, there appeared to be contradictory data for similar but slightly different test conditions (e.g., comparing effects with CTPB or PU binder). One interesting observation is that CARDE testing indicates a higher level of instability at higher frequencies while SRI reports the opposite. It would appear that for the given test conditions, each was on opposite sides of a peaked response curve of some nature. In spite of all the apparent contradictions, there is a wealth of experimental information waiting to be explained.

The review of various pressure-coupled devices indicates that quantitative pressure coupling has been determined only from resonant systems in which the amplitude of the pressure oscillations was measured. It was possible to use other experiments to obtain qualitative but not quantitative results. This observation must be considered in the selection of an experiment to quantitatively measure velocity coupling.

Based on the above review, it appeared (at the beginning of this program) that to obtain quantitative data on velocity coupling an adaptation of the T-burner looked most promising. Utilization of Stepp's approach adapted to overcome the disadvantages of the modified T-burner appeared to have the potential of being the sought after laboratory tool.

It is for these several reasons that the emphasis of the proposed program is placed on various modifications of the T-burner as a practical tool for evaluating velocity-coupled instability.

SECTION IV

ANALYTICAL APPROACH

The initial phase of the program (Phase I) was performed to provide analytical support and direction for the later experimental phases. The work is discussed in this section.

A study of the fundamental interaction between acoustic velocity and propellant combustion was performed and is discussed in paragraph A. An existing BYU computer program describing instability in a T-burner was modified and parametric calculations made, which ultimately led to the development of a computer program describing the velocity-coupled T-burner. (See paragraphs B and C.) The third portion of Phase I was the generalization of the existing Hercules motor stability analysis program to include the effects of flow reversal and a threshold velocity on velocity-coupled acoustic driving. This derivation and corresponding calculations are described in paragraph D.

A. FUNDAMENTALS

This subsection considers fundamental velocity coupling phenomenon at the burning surface. The prior status is first reviewed. Then, the related topics of hybrid combustion, erosive burning, and oscillating viscous flow fields are examined for relevance to velocity coupling.

The topic of velocity coupling has received limited attention. Most of the effort has been theoretical with only a small amount of experimental work performed.

1. Prior Work

Theoreticians at the Applied Physics Laboratory dealt with velocity coupling in several papers.[2-5] However, their treatment did not evolve from a consideration of fundamentals. Instead, they assumed that the propellant burning rate dependence on pressure and velocity was either additive

$$r = f(p) + f(u) \tag{4-1}$$

or multiplicative

$$r = f(p)f(u) \tag{4-2}$$

Based upon these assumptions, they developed stability equations for various motor configurations.

Equations (4-1) and (4-2) were used because these forms are useful in describing steady-state erosive burning. Such forms were intuitively argued to apply also to transient erosive combustion which we call velocity coupling.

2. Present Effort

Two logical approaches might be used to study the fundamental phenomenon of velocity coupling. The first is the very rigorous theoretical approach in which the pertinent relationships would be developed from the fundamental mass, energy, momentum, and kinetic equations at and near the burning surface. Such an effort was clearly beyond the scope of this rather limited program. Instead, a second approach, that of examining existing analytical work in related areas and applying the relevant portions to velocity coupling, was used to study the velocity coupling phenomenon.

The objective of this task was to identify on the basis of available analytical treatments, whether the combustion dependence on pressure and velocity is additive, multiplicative (Equations (4-1) and (4-2)), or a more complicated relationship.

Work carried out in the fields of steady-state heat transfer, hybrid combustion, erosive burning, and oscillating viscous flow fields yielded results meaningful to velocity coupling. Therefore, the approaches defined on these subjects but relevant to velocity coupling will be presented in the following paragraphs.

a. Steady-State Heat Transfer

Velocity coupling is the result of changes in the propellant burning rate induced by a transient parallel gas velocity. Presumably, burning rate changes are caused by changes in rate of heat transfer to the propellant. Therefore, it seems likely that steady-state heat transfer equations that apply to turbulent gas flow should be of a form pertinent to velocity coupling. Accordingly, the Dittus-Boelter equation[48] which is applicable to fully developed flow was selected for analysis.

This equation (definition of the symbols is given in the Listing of Nomenclature)

$$\frac{hD_{co}}{k_g} = \left(\frac{D_{co}u\rho}{\mu}\right)^{0.8} (Pr)^{0.4} \qquad (4\text{-}3)$$

may be written as

$$h = K_1 (u\rho)^{0.8} \qquad (4\text{-}4)$$

if a given chamber diameter is selected for analysis and it is noted that the Prandtl Number has a value of about 1 and is independent of pressure

or temperature and the ratio k_g/μ is relatively independent of temperature and pressure.[49] Assuming an adiabatic oscillation and noting that in steady-state, the burning rate is proportional to the heat transfer rate,

$$r = K_2 h = K_3 u^{0.8} p^{0.8/\gamma} \tag{4-5}$$

which has the same form as Equation (4-2). Therefore, this treatment leads to the conclusion that the interaction between the effects of velocity and pressure on burn rate should be of the multiplicative type. Other correlations for heat transfer are similar to Equation (4-3) and lead to the same conclusion.

b. Hybrid Combustion

Previous work[50,51] in hybrid combustion has not dealt with parameters that change rapidly with time. This deficiency means that the equations developed are probably oversimplified when compared to equations required to include transient effects. However, the effect of flow on hybrid combustion may be similar to the effect of flow on solid propellant combustion. Thus, an examination of how pressure and velocity changes affect the burning rate of a hybrid propellant could suggest the form of the interaction in velocity coupling. Marxman[50] suggests that a hybrid propellant grain burns according to the equation:

$$\dot{m} = K_4 \left(\frac{C_H}{C_{HO}}\right)\left(\frac{u_w}{u}\right)\left(\frac{h_{cs} - h_{wg}}{\Delta h}\right)(\rho u)\left(\frac{z\,\rho u}{\mu}\right)^{-0.2} \tag{4-6}$$

Because the product $\left(\frac{u_w}{u}\right)\left(\frac{h_{cs} - h_{wg}}{\Delta h}\right)$ is weakly affected by an adiabatic change in chamber pressure,

$$\dot{m} = K_5 (\rho u)^{0.8} (z)^{-0.2} \tag{4-7}$$

This equation is similar to Equation (4-5), so for this case also, the interaction is of the multiplicative type.

Alternately, the expression derived by Smoot[51] may be used to describe the hybrid grain burning rate. In this case,

$$\dot{m} = 0.03(\rho u)^{0.8}\left(\frac{u}{z}\right)^{0.2}\left(\frac{1}{\lambda}\right)\ln\left[1 + \frac{67m\left(\frac{z}{\mu}\right)^{0.2}}{(\rho u)^{0.8}}\right] \tag{4-8}$$

which, when an adiabatic oscillation is assumed, can be rewritten in functional form resembling Equations (4-1) or (4-2) to give

$$\dot{m} \equiv r\rho_s = f(p)f(u)f(p,u,r) \tag{4-9}$$

This represents neither an additive nor multiplicative but what must be called a complex form of interaction.

c. Erosive Burning

The form of the steady-state erosive burning law should relate directly to velocity coupling. An older equation that fits erosive burning data[52] is of the form

$$r = bp^n \text{ if } u < u_t \tag{4-10}$$

$$r = bp^n \left[1+k_v(u-u_t)\right] \text{ if } u > u_t$$

which can be written as

$$r = f(p) + f(p)f(u) \tag{4-11}$$

This result is similar to Equation (4-9) and again should be described as a complex form of interaction.

An erosive burning rate law that rests on a more solid theoretical foundation is the Lenoir-Robillard equation[53]

$$\dot{m} = bp^n + \frac{K_5(\rho u)^{0.8}}{z^{0.2}} \exp\left[\frac{-K_6 m}{\rho u}\right] \tag{4-12}$$

Assuming an adiabatic oscillation and rewriting in functional form

$$\dot{m} = f(p) + f(p)f(u)f(m,p,u) \tag{4-13}$$

This suggests a very complex form of interaction between pressure and velocity burn rate effects.

d. Oscillating Flow Fields

An extensive amount of effort has been expended in the study of blood flow in a vein or artery. This work has involved investigating an

oscillating flow superimposed on a mean flow. Clearly, this is closely related to the oscillating velocity field in a rocket motor and the results from the blood flow studies could be instructive.

Considering an incompressible fluid oscillating under the influence of a spatially uniform pressure gradient of the type

$$-\frac{dp}{dz} = p'Qe^{i\omega t} \tag{4-14}$$

Wormersley[54] solved the Navier-Stokes equation and found that the velocity oscillation in a tube could be described as

$$u' = \frac{p'Q}{i\rho\omega}\left\{1 + \frac{J_o\left[r\left(\frac{\omega\rho}{\mu}\right)^{1/2} i^{3/2}\right]}{J_o\left[R\left(\frac{\omega\rho}{\mu}\right)^{1/2} i^{3/2}\right]}\right\} \tag{4-15}$$

This velocity distribution, which is extremely difficult to visualize, was subsequently verified experimentally by Linford.[55] Interpretation of the velocity field described by Equation (4-15) shows that the fluid near the wall oscillates with an amplitude larger than the mean amplitude and the phase is shifted with respect to the phase of the bulk fluid. The importance of this effect increases with increasing frequency.

There are two important conclusions to be drawn. First of all, the ordinary equation used to describe the acoustic velocity

$$u' = \frac{aQ}{\gamma}\sin\frac{\omega z}{a}\sin\omega t \tag{4-16}$$

is not correct, and any results derived by its use are suspect.

The second conclusion pertains to the means by which a velocity oscillation leads to an amplification of the acoustic wave. Amplification has been postulated to occur when a velocity oscillation such as that described by Equation (4-16) leads to a perturbation in the mass burning rate of the propellant. Then, if there is a lead or lag in the perturbed burning rate, amplification or attenuation of the acoustic wave may occur. If the acoustic velocity and velocity-induced burning rate oscillations are exactly in phase, there is no coupling between the velocity-induced burning rate perturbation and the acoustic pressure since they are 90^o out of phase. (The mathematics behind these statements are presented in Section IV-B.)

If, however, the more correct Equation (4-15) is used to describe the velocity oscillation, it becomes apparent that the phase of the boundary layer velocity usually leads the bulk velocity phase. Thus, the velocity perturbed burning rate can be in phase with respect to the boundary layer, yet out of phase with respect to the bulk velocity. Accordingly, because of the phase shifting of the boundary layer, the velocity perturbed burning rate should usually be out of phase with respect to bulk velocity oscillation. Therefore, velocity coupling between the perturbed combustion and the acoustic wave is likely whenever such a boundary layer exists.

To make these conclusions definitive, it would be necessary to derive the oscillating velocity considering a compressible fluid, a sinusoidal pressure oscillation, and a nonisothermal transpiring wall. Such a solution has been made by Flandro[56] for tangential oscillations in a rocket motor and results similar to those of Reference 55 were found.

Thus, the results suggest a fundamental mechanism that may be responsible for velocity coupling. Whether or not such a mechanism would lead to additive or multiplicative interaction between velocity and pressure coupling cannot be determined until a complete analysis is actually carried out.

3. Conclusions

Table 4-I summarizes the type of interaction suggested by the various approaches considered in the study reported herein. Considering that the erosive burning approach is probably most valid, it is concluded that the form of interaction is complex. However, the primitive level of experimental effort in the field does not justify a complex representation. Therefore, the use of the multiplicative form is recommended until such time as a fundamental theroretical study coupled with better experimental data leads to a more satisfactory form.

TABLE 4-I

INTERACTION FORMS BASED ON VARIOUS APPROACHES

Approach	Likely Interaction Form	Equation No.
Steady-State Heat Transfer	$f(u)f(p)$ (multiplicative)	4-5
Hybrid Combustion	$f(u)f(p)f(p,u,r)$ (multiplicative or complex)	4-9
Erosive Burning	$f(p) + f(p)f(u)f(u,p,r)$ (complex)	4-13
Oscillating Flow Fields	(unknown)	---

B. VELOCITY COUPLING ANALYSIS

1. Analysis Approaches

The literature currently available on the theory of acoustic instability in solid propellant rocket motors is very extensive. The principal contributors to the development of the theory are McClure, Hart, and Cantrell, at the Johns Hopkins University Applied Physics Laboratory, who concentrated their efforts on instability theory during the period 1960 to 1965. They recognized the importance of the coupling of the burning rate of the solid with the acoustic velocity of the gas in their early work.[2-5] In later publications[57,58], the steady-state velocity of the combustion products was recognized to have an important effect on the burning rate response to acoustic oscillations and the theory was revised to better account for these effects.

The problem of describing velocity effects was recently reexamined by Culick.[13] Following an approach that was different from that of McClure, et al., he obtained equations for predicting the rate of growth of longitudinal acoustic oscillations in T-burners and motors containing internal-burning cylindrical grains that contained a damping term not present in the prior results. This term arose from considerations of the exchange of momentum between the acoustic velocity and the mean flow from a burning surface oriented parallel to the acoustic motion. The importance of considering this damping mechanism was supported by a simplified analysis carried out by Coates.[59]

In this section, the McClure, Hart, Cantrell Theory (MHC Theory) has been critically reviewed and the treatment of steady velocity effects has been modified. The modified theory has then been compared with more recent equations of Culick. A series of parametric calculations has also been carried out to clearly show the velocity-coupling effects predicted by the two theories.

2. McClure, Hart, Cantrell Theory

In the most recent publication by McClure and Hart[60], the general equation for the exponential growth constant is given as (See Equation 3-1).

$$\alpha = -(1/2)\ \frac{\left\langle \int \left[p'\underset{\sim}{u}' + \frac{\underset{\sim}{u}(p')^2}{\rho a^2} + \rho(\underset{\sim}{u}\cdot\underset{\sim}{u}')\underset{\sim}{u}' \right] \cdot dS \right\rangle}{\left\langle \int_V \rho(u')^2 dV \right\rangle} + \alpha_v \qquad (4\text{-}17)$$

where $< >$ indicates the time average, p' and u' are the acoustic pressure and velocity, and a, ρ, and u are the steady-state sound speed, density, and velocity. It is noted that the velocities are treated as vector quantities, and that the components in a direction normal to the surface of the combustion chamber are employed in the integrand of the numerator. The vectors are taken as positive if they are directed outward from the chamber.

For comparison with the more recent theory, it will be convenient to replace the denominator of Equation (4-17) with an equivalent integral in which p' is the variable. Since acoustic oscillations of an enclosed gas are assumed to follow the general theorem of mechanics that the time-average of the total kinetic energy of a system executing small oscillations is equal to the time-average of the total potential energy[61], it follows that

$$\left\langle \int_V \rho(u')^2 \, dV \right\rangle = \left\langle \int_V \frac{(p')^2}{\rho a^2} \, dV \right\rangle. \tag{4-18}$$

It will also be more convenient for comparison with the theory if the velocity vectors are taken as positive if directed into the chamber. With this assumption and Equation (4-18), then, Equation (4-17) may be rewritten as

$$\alpha = \frac{a}{2} \frac{\int_S [\rho a \hat{p} \hat{u}^r + \underset{\rightarrow}{M} (\hat{p})^2 + (\rho a)^2 (\underset{\rightarrow}{M} \cdot \hat{u}) \hat{u}] \cdot dS}{\int_V (p)^2 dV} + \alpha_v \tag{4-19}$$

where $\hat{p}$ and $\hat{u}$ are the amplitudes of the acoustic pressure and velocity, u'^r is the time-average component of the velocity in phase with the pressure, and M is the steady-state Mach number.

In Reference 3, McClure, et al., derived equations relating u'^r at the burning surface to the burning rate response and in turn showed how the burning rate response depended upon the acoustic and steady velocities. According to their analysis

$$\hat{u}_b^r = u_b \left\{ \frac{\hat{p}}{p} \left(R_b^r - \frac{1}{\gamma} \right) + \text{Real} \left(\widetilde{R_v \left[\left| u'_e + u_e \right| - \left| u_e \right| \right]} \right) \right\} \tag{4-20}$$

where u_e is the steady erosive velocity, or the component of the steady velocity parallel to the burning surface, and where u_e' is erosive component of the acoustic velocity.

For the case of longitudinal waves the acoustic field may be described by

$$\hat{p} = pQ \cos\left(\ell\frac{\pi}{2}\beta_o\right) \tag{4-21a}$$

$$\hat{u} = \hat{u}_e = (aQ/\gamma) \sin\left(\ell\frac{\pi}{2}\beta_o\right) \tag{4-21b}$$

During the present study it has been shown for the general case where u_e may be either positive or negative that

$$\left[\left|\hat{u}_e + u_e\right| - \left|u_e\right|\right] = -(iaQ/\gamma)\left|\sin\left(\ell\frac{\pi}{2}\beta_o\right)\right| F \tag{4-22}$$

with

$$F = \frac{1}{\pi}\begin{cases} \pi & \dfrac{u_e}{\hat{u}_e} > 1 \\ -(\sin 2\theta + 2\theta) & -1 \le \dfrac{u_e}{\hat{u}_e} \le 1 \\ -\pi & \dfrac{u_e}{\hat{u}_e} < -1 \end{cases} \tag{4-23}$$

and

$$\sin\theta = -\frac{u_e}{\hat{u}_e} \tag{4-24}$$

Combining Equations (4-20) and (4-22), the magnitude of u_b^r for longitudinal oscillations can therefore be computed by the equation

$$\hat{u}_b^r = u_b\left[\frac{\hat{p}}{p}\left(R_b^r - \frac{1}{\gamma}\right) + \left(\frac{R_v^i aQ}{v}\right)\left|\sin\left(\ell\frac{\pi}{2}\beta_o\right)\right| F\right] \tag{4-25}$$

and, by defining

$$E \equiv (a/\gamma) \frac{R_v^i}{R_b^r} \tag{4-26}$$

$$y \equiv \frac{\pi z}{2} \beta_o \tag{4-27}$$

the magnitude of the product $\rho a \hat{p} \hat{u}^r$ at the burning surface may be computed from the equation

$$(\rho a \hat{p} \hat{u}^r)_b = M_b \left\{ \gamma R_b^r \left(1 + EF \frac{|\sin y|}{\cos y} \right) - 1 \right\} (\hat{p})^2 \tag{4-28}$$

The magnitudes of the second and third terms of the surface integral of Equation (4-19) may be evaluated rather easily at the burning surface. The second term is simply $M_b(\hat{p})^2$ since the steady Mach number is that of the gases issuing from the burning surface. The third term vanishes for burning surfaces parallel to the acoustic motion since $M_b \cdot \hat{u} = 0$. For surfaces perpendicular to the acoustic motion it may be shown that

$$(\rho a)^2 (\underset{\rightarrow}{M} \cdot \underset{\rightarrow}{\hat{u}}) \underset{\rightarrow}{\hat{u}} = \left[M_b (\gamma R_b - 1) \right]^2 (\hat{p})^2 \tag{4-29}$$

and since R_b is known to be of order unity and M_b to be a very small quantity, comparison of Equations (4-28) and (4-29) shows that this term is negligible compared with the first term in the integrand.

It is appropriate at this point to consider the magnitude of the terms of the surface integrand at the position of the nozzle or vent. The first term is usually expressed in terms of an acoustic admittance.

$$A = - \rho a \frac{\hat{u}}{\hat{p}} \tag{4-30}$$

Thus, for an imaginary surface extending across the nozzle to enclose the control volume, for which Equation (4-19) applies, the magnitude of the first term of the surface integrand can be expressed as

$$(\rho a \hat{p} \hat{u}^r)_n = -A_n (\hat{p}_n)^2 \tag{4-31}$$

The second term would be given by

$$\left[\underset{\sim}{M}(\hat{p})^2\right]_n = -M_n(\hat{p}_n)^2$$

where M_n is the steady Mach number at the nozzle entrance.

For nozzles located at one end of the motor or burner, where for longitudinal modes $\hat{u} = 0$, the third term would be equal to zero. For a nozzle or vent located at the center of the burner, McClure, et al., also assumed the magnitude of this term to be negligible. This assumption seems questionable, however, since it implies $\underset{\sim}{M}\cdot\hat{u} = 0$.

The problem of flow through a nozzle having a cross section parallel to the acoustic motion inside the combustion chamber has been considered by Crocco and Sirignano.[62] They assume that when the nozzle entrance is short relative to the wave length of the acoustic motion that the total flow, composed of both steady-state and acoustic components, can be treated as quasi-steady and that the expansion process is adiabatic and isentropic. These assumptions imply that the gas retains both its mean-flow kinetic energy and its acoustic kinetic energy as it passes through the vent, and that the direction of the acoustic velocity vector changes along with that of the steady-flow vector, so that both vector components are always parallel. Thus, following their reasoning

$$\left[(\rho a)^2(\underset{\sim}{M}\cdot\hat{u})\hat{u}\right]_n = -(\rho a)^2(\hat{u})_n^2\,\underset{\sim}{M}_n \tag{4-32}$$

Since the acoustic kinetic energy is assumed to be conserved, $(\hat{u})_n^2$ may be evaluated at a position near the entrance where the acoustic field is approximated by Equation (4-21b), with the result for the center vent that

$$(\hat{u})_n^2 = (aQ/\gamma)^2 \tag{4-33}$$

The resulting equation for the growth constant for the first longitudinal mode in the center-vented T-burner for which Equations (4-21a) and (4-21b) apply, therefore, reduces to

$$\alpha = 2fM_b\left\{\int_{S_b}\gamma R_b^r\,(\cos^2 y + EF\cos y\,|\sin y|)\,\frac{dS_b}{S_c} - \frac{S_b}{S_c}\right\} + \alpha_v \tag{4-34}$$

The corresponding equation for the first longitudinal mode in a motor with a cylindrical internal-burning grain and an end nozzle is

$$\alpha = 2fM_b \left\{ \int_{S_b} \gamma R_b^r \left(\cos^2 y + EF \cos y \,|\sin y|\right) \frac{dS_b}{S_c} - \left(1+\frac{A_n}{M_n}\right) S_b \right\} + \alpha_v \qquad (4\text{-}35)$$

3. Culick Theory

The equation for the linear stability of a rocket motor or T-burner which is subjected to one-dimensional longitudinal oscillations is given by Culick[63] as

$$(k-k_\ell)^2 E_\ell^2 S_c = \left\{ i\rho a k_\ell \left[\left(\hat{p}\hat{u}^r + \frac{u(\hat{p})^2}{\rho a^2} \right) S_{be} \right]_o^L - iak_\ell \int_o^L p \oint \hat{m}^r dq dz \right\}$$

$$+ \left\{ \frac{ik_\ell}{\rho a} \int_o^L \left[(\hat{p})^2 + \frac{1}{k_\ell^2} \left(\frac{d\hat{p}}{dz}\right)^2 \right] \int_o^L m dq dz \right\}$$

$$- \frac{ik_\ell}{a} \int_o^L (\hat{p})^2 \frac{du}{dz} S_c dz - (1/2) \int_o^L S_c \left(\frac{dp}{dz}\right)^2 \frac{dS_c}{dz} dz$$

$$+ \text{nonisentropic terms} + \text{volume terms} \qquad (4\text{-}36)$$

If the following assumptions or definitions are employed:

(1) $\frac{dS_c}{dz} = 0$

(2) $\frac{du}{dz} = \frac{1}{\rho S_c} \int m \, dq$

(3) $\int dq dz = dS_b$

(4) $\frac{1}{k_\ell^2} \left(\frac{d\hat{p}}{dz}\right)^2 = (\rho a \hat{u})^2$

(5) $S_c E_\ell^2 = \int_V (\hat{p})^2 \, dV$

$$(6) \quad \rho = -\frac{a\,\mathrm{Im}(k^2)}{2k_\ell}$$

$$(7) \quad M = u/a = m/\rho a$$

Equation (4-36) may be written as

$$\alpha = \frac{a}{2}\frac{-\rho_a\left[\hat{p}\hat{u}^r + \frac{u(\hat{p})^2}{\rho_a{}^2}\right]_o^L + \int_{S_{bs}}\left[a\hat{p}\hat{m}^r - \frac{m}{\rho_a}(\rho_a\hat{u})^2\right]dS_s}{\int_V(\hat{p})^2\,dV} + \alpha_v + \alpha_i \qquad (4\text{-}37)$$

It is noted that Culick defines $\hat{u}$ and u as positive for motion to the right, and $\hat{m}$ and m positive for motion inward. Alternatively, they may all be defined as positive if directed into the chamber. In this case, the term for the end contributions in the numerator of Equation (4-37) may be replaced by the integral $\int_{S_{be}}\left[\rho_a\hat{p}\hat{u}^r + M(\hat{p})^2\right]\cdot dS_{be}$.

For purposes of comparison with the prior theory, the fluctuation in mass flow, $\hat{m}$, may be expressed in terms of the fluctuations in pressure and velocity utilizing the following isentropic compression relationships.

$$\hat{m} = \hat{p}u + \hat{u}\rho \qquad (4\text{-}38)$$

$$\hat{\rho} = \hat{p}/a^2 \qquad (4\text{-}39)$$

Thus

$$a\hat{p}\hat{m}^r = \rho_a\hat{p}\hat{u}^r + M(\hat{p})^2 \qquad (4\text{-}40)$$

and Equation (4-37) can be rewritten as

$$\alpha = \frac{a}{2}\frac{\int_S\left[\rho_a\hat{p}\hat{\underrightarrow{u}}^r + \underrightarrow{M}(\hat{p})^2 - \underrightarrow{M}(\rho_a\hat{u})^2\right]\cdot dS}{\int_V(\hat{p})^2\,dV} + \alpha_v \qquad (4\text{-}41)$$

where the surface integral applies to both the sides and the ends of the burner.

On comparing Equation (4-41) with Equation (4-19) it is apparent that they are identical except for the last term in the integrand of the surface integral. In the MHC theory, the sign of this term is positive and the vector dot product $\vec{M}\cdot\hat{u}$ appears. In the Culick theory, the sign of the term is negative, and the acoustic velocity appears as a scalar quantity.

From an intuitive point of view, the positive sign of the MHC theory is more appealing since this term ostensibly represents the convection of kinetic energy while the second term in the integrand ostensibly represents convection of potential energy. Thus, the two terms might be expected to have the same sign, both being positive if the energy is convected into the chamber and vice-versa.

The Culick theory also implies that when the nozzle or vent is located at a velocity anti-node, as in the T-burner, that the flow through the vent serves as a source of acoustic energy rather than as a sink. This is contrary to the reasoning of Crocco and Sirignano.[62]

For a T-burner configuration in which Equations (4-21a) and (4-21b) apply, Equation (4-41) can be simplified following the same reasoning with regard to $\hat{u}^r$ as used above in the MHC theory to

$$\alpha = 2fM_b \int_{S_b} \left\{ \gamma R_b^r (\cos^2 y + EF \cos y |\sin y|) + \cos^2 y \right\} \frac{dS_b}{S_c} + \alpha_v \qquad (4\text{-}42)$$

For a motor with a cylindrical cavity, Culick's theory reduces to an equation identical with the MHC result. (Refer to Equation (4-35).)

4. Initial Parametric Calculations

Two series of parametric calculations were made in order to show the differences in the predictions resulting from the MHC and Culick theories. The first series of calculations were carried out for the T-burner configuration of Figure 4-1. Burning propellant was assumed to cover the ends of the burner and two small internal-burning cylindrical samples were assumed to be placed at various locations between the end of the burner and the vent. Displaced samples were assumed to be flush with the T-burner wall, and the acoustic mode shape was assumed to be described by Equations (4-21a) and (4-21b). Thus, the end grains would be subjected only to an acoustic pressure perturbation and the contribution of acoustic velocity coupling would be produced only by the small internal-burning cylindrical grains. Parametric calculations, therefore, were made for the contribution of the cylindrical grains to the growth constant.

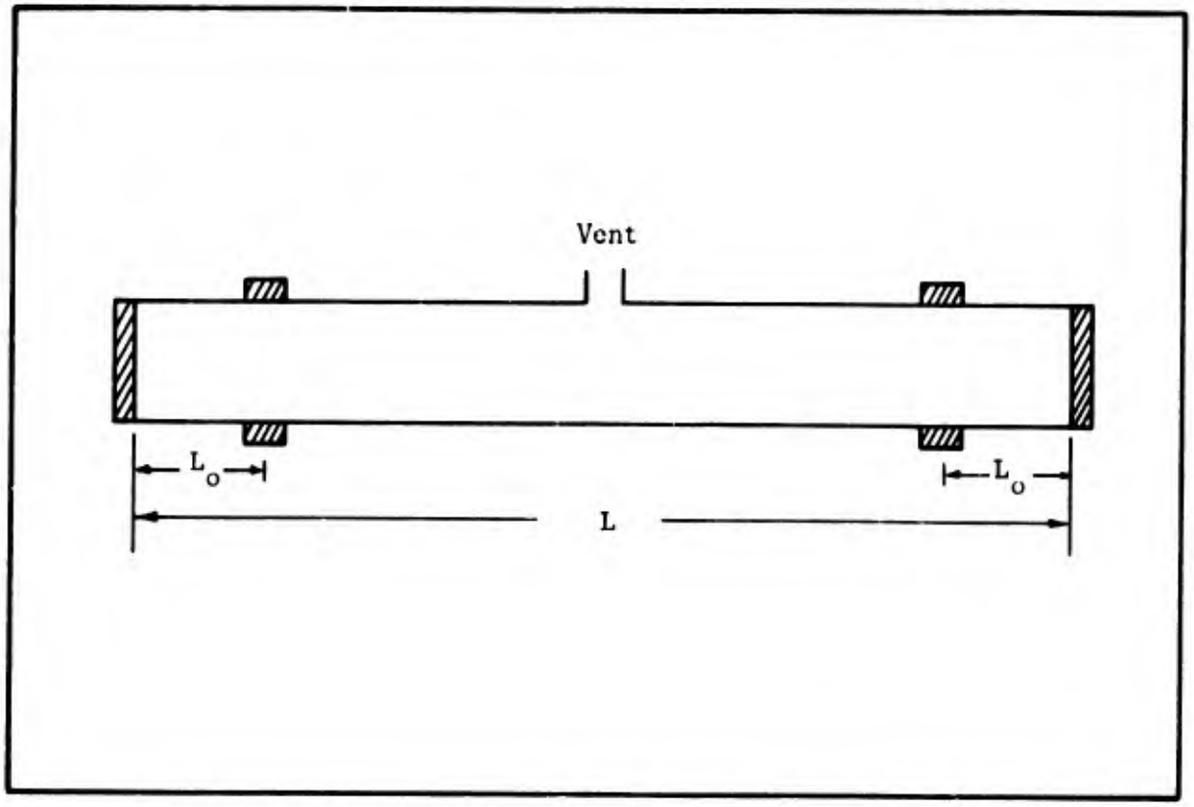

Figure 4-1. T-Burner Configuration Assumed in Parametric Calculations for Comparison of Theories

a. Modified MHC Theory

The contribution of the small cylindrical grains due to coupling with the acoustic pressure and mean velocity as obtained from Equation (4-34) is

$$\frac{\alpha_{pc}}{4fM_b(S_{bs}/S_{co})} = \gamma R_b^r \cos^2\left(\frac{\pi}{2}\beta_o\right) - 1 \qquad (4\text{-}43)$$

where S_{bs} now denotes the burning surface in one end of the burner.

Figure 4-2 shows the predicted variation of the pressure-coupled contribution with sample position and with the magnitude of the product γR_b^r. It is interesting to note that the modified MHC theory predicts a damping effect for $\gamma R_b^r > 1.0$ if the grains are located sufficiently close to the vent. Thus, if $\gamma R_b^r = 3.0$, damping is predicted to occur if the sample position is a distance of 0.3L from the end of the burner. Experimental data which conform to these predictions have been reported by the Thiokol Chemical Corp.[64]

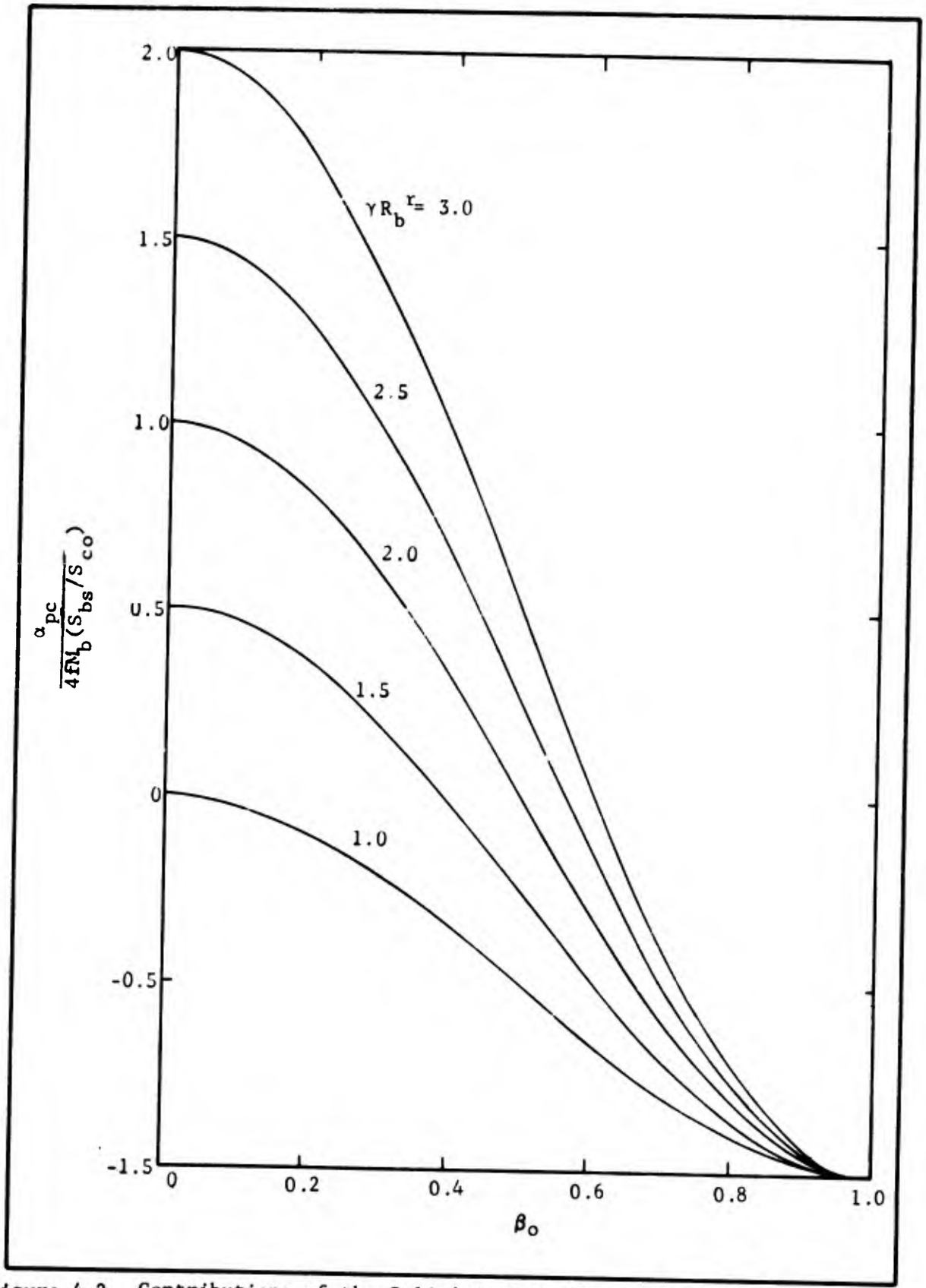

Figure 4-2. Contributions of the Cylindrical Sample to the Growth Constant According to the Modified McClure-Hart-Cantrell Theory (Pressure and Steady Velocity Coupling Only)

These calculations suggest that, in the absence of acoustic-velocity coupling, an alternative procedure to the variable-area technique for measuring the effective magnitude of γR_b^r would be to use fixed size samples and to vary the sample position with respect to the burner vent. The resulting effect on the growth constant could then be compared with the theory using a plot similar to that shown in Figure 4-2.

The contribution to the growth constant due to coupling of the burning rate with the acoustic velocity is obtained from Equation (4-34) as

$$\frac{\alpha_{vc}}{4fM_b(S_{bs}/S_{co})} = \gamma R_b^r EF \cos\left(\frac{\pi\beta_o}{2}\right) \left|\sin\left(\frac{\pi\beta_o}{2}\right)\right| \qquad (4\text{-}44)$$

Figure 4-3 shows the predicted variation of this contribution with sample position and with the magnitude of the ratio of the steady velocity to the amplitude of the acoustic velocity. The most notable feature of these predictions is that for a fixed steady velocity, the acoustic velocity-coupled contribution diminishes with increasing amplitude of the acoustic oscillations. Thus, if oscillations build up to the point where $\bar{u}/\hat{u} < 1.0$ the effect of this type of coupling would be greatest at the onset of acoustic oscillations. Another interesting feature of these predictions is that there should be no effect of acoustic velocity coupling if the samples are located in the center of the burner. The effect should be greatest when the samples are located midway between the end and the vent.

It is not unreasonable that the acoustic erosivity might exhibit a threshold velocity effect similar to that of Equation (4-10). The result would be that the acoustic velocity coupling would diminish when the amplitude of the acoustic velocity was greater than the mean velocity minus the threshold velocity. In other words, as the oscillations grow in amplitude, the acoustic velocity coupling begins to diminish sooner than is the case if there is not a threshold velocity. Qualitatively, the behavior is otherwise similar, although there would be quantitative differences that might be observed if very accurate experimental data were obtained.

b. Culick Theory

Utilizing Equation (4-42), the contribution of the small cylindrical grains to the growth constant as a result of coupling with the acoustic pressure and mean velocity is found to be

$$\frac{\alpha_{pc}}{4fM_b(S_{bs}/S_{co})} = \left(\gamma R_b^r + 1\right) \cos^2\left(\frac{\pi\beta_1}{2}\right) \qquad (4\text{-}45)$$

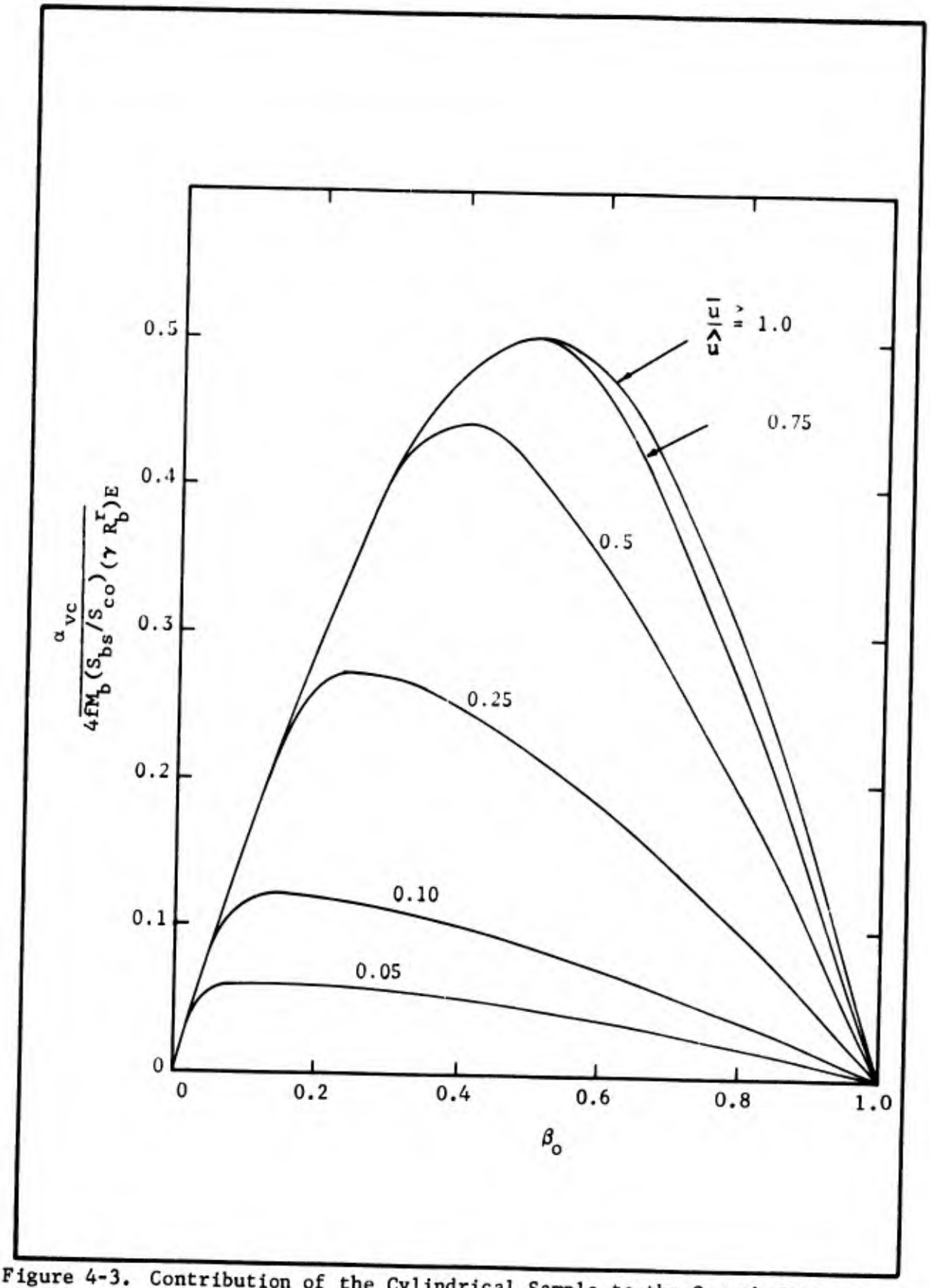

Figure 4-3. Contribution of the Cylindrical Sample to the Growth Constant According to the McClure-Hart-Cantrell Theory (Acoustic Velocity Coupling Only)

Figure 4-4 presents the results of parametric calculations using this equation. The curves in Figure 4-4 illustrate that Culick's theory predicts a positive contribution if $\gamma R_b^r > 0$ for all sample positions except at the center of the burner. This prediction is in contrast to the predictions of the MHC theory shown in Figure 4-2.

It may, therefore, be concluded from these calculations that a simple test of the validity of the theories would be to carry out T-burner tests using the configuration of Figure 4-2 with the cylindrical samples placed at the center of the burner. If the growth constant measured with this contribution is found to be less than the growth constant resulting with only end-burning samples in the burner, the MHC theory would be indicated as the better description of the unstable burning process. On the other hand, if the difference between the tests with cylindrical samples were negligible, Culick's theory would be indicated as better.

5. Calculations for Cylindrical Grains of Extended Length

A second series of parametric calculations was made by applying the modified MHC theory to the T-burner configuration shown in Figure 4-5. These calculations were made to provide insight as to the relative contributions from pressure and velocity coupling resulting from the type of configuration currently being used in the variable-area T-burner technique.

The contribution to the growth constant produced by coupling the burning rate to acoustic pressure and steady velocity is obtained by carrying out the integrations of Equation (4-24) for the mode shapes of Equations (4-21a) and (4-21b) and the configuration of Figure 4-5. The equation is

$$\frac{\alpha_{pc}}{8fM_b(L/D)} = \left(\frac{\beta_1}{2}\right)\left\{\gamma R_b^r\left[1 + \frac{\sin(\pi\beta_1)}{\pi\beta_1}\right] - 2\right\} \qquad (4\text{-}46)$$

Figure 4-6 presents the results of the calculations made with this equation. The interesting feature of these calculations is the prediction that, in general, cylindrical grains of length equal to approximately one-fourth the burner length provide stronger driving of acoustic oscillations than do longer length grains. Furthermore, the theory predicts that if the product γR_b^r is less than 1.5, a full length grain would be stable, but quarter-length grains would produce substantial driving energy.

The contribution to the growth constant of coupling with the acoustic velocity is obtained from Equation (4-34) as

$$\frac{\alpha_{vc}}{8fM_b(L/D)\,a\,R_{vi}} = \int_0^{\frac{\beta_1}{2}} F\left|\sin(\pi z/L)\right|\cos(\pi z/L)\,d\left(\frac{z}{L}\right) \qquad (4\text{-}47)$$

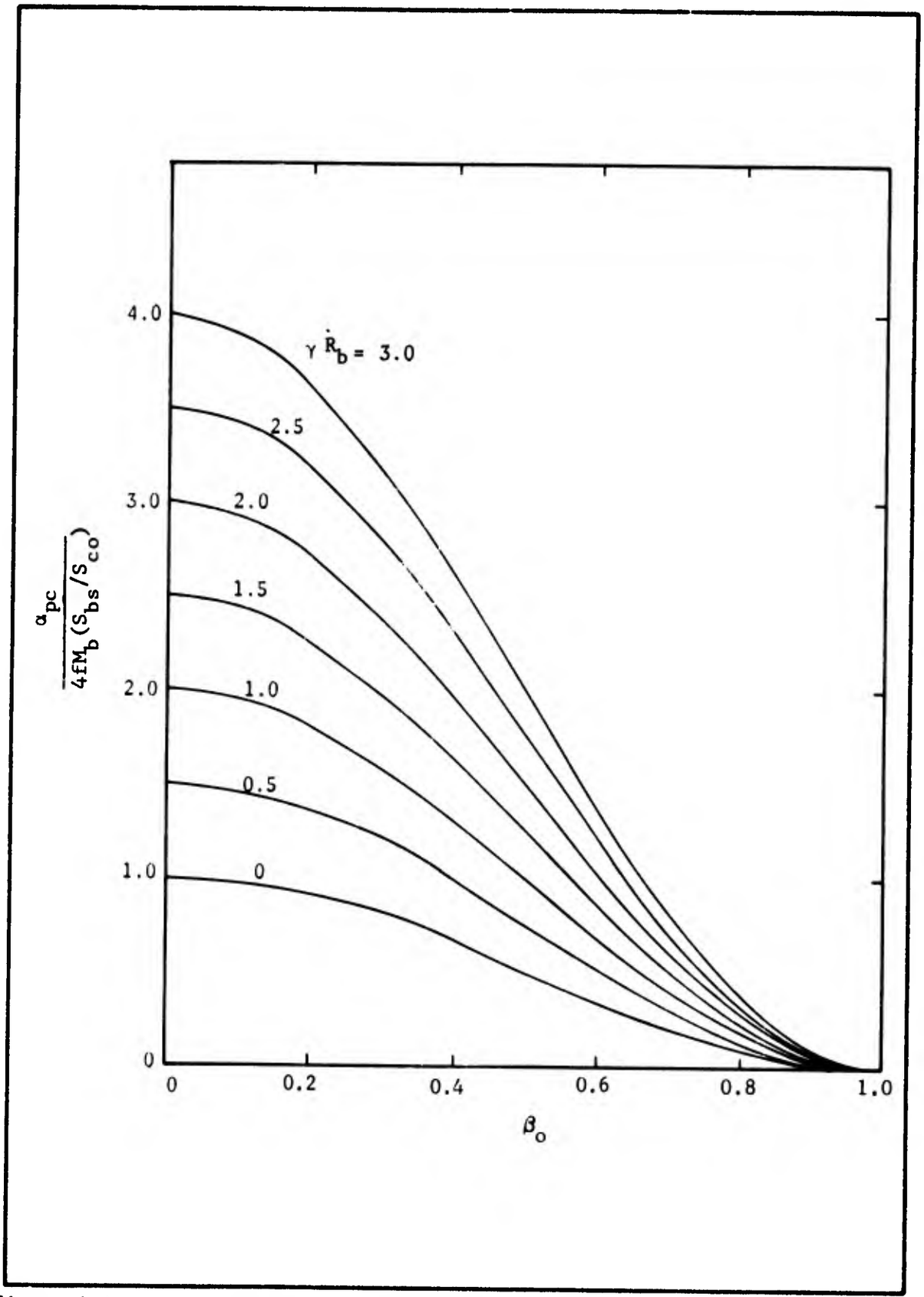

Figure 4-4. Contribution of the Cylindrical Sample to the Growth Constant According to Culick's Theory (Pressure and Steady Velocity Coupling Only)

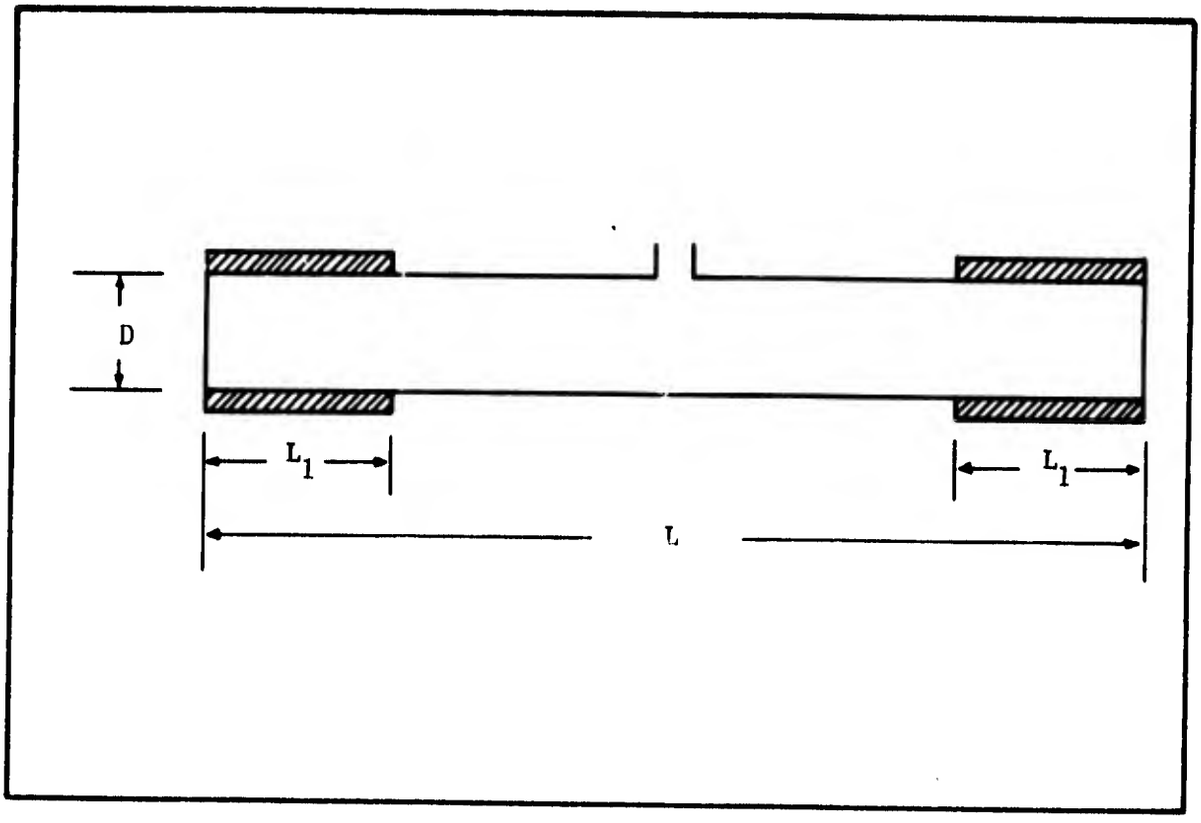

Figure 4-5. T-Burner Configuration Used in Parametric Calculations Showing the Effect of Extended Grain Length

The integration indicated by this equation was carried out numerically for four different combinations of M_b and Q. The results are presented in Figure 4-7. The curves in Figure 4-7 show that the theory predicts the velocity-coupled contribution to increase continuously as the grain length is increased, with the maximum occurring for a full-length grain. It also predicts that the effect increases with increasing M_b and diminishes as the amplitudes of the oscillations increase.

C. T-BURNER APPLICATION

1. Approach

The objective of this study was to develop a computer program to calculate the linear acoustic behavior of a velocity coupled T-burner, accounting for the effects of burner geometry, steady flow, particles, and propellant combustion. The approach taken was to extend the modified one-dimensional analysis of T-burners developed by Culick.[65] This was done by adding a velocity coupling response calculation and by modifying the mode shape and complex wave number analyses to account for effects of an additional pair of propellant samples. The analyses and nomenclature of References 63 and 65 were used without change wherever possible. Extensions of these previous analyses are described in subparagraph 2.

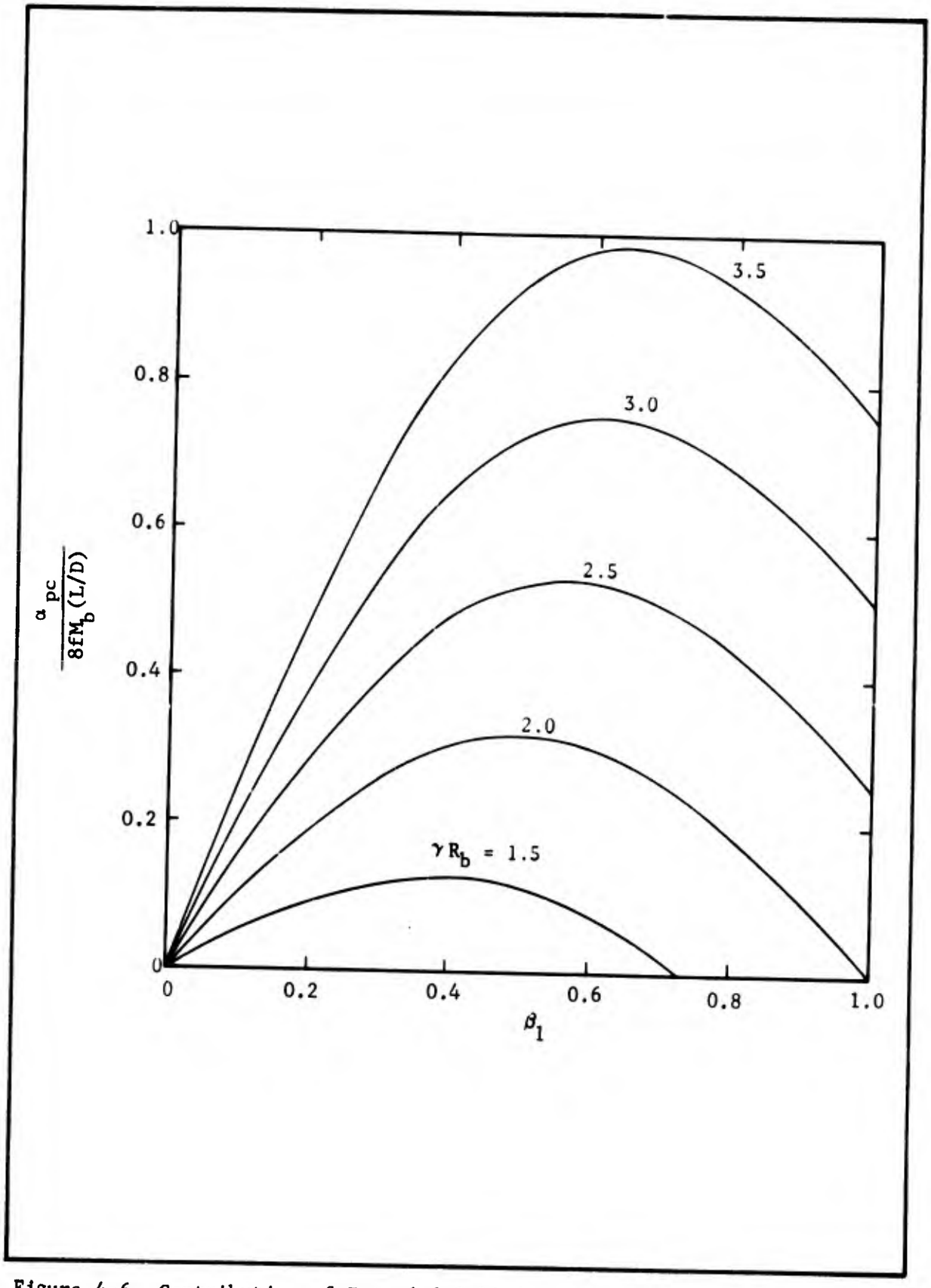

Figure 4-6. Contribution of Extended Cylindrical Samples to the Growth Constant According to the Modified McClure-Hart-Cantrell Theory (Acoustic Pressure and Steady Velocity Coupling Only)

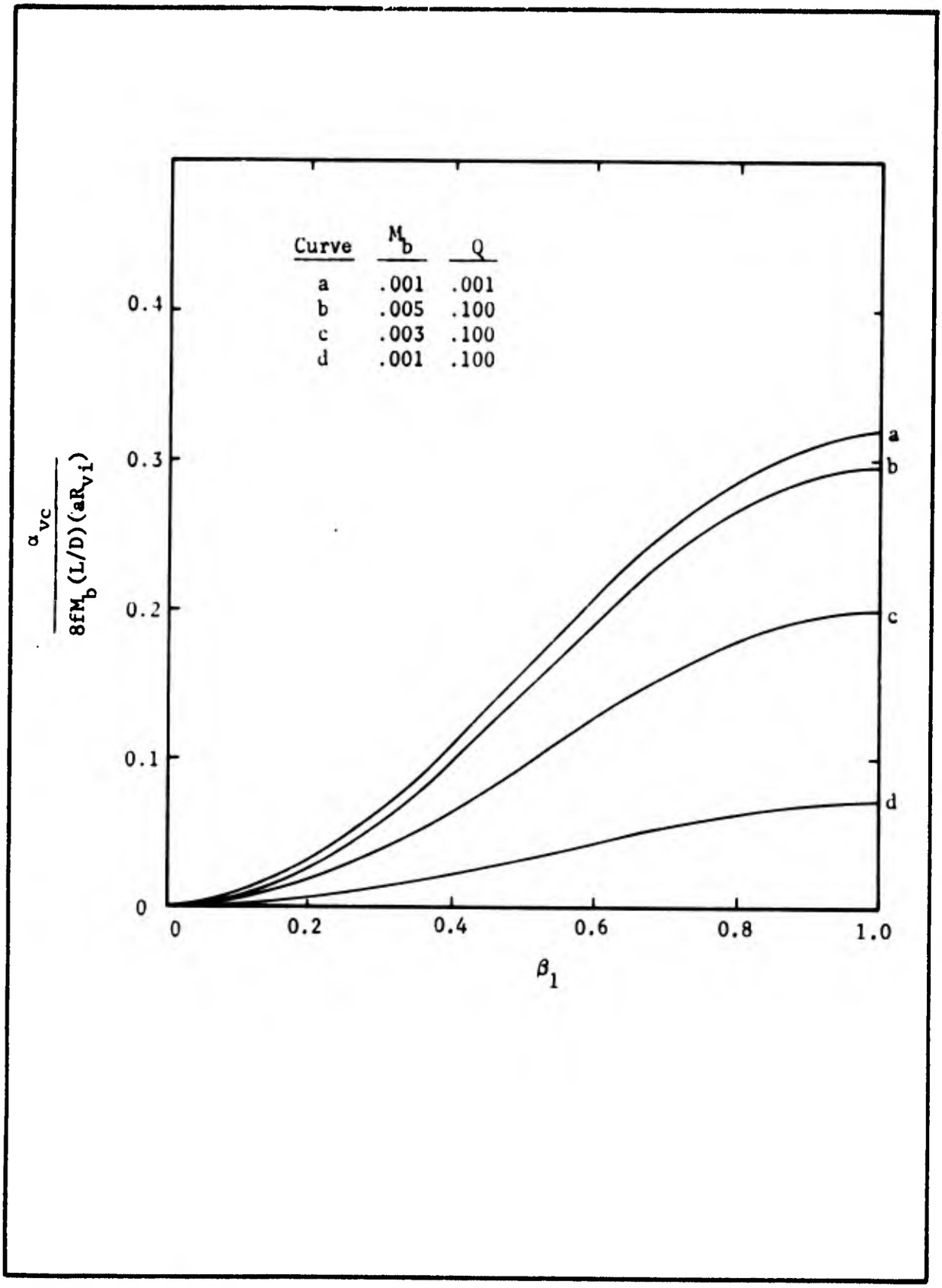

Figure 4-7. Velocity Coupling Contribution of Extended Cylindrical Samples According to the McClure-Hart-Cantrell Theory

The extended analysis was incorporated into a comprehensive computer program that calculates velocity coupling in addition to the other driving and damping effects that control T-burner acoustic behavior. Calculations may be performed for variations of seven basic burner configurations. Each configuration involves a practical combination of disk (or cup) and cylindrical propellant samples. The computer program is used in conjunction with a nonlinear regression analysis to yield estimates of propellant acoustic parameters from experimental test data. It may also be used alone to calculate the theoretical variation of acoustic growth rate as a function of the T-burner configuration. The program was successfully tested and used to reduce data as described in Section VII.

2. One-Dimensional Acoustic Mode Analysis

Seven basic configurations that are considered in the analysis are shown in Figure 4-8. One or two pair of symmetrically placed propellant samples have equal diameters, which may be larger or smaller than that of the tube. Ends of the samples may be either tapered (to maintain a constant burn area) or squared. Fillets of partially burned cup samples are rounded. In the modal analysis, sample surfaces are all assumed to be square with volumetrically equivalent lengths calculated for tapered samples and rounded fillets to simplify subsequent calculations. These configurations may be characterized by a single cup-cylinder configuration, as shown by the half-burner schematic in Figure 4-9, by properly choosing the values of the sample dimensions. (Thus, for example, if the choice $L_1 = L_v = 0$ and $D_c = D_{co}$ is made, then a simple disk configuration is obtained). Lengths and cross-sectional areas are shown in both dimensional and non-dimensional forms in Figure 4-9. Mode shapes of the first three pressure modes for the flush surface condition are also given.

Gas dynamics of the T-burner are assumed to be 1-D for the characteristic mode analysis. Wave behavior is assumed to involve isentropic variations of a perfect gas. The continuity and momentum equations are therefore[66]

$$\frac{\partial}{\partial z}(\rho u S_c) + \frac{\partial}{\partial t}(\rho S_c) = 0 \qquad \text{Continuity} \qquad (4\text{-}48)$$

$$\frac{\partial}{\partial t}(\rho u S_c) + \frac{\partial}{\partial z}(\rho u^2 S_c) + S_c \frac{\partial p}{\partial z} = 0 \qquad \text{Momentum} \qquad (4\text{-}49)$$

Differentiating the continuity equation with respect to time and the momentum equation with respect to z and combining yields

$$\frac{\partial^2}{\partial z^2}(\rho u^2 S_c) + \frac{\partial}{\partial z}\left(S_c \frac{\partial p}{\partial z}\right) - S_c \frac{\partial^2 \rho}{\partial t^2} = 0 \qquad (4\text{-}50)$$

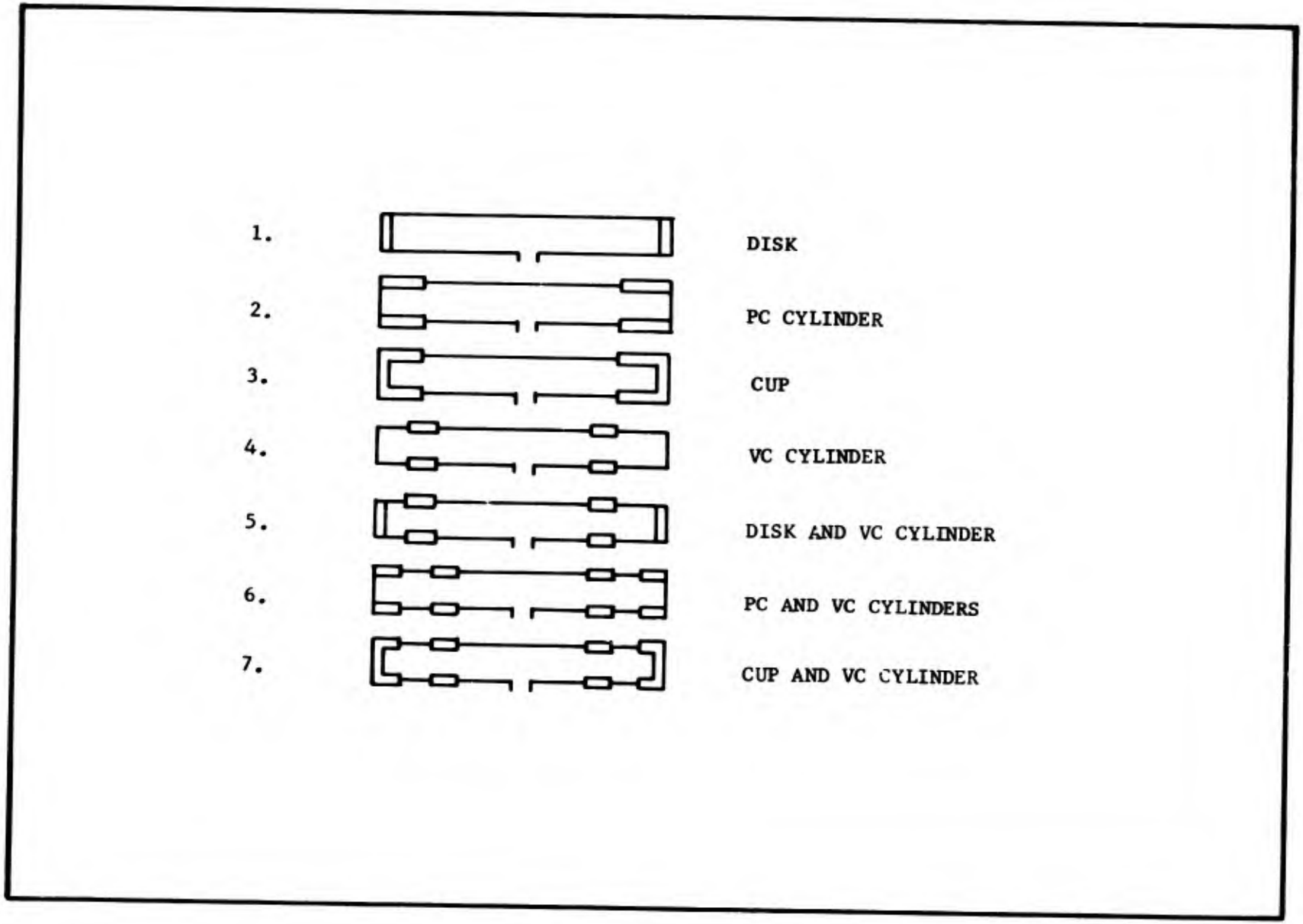

Figure 4-8. Seven Basic Configurations Used in T-Burner Analysis Program

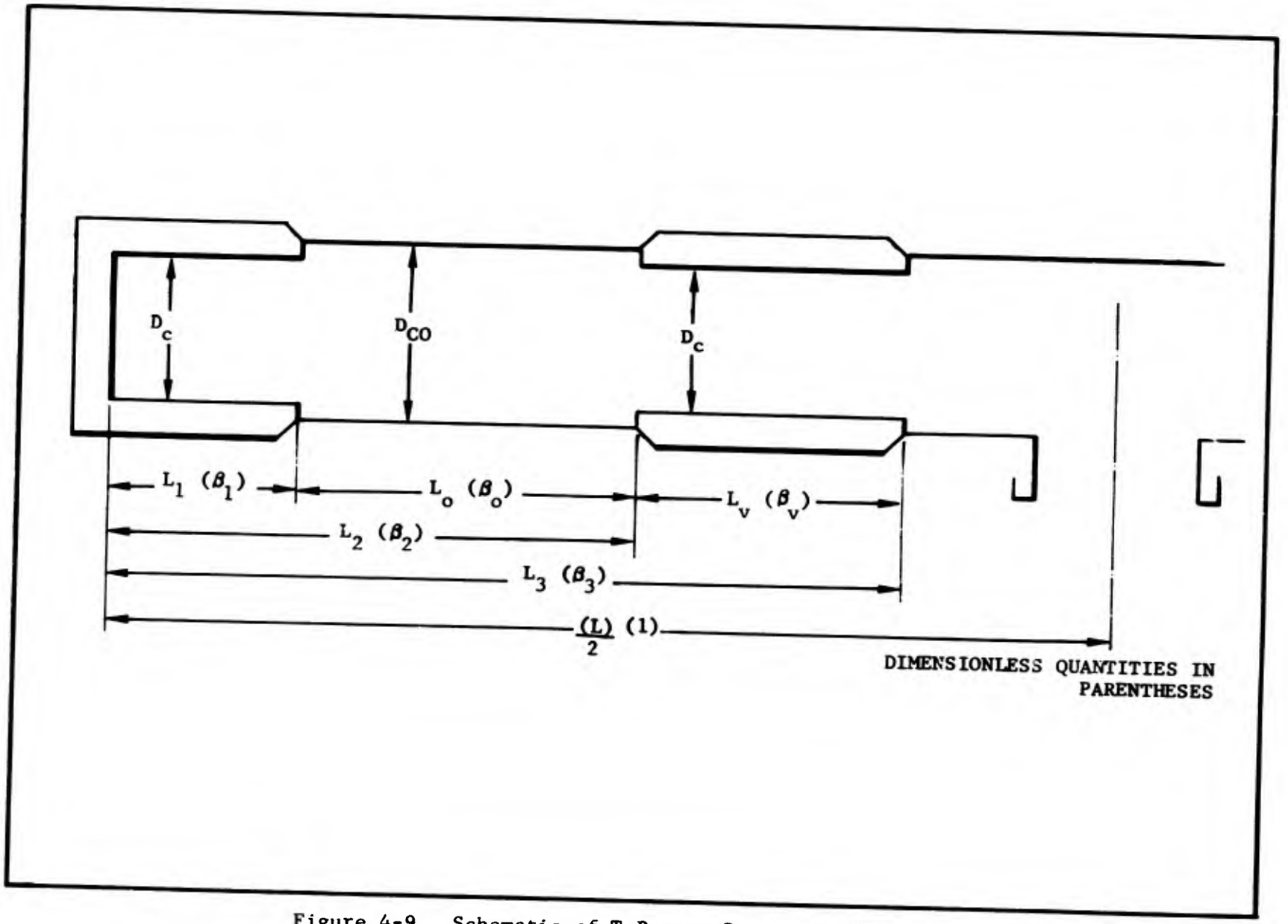

Figure 4-9. Schematic of T-Burner Geometric Characteristics

The gas variables are expanded into their steady and linear acoustic mode terms: $\rho = \bar{\rho} + \rho'$, $u = \bar{u} + u' = u'$ and $p = \bar{p} + p'$, where the unperturbed condition is assumed for the modal analysis. The speed of sound formula, $a^2 = \frac{\gamma \bar{P}_c}{\bar{\rho}}$, is combined with the isentropic condition $\frac{p'}{\bar{p}} = \gamma \frac{\rho'}{\bar{\rho}}$ to obtain $a^2 = p'/\rho'$. For sinusoidal oscillations, $p' = p_\ell e^{i\,\omega_\ell t}$, therefore $\frac{\partial p'}{\partial t} = i\,\omega\,p'$. Combining the foregoing results with Equation (4-50), the 1-D acoustic field equation is obtained as

$$\frac{\partial^2 p_\ell}{\partial z^2} + \frac{1}{S_c}\,\frac{\partial S_c}{\partial z}\,\frac{\partial p_\ell}{\partial z} + k_\ell^2 p_\ell = 0 \qquad (4\text{-}51)$$

where $k_\ell = \omega_\ell / a$ is the wave number of the ℓth acoustic mode.

The mode shape is assumed to be piecewise sinusoidal with continuity of pressure and mass flow existing at discontinuities of area created by propellant samples. These assumptions imply discontinuities of momentum, and therefore energy, at the area discontinuities. The result is that on opposite ends of the burner, energy appears to be respectively removed and added. The effects on the mode shape of this contradiction to the conservation of energy have not been fully investigated but appear to be small.

The frequency and mode shape analysis is simplified by considering only a half-length section of the T-burner and applying the appropriate boundary condition at the center for the particular mode being determined. The boundary conditions are

$$p_\ell\Big|_{L/2} = 0 \qquad \text{Odd Modes} \qquad (4\text{-}52)$$

$$\left.\frac{dp_\ell}{dz_\ell}\right|_{L/2} = 0 \qquad \text{Even Modes} \qquad (4\text{-}53)$$

and

$$\left.\frac{dp_\ell}{dz}\right|_{o} = 0 \qquad \text{All Modes} \qquad (4\text{-}54)$$

Using these conditions and the piecewise sinusoidal pressure distribution, the acoustic pressure for the general configuration of Figure 4-9 is defined by

$$0 \le z \le L_1 \qquad p_\ell = \cos k_\ell z \qquad \text{All Modes} \qquad (4\text{-}55)$$

$$L_1 \le z \le L_2 \qquad p_\ell = \cos k_\ell z + A_\ell \cdot \sin k_\ell (z - L_1) \qquad \text{All Modes} \qquad (4\text{-}56)$$

$$L_2 \le z \le L_3 \qquad P_\ell = \cos k_\ell z + A_\ell \cdot \sin k_\ell (z-L_1) + B_\ell \cdot \sin k_\ell (z-L_2) \qquad \text{All Modes} \quad (4\text{-}57)$$

$$L_3 \le z \le \frac{L}{2} \qquad P_\ell = \begin{cases} C_\ell^o \cdot \sin k_\ell \left(\frac{L}{2} - z\right) & \text{Odd Modes} \quad (4\text{-}58) \\ C_\ell^e \cdot \cos k_\ell \left(\frac{L}{2} - z\right) & \text{Even Modes} \quad (4\text{-}59) \end{cases}$$

Equations (4-55) through (4-59) satisfy the acoustic field Equation (4-51) and the boundary conditions (4-52), (4-53), and (4-54) for the proper choice of coefficients A_ℓ, B_ℓ, C_ℓ^o and C_ℓ^e and the wave number k_ℓ. Subsequent analysis is made more convenient by transformation of the equations to their equivalents in nondimensional variables. For the transformation the following definitions are made. (Refer to Figure 4-9.)

$$k_\ell = \frac{2K_\ell}{L} \qquad (a)$$

$$L_o = L_2 - L_1, \; L_v = L_3 - L_1, \; L_b = L_1 + L_v \qquad (b)$$

$$\beta_i = 2L_i/L \qquad i = 0, 1, 2, 3, v \qquad (c)$$

$$\beta = 2 L_b/L \qquad (d) \qquad (4\text{-}60)$$

$$k_\ell L_i = K_\ell \beta_i \qquad (e)$$

$$\xi = 2z/L \qquad (f)$$

By the use of Equations (4-60) in Equations (4-55) through (4-59), the nondimensional forms are obtained as follows:

$$0 \le \xi \le \beta_1 \qquad P_\ell = \cos K_\ell \xi \qquad \text{All Modes} \quad (4\text{-}61)$$

$$\beta_1 \le \xi \le \beta_2 \qquad P_\ell = \cos K_\ell \xi + A_\ell \cdot \sin K_\ell (\xi - \beta_1) \qquad \text{All Modes} \quad (4\text{-}62)$$

$$\beta_2 \le \xi \le \beta_3 \qquad P_\ell = \cos K_\ell \xi + A_\ell \cdot \sin K_\ell (\xi - \beta_1) + B_\ell \cdot \sin K_\ell (\xi - \beta_2) \qquad \text{All Modes} \quad (4\text{-}63)$$

$$\beta_3 \le \xi \le 1 \qquad P_\ell = \begin{cases} C_\ell^o \cdot \sin K_\ell (1-\xi) & \text{Odd Modes} \quad (4\text{-}64) \\ C_\ell^e \cdot \cos K_\ell (1-\xi) & \text{Even Modes} \quad (4\text{-}65) \end{cases}$$

Continuity of pressure and mass flow across the changes of cross-sectional area at the propellant sample ends are used to simplify the determination of wave distribution coefficients and wave number. Thus:

$$\text{At } \xi = \beta_1 \left\{ \begin{array}{l} \cos K_\ell \beta_1 = \cos K_\ell \beta_1 + A_\ell \cdot \sin (K_\ell \cdot 0) \\ \\ S_c \cdot \sin K_\ell \beta_1 = S_{co} \left[\sin K_\ell \beta_1 - A_\ell \cdot \cos(K_\ell \cdot 0) \right] \end{array} \right\}$$

$$\text{so } A_\ell = (1 - \frac{S_c}{S_{co}}) \qquad \text{All Mode(s)} \tag{4-66}$$

$$\text{At } \xi = \beta_2 \left\{ \begin{array}{l} B_\ell \cdot \sin (K_\ell \cdot 0) = 0 \\ \\ S_{co} \left[\sin K_\ell \beta_2 - A_\ell \cdot \cos K_\ell \beta_o \right] = S_c \left[\sin K_\ell \beta_2 - A_\ell \cdot \cos K_\ell \beta_o \right. \\ \qquad \left. - B_\ell \cdot \cos (K_\ell \cdot 0) \right] \end{array} \right\}$$

$$\text{so } B_\ell = -(1 - \frac{S_{co}}{S_c})(A_\ell \cdot \cos K_\ell \beta_o - \sin K_\ell \beta_2) \tag{4-67}$$

Let

$$D_\ell = \cos K_\ell \beta_3 + A_\ell \sin K_\ell (\beta_3 - \beta_1) + B_\ell \sin K_\ell \beta_v = p_\ell (\xi = \beta_3) \tag{4-68}$$

and

$$F_\ell = -\sin K_\ell \beta_3 + A_\ell \cos K_\ell (\beta_3 - \beta_1) + B_\ell \cos K_\ell \beta_v$$

$$= \frac{1}{K_\ell} \frac{dp_\ell}{d\xi} (\xi = \beta_3); \tag{4-69}$$

then at $\xi = \beta_3$

$$D_\ell = \left\{ \begin{array}{ll} C_\ell^o \sin K_\ell (1 - \beta_3) & \text{Odd Modes} \quad (4\text{-}70) \\ \\ C_\ell^e \cos K_\ell (1 - \beta_3) & \text{Even Modes} \quad (4\text{-}71) \end{array} \right.$$

and

$$F_\ell = \frac{S_{co}}{S_c} \left\{ \begin{array}{ll} -C_\ell^o \cos K_\ell (1 - \beta_3) & \text{Odd Modes} \quad (4\text{-}72) \\ \\ C_\ell^e \sin K_\ell (1 - \beta_3) & \text{Even Modes} \quad (4\text{-}73) \end{array} \right.$$

The values of D_ℓ and F_ℓ are known from Equations (4-60) through (4-69). By combining related pairs of Equations (4-70) through (4-73) the unknown coefficients C^o_ℓ and C^e_ℓ are eliminated to obtain respectively the odd and even characteristic equations:

$$D_\ell \cos K_\ell(1 - \beta_3) + \frac{S_c}{S_{co}} F_\ell \sin K_\ell(1 - \beta_3) = 0 \qquad \text{Odd Modes} \qquad (4\text{-}74)$$

$$D_\ell \sin K_\ell(1 - \beta_3) - \frac{S_{co}}{S_c} F_\ell \cos K_\ell(1 - \beta_3) = 0 \qquad \text{Even Modes} \qquad (4\text{-}75)$$

The characteristic equations are solved by assuming a preliminary estimate of K_ℓ and solving by Newton's method. A_ℓ and B_ℓ are also known so the determination of K_ℓ completely determines the acoustic field.

3. Energy and Acoustic Growth Rate Equations

The customary method of solving the governing equations and boundary conditions for a T-burner is to linearize the equations and obtain a linear wave equation. An integral equation solution of the wave equation is then obtained in the form of a complex wave number. The acoustic growth rates are then calculated by evaluating the terms of this solution. The development of this solution is found in Reference 63 and in Reference 65. The result in the same notation as Reference 65 is:

$$\alpha = -\frac{\bar{a}}{2k_\ell L S_{co} \xi_\ell^2} \mathrm{Im} \left\{ i\bar{\rho}\bar{a}k_\ell \left[\left(u' p_\ell + \frac{\bar{u} p_\ell^2}{\bar{\rho}\bar{a}^2} \right) S_{be} \right]_0^L - i\bar{a}k_\ell \int_0^L p_\ell \int m_b' \, dq \, dz \right\}$$

$$+ i \frac{k_\ell}{\bar{a}} \left\{ \frac{1}{\bar{\rho}} \int_0^L \left[p_\ell^2 + \frac{1}{k_\ell^2} \left(\frac{dp_\ell}{dz} \right)^2 \right] \int \bar{m}_b \, dq \, dz - \int_0^L p_\ell^2 \frac{1}{S_c} \frac{d}{dz} \left(\bar{u} S_c \right) S_c \, dz \right\}$$

$$+ \left\{ \int_0^L u_p' \frac{dp_\ell}{dz} \int \bar{m}_b \, dq \, dz - \int_0^L F' \frac{dp_\ell}{dz} S_c \, dz \right\}$$

$$+ \left\{ i \frac{k_\ell}{\bar{a}} \gamma \int_0^L \bar{w}_p p_\ell^2 S_c \, dz - i \frac{k_\ell}{\bar{a}} \frac{R}{C_v} \int_0^L p_\ell \left[e_p' \bar{w}_p \right. \right. \qquad (4\text{-}76)$$

$$\left. \left. + \bar{e}_p w_p' + (Q' + Q_p') S_c \, dz + \int_0^L (u' - u_p') \bar{w}_p \frac{dp_\ell}{dz} S_c \, dz \right] \right\}$$

$$- i \frac{k_\ell}{\bar{a}} R \int_0^L \Delta T' p_\ell \int \bar{m}_b \, dq \, dz$$

The Hercules extensions to this analysis were made in the evaluation of the integrals of Equation (4-76). The effects of velocity coupling on T-burner stability were accounted for by modifying the integrals involving mass addition to include the effects of acoustic velocity coupled propellant combustion. The damping and driving integrals were also evaluated using the acoustic mode shape equations derived for two sets of propellant samples.

Individual acoustic growth and damping rates for mean flow interaction, particle damping, and pressure and velocity coupling are obtained by evaluating the related integral terms in Equation (4-76). Thus,

$$\alpha_{TOT} = \alpha_{mf} + \alpha_{pd} + \alpha_{pc} + \alpha_{vc} + \alpha_{d} \tag{4-77}$$

The equations for the individual growth and damping rates used in the computer program are given in the following paragraphs.

MEAN FLOW INTERACTION:

$$\alpha_{mf} = -\frac{\bar{a}\,\bar{M}_b}{2L\xi_\ell^2}\left[\left(\frac{S_{b1}}{S_{co}}\,g_{\ell 1} + \frac{S_{bv}}{S_{co}}\,g_{\ell v}\right)VFG + 2\,VF\,\frac{S_b}{S_{co}}\,C_\ell^{o\,2}\right] \tag{4-78}$$

$$g_{\ell 1} = \frac{2}{L_1}\int_o^{L_1} \sin^2 k_\ell z\, dz \tag{4-80}$$

$$g_{\ell v} = \frac{2}{L_v}\int_{L_2}^{L_3}\left[\sin k_\ell z - A_\ell \cos k_\ell (z - L_1) - B_\ell \cos k_\ell (z - L_2)\right]^2 dz \tag{4-81}$$

The term $g_{\ell v}$ includes the effect on mode shape of the second pair of propellant samples. Parametric plots of $g_{\ell v}$ versus β_v, the nondimensional length of the velocity coupling propellant samples, are given in Figure 4-10.

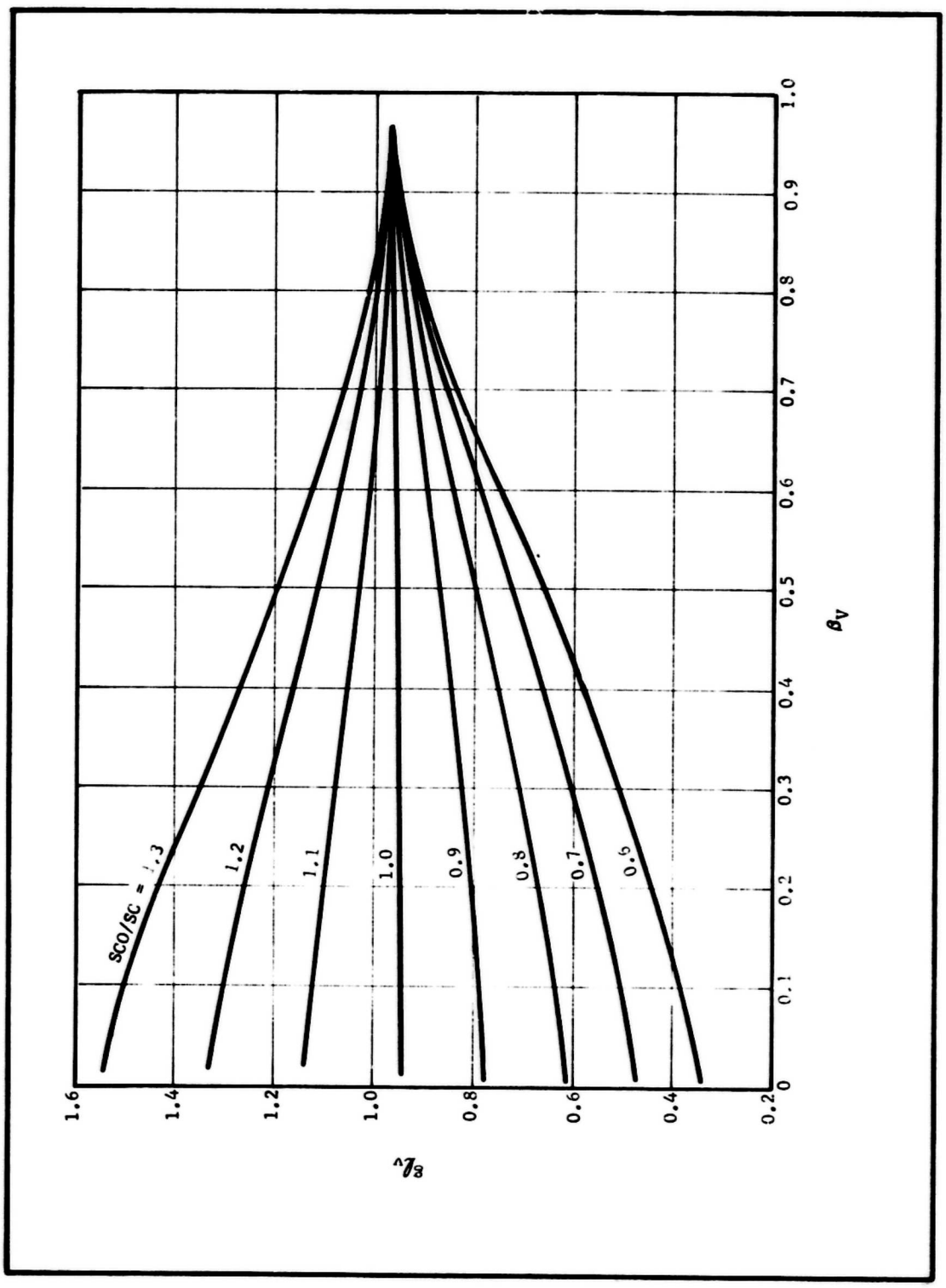

Figure 4-10. Mean Flow Geometric Coefficient as a Function of Nondimensional Length and Diameter Ratio

PARTICLE DAMPING:

$$\alpha_{pd} = -\frac{C_m}{1+(\omega\tau)^2}\left\{\frac{(\omega\tau)^2}{2\tau} + 2\frac{\bar{a}\,\bar{M}_b}{2L\xi_\ell^2}\left[\frac{S_{bl}}{S_{co}} g_{\ell 1} + \frac{S_{bv}}{S_{co}} g_{\ell v}\right] VFG\right\} \quad (4\text{-}82)$$

The effects of the mode shape changes on particulate damping are also contained in the $g_{\ell v}$ term.

PRESSURE COUPLED DRIVING:

$$\alpha_{pc} = 2\frac{\bar{a}\,\bar{M}_b}{2L\xi_\ell^2}\left\{\left[\left[A_b^r/\bar{M}_b + 1\right]\frac{S_{be}}{S_{co}} + \left[R_b^r + \frac{1}{\gamma}(A_b^r/\bar{M}_b + 1 - R_b^r)\right]\left[\frac{S_{bl}}{S_{co}}\mathcal{E}_{\ell 1} + \frac{S_{bv}}{S_{co}}\mathcal{E}_{\ell v}\right]\right\}\right. \quad (4\text{-}83)$$

$$\mathcal{E}_{\ell 1} = \frac{2}{L_1}\int_0^{L_1} \cos^2 k_\ell z\, dz \quad (4\text{-}84)$$

$$\mathcal{E}_{\ell v} = \frac{2}{L_v}\int_{L_2}^{L_3}\left[\cos k_\ell z + A_\ell \sin k_\ell(z - L_1) + B_\ell \sin k_\ell(z - L_2)\right]^2 dz \quad (4\text{-}85)$$

The effect of the mode shape changes on pressure-coupled acoustic driving are contained in the term $\mathcal{E}_{\ell v}$. The magnitude of this term has been calculated and is plotted as a function of β_v in Figure 4-11.

VELOCITY COUPLED DRIVING:

$$\alpha_{vc} = -\frac{\bar{a}\,\bar{M}_b}{2L\xi_\ell^2}\left(\frac{\bar{a}}{a_m}\right)\left[\frac{S_{bl}}{S_{co}} P_{\ell 1} + \frac{S_{bv}}{S_{co}} P_{\ell v}\right] R_{vi} \quad (4\text{-}86)$$

$$P_{\ell 1} = \frac{L}{2L_1}(\cos^2 k_\ell L_1 - 1) \quad (4\text{-}87)$$

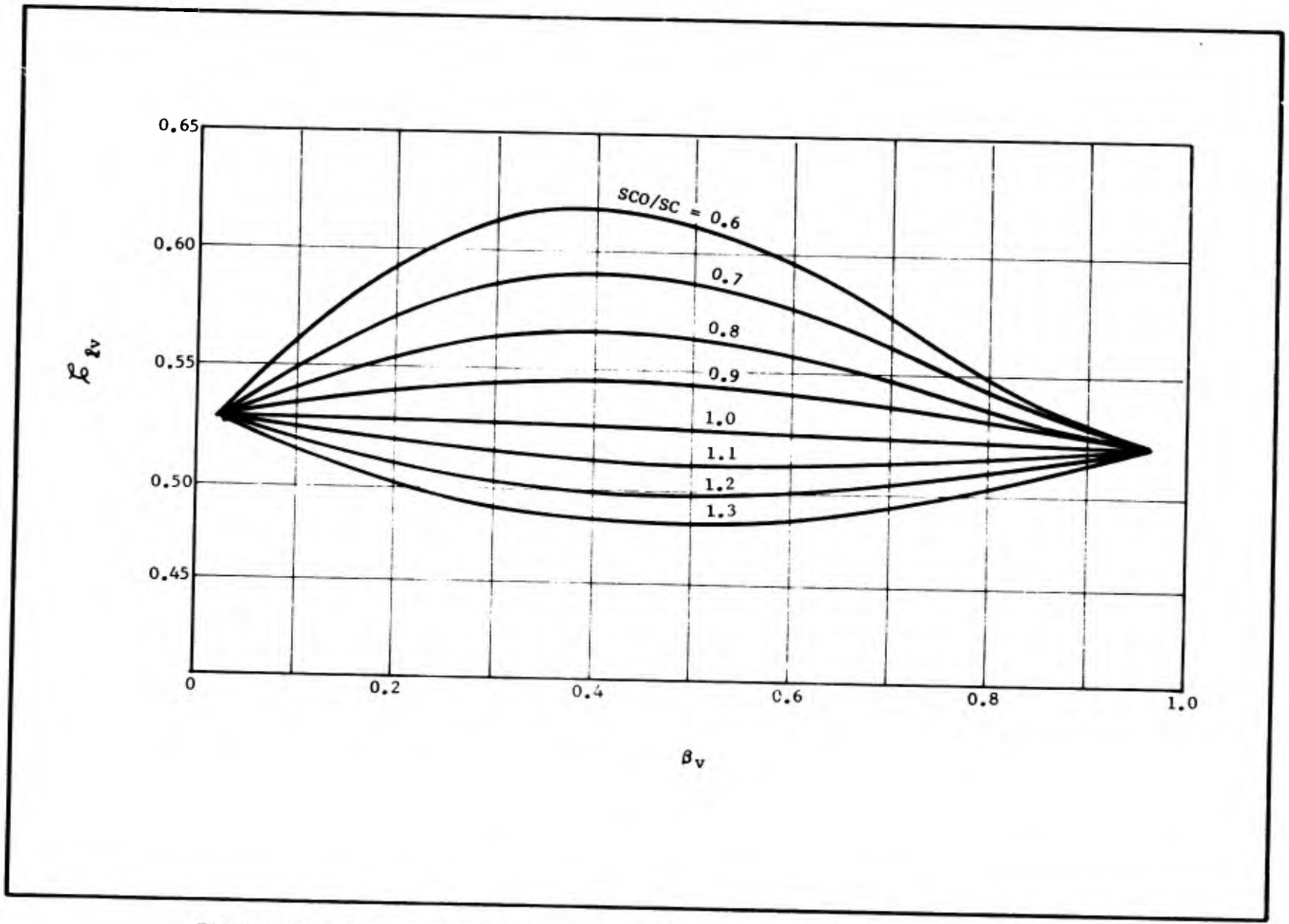

Figure 4-11. Pressure Coupled Geometric Coefficient as a Function of Nondimensional Length and Diameter Ratio

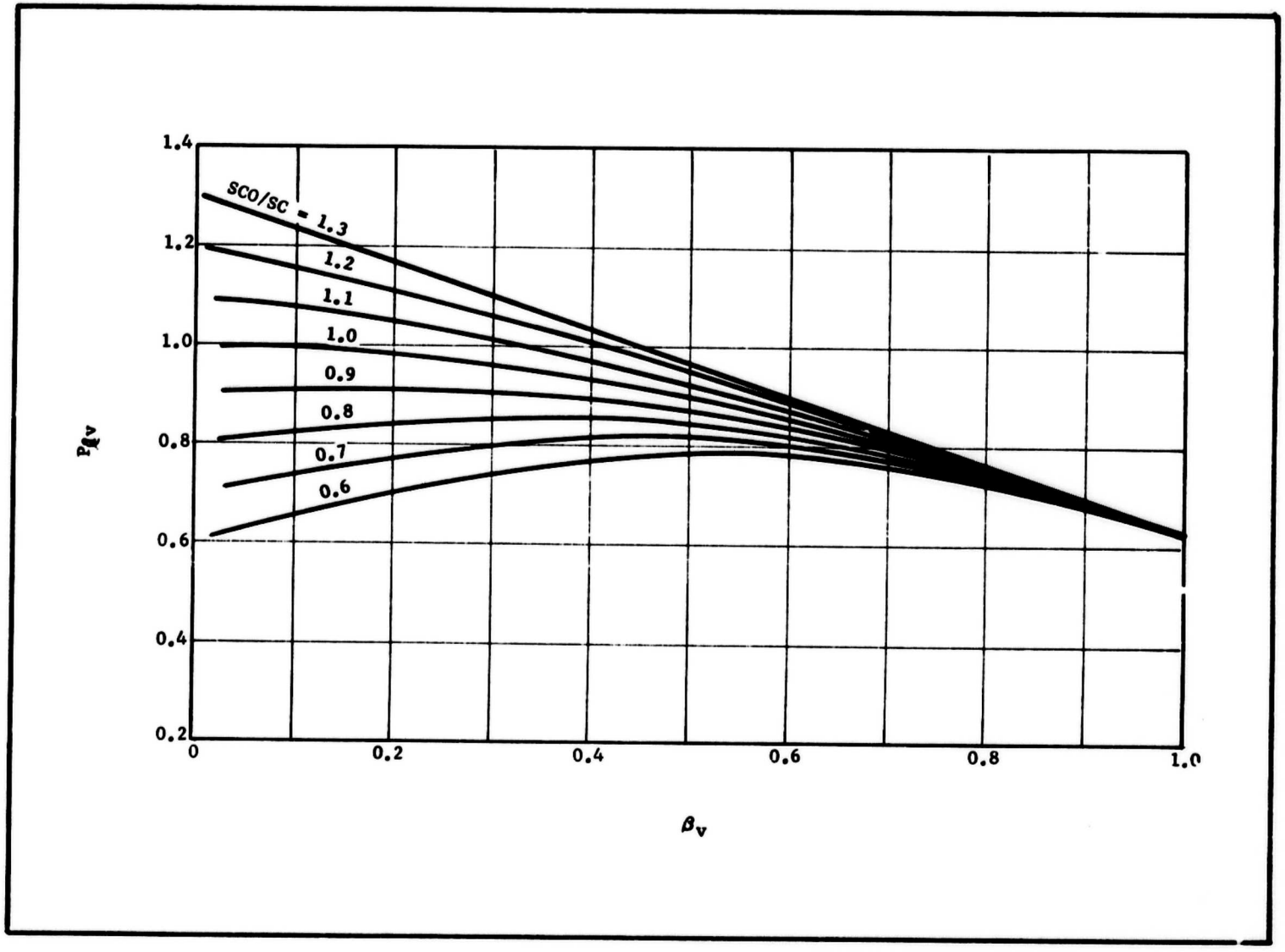

Figure 4-12. Velocity Coupled Geometric Coefficient as a Function of Nondimensional Length and Diameter Ratio

$$P_{\ell v} = \frac{L}{2L_v} \left\{ \left[\begin{array}{ll} C_\ell^{o\,2} & \sin^2 k_\ell (L/2 - L_3) \\ & \\ C_\ell^{e\,2} & \cos^2 k_\ell (L/2 - L_3) \end{array} \right] - \left| \cos k_\ell L_2 + A_\ell \sin k_\ell (L_2 - L_1) \right|^2 \right\} \qquad (4\text{-}88)$$

First Mode

Second Mode

The derived expression for velocity-coupled driving has a form similar to the expression for the mean flow interaction at the propellant surface. The quantity P_{ℓ_v} has been calculated and is shown in Figure 4-12 as a function of the nondimensionalized velocity coupled sample grain length, β_v, for several parametric values of sample diameter/T-burner diameter ratio.

The energy in cavity is proportional to ξ_ℓ^2 which, in turn, is given by:

$$\xi_\ell^2 = \frac{2\,S_c}{L\,S_{co}} \int_0^{L_1} \cos^2 k_\ell z \, dz + \frac{2}{L} \int_{L_1}^{L_2} \left| \cos k_\ell z + A_\ell \sin k_\ell (z - L_1) \right|^2 dz$$

$$+ \frac{2\,S_c}{L\,S_{co}} \int_{L_2}^{L_3} \left| \cos k_\ell z + A_\ell \sin k_\ell (z - L_1) + B_\ell \sin k_\ell (z - L_2) \right|^2 dz$$

$$+ \frac{2}{L} \int_{L_3}^{L/2} \left\{ \begin{array}{ll} C_\ell^{o\,2} \sin^2 k_\ell \left(\frac{L}{2} - z\right) & \text{Odd Modes} \\ & \\ C_\ell^{e\,2} \cos^2 k_\ell \left(\frac{L}{2} - z\right) & \text{Even Modes} \end{array} \right\} dz \qquad (4\text{-}89)$$

The quantity ξ_ℓ^2 is plotted as a function of β_v in Figure 4-13. As the nondimensionalized sample length approaches zero, the value of ξ_ℓ^2 for all parametric values of S_{co}/S_c approaches a limiting value of 0.5.

These individual driving and damping rate calculations are combined with experimentally based wall drag and heat transfer damping rates. The calculated acoustic growth and damping rates and the measured T-burner net growth rates are used in a nonlinear regression analysis to determine the magnitudes of the propellant acoustic response parameters. Acoustic parameter confidence limits are also calculated. Sample parametric calculations illustrating the utility and versatility of the computer program are given in subparagraph 4.

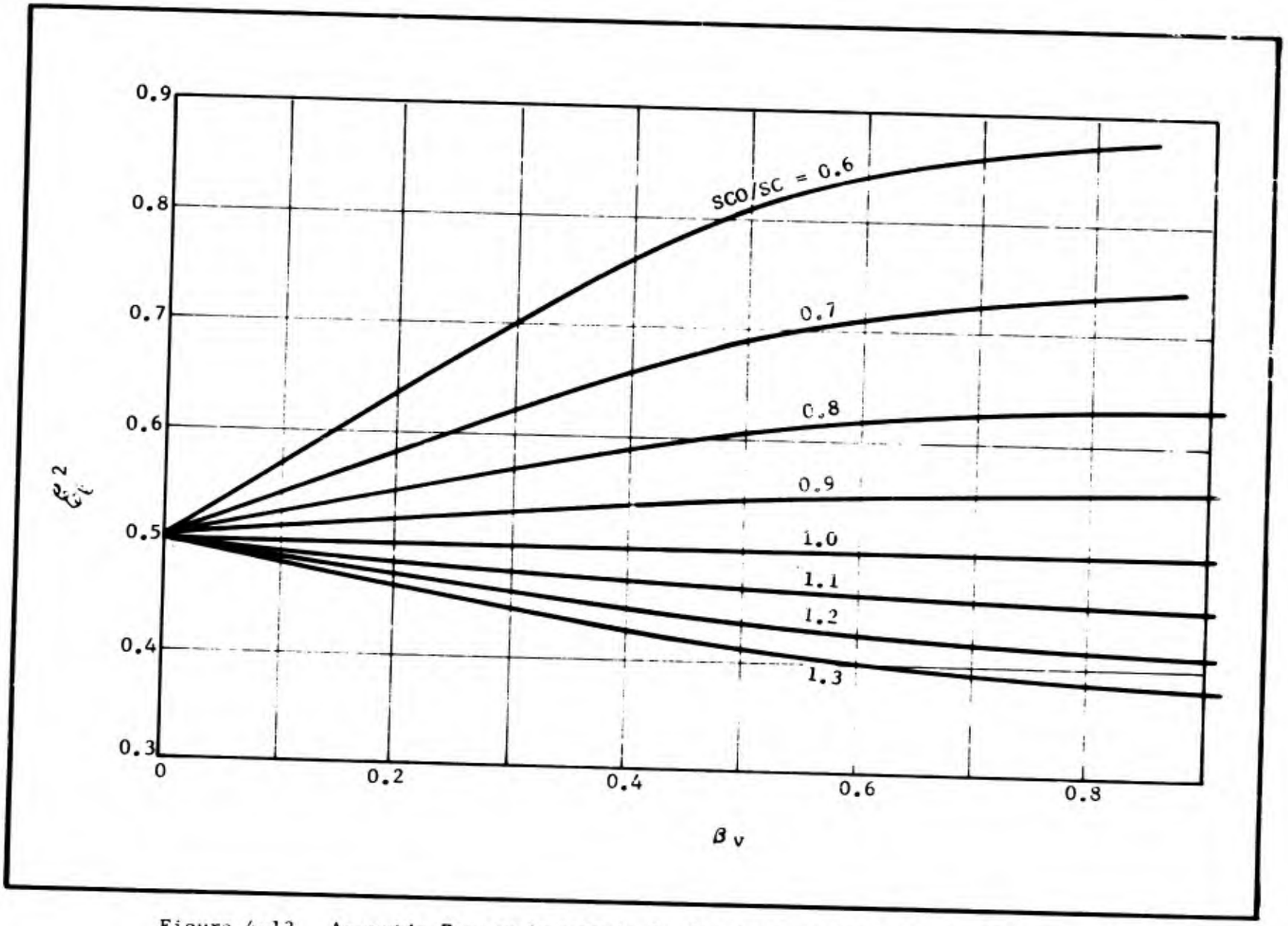

Figure 4-13. Acoustic Energy Geometric Coefficient as a Function of Nondimensional Length and Diameter Ratio

4. Parametric Calculations

Two series of parametric calculations were carried out using the comprehensive T-burner analysis computer program. One set of calculations was performed for the pressure coupled T-burner, determining the individual pressure coupled, mean flow coupled, and velocity coupled acoustic driving rates and the effects of sample area ratio and T-burner diameter/sample diameter ratio on the net acoustic growth rate. A similar set of calculations was also carried out for the velocity coupled T-burner.

Identical propellant and T-burner acoustic parameters were used in both sets of calculations: CYH propellant at 300 psi and 450 Hz, VF (vent function) = -1 indicating acoustic damping at the vent, VFG (flow turning) = +1 indicating acoustic damping due to flow turning, CYH propellant pressure coupled response parameter of 3.0, velocity coupled response parameter of 11.8, and a propellant total damping rate of -66 sec^{-1}. Parametric values of propellant area ratio from 0 to 6 and parametric values of T-burner diameter/sample diameter ratios from 0.6 to 1.2 were used in the calculations.

The calculated net growth as a function of sample area ratio is given in Figure 4-14 for the pressure-coupled T-burner and Figure 4-15 for the velocity coupled T-burner. It is evident that for equal area ratios of CYH propellant, considerably larger growth rates can be expected in the velocity coupled T-burner than in the pressure coupled T-burner. It is also evident that the effect of T-burner diameter/sample diameter on growth rate is much greater in the velocity coupled T-burner. At an area ratio of 5, varying the diameter ratio from 0.6 to 1.2 in the pressure coupled T-burner changes the net growth rate by 15 sec^{-1}; the comparable change in net growth rate in the velocity coupled T-burner is 143 sec^{-1}.

The acoustic driving by the driver propellant samples (area ratio = 1.5) at the ends of the velocity coupled T-burner is given by the difference between the total damping rate (-66 sec^{-1}) and the net growth rate at a test sample area ratio of zero. This acoustic driving, +29 sec^{-1}, is the same as the acoustic driving in the pressure coupled T-burner at an area ratio of 1.5.

The separation of total acoustic driving into pressure coupled, mean flow coupled, and velocity coupled driving rates is given in Figures 4-16 and 4-17 for the pressure-coupled and velocity-coupled T-burners, respectively. These driving rates are for the flush sample diameter, i.e., a T-burner diameter/sample diameter ratio of 1.0.

Figure 4-16 shows that, for the pressure-coupled T-burner, both pressure-coupled driving and mean flow damping are essentially linear with area ratio up to an area ratio of 9, while velocity coupled driving is nonlinear with area ratio. This velocity coupling nonlinearity provides

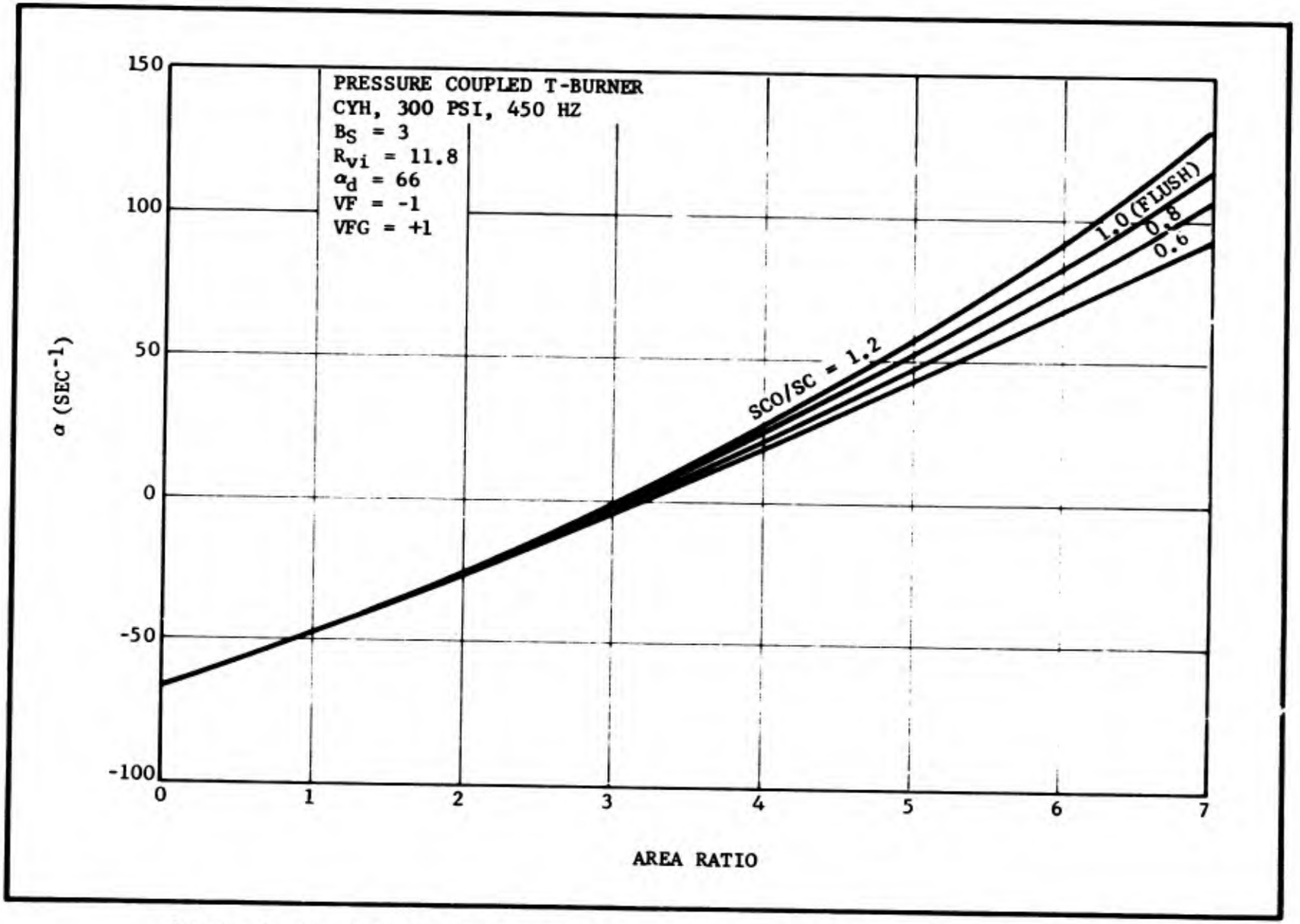

Figure 4-14. Calculated α Versus Area Ratio for Pressure Coupled T-Burner

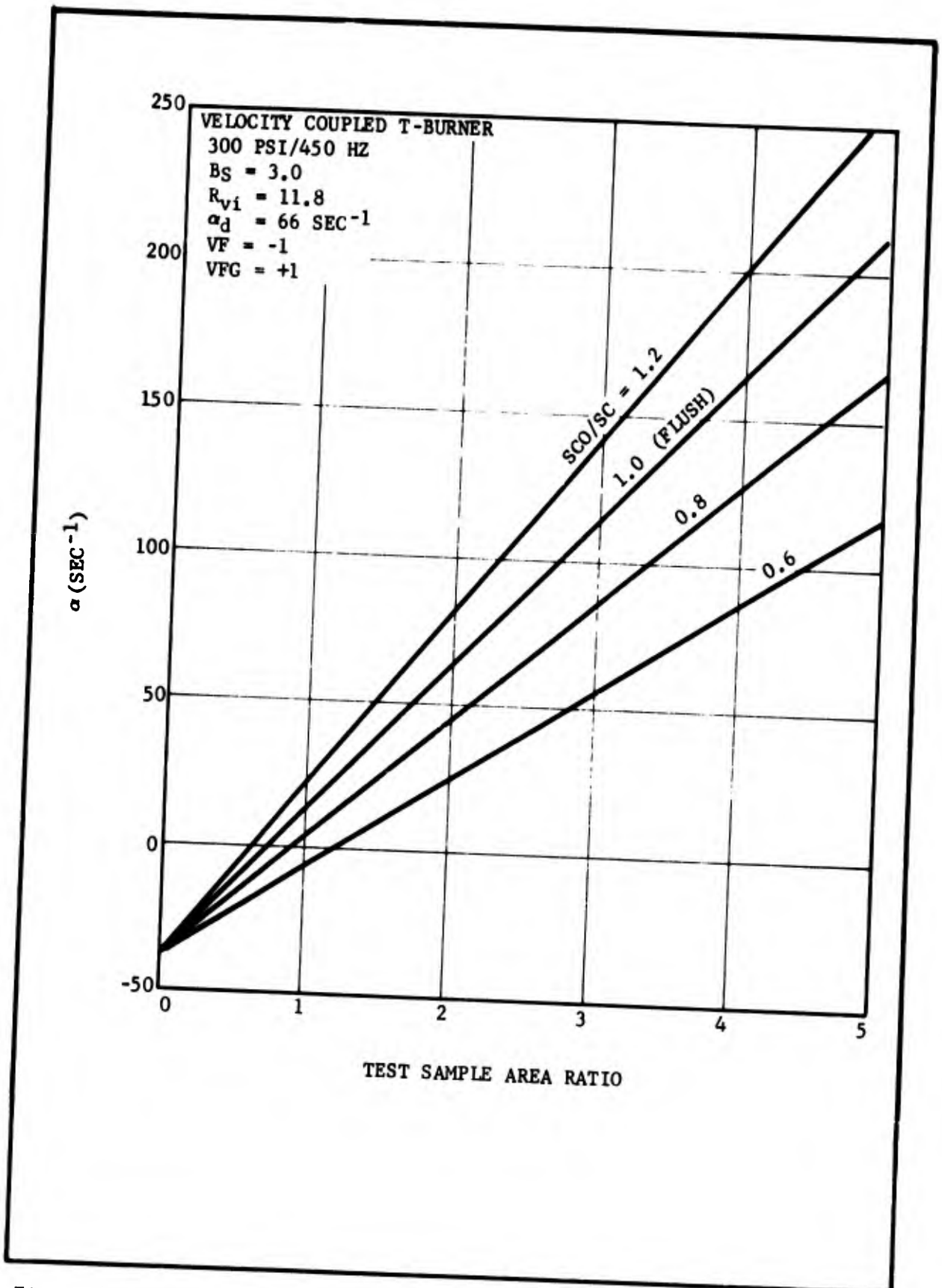

Figure 4-15. Calculated α Versus Test Sample Area Ratio for the Velocity Coupled T-Burner

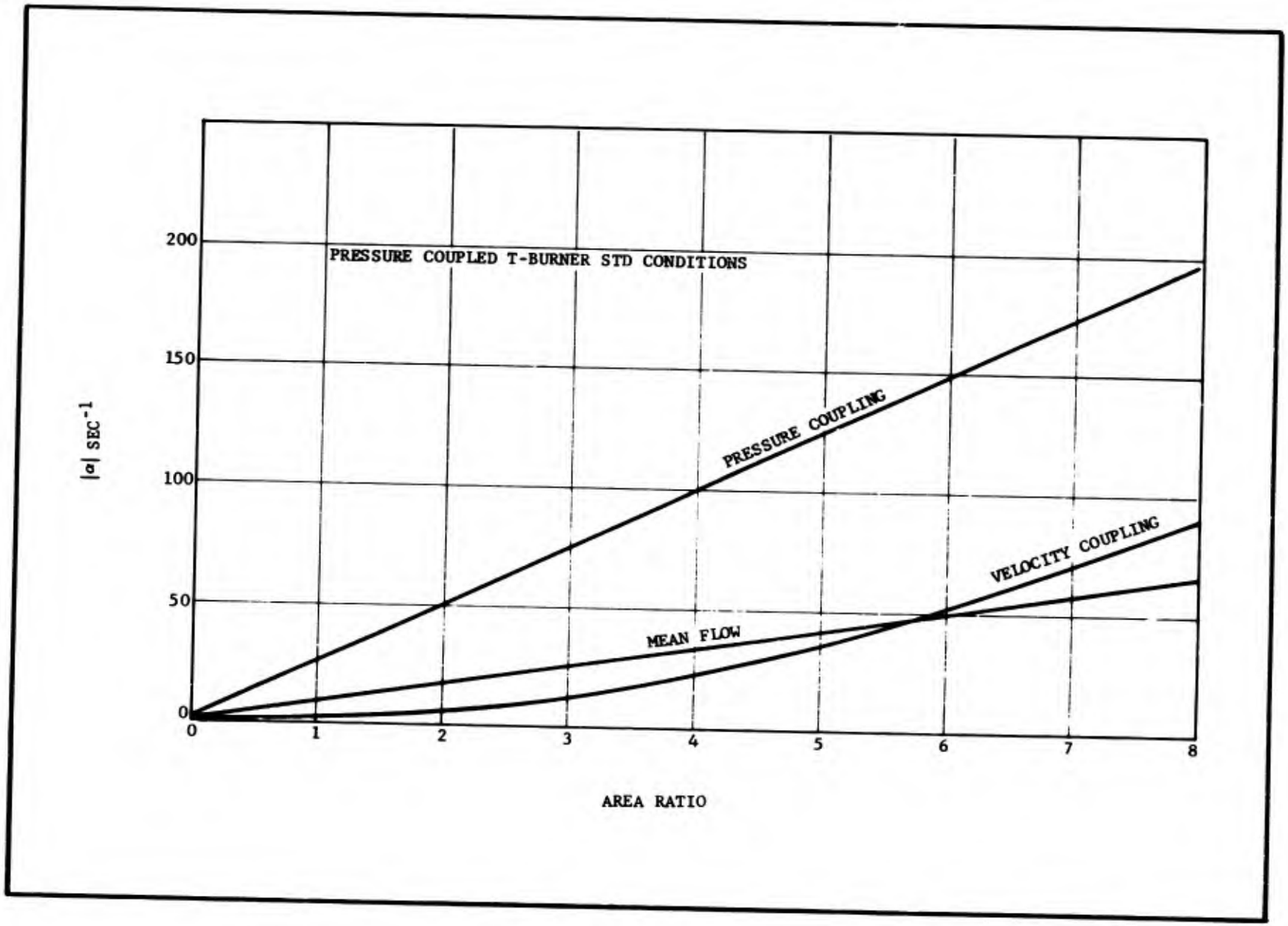

Figure 4-16. Contributions of Individual Mechanisms in Pressure Coupled T-Burner

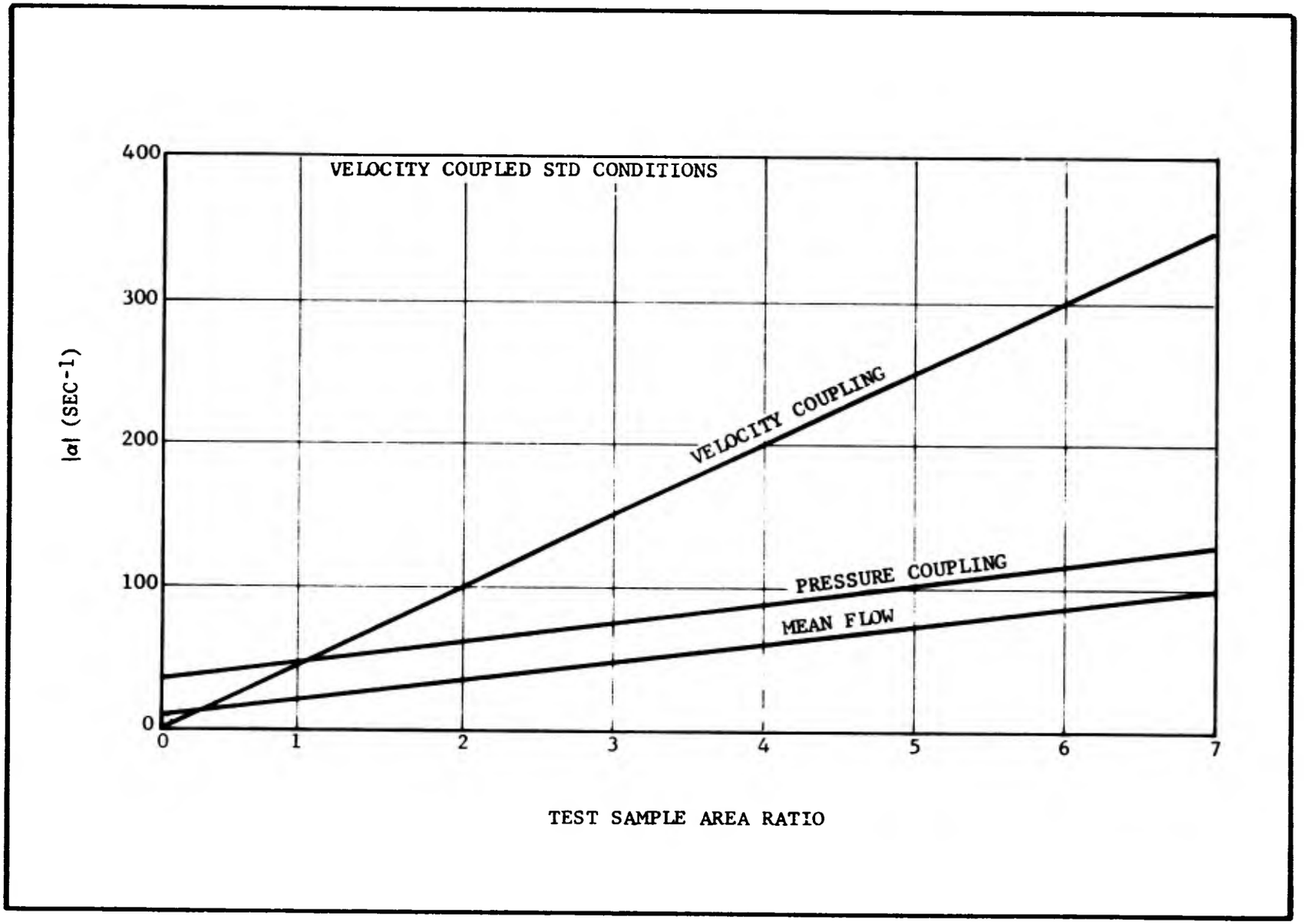

Figure 4-17. Contributions of Individual Mechanisms in Velocity Coupled T-Burner

slight curvature in the net growth rate versus area ratio curve seen in Figure 4-14. The small magnitude of velocity coupling at low area ratios is a result of the low acoustic velocity amplitude near the T-burner ends. As the area ratio increases the propellant sample enters regions of greater acoustic velocity amplitudes resulting in a nonlinear driving rate-area ratio curve. At high area ratios the velocity coupled driving exceeds 40 percent of the pressure coupled driving and failure to consider velocity coupling in pressure coupled T-burners will lead to erroneous propellant response values being obtained.

The individual driving rates in the velocity-coupled T-burner (Figure 4-17) are all linear with test sample area ratio. In the velocity coupled T-burner, the sample is centered at the maximum value of the product of acoustic velocity and acoustic pressure amplitudes. Increasing the area ratio adds propellant to regions with lower values of the velocity-pressure amplitude product but the magnitude of this product changes relatively slowly so that the velocity coupling-area ratio curve is practically linear over a wide range of conditions. This can also be inferred from Figures 4-10 to 4-12 where it is seen that $g_{\ell v}$, $\mathcal{C}_{\ell v}$, and $P_{\ell v}$ are all relatively constant up to $\beta_v \sim 0.2$.

Cross plots showing the correction α as a function of T-burner diameter/sample diameter ratio with area ratio as a parameter are given in Figure 4-18 for the pressure coupled T-burner and in Figure 4-19 for the velocity coupled T-burner. The correction α is defined as the difference between the net α with a given diameter ratio and the net α at the flush condition. The correction α is much larger in magnitude for the velocity coupled T-burner than for the pressure coupled T-burner.

These calculations also point out the necessity of including acoustic driving contributions from both pressure-coupled and velocity-coupled mechanisms in the T-burner data reduction procedure. The general agreement between the trends observed from these calculations and the actual experimental data is apparent and will be discussed in more detail in Section VII.

D. MOTOR APPLICATION

The Hercules velocity-coupling computer program was written to enable an analyst to calculate velocity-coupled acoustic growth rates in full-scale operational motors. The computer program can accommodate a general three-dimensional grain cavity geometry and any arbitrary three-dimensional acoustic pressure distribution. As originally written, use of the computer program was limited to those situations where flow reversal and threshold velocity effects were absent. This limitation has now been removed. The following paragraphs describe the computer program modifications[67] carried out to include flow reversal and threshold velocity

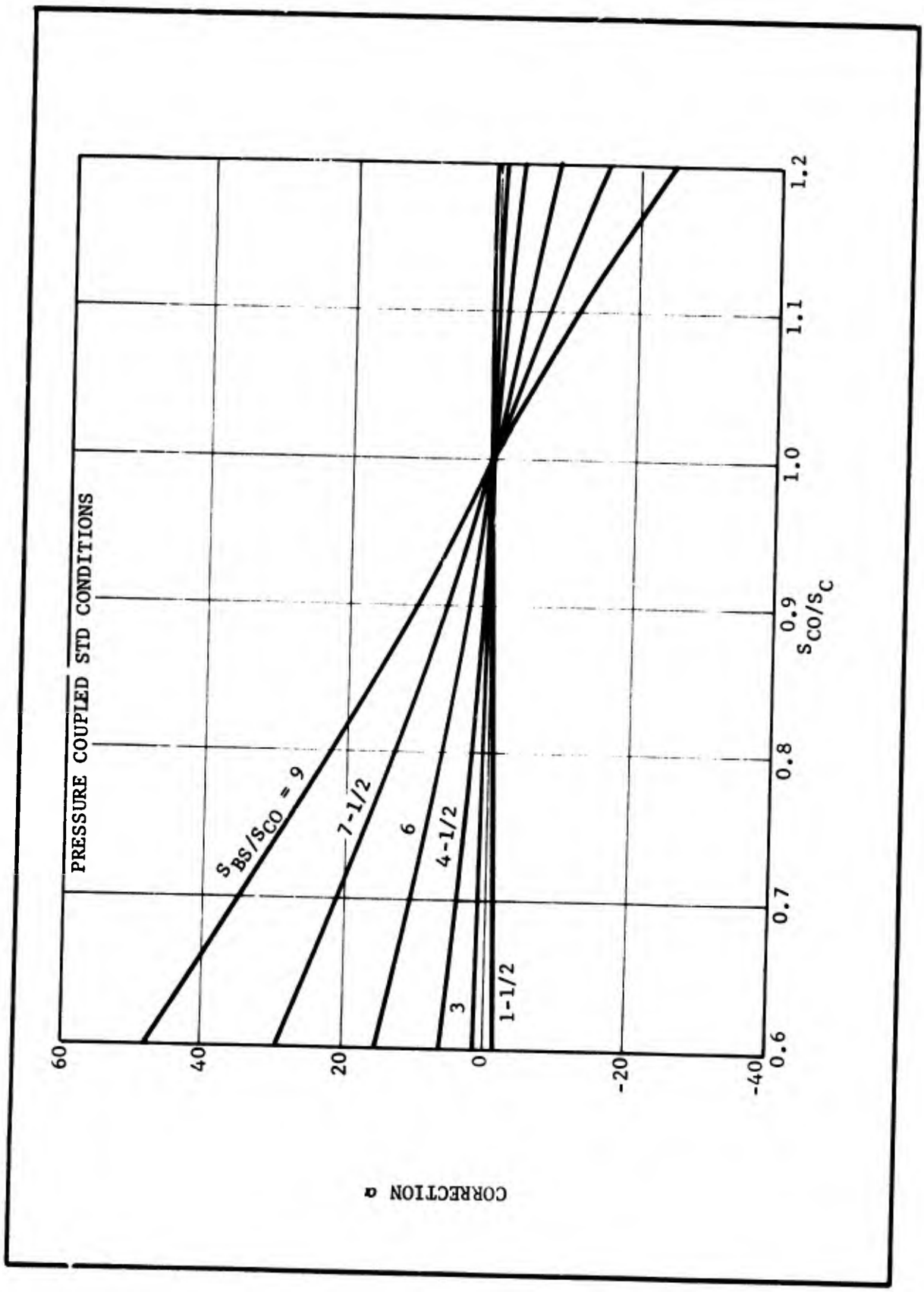

Figure 4-18. Calculated Correction α for Pressure Coupled T-Burner

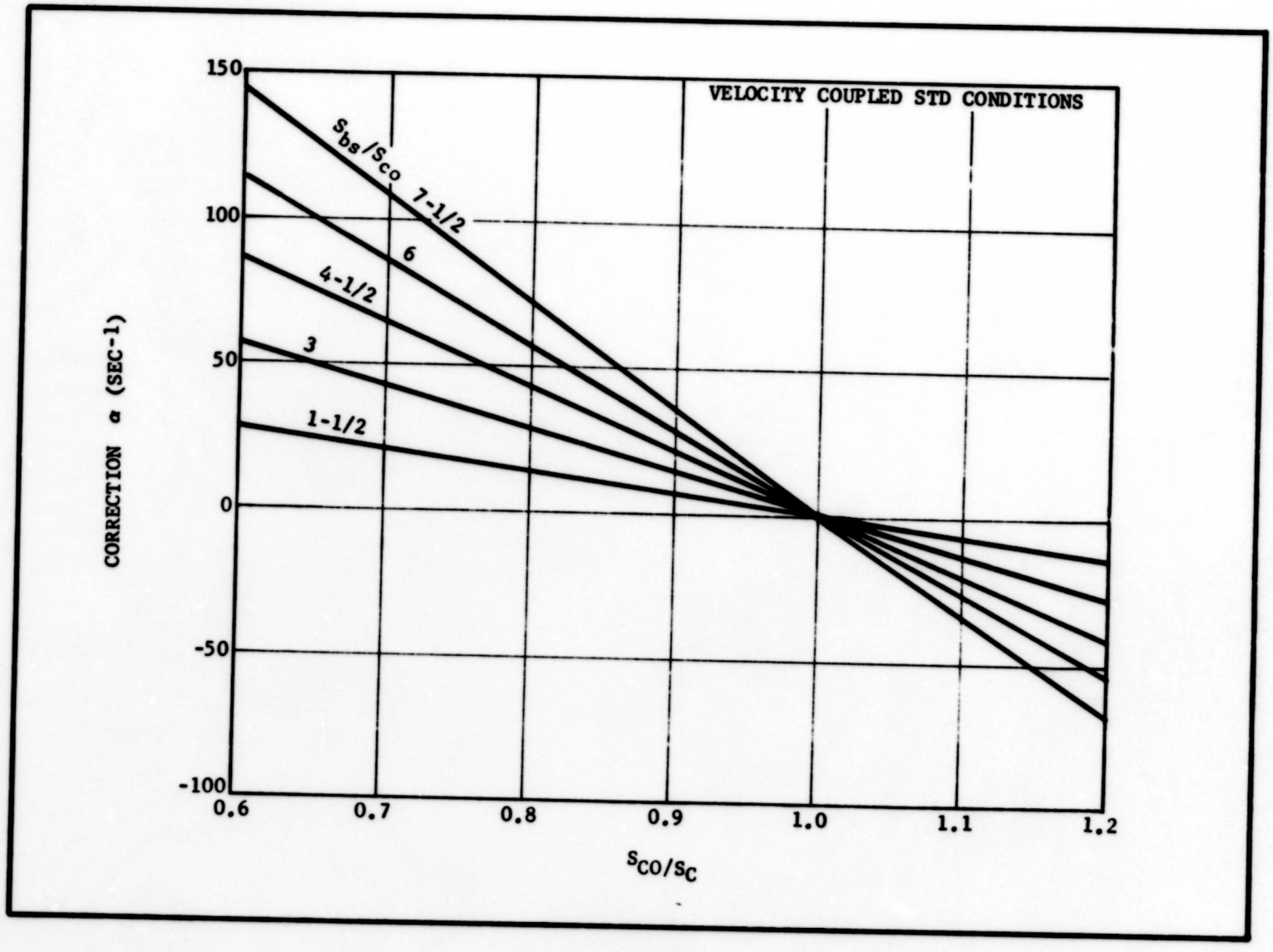

Figure 4-19. Calculated Correction α for Velocity Coupled T-Burner

effects in the acoustic growth rate calculations. The application of the modified program is illustrated by a parametric analysis of velocity-coupling in the Minuteman II stage III motor at 2 in. burn distance.

1. Velocity Coupling Equation

An equation was derived for the velocity-coupled driving contribution to the acoustic growth rate following the procedure used by Flandro[15] for pressure-coupled acoustic driving. The MHC model was used to describe the coupling of the acoustic wave and the propellant combustion. This model assumes that the oscillating mass flux leaving an incremental propellant surface consists of a pressure dependent mass flux that is proportional to the difference between the instantaneous pressure and the steady chamber pressure and a velocity dependent mass flux proportional to the difference between the instantaneous parallel (or tangential) velocity and the parallel mean flow velocity.

By further assuming that the maximum amplitude of the acoustic velocity is always less than the mean flow velocity (no flow reversal) and that the mean flow velocity is always greater than any threshold velocity (defined as that velocity below which mass flux is independent of velocity), the velocity-coupled mass flux contribution is obtained as a term with sinusoidal time dependence and a frequency equal to the acoustic frequency. Since all other quantities entering into the nonhomogenous wave equation and nonhomogeneous boundary conditions describing the acoustic oscillations have the same time dependency, the time dependency can be factored out and the wave equation solved to give the acoustic growth rate as a function of space and acoustic variables.

The resulting velocity-coupled contribution to the acoustic growth rate is

$$\alpha_{vc} = \frac{a^2}{2} \frac{\text{Real}\left[\int_S p'(\rho u_b R_v)\hat{U}_t\left(\frac{i\nabla_t p'}{\omega \rho}\right) dS\right]}{\int_V p'^2 \, dV} \qquad (4\text{-}90)$$

Where $\nabla_t p$ is the acoustic pressure gradient tangent (or parallel) to the propellant surface, the quantity $\rho u_b R_v$ is the change in mass flux normal to the propellant surface/unit velocity difference (instantaneous minus mean flow) and $\hat{U}_t$ is a unit vector in the direction of the mean flow.

Acoustic growth occurs when the mass addition is in phase with the acoustic pressure. Damping will result when the mass addition is 180° out of phase with the acoustic pressure. Since the acoustic velocity is 90° out of phase with the acoustic pressure, it is the imaginary part of the velocity-coupled propellant response function iR_v^i which gives that part of the oscillating mass flux which contributes to the growth rate.

2. Modifications to Include Flow Reversal and the Threshold Velocity Effects

Recalling that the derivation of Equation (4-90) was for the case of no threshold velocity and no flow reversal, it was desired to extend the applicability of Equation (4-90) to include these nonlinear effects. The additional mass flux due to a fluctuating velocity tangent to the propellant surface is

$$\dot{m} \sim R_v \left[\left| u_e + \hat{u} \cos \omega t \right| - \left| u_e \right| \right] \quad \text{if } u_e + \hat{u} \cos \omega t > u_t \qquad (4\text{-}91)$$

$$\dot{m} = 0 \qquad \text{if } u_e + \hat{u} \cos \omega t \leq u_t \qquad (4\text{-}92)$$

where:

u_e = mean flow velocity tangent to propellant surface

$\hat{u}$ = amplitude of acoustic velocity tangent to propellant surface

u_t = threshold velocity

The general case (Equations (4-91) and (4-92)) shows that the change in mass flux caused by tangential velocity oscillations is periodic but nonsinusoidal. The time dependency, therefore, cannot be factored out of the governing nonhomogeneous wave equation and boundary conditions. A rigorous solution of the wave equation would include a time variable and would result in nonsinusoidal acoustic oscillations (since the driving is nonsinusoidal). Obtaining such a solution would be a problem of extreme difficulty and is far beyond the scope of this program.

Instead, the assumption is made that the nonlinear effects of velocity-coupled driving (flow reversal and threshold velocity effects) are small in comparison with linear velocity-coupled driving, mean flow driving, and pressure-coupled driving. This assumption will allow us to further assume that the acoustic pressure and acoustic velocity retain sinusoidal time-dependence. At those locations on the propellant surface where nonlinearities occur, nonsinusoidal oscillations in tangential velocity are replaced by sinusoidal velocity oscillations with an amplitude so calculated that the acoustic driving (or damping) per cycle is identical to the driving (or damping) produced by the actual nonsinusoidal oscillation. The oscillating mass flux resulting from these linearized velocity oscillations is sinusoidal and, therefore, the time dependency can still be factored out of the wave equation and boundary conditions. The velocity-coupled part of the solution to the wave equation, the velocity-coupled acoustic growth rate given in Equation (4-90), remains valid.

Solving Equation (4-90) to evaluate the velocity-coupled growth rate requires two steps. First, for each incremental propellant surface area, determine whether flow reversal and threshold velocity effects occur. Then, the magnitude of these effects and the amplitude of a sinusoidal acoustic velocity is calculated that results in equivalent acoustic driving (or damping) per cycle. The calculated amplitude is used in place of $\left|\frac{\nabla_t p'}{\omega \rho}\right|$, the amplitude of the true acoustic velocity, in Equation (4-90) to determine the growth rate contribution of the incremental area. At each incremental surface area, there are four possible combinations of mean flow velocity, u_e; acoustic velocity, $\hat{u} \cos \omega t$; and threshold velocity, u_t. These cases are:

Case I	$(u_e - \hat{u}) > 0$	no flow reversal
	$(u_e - \hat{u}) > u_t$	no threshold velocity effects
Case II	$(u_e - \hat{u}) > 0$	no flow reversal
	$(u_e - \hat{u}) < u_t$	velocity is smaller than the threshold velocity at some time during a cycle
Case III	$(u_e - \hat{u}) < 0$	flow reversal
	$u_t = 0$	no threshold effect
Case IV	$(u_e - \hat{u}) < 0$	flow reversal
	$(u_e - \hat{u}) < u_t$	velocity is smaller than the threshold velocity at some time during a cycle

The equations giving the amplitudes of sinusoidal velocity oscillations to be used in Equation (4-90) for Cases II, III, and IV are derived in Reference 67 and given in the following paragraphs.

The effects of a threshold velocity and flow reversal occur during the half-cycle when the acoustic velocity is negative. Figure 20a shows the absolute value of the total tangential velocity for one cycle of oscillation. When the magnitude of the negative acoustic velocity, $\hat{u} \cos \omega t$, is larger than the mean velocity, u_e, flow reversal occurs. When the total tangential velocity is less than the threshold velocity, u_t, there is no effect on the velocity-coupled mass flux. The times when this situation exists are shown in Figure 4-20a as Δt_1 and Δt_2.

The instantaneous velocity minus the mean velocity, that is effective in producing the velocity-coupled mass flux, is shown as the crosshatched area in Figure 4-20b. The effect of velocity on mass flux is reduced during the negative acoustic velocity half-cycle because of the flow reversal and the absence of mass flux effects during Δt_1 and Δt_2.

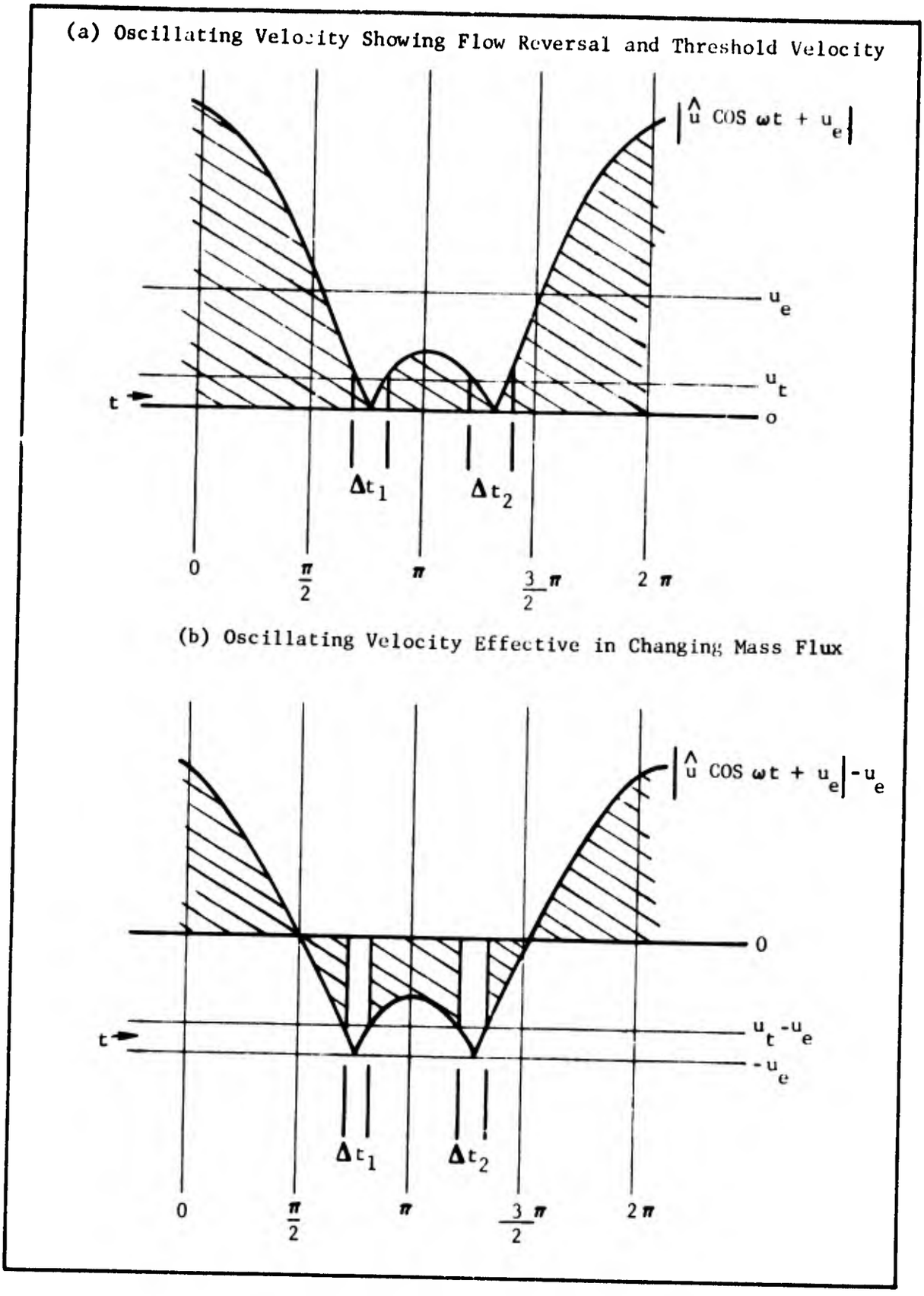

Figure 4-20. Nonlinear Velocity-Coupling Effects

Assume that the phase relationships between acoustic velocity and acoustic pressure are such that Figure 4-20 illustrates an incremental area where the velocity effects are driving, then the increase in mass flux above the mean between $\omega t = 0$ and $\frac{\pi}{2}$ and $\omega t = \frac{3}{2}\pi$ and 2π reinforces the acoustic pressure. The decrease in mass flux below the mean between $\omega t = \frac{\pi}{2}$ and $\frac{3}{2}\pi$ reinforces the negative pressure (rarefaction) occurring during this time. Because of the flow reversal and threshold velocity, the decrease in mass flux will be reduced in magnitude and the amount of reinforcement during the pressure rarefaction will be less than that which would occur in the absence of these nonlinear effects.

The correction for the flow reversal and threshold velocity effects consists of calculating the total crosshatched area in Figure 4-20b, which is proportional to the amount of velocity-coupled driving and finding the amplitude of the sinusoidal acoustic velocity that would give the same crosshatched area.

a. Case II - No Flow Reversal, Threshold Velocity Effects

The area during the negative acoustic velocity half cycle is

$$\int_{\frac{\pi}{2}}^{\frac{3}{2}\pi} \hat{u} \cos \omega t - 2 \int_{\cos^{-1}\left(\frac{u_t - u_e}{\hat{u}}\right)}^{\pi} \hat{u} \cos \omega t \qquad (4\text{-}93)$$

where the first integral is the area in the absence of threshold velocity effects and the second integral is the threshold velocity correction. The lower limit of integration of the second integral is the time in the cycle where the total velocity equals the threshold velocity, $\hat{u} \cos \omega t + u_e = u_t$. Adding the area under the positive half cycle, integrating, and equating to the area under a sinusoidal velocity with amplitude A gives:

$$A = \frac{\hat{u}}{2}\left[1 + \left| -1 + \frac{\left[\hat{u}^2 - (u_t - u_e)^2\right]^{\frac{1}{2}}}{\hat{u}} \right|\right] \qquad (4\text{-}94)$$

b. Case III - Flow Reversal, No Threshold Velocity

The total area is:

$$2\int_{o}^{\frac{\pi}{2}} \hat{u} \cos \omega t + \left| \int_{\frac{\pi}{2}}^{\frac{3}{2}\pi} \hat{u} \cos \omega t - 4 \int_{\cos^{-1}\left(\frac{-u_e}{\hat{u}}\right)}^{\pi} \left[\hat{u} \cos \omega t - (-u_e)\right] \right| \qquad (4\text{-}95)$$

The first integral gives the positive area during the half cycle where the mass flux is greater than the mean. The second integral gives the negative area in the absence of flow reversal while the third integral gives the reduction in negative area due to flow reversal. The lower limit of integration in the third integral is that time in the cycle where flow reversal begins, $\hat{u} \cos \omega t = -u_e$. Integrating and equating to the area under a sinusoidal velocity with amplitude A gives:

$$A = \frac{\hat{u}}{2}\left[1 + \left| -1 + 2\frac{(\hat{u}^2 - u_e^2)^{\frac{1}{2}}}{\hat{u}} - \frac{2u_e}{\hat{u}}\left[\pi - \cos^{-1}\left(\frac{-u_e}{\hat{u}}\right)\right]\right|\right] \qquad (4\text{-}96)$$

c. Case IV - Flow Reversal and Threshold Velocity

The area during the negative acoustic velocity half cycle is

$$\int_{\frac{\pi}{2}}^{\frac{3}{2}\pi} \hat{u} \cos \omega t \, dt - 4\int_{\cos^{-1}\left(\frac{-u_e}{\hat{u}}\right)}^{\pi} \left|\hat{u} \cos \omega t + u_e\right| dt - 2\int_{\cos^{-1}\left(\frac{u_t - u_e}{\hat{u}}\right)}^{\cos^{-1}\left(\frac{-u_e}{\hat{u}}\right)} \hat{u} \cos \omega t \, dt - 2\int_{\cos^{-1}\left(\frac{-u_e}{\hat{u}}\right)}^{\cos^{-1}\left(\frac{-u_t - u_e}{\hat{u}}\right)} \left|-\hat{u} \cos \omega t - 2u_e\right| dt \qquad (4\text{-}97)$$

where the first integral is the area in the absence of flow reversal or threshold velocity effects, the second integral gives the contribution of the flow reversal area, and the last two integrals give the area when the total velocity is less than the threshold velocity. Equation (4-97) is applicable only if the reversed velocity is greater than the threshold velocity. That is, if

$$(\hat{u} - u_e) > u_t \qquad \text{or} \qquad \frac{u_t + u_e}{\hat{u}} < 1$$

If the reversed velocity is less than the threshold velocity, the flow reversal does not affect that mass flux and the situation is equivalent to Case II, threshold velocity effects but no flow reversal. This can be seen in Equation (4-97). For $\frac{u_t + u_e}{\hat{u}} \geq 1$ the upper limit in the fourth integral must become π and the terms involving u_e in integrals two and four cancel each other. Adding the contribution of the positive acoustic velocity half cycle, integrating, and equating to a sinusoidal

velocity with amplitude $\hat{u}$ gives

$$\hat{U} = \frac{\hat{u}}{2}\left[1 + \left| -1 + 2\frac{(\hat{u}^2 - u_e^2)^{\frac{1}{2}}}{\hat{u}} - \frac{2u_e}{\hat{u}}\left[\pi - \cos^{-1}\left(\frac{-u_e}{\hat{u}}\right)\right]\right.\right.$$

$$\left. - \frac{(\hat{u}^2 - u_e^2)^{\frac{1}{2}} - \left[\hat{u}^2 - (u_t - u_e)^2\right]^{\frac{1}{2}}}{\hat{u}}\right. \qquad (4\text{-}98)$$

$$\left.\left. + \frac{\left[\hat{u}^2 - (u_t + u_e)^2\right]^{\frac{1}{2}} - (\hat{u}^2 - u_e^2)^{\frac{1}{2}}}{\hat{u}} + \frac{2u_e}{\hat{u}_m}\left[\cos^{-1}\left(\frac{-u_t - u_e}{\hat{u}}\right) - \cos^{-1}\left(\frac{-u_e}{\hat{u}}\right)\right]\right|\right]$$

3. Parametric Calculations for the Minuteman II Stage III Motor

The modified Hercules velocity coupling computer program was used to calculate the velocity-coupled acoustic driving in the Minuteman II stage III (M57A1) motor. The grain configuration at 2 in. burn distance was used in the analysis. The grain design in this motor is essentially a slotted tube type in which the center core extends only part way through the chamber. Slots connect the center tube with four hollow cones that extend into the four nozzles. The M57A1 grain geometry at zero burn time is shown in Figure 4-21.

The acoustic pressure distribution used in the analysis was measured in a full-scale inert model of the grain geometry. This acoustic pressure distribution is shown in Figure 4-22. The frequency of oscillation is 550 Hz.

A constant value of 1.0 was used for the propellant velocity-coupled response function. Since the velocity-coupled acoustic driving is proportional to the response function, acoustic driving rates for other values of the response function can be calculated by simple scaling.

Three parametric values of threshold velocity were used in combination with three levels of acoustic pressure amplitude. The threshold velocities used were zero and 100 and 200 ft/sec. Acoustic pressure amplitudes used were 1.0, 10.0, and 20.0 psi at the aft end of the motor. The maximum acoustic pressures produced by these aft end amplitudes are 3.3, 33, and 66 psi at the forward end of the motor. These maximum acoustic pressure levels are approximately 1, 10, and 20 percent of the motor operating pressure.

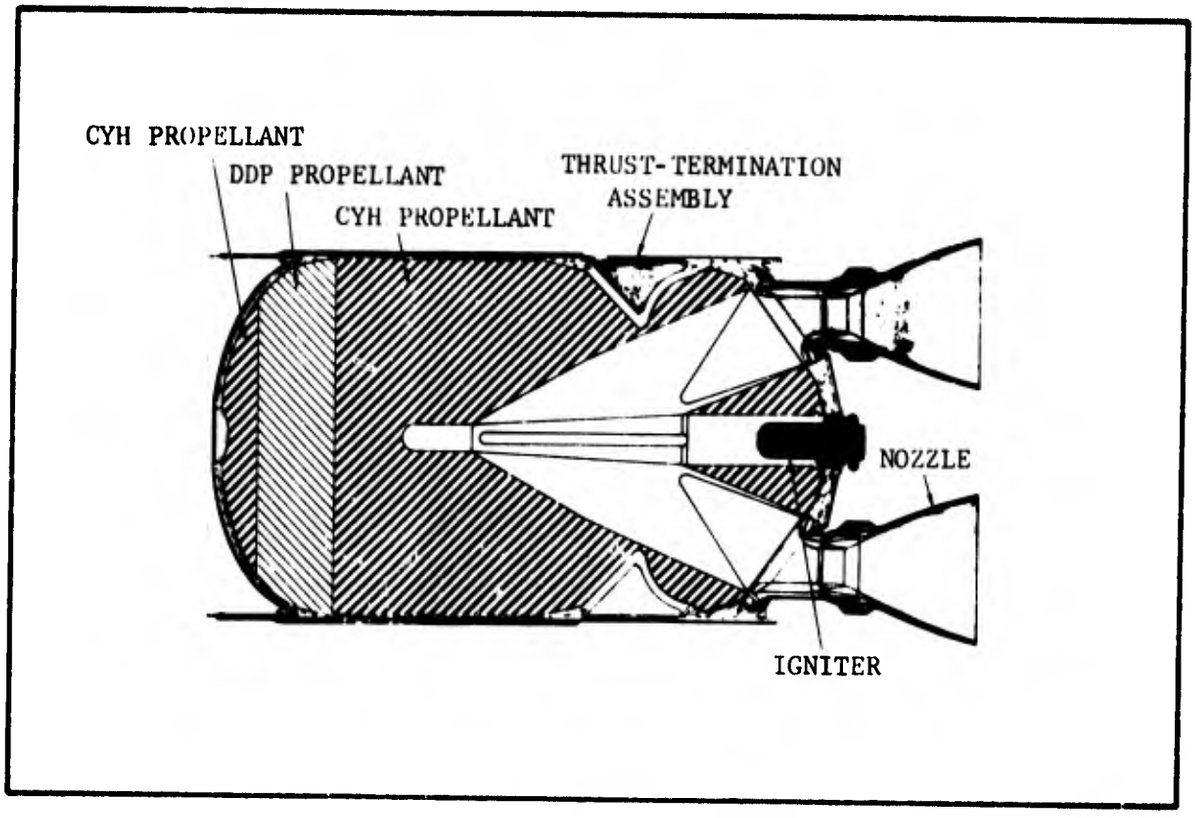

Figure 4-21. Minuteman II Stage III (M57A1) Motor

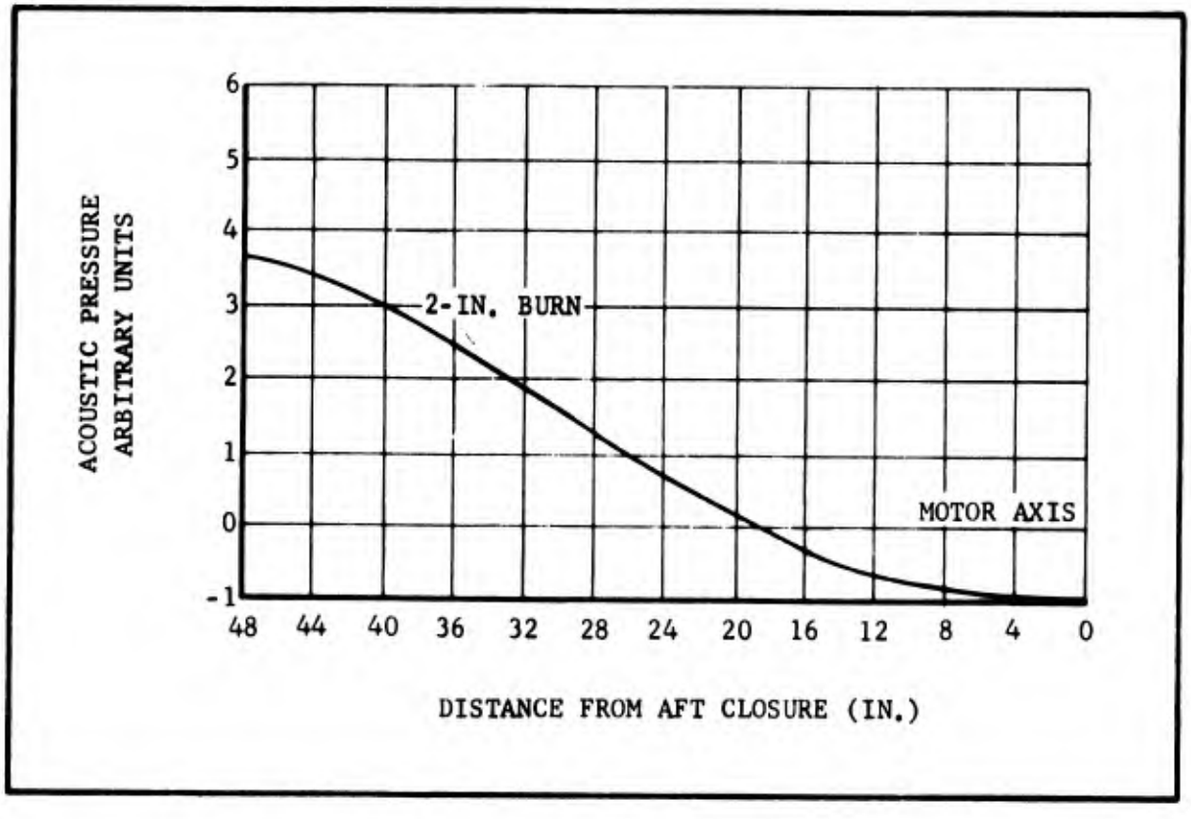

Figure 4-22. Wave Form of First Longitudinal Mode in M57A1 Acoustic Model

The results of the analysis is given in Figure 4-23. The effect of a threshold velocity is to decrease the magnitude of the velocity-coupled driving. At low acoustic amplitudes, approximately 1 percent of the mean chamber pressure, the velocity-coupled growth rate is halved by increasing the threshold velocity from 0 to 100 ft/sec. An additional increase to 200 ft/sec results in the velocity coupled damping the oscillation.

With the 10 and 20 psi acoustic pressure amplitudes, the decrease in acoustic driving in going to higher threshold velocities is considerably reduced. The larger amplitude waves provide a total velocity (mean flow plus acoustic) that exceeds the threshold velocity over a larger fraction of the propellant surface area.

The effects of flow reversal on acoustic driving can be seen by comparing the growth rates for the three pressure amplitudes at zero threshold velocity. An increase in amplitude from 1 to 10 psi decreases the growth rate slightly while increasing the amplitude to 20 psi decreases the growth rate by almost half.

Table 4-II gives the fraction of the total propellant surface that falls into Cases I-V for each analyzed combination of pressure amplitude and threshold velocity. Table 4-II shows that the extent of flow reversal decreases with an increasing threshold velocity.

While the numerical results presented are specific to the M57A1 motor at 2 in. burn, the analysis clearly shows that flow reversal and threshold velocity effects can strongly affect the magnitude of velocity-coupled acoustic driving. Under some conditions, velocity coupling may even provide acoustic damping.

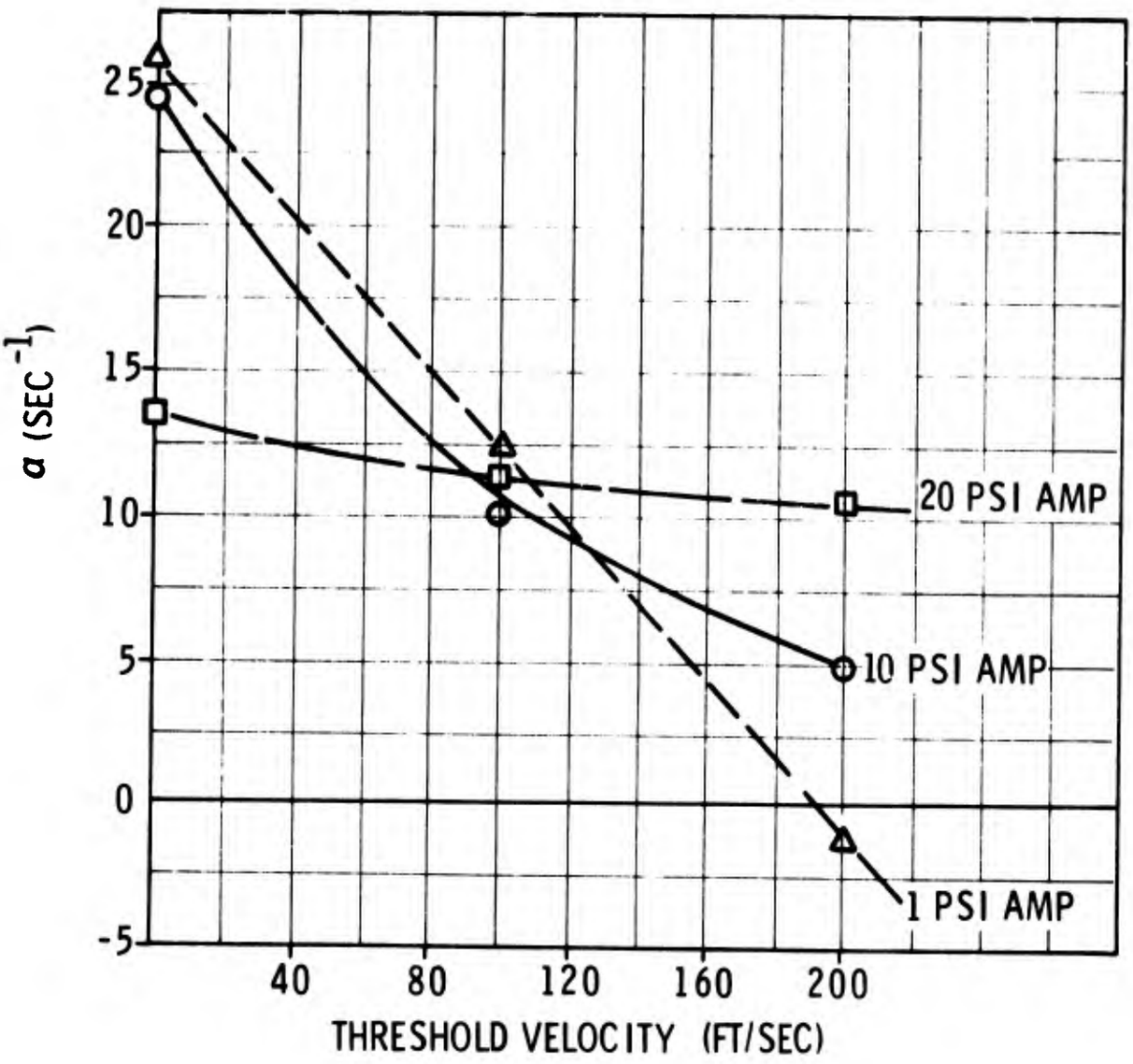

Figure 4-23. Minuteman Velocity-Coupled Growth Rates

TABLE 4-II

PERCENT PROPELLANT SURFACE AREA WITH
FLOW REVERSAL AND THRESHOLD VELOCITY EFFECTS

Percent Propellant Surface Area		Threshold Velocity (ft/sec)								
		0			100			200		
		Pressure Amplitude (psi)			Pressure Amplitude (psi)			Pressure Amplitude (psi)		
		1	10	20	1	10	20	1	10	20
Case I	No Flow Reversal No Threshold Effects	100	65	49	53	31	22	17	17	13
Case II	No Flow Reversal Threshold Effects	0	0	0	43	67	48	5	40	82
Case III	Flow Reversal No Threshold Effects	0	35	51	0	0	0	0	0	0
Case IV	Flow Reversal Threshold Effects	0	0	0	0	0	29	0	0	0
Case V	No Effect on Mass Flux	0	0	0	4	2	1	78	43	5

SECTION V

PHENOMENOLOGICAL STUDY

A. INTRODUCTION

This phase of the program was used to identify test conditions where the propellant combustion was strongly influenced by acoustic velocity oscillations. It was not intended that the measurements be quantitative. Rather, it was intended that an inexpensive test technique be used to screen propellants and test conditions so that regions of strong interaction could be identified. Then, in Phase III, a more sophisticated technique could be used with a higher probability of success because of the guidance available from the Phase II results.

The approach used was to find a device capable of imposing high amplitude velocity oscillations on a burning propellant sample but with negligible pressure perturbations. The response of the combustion was inferred from the fluctuating luminosity of the flame. The test variables were frequency, pressure, propellant composition, mean gas velocity, and acoustic gas velocity.

In the following paragraphs, the test device is described as are the tests conducted, the results obtained, and the conclusions reached.

B. EXPERIMENTAL APPROACH

1. Test Device

The selection of an experimental combustor depended on several factors that are not intuitively obvious. Therefore, prior to describing the device, the reasons for its choice will be examined which can best be done by considering some pertinent equations.

For illustrative purposes, a cylindrical chamber containing a first-mode longitudinal, standing acoustic wave will be considered. The acoustic field can be described by cosine and sine functions (see Equations 4-21a and 4-21b). Such an acoustic field can interact with the combustion of a solid propellant in several ways. Of particular concern relative to acoustic instability is the perturbation in burning rate due to the coupling of the combustion with the acoustic velocity and pressure.

The perturbed velocity of the gases leaving the combusting surface can be written in terms of a pressure coupled response R_b and an acoustic erosive constant R_v. (See Equation 4-25.)

Equation 4-25 shows that in general, the combustion simultaneously exhibits a pressure coupled and a velocity coupled response. Only when propellant is located at the T-burner midpoint does the propellant show only velocity response. This conclusion is general and applies to all test devices and acoustic fields. If it is desirable to study velocity coupling in the absence of pressure coupling, experiments must be conducted so that the propellant is subject to velocity oscillations only.

The acoustic field best suited to the study of velocity coupling has thus been defined. Equation 4-25 implies that the velocity of the gas leaving the combusting surface should be measured in order to characterize the velocity coupled response. Alternately, the instantaneous mass burning rate could be measured. Unfortunately, the required experimental technique for measuring either of these parameters has not been developed.

Because this program was largely concerned with aluminized propellants, it was possible to select a variable that would indirectly indicate the burning rate of the gases leaving the propellant surface. This variable was the luminosity of the flame and the rationale behind its choice was as follows: It was first assumed that the amount of light emitted by the flame was proportional to the number of burning particles in the flame. The number of particles being emitted would then be proportional to the burning rate of the propellant so that the amount of light being emitted would be directly related to the burning rate. Therefore, it was reasoned that the velocity coupled response of a propellant could be qualitatively determined from measurements of the luminosity of the propellant flame when the propellant was burned at the theoretical velocity anti-node (pressure node) in an intense acoustic field.

To satisfy the need for flexibility in test conditions and to satisfy the requirements discussed above, the half T-burned shown in Figure 5-1 was initially selected as the test device. However, before tests began, results from another program showed the operation of the half T-burner to be more complex than preliminary results [68] had suggested. (See Discussion in paragraph D.) Accordingly, the alternate T-burner shown in Figure 5-2 was selected as the basic test device. This burner differed from a conventional T-burner in three ways. First, a sample of test propellant was placed and burned in a small recessed cavity (1/2 x 1/2 x 1/16 in. deep) located at the center of the burner (at the theoretical pressure node). Adjacent to the cavity was a window through which the combustion of the test sample could be observed. (See Figures 5-3 and 5-4.) Second, the gas vent was displaced 2 in. from the center of the burner toward one end so that the test sample would be subject to an erosive velocity determined by the amount of driver propellant burning in the end of the T-burner. Third, the inside cross section of the burner was a 1 in. square rather than the usual circle. Thus, inexpensive, rectangular, flat propellant samples could be used in the burner rather than more complex, cylindrical samples that would be required in a conventional T-burner.

In a given test, it was desired that the test sample of propellant be observed as it burned at a given steady pressure and mean erosive velocity with an imposed acoustic velocity wave of a specified frequency and amplitude and no acoustic pressure. (As will be discussed in paragraph D, it was virtually impossible to achieve these conditions.) Initially, the specified conditions in the test device were to be achieved as follows: The desired

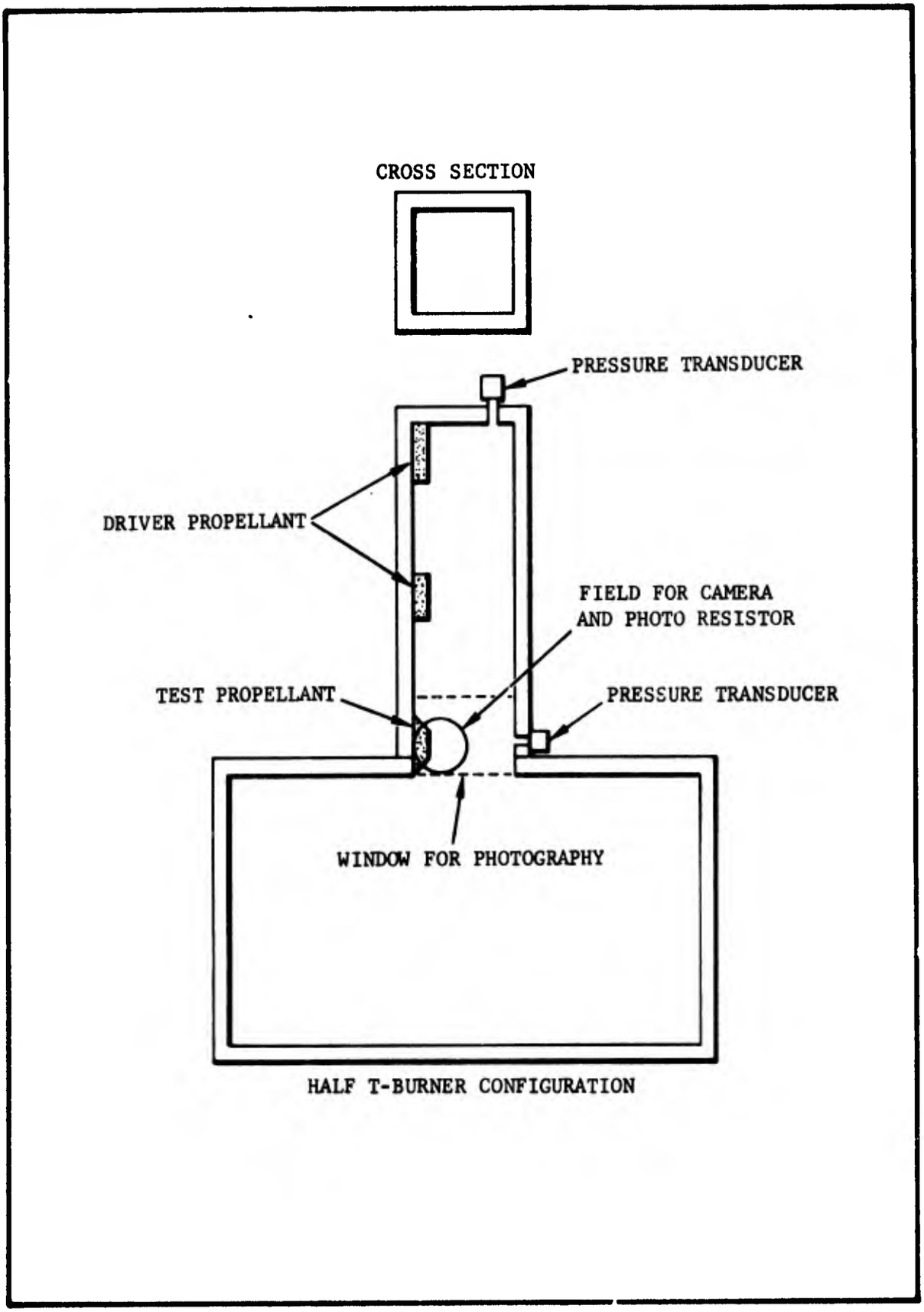

Figure 5-1. Half T-Burner Configuration for Phenomenological Study

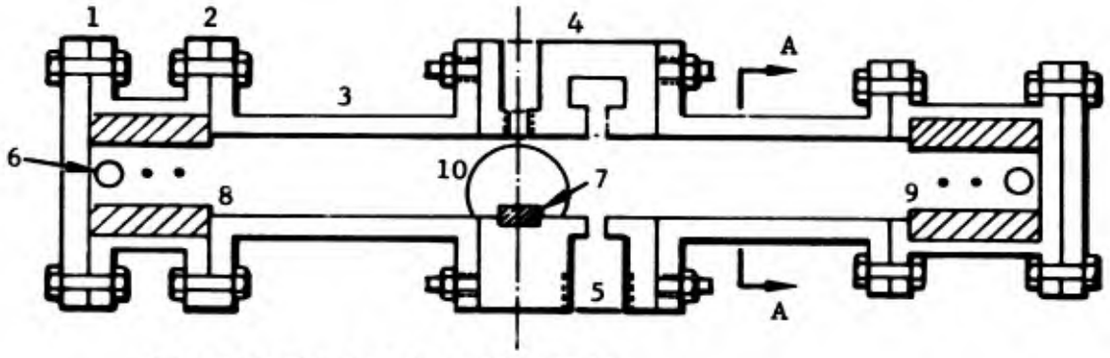

(a) T-BURNER WITH OFFSET VENT

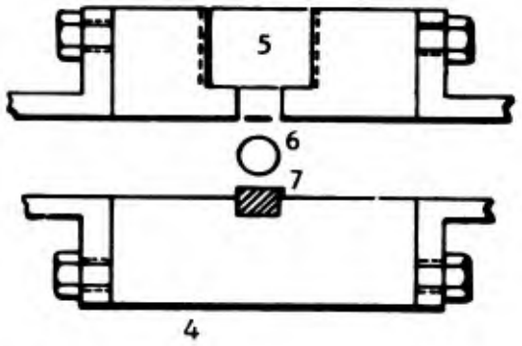

1. END PLATE
2. END PROPELLANT HOLDER
3. EXTENSION PIECE
4. CENTER BODY
5. GAS VENT
6. TRANSDUCER HOLES
7. TEST PROPELLANT
8. DRIVER PROPELLANT
9. IGNITER LEAD HOLES
10. WINDOW

(b) FINAL T-BURNER CONFIGURATION WITH CENTERED VENT

Figure 5-2. T-Burner Configurations Used for Phenomenological Study

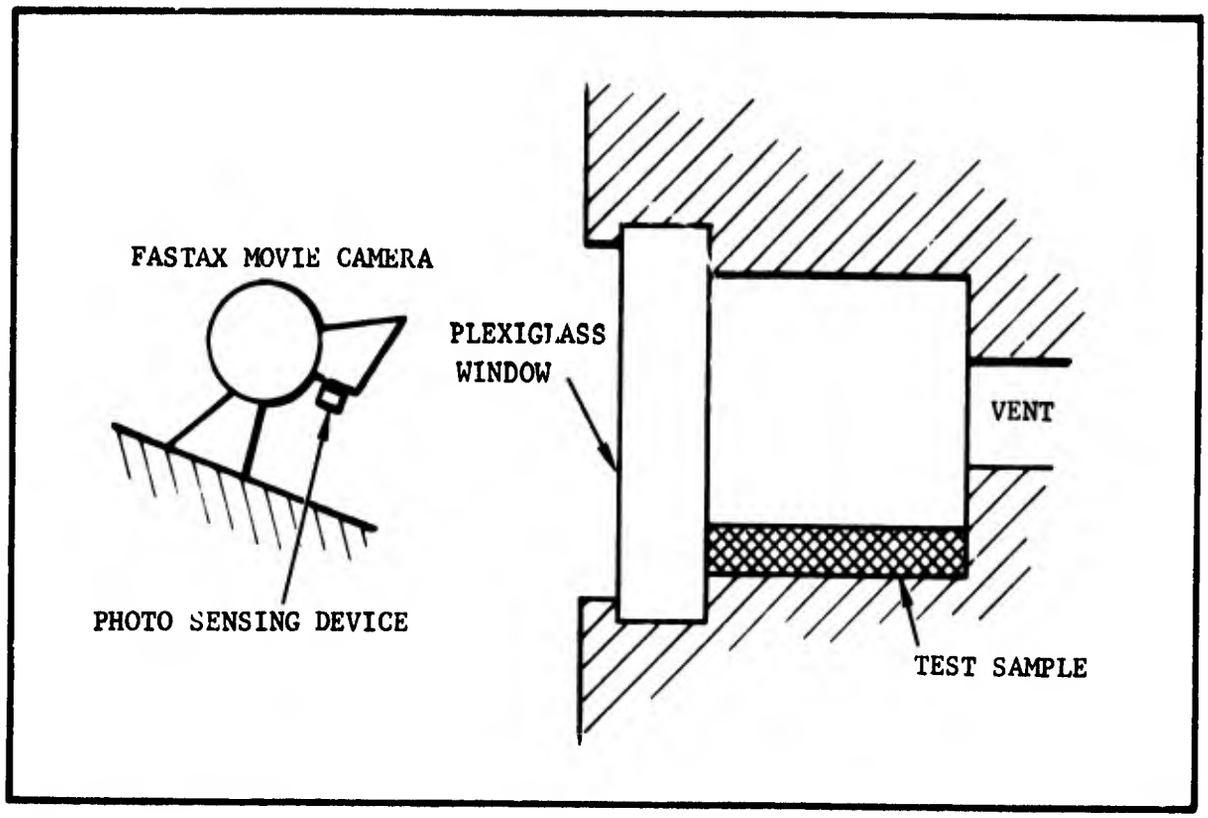

Figure 5-3. Cross Section View of Test Sample

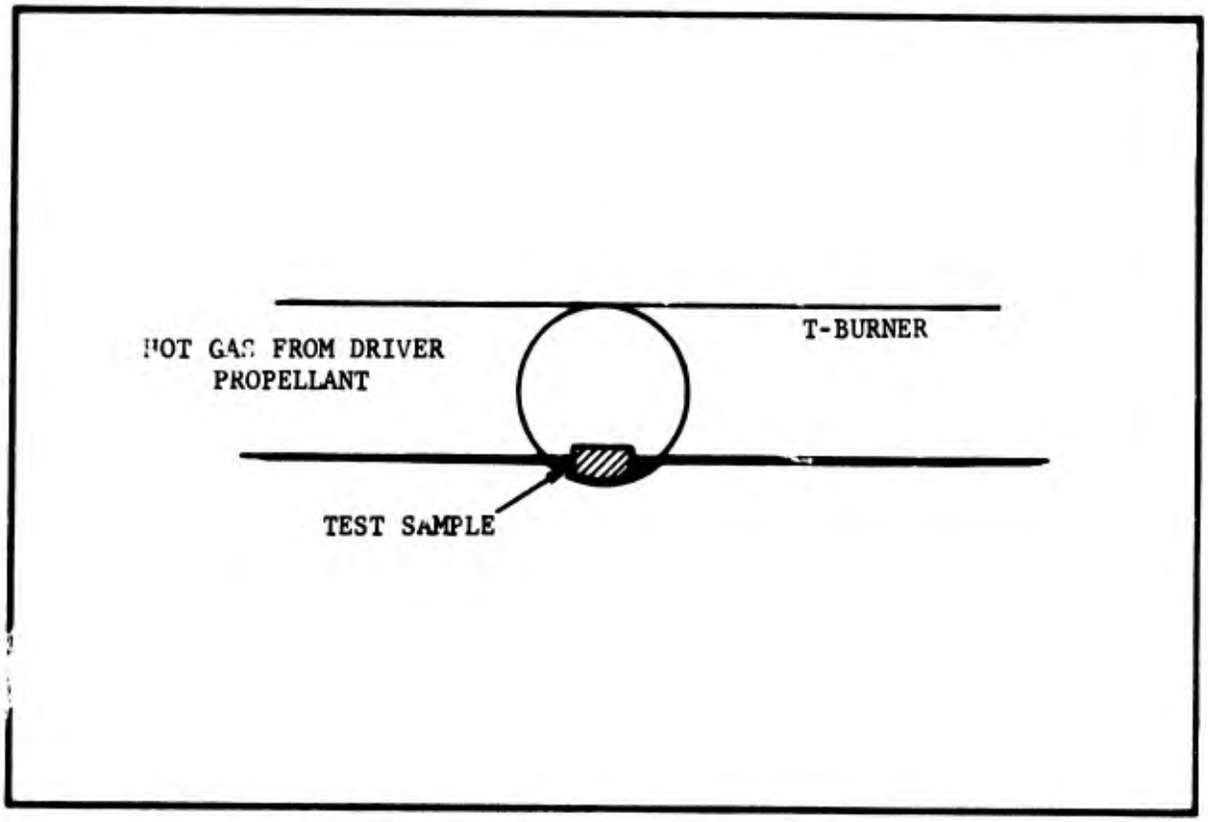

Figure 5-4. Side View of Test Sample

pressure was to be controlled by mounting the T-burner on a prepressurized surge tank. Mounting the test sample at the center of the burner would place it at a theoretical pressure node so a steady pressure but not an oscillating pressure would be experienced by the sample. The sample would only be exposed to velocity oscillations. The amplitude of the velocity oscillations would be controlled by placing slabs of JPN propellant at the sides of the burner near the ends. Because JPN was known to be rather unstable, only a small amount of propellant was needed to produce the specified oscillation amplitudes. To also achieve the desired mean velocity, unequal amounts of JPN driver propellant were used in the two burner ends. In the end containing the test sample, sufficient JPN was used to achieve the specified mean velocity across the face of the test sample. The balance of the driver propellant required to generate the desired acoustic velocity was placed in the other end of the burner. In the event that a very low acoustic velocity was specified, the driver propellant samples were displaced from the burner ends toward the nozzle, thus maintaining the desired mean velocity but with reduced oscillatory amplitude.

2. Experimental Procedure

Figure 5-2a shows that the T-burner consists of four main parts: (1) The center body, (b) the extensions, (c) the propellant holders, and (d) the end caps. These parts were assembled as follows in order to conduct a test: First, the 6 in. long center body was mounted on the surge tank. Then, two extensions, the lengths of which were chosen so that the burner would oscillate at the desired frequency, were fastened to the center body. Before the burner was further assembled, the required amount of driver propellant (usually two 1-in. square pieces of JPN) was cut with a knife from 1/4 in. thick slabs. The sides and back of the propellant were then inhibited with transparent General Electric RTV silicone rubber and the propellant was slipped into the propellant holders. Thiokol X-255 igniter was painted on the top surface of the propellant. Next, an igniter-covered piece of high resistance wire connected to copper lead wires was placed in the holder and the copper wires soldered into the power leads.

The propellant holders were then mounted on the extensions and the end caps fastened to the holders. A previously cut 1/8 in. thick by 1/2 in. square piece of test propellant was inhibited with RTV silicone on all faces except the top (i.e., that exposed to the burner cavity) and the one adjacent to the window. A new plexiglass window was fastened into place, care being taken to insure a snug fit of the window against the adjacent propellant. The propellant face adjacent to the window was not inhibited because inhibitor was found to dirty the window and obscure the field of view. No igniter was used on the test propellant sample because the combustion products of the igniter also fouled the window.

Two Kistler 606 A pressure transducers were mounted on the burner and connected to 504 D charge amplifiers. One transducer was mounted in the end of the burner and the other was mounted opposite the sample of test propellant. A 16 mm Wollensak Fastax camera containing 100 ft of Ektachrome

EF 7241 film was placed outside the window and focused on the test propellant surface. Alongside the camera lens a Texas Instrument Co. LS-400 photo resistor was mounted.* Thus, both optical devices were about 2 in. from the propellant surface "looking" down at the propellant surface with an angle of about 30 degrees. The output from the charge amplifiers and the photo resistor circuitry were connected to three M-1000 galvanometers in a Honeywell Model 1501 Visicorder.

The surge tank was pressurized and then leads from a 35 volt ac source connected to the igniters. A prefiring check list was reviewed to insure that the instrument settings were correct and the burner was ready to fire. A Bliss Signal Co. Eagle timer (model HM701A607) started the camera first so that a speed of 4000 frames/sec would be achieved prior to ignition. Later, the Visicorder was started and allowed to reach its operating speed of 80 in./sec. At that point the power switch was closed so that the propellants ignited. After a time sufficient to allow all of the propellant to burn, the instruments were turned off. The surge tank was bled down and the test record was rolled up, marked, and stored. The film was taken from the camera and sent to be developed. Any apparent peculiarities were noted on the data sheet, and the run was completed.

3. Data Analysis

From viewing the movie film, it was usually possible to determine the propellant combustion characteristics before and after the oscillations began. Inhibitor failure and window fouling could also be identified and taken into account when the Visicorder trace was analyzed. The field of view was such that the propellant surface and about 1/4 in. of the flame above the surface could be observed. To some extent, the agglomeration of Al on the surface as well as its ignition and subsequent combustion could thus be described.

The alternating current pressure traces and the total luminosity trace were recorded on the Visicorder record. Conditions varied during the firing so most measurements were made midway through the combustion of the test sample when the propellant surface was flush with the burner wall. At this time, the pressure and luminosity oscillations were measured and recorded. However, there were some amplitude-dependent phenomena that occurred when the flush condition did not exist. Naturally, measurements of interest were taken when such phenomena were observed.

*In series with the LS-400 photo resistor were a 22.5 volt dc battery, a 510 ohm resistor, and the combination of a M-1000 galvanometer and a 22 ohm resistor in parallel. The circuit provided a linear deflection up to about 3 in. (2000 foot candle luminosity). Above this level, the circuit became nonlinear with saturation occurring at a deflection near 7 in.

C. TEST PROGRAM

Variables of interest in the test program were propellant composition, frequency, mean pressure, steady erosive velocity, and acoustic velocity. The standard test conditions selected were 60 ft/sec, 500 Hz, 300 psi, and 200 ft/sec peak-to-peak oscillatory amplitudes. A low mean velocity should enhance instability, therefore the value of 60 ft/sec was selected. A frequency of 500 Hz was selected as the midpoint in 100 to 1000 Hz frequency range normally associated with velocity coupling and because this is typical of the oscillation frequencies observed in many full-scale motors that at present are exhibiting instability. Three hundred psi was selected because it is a typical operating pressure for the first propellant to be tested (CYH). The 200 ft/sec amplitude was selected as being a typical oscillatory velocity that might be observed.

During the program, these conditions were found to be equally satisfactory as a baseline for all propellants and were so used.

Table 5-I presents a summary of the tests that were planned and conducted. Essentially, the program called for testing a variety of propellants over a range of experimental conditions to screen for regimes where velocity coupling was apparently large. The test matrix encompassed a wide range of test conditions for several propellant formulations (Table 5-II) with a considerable degree of flexibility. In addition to looking at different propellant families, the variation of ingredients for a single formulation was to assist in pinpointing relative effects of ingredients on velocity coupling. The ANB-3066 propellant system was chosen for the formulation study because of ease of mixing at Brigham Young University and because it is a typical state-of-the-art composite propellant. Formulation variations (Table 5-II) were mixed containing less* aluminum, coarser* aluminum, finer* aluminim, coarser* ammonium perchlorate and finer* ammonium perchlorate. The variations were considered typical of the changes that might be made either during propellant development or in an attempt to solve an instability problem.

The test variables shown in the Test Matrix (Table 5-I) included ranges of 300 to 1100 cps in frequency, 13 to 700 psia mean pressure, 0 to 200 ft/sec steady erosive velocity, 0 to 500 ft/sec acoustic erosive velocity, and 0 to 70 psi peak-to-peak oscillatory pressure.

*All formulation variations were made relative to the basic ANB-5066 formulation.

TABLE 5-I

ORIGINAL TEST MATRIX

Test Variable	Propellant			ANB Variations					
	CYH	ANB-3066	A-87	No Al	1/2 Al	H-15	H-5	40μ	400μ
Number of Check Out Tests	5/7*	5/8							
Base Line (No. of tests) (60 ft/sec, 300 psi) (500 Hz, 10% amplitude)	2/2	2/4	2/2	2/2	1/4	1/2	1/1	1/2	1/1
Velocity Variation (No. of tests)									
20 ft/sec	1/2	1/1	1/0	1/0					
200 ft/sec	1/1	1/1	1/1	1/1					
500 ft/sec	1/0	1/0	1/0	1/0					
Pressure Variation (No. of tests)									
500 psi	1/1	1/1	1/2	1/2					
700 psi	1/0	1/2	1/0	1/1					
Frequency Variation (No. of tests)									
300 Hz	1/3	1/3	1/1	1/1					
700 Hz	1/2	1/2	1/2	1/1					
1000 Hz	1/1	1/1	1/0	1/1					
Amplitude Variation (No. of tests)									
0	1/1	1/1	1/0	1/1					
20%	1/2	1/2	1/1	1/1	1/2	1/1	1/1	1/1	1/1
Other	0/3	0/4	0/2	0/1					

*Number of tests originally planned/actual tests fired

TABLE 5-II

PROPELLANT COMPOSITIONS

CYH is a typical composite modified double base propellant that contains Al and added oxidizer.

ANB 3066 is a typical composite propellant made with aluminum, ammonium perchlorate, and Butarez.

A-87 (modified) is a standard ICRPG research propellant made with aluminum, a unimodal ammonium perchlorate grind, 1 percent copper chromite burn rate catalyst, and 18.5 percent PBAN binder

No Al is the designation for the base ANB 3066 modified by replacing the Al with AP and keeping the ratio of ground to as-received AP constant.

1/2 Al is the designation for the base ANB 3066 modified by replacing half the Al with AP, the ratio of ground to as-received AP was kept constant.

H-15 is the designation for the base ANB 3066 modified by replacing the Al which has a weight average size of 17μ* by H-15 Al having a weight average size of 25μ.

H-5 is the designation for the base ANB 3066 modified by replacing the 17μ Al with 8μ H-5 Al.

40μ is the designation for the base ANB 3066 modified by replacing the fine AP having a weight average particle size** of 120μ with American Potash spherical 40μ ammonium perchlorate.

400μ is the designation for the base ANB 3066 modified by replacing the coarse AP having a weight average particle size of 220μ with American Potash spherical 400μ ammonium perchlorate.

*Values were established by analyzing the ingredients with a Coulter Counter

**AP sizes were determined by sieve analysis

D. EXPERIMENTAL RESULTS

1. T-burner Behavior

There were several interesting discoveries made about the operation of T-burners and these will be related before the more relevant velocity coupling results are discussed. First, before experiments began, it was learned on another program that the proposed half T-burner was a rather complex device not suited to the program. This was because the burner would couple with the surge tank to produce unanticipated frequencies; hence, it would be difficult to test at the specified variety of conditions.

It was, therefore, decided that the program would be carried out with the T-burner having a vent displaced 2 in. from the center. The displaced vent allowed the test sample to be placed at the velocity antinode. It was believed that this burner would be satisfactory inasmuch as prior experiments[69] showed that the major effect of the displaced vent was to slightly stabilize the burner. It appeared that the test conditions could be realized if enough driver propellant were placed in the end containing the test sample to produce the desired mean velocity. Then, a judicious location of the proper amount of driver propellant along the side and in the other end would yield the programmed oscillatory amplitude. However, it quickly became apparent that this burner also functioned in an unexpected way. When the desired test conditions required that different amounts of driver propellant be used in the two ends the standing wave was no longer of the type described by simple sine and cosine functions. Rather than being a cosine wave having a pressure node at the center, the wave had some other functional form. In general, the amplitude of the first mode pressure oscillation at the center position was about 25 percent of the amplitude at the end. This pressure oscillation confused the results, as it was impossible to separate pressure and velocity coupled response since the test sample was subject to both.

Accordingly, the ability to obtain mean erosive velocities across the test sample was sacrificed and the center-vented T-burner, as shown in Figure 5-2b, was used. The acoustic mode structure in this burner was much improved. However, the loaction of the test sample of propellant was optimum to generate second mode pressure oscillations, which it did to some extent. Nevertheless, this system performed sufficiently well that it was used for most of the tests.

Very early in the program, personnel training tests were conducted. In these tests, a conventional double-end T-burner was fired at room pressure. Surprisingly, intense oscillations ($Q = 0.6$, $\alpha = 30$ sec^{-1}) were observed. This severity of oscillation was beyond that shown by the propellant at higher pressures. The conclusion is that atmospheric pressure is a favorable test condition to be used in studying T-burner behavior inasmuch as neither a surge tank or nozzle need be used.

2. Test Results

Over a hundred tests were conducted in the program and the results from each were fairly complicated. So that the following reading will not be tedious, the detailed results are presented elsewhere[70] while only the general results are discussed here.

a. Conventional Velocity Coupling

As was mentioned in paragraph B, the velocity coupling was to be inferred from a recording of the fluctuating luminosity caused by the velocity oscillations. In the absence of a mean erosive velocity, each velocity maximum, regardless of direction, should produce a maximum perturbation in burning rate. The absolute value of the acoustic velocity reaches a maximum twice for each pressure cycle. Hence, a first mode pressure oscillation in the burner ought to generate second-mode velocity coupling response from the test sample located at the velocity antinode. A large second mode luminosity fluctuation ought to indicate a large degree of velocity coupling. In addition, the velocity induced perturbation in burning rate can only transfer energy to or from the acoustic wave if the burning rate response and acoustic velocity are 90° out of phase so this condition would be of particular interest.

One of the most important results of the program was that the behavior described above did not occur. It is true that second mode luminosity oscillations, sometimes of a fairly large amplitude, were sporadically observed. However, the oscillations were invariably in phase with the pressure oscillations and out of phase with the velocity oscillations. Because the luminosity oscillations always had this peculiar phasing, the inescapable conclusion is that they are not due to a velocity-induced change in burning rate but rather were the product of the test procedure. They are probably caused by motion of the combustion plume from the test sample of propellant. At any rate, if the anticipated form of velocity coupling was present, it was too small to be observed by the present test method.

b. Dark Combustion

Another important discovery made during the program was that a totally unexpected form of velocity coupling was observed. It was found that as the oscillations grew in amplitude, a point was reached where the luminosity of the flame decreased by an order of magnitude or more. As Figures 5-5 and 5-6 illustrate, the movies showed that the oscillations largely prevented or retarded the combustion of the aluminum in the propellants. In the case of the unaluminized propellant, the change in luminosity seemed related to changes occurring in the number of hot spots seen on the propellant surface.

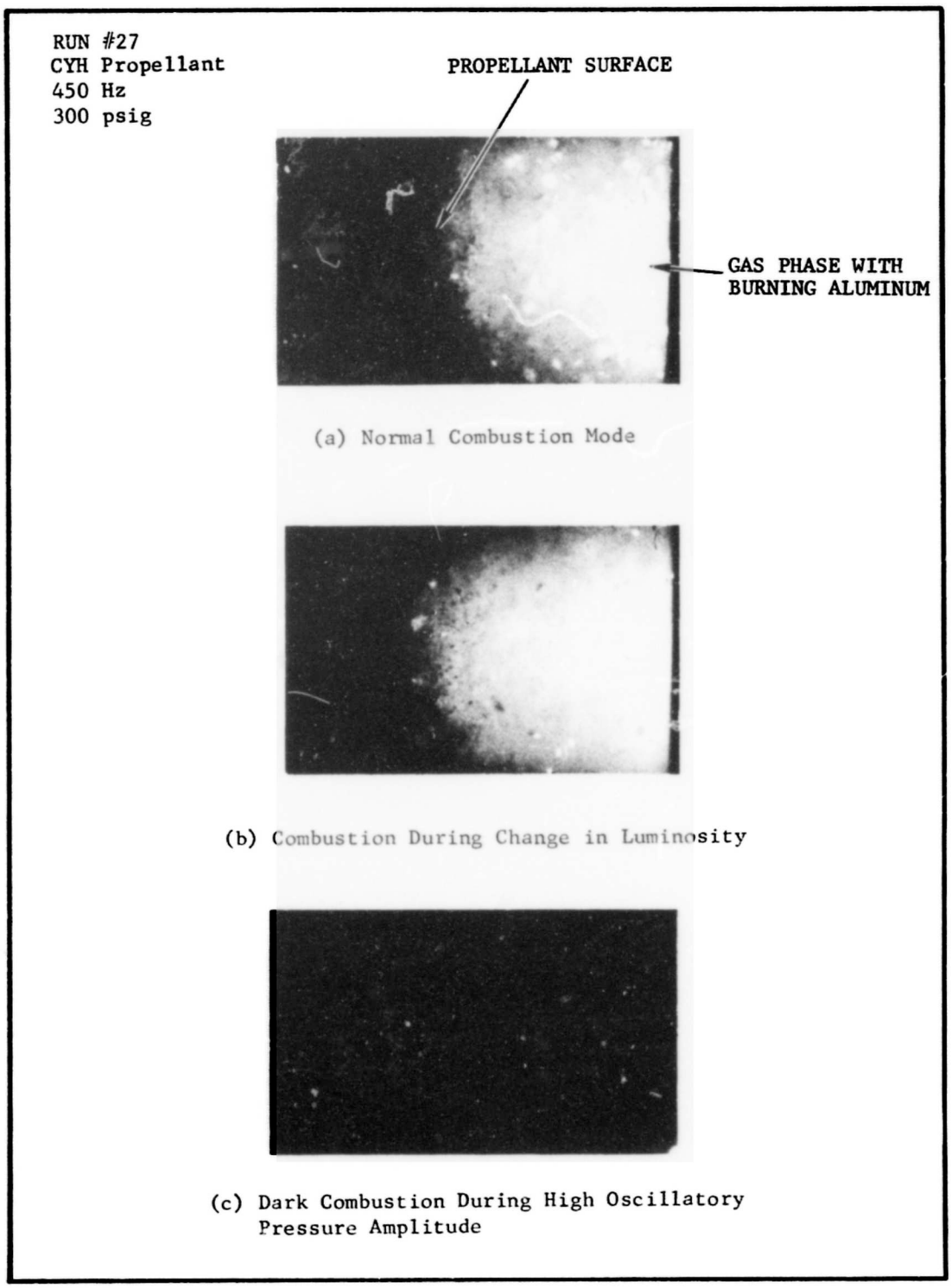

Figure 5-5. Film Sequences Showing the Transition from Normal Combustion to the Dark Combustion Mode for CYH Propellant

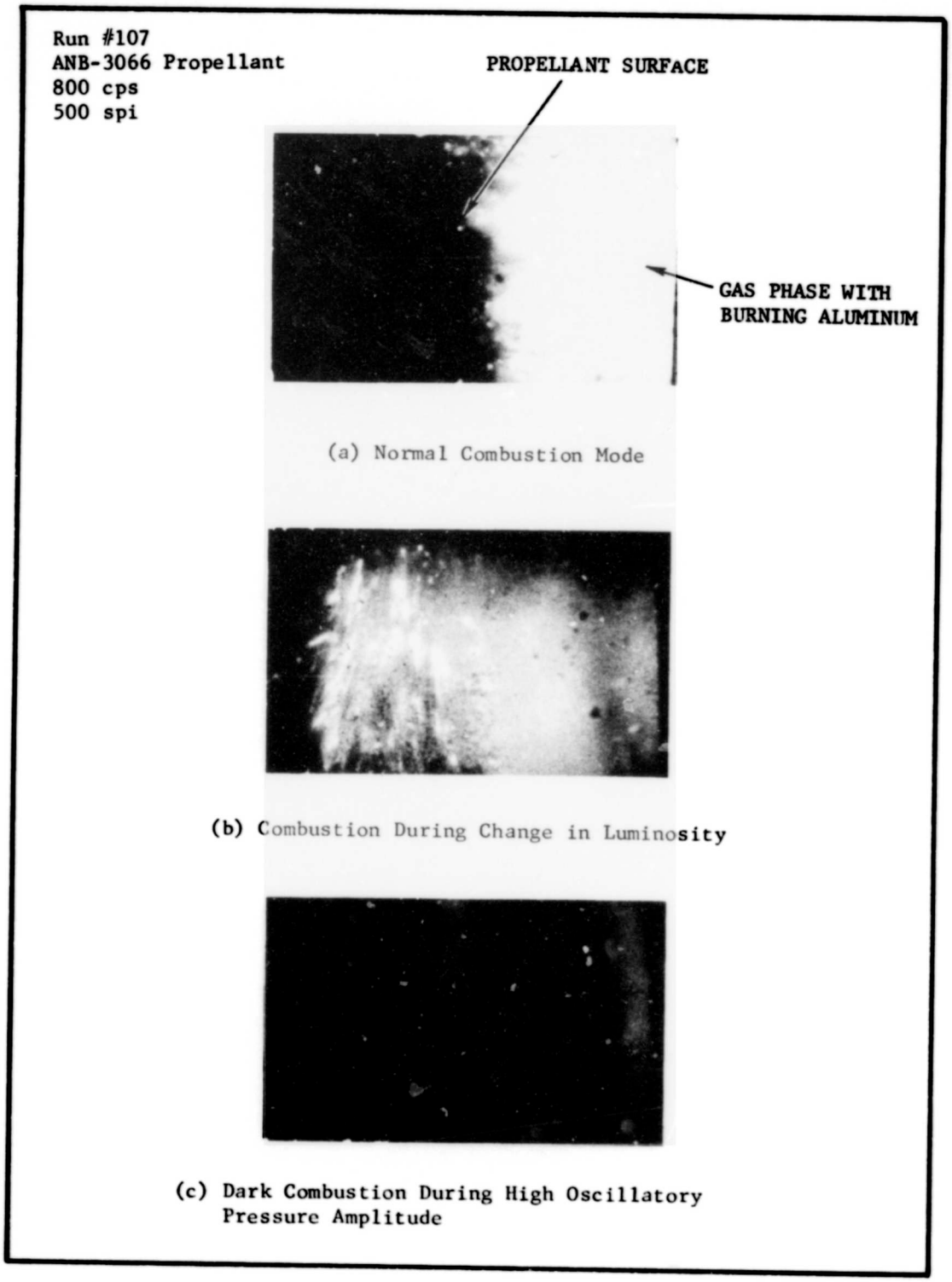

Figure 5-6. Film Sequences Showing the Transition from Normal Combustion to the Dark Combustion Mode for ANB-3066 Propellant

There were some minor differences that could be attributed to different propellant compositions and these will be discussed later. At this point, those features common to all the compositions will be discussed. First of all, as Figure 5-7 shows, the change in luminosity occurred almost as a step function. The oscillatory level which caused the change varied but when the change occurred it was usually sudden and large. Second, the change was reversible in that bright combustion was suppressed early in the firing as the oscillations grew. This is illustrated in Figure 5-8. Later, as the driver propellant burned out, the amplitude diminished and the bright form of combustion was reestablished. There was some suggestion that a large steady erosive velocity could also induce the dark combustion. However, the acoustic erosive velocity was much more effective in causing the dark combustion.

When the dark combustion occurred, there was not only a velocity oscillation present but also a small pressure oscillation. Hence, it was necessary to show that the change was not caused by the pressure oscillation. This was done by conducting tests wherein the test sample was displaced toward the burner end thereby increasing the oscillatory pressure seen by the sample. The observed result was that unless the oscillating velocity grew to the usual critical value, dark combustion did not occur regardless of the oscillating pressure amplitude. Much larger pressure oscillations by themselves were inadequate to cause the dark form of combustion.

At 300 psi and 500 cps, the dark form of combustion resulted when the oscillating velocity was greater than about 70 ft/sec. At higher frequencies or higher pressures, the critical velocity became slightly larger in general. At lower pressures or frequencies, interpretation of the data was difficult and no quantitative evaluation could be made. However, it appears that the phenomena is produced in much the same way as at the baseline condition. It was clear that the dark form of combustion was less dark at higher pressures so not only was the phenomena harder to cause but it was also less apparent when it did occur. Particularly interesting was the fact that dark combustion was fairly easily produced ($\hat{u} \simeq 80$ ft/sec) with ANB 3066 at the RPL T-burner workshop condition[71] of 500 psi and 800 cps.

Several differences were attributed to propellant composition. First of all, somewhat different velocity amplitudes were required to produce the dark combustion. Most of the propellants (CYH, A-87, ANB 3066, No Al, 400μ, and H 5) required a peak oscillating velocity of about 70 ft/sec before dark combustion would occur. The others (1/2 Al, H-15, and 40) required larger acoustic velocities of about 150 ft/sec to produce the dark combustion. The luminosity of the dark combustion differed greatly from propellant to propellant. These results are summarized in Table 5-III where the velocity required to produce the dark combustion and the luminosity of the dark combustion are tabulated. The numbers shown in Table

There were some minor differences that could be attributed to different propellant compositions and these will be discussed later. At this point, those features common to all the compositions will be discussed. First of all, as Figure 5-7 shows, the change in luminosity occurred almost as a step function. The oscillatory level which caused the change varied but when the change occurred it was usually sudden and large. Second, the change was reversible in that bright combustion was suppressed early in the firing as the oscillations grew. This is illustrated in Figure 5-8. Later, as the driver propellant burned out, the amplitude diminished and the bright form of combustion was reestablished. There was some suggestion that a large steady erosive velocity could also induce the dark combustion. However, the acoustic erosive velocity was much more effective in causing the dark combustion.

When the dark combustion occurred, there was not only a velocity oscillation present but also a small pressure oscillation. Hence, it was necessary to show that the change was not caused by the pressure oscillation. This was done by conducting tests wherein the test sample was displaced toward the burner end thereby increasing the oscillatory pressure seen by the sample. The observed result was that unless the oscillating velocity grew to the usual critical value, dark combustion did not occur regardless of the oscillating pressure amplitude. Much larger pressure oscillations by themselves were inadequate to cause the dark form of combustion.

At 300 psi and 500 cps, the dark form of combustion resulted when the oscillating velocity was greater than about 70 ft/sec. At higher frequencies or higher pressures, the critical velocity became slightly larger in general. At lower pressures or frequencies, interpretation of the data was difficult and no quantitative evaluation could be made. However, it appears that the phenomena is produced in much the same way as at the baseline condition. It was clear that the dark form of combustion was less dark at higher pressures so not only was the phenomena harder to cause but it was also less apparent when it did occur. Particularly interesting was the fact that dark combustion was fairly easily produced ($\hat{u} \simeq 80$ ft/sec) with ANB 3066 at the RPL T-burner workshop condition[71] of 500 psi and 800 cps.

Several differences were attributed to propellant composition. First of all, somewhat different velocity amplitudes were required to produce the dark combustion. Most of the propellants (CYH, A-87, ANB 3066, No Al, 400μ, and H 5) required a peak oscillating velocity of about 70 ft/sec before dark combustion would occur. The others (1/2 Al, H-15, and 40) required larger acoustic velocities of about 150 ft/sec to produce the dark combustion. The luminosity of the dark combustion differed greatly from propellant to propellant. These results are summarized in Table 5-III where the velocity required to produce the dark combustion and the luminosity of the dark combustion are tabulated. The numbers shown in Table

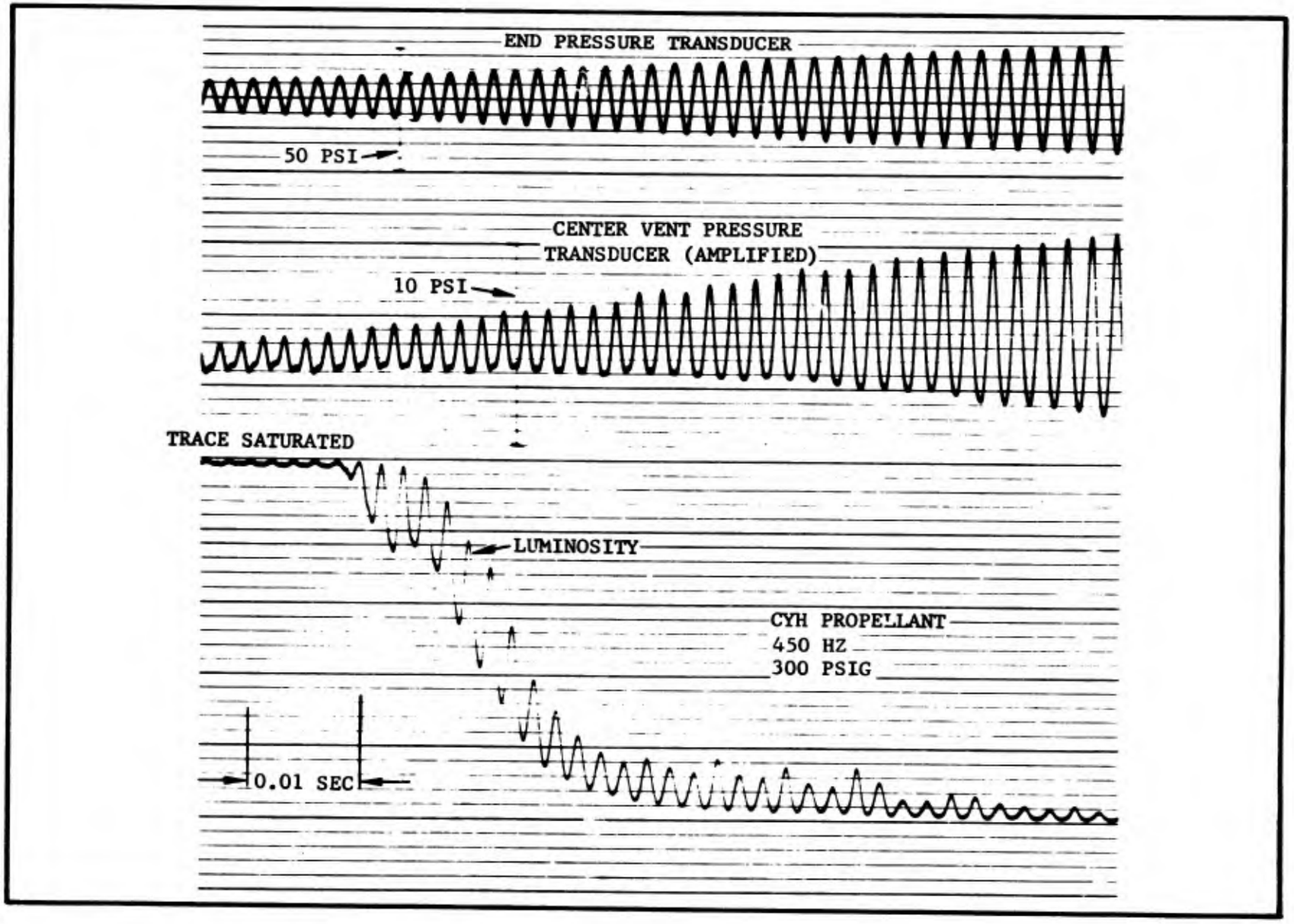

Figure 5-7. Typical Firing with CYH (Firing No. 23) Showing the Onset of Dark Combustion Mode During High Amplitude Oscillations

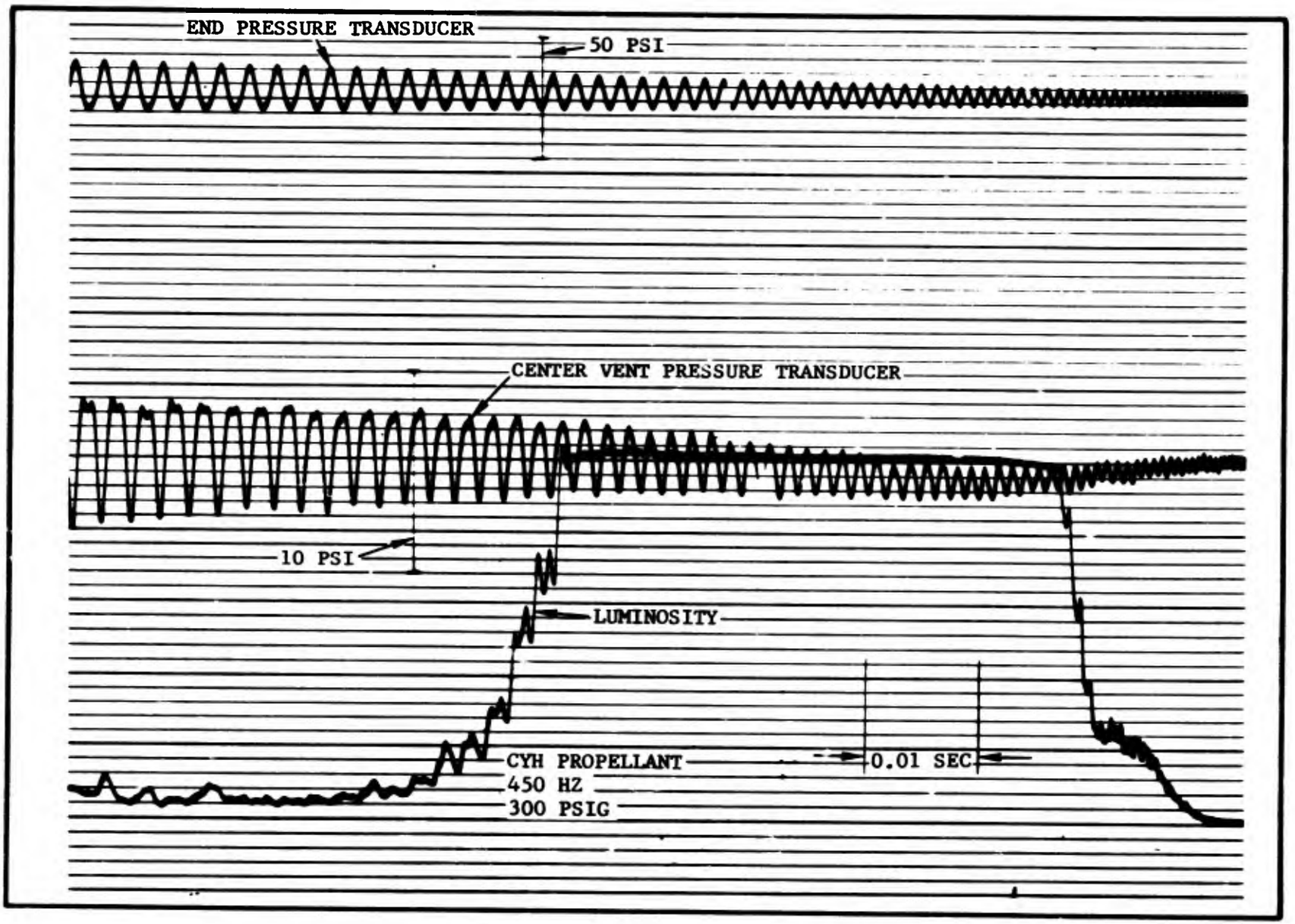

Figure 5-8. CYH Firing No. 23 (See Figure 5-7) Showing the Return of Normal Combustion as the Driver Propellant Burns Out and the Oscillatory Pressure Decays

TABLE 5-III

EFFECT OF PROPELLANT COMPOSITION* ON THE TRANSITION TO THE DARK COMBUSTION MODE

Propellant	u_d (ft/sec)	L_d (foot candles)
CYH	70	200
A-87	70	1000
ANB-3066	60	1200
NO Al	60	1500
1/2 Al	140	2000
H 5	60	600
H-15	170	2000
40μ	100	2000
400μ	80	1200

*The data are for 300 psi and less than 600 cps when dark combustion was clearly established

5-III are only qualitative but do show that the harder it was to produce the dark combustion, the brighter the resultant dark combustion. It is noteworthy that at the baseline conditions, the CYH flame became almost invisible during the dark form of combustion.

Another phenomena that was frequently observed was an interrelated change in mean luminosity and oscillatory amplitude. As the slowly growing oscillations caused the luminosity to decrease abruptly, there was often a simultaneous rapid increase in the oscillatory amplitude. An example of this phenomenon is shown in Figure 5-9. In some cases the amplitude doubled. This phenomena was especially prevalent with ANB 3066. A reasonable explanation for this is that as the aluminum ceases to burn efficiently, the Al_2O_3 particles ordinarily formed are no longer present or are present in a different configuration and concentration. With this source of acoustic damping now absent or modified, the oscillations suddenly grow to a larger amplitude.

It also seemed possible that the JPN driver propellant might be responsible for causing dark combustion. This possibility was eliminated by utilizing the same driver propellant in the ends of the burner as was tested at the center of the burner. The movies also clearly showed that the dark form of combustion resulted from a given amplitude of oscillations regardless of the propellant used to drive the oscillations. In one test a T-burner with a transparent wall was used to study this phenomenon. CYH propellant was used in the ends and at the center. The test sample was seen to burn with a very luminous flame until the velocity oscillations became large, at which time the flame became too dark to see. The CYH propellant in the ends of the burner continued to burn brightly throughout the test.

In a second test in the transparent T-burner, several CYH propellant samples were spaced down the wall of the T-burner as is shown in Figure 5-10. This was done to more closely approximate the combustion field present in a motor. The results showed that the 1/2 in. wide test sample located at the burner center transisted from the light to dark form of combustion in the characteristic way and at the usual amplitude. However, the 1 in. wide samples located next to the center did not transist even though the velocity amplitude became well larger than the critical value for that location. The apparent conclusion is that the dark combustion is produced only with small propellant samples and is not relevant to situations such as are encountered in a motor. Nevertheless, when dark combustion is encountered, it is apparent that the velocity fluctuations are strongly interacting with the combustion. Larger propellant samples should also interact strongly under the same test conditions although the interaction would show in different ways.

c. Burning Rates

An attempt was also made to observe the effect of the acoustic velocity on the burning rates of the test samples. However, in general, the test samples were so thin (1/8 in.) that the measured burning

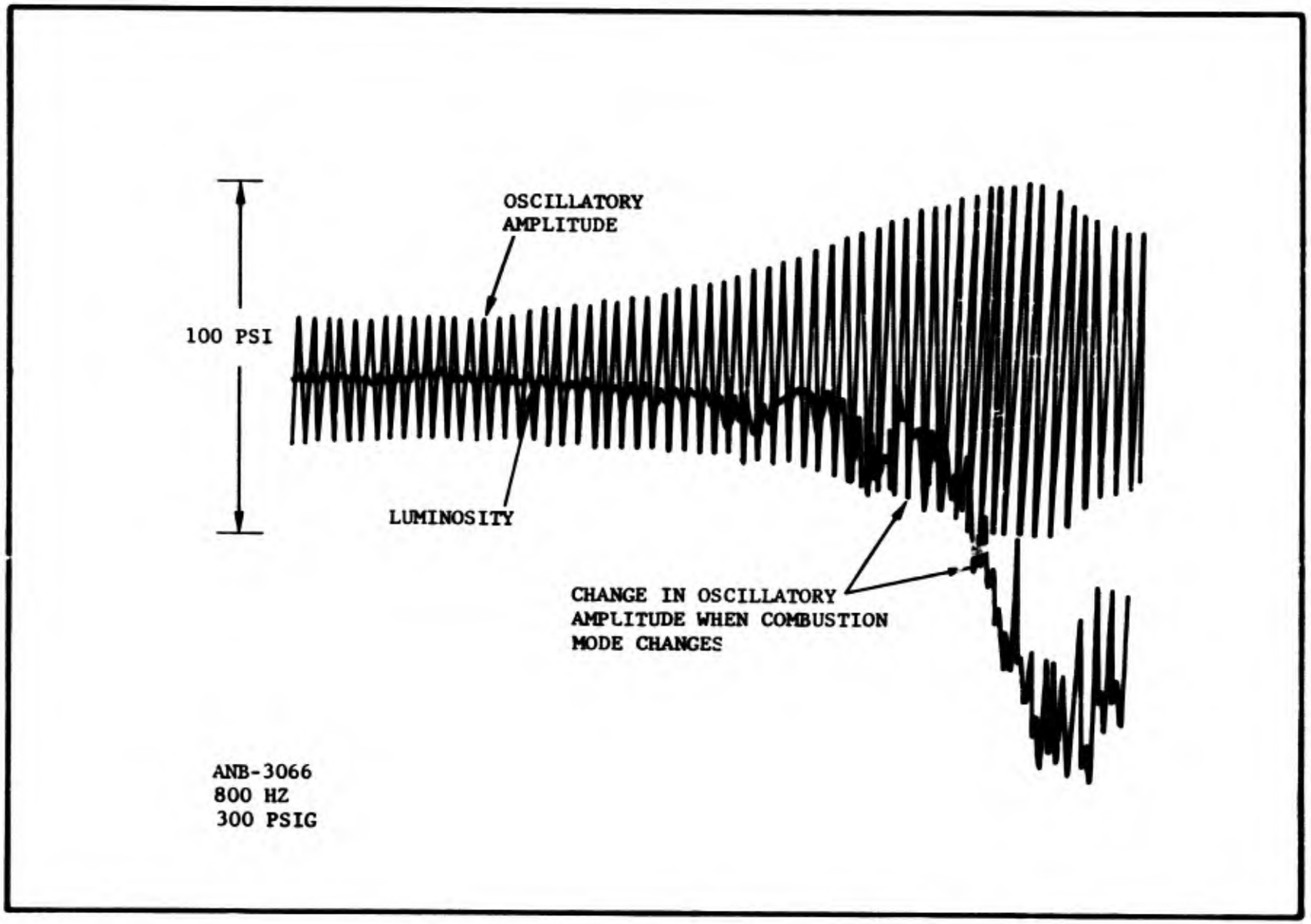

Figure 5-9. ANB-3066 Firing No. 57 Showing the Change in Oscillatory Pressure Amplitude at the Time When the Combustion Mode Changes as Indicated by the Decrease in Luminosity

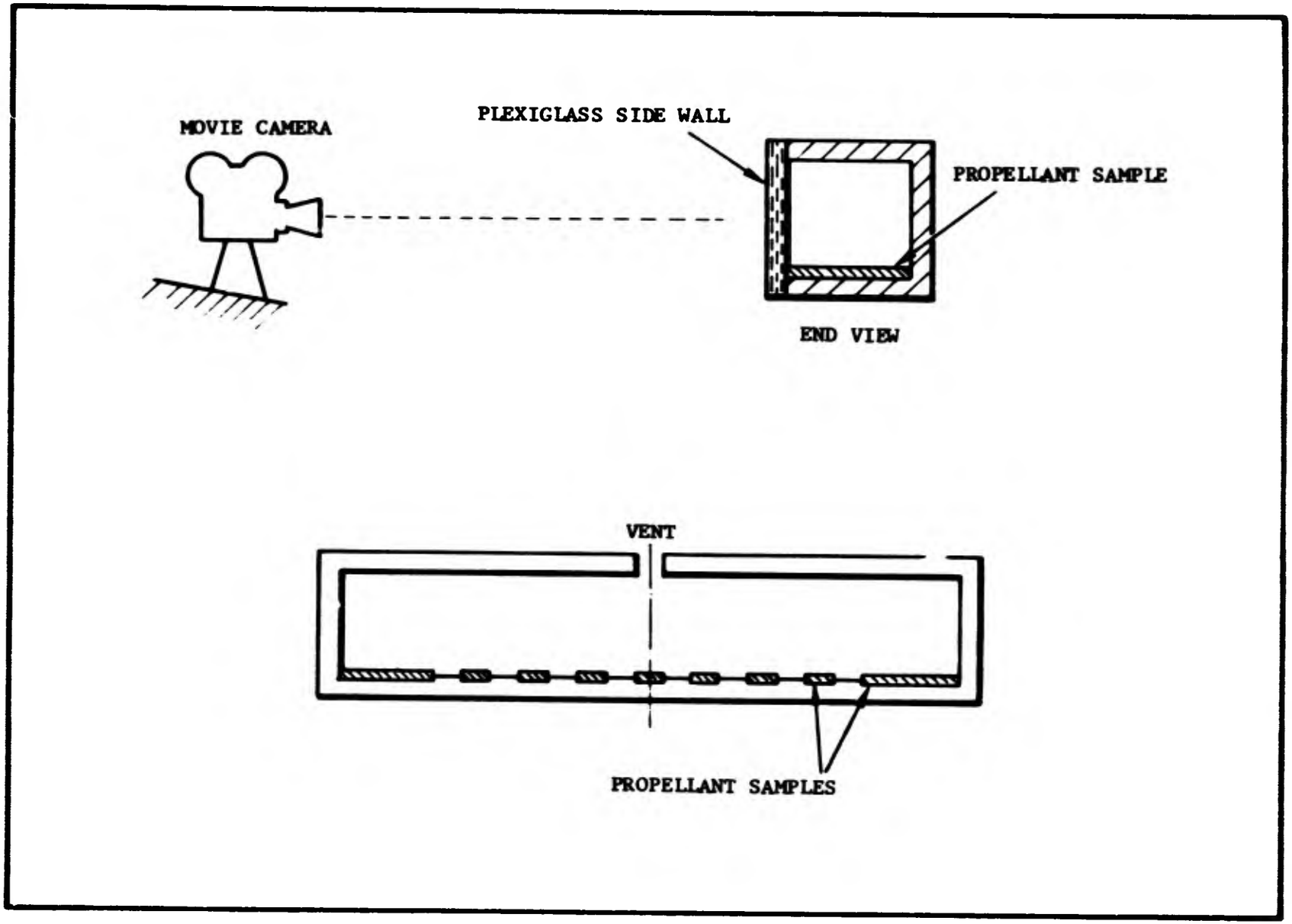

Figure 5-10. T-Burner Modified with Transparent Side Wall

rates were very imprecise. No conclusions could be drawn from the scattered data. In a few cases, however, the driver propellant and test sample were of the same composition. In these tests, the burning rates at the end and center of the burner were essentially identical (within 5 percent, the maximum resolution possible). The conclusion is, at least in these cases, that the acoustic velocity did not alter the burning rate. This is in agreement with other work [72] which suggests that such small amplitudes should not influence the burning rates significantly.

E. SUMMARY

The results of the program are summarized as follows:

(1) A nonsymmetrical T-burner produces unusual oscillations that differ from the usual sinusoidal form.

(2) A peculiar, nonluminous form of combustion is caused by velocity oscillations when small propellant samples are used.

(3) Propellants interact most strongly with velocity oscillations in the neighborhood of 500 cps and 300 psi.

(4) The propellants tested all responded in a similar manner and propellant composition was a surprisingly weak variable.

SECTION VI

EXPERIMENTAL TECHNIQUE

A. INTRODUCTION

A fundamental objective of the program was to evaluate methods for measuring velocity coupling. Several techniques were considered for possible application based on the results of Phases I and II as discussed in Sections III, IV, and V. Those appearing to be most practical were the modified T-burner, the velocity-coupled T-burner, the 1/2 T-burner, and an end-vented device (utilizing T-burner hardware) adapted for measuring velocity coupling (See Figure 6-1 and Table 6-I.) Calculations discussed in Section III.C.2 have shown that the modified T-burner (Figure 6-1a) will not provide the desired resolution unless large, impractical test samples are used. It also has the disadvantage of being somewhat large and cumbersome. The Phase II results indicated that in the 1/2 T-burner (Figure 6-1c), the disadvantages outweigh the advantages for quantitative testing over a range of test conditions due to coupling with the surge system. The calculations performed during Phase I (Section III) indicated that the velocity-coupled T-burner showed promise as a quantitative device. Therefore, it was selected as a technique for experimental evaluation. The end-vented configuration (Figure 6-1d), was proposed as a second technique for evaluation. The principal disadvantages of the end-vented burner are that the nozzle damping must be determined accurately if quantitative velocity coupled measurements are to be made. It has the advantage of eliminating the "vent term" from the necessary analysis and the velocity coupling is determined in a slightly different way. Thus, based on this line of logic, the velocity-coupled T-burner and the end-vented burner were selected as the most promising devices to be tested in the screening tests.

Approximately 30 screening tests were performed, analyzed, and evaluated to determine which of these two devices appeared to be most sensitive to velocity coupling, and which was the most practical to operate in a laboratory environment. Based on an evaluation of the screening test results, the velocity-coupled T-burner was chosen for further evaluation. As the final phase of the program, approximately 60 characterization tests were performed varying frequency, oscillation amplitude, and propellant formulation. The purpose of these final tests was to determine the sensitivity of the velocity-coupled T-burner to typical variations in test conditions, and particularly to determine if the velocity-coupled T-burner could differentiate between propellant formulations.

This section discusses the experimental hardware/system used for the velocity-coupled T-burner and the end-vented burner, and a summary of the test matrix that was pursued.

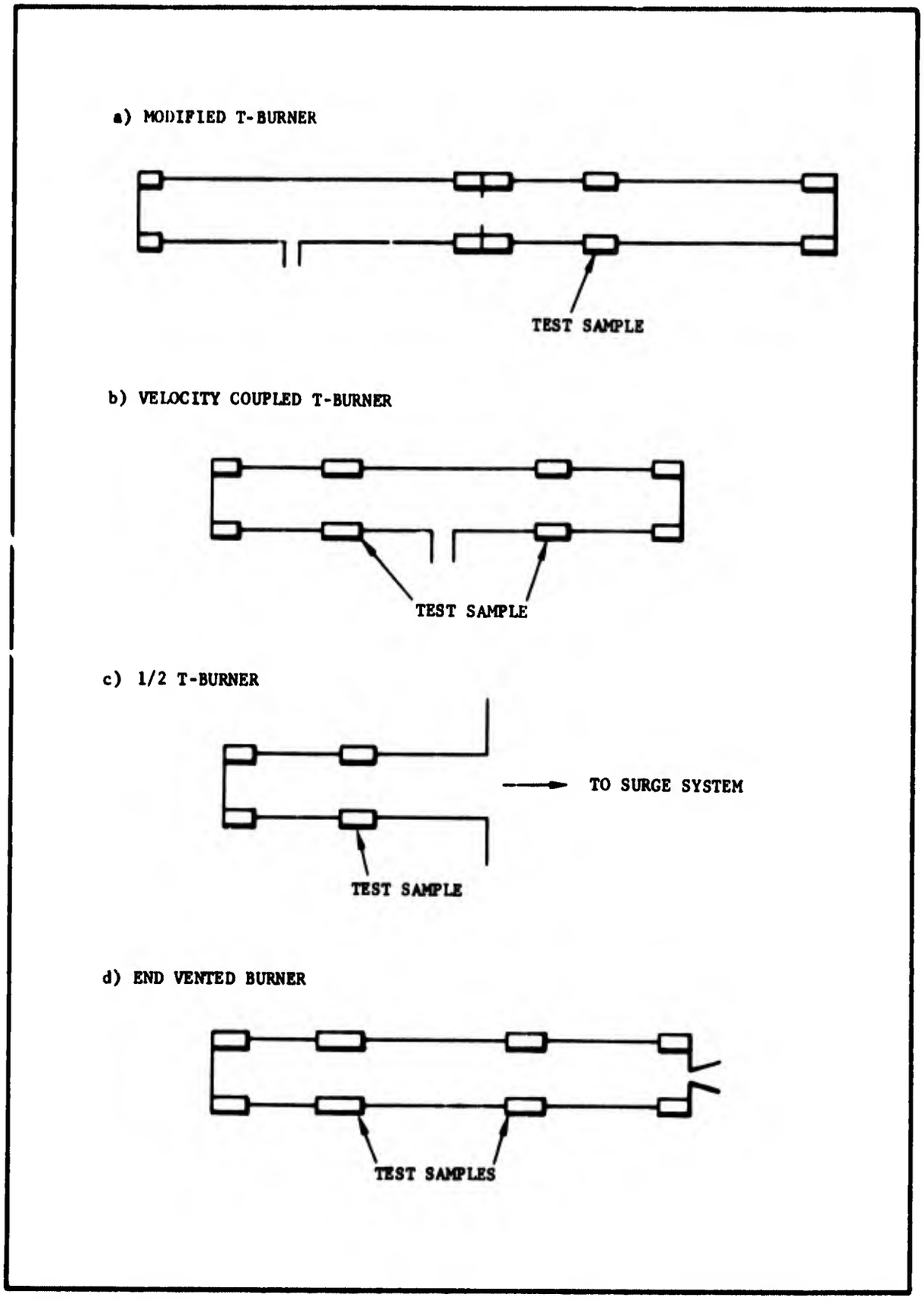

Figure 6-1. Configurations Considered for Velocity Coupling Testing

TABLE 6-I

INITIAL EVALUATION OF LABORATORY DEVICES

Device	Oscillatory Nature	Data Obtained	Practicality
Modified T-burner	Usually spontaneous	α, ΔP, $\bar{T}$	Large propellant samples required to overcome large volume Several propellant samples used
Velocity-Coupled T-burner	Usually spontaneous	α, ΔP, $\bar{r}$	Four propellant samples used
1/2 T-burner	Usually Spontaneous	α, ΔP, $\bar{r}$	Coupling between burner and surge tank is excessive
End-Vented Burner	Requires pulsing due to nozzle damping	α	Nozzle damping must be determined accurately Controversial "vent term" is eliminated

B. GENERAL T-BURNER DESCRIPTION

The basic hardware used in support of the present contract was the 1.5 in. hardware used for the variable area T-burner with the appropriate modifications. The test procedures, support hardware, and instrumentation for the variable area T-burner have recently been reported in detail.[71,73] Therefore, in the following paragraphs the techniques, procedures, and hardware common to the velocity-coupled T-burner and the variable area T-burner are only described in brief.

1. T-Burner Hardware

The 1.5 in. variable area T-burner is basically a length of 1.5 in. inside diameter steel tubing with provisions for bolting end plates to a center section. Propellant grains are located at the ends of the burner and grain lengths can be varied to achieve different area ratios. Standard sized spacers are available for conducting tests at area ratios of 1.5 to 7.5.

The pressure transducer, a Kistler model 701A, is located in the end plate and is exposed directly to the gas cavity. The pressure is measured from this location for both spontaneous growth and pulse tests. The squib used for pulsing is brought into the burner through the end plate opposite the transducer.

T-burner extension tubes were available for testing at two frequencies, 450 Hz which corresponded to a length of 40-1/2 in., and 800 Hz requiring a length of 24-1/2 in.

2. Surge Tank and Heat Exchanger

A 35 cubic foot surge tank was used for all testing to hold a nearly constant pressure during the tests.[73] A heat exchanger filled with chain was used to cool the exhaust gas before it passed into the surge tank. Typically, less than 10 psi static pressure rise was observed in the burner with the use of the heat exchanger and surge tank even for large area ratio firings.

3. Grain Configuration

The basic test configuration was a cylindrical grain tapered on the downstream end. The standard grain had a 1.25 in. ID and a 2.0 in. OD. This resulted in a positive lip initially, a flush condition at 1/3 of the burn distance, and finally a negative lip, as shown in Figure 6-2. This means that it is possible to analyze the effects of propellant lips, both positive and negative, along with the effect of increased volume in the burner as a result of burning.

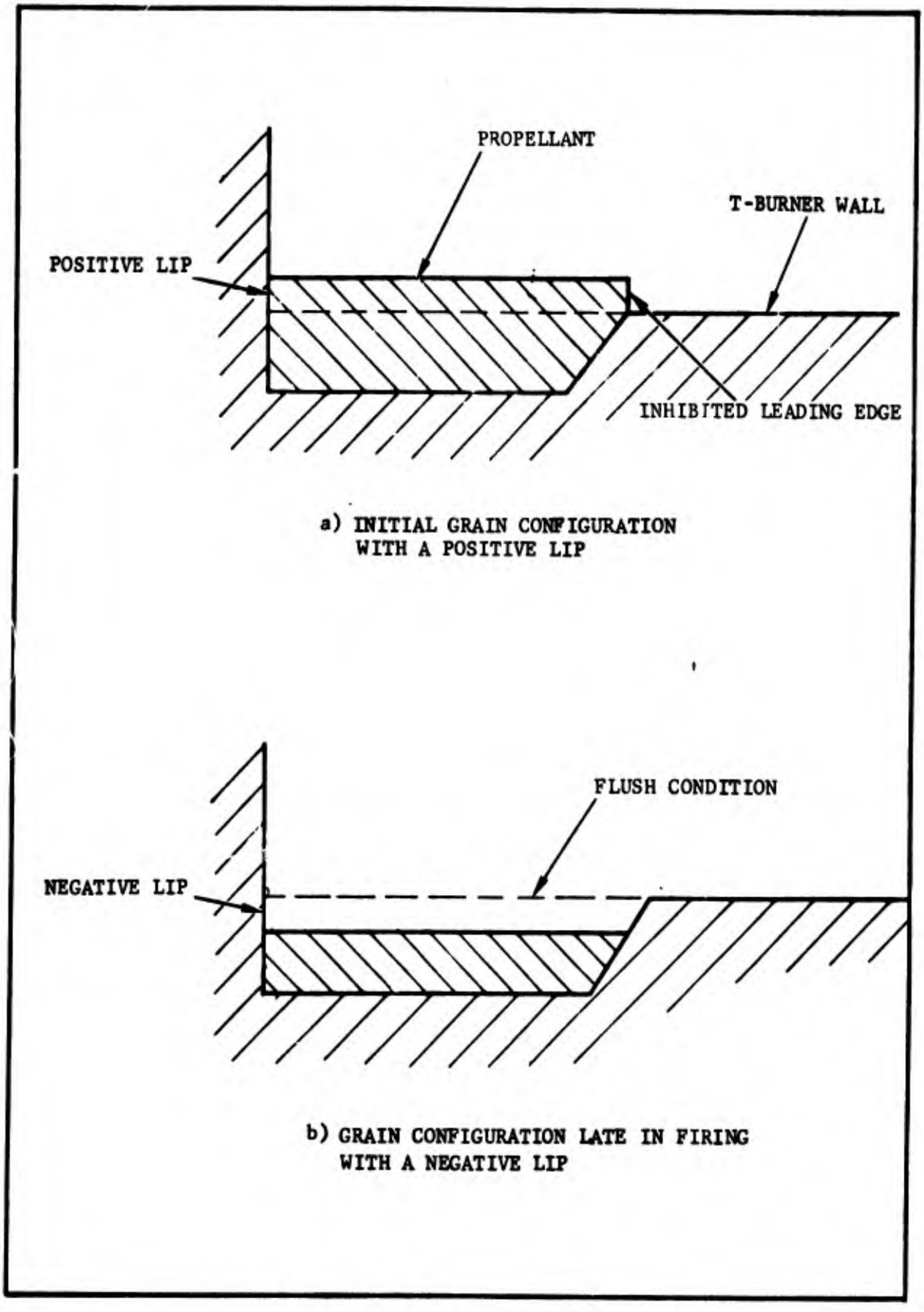

Figure 6-2. Grain Configuration During Burning with Definition of Propellant Lip as Related to the T-Burner Wall

The grains were tapered to provide a near-constant area ratio during the burn time and to reduce possible flow effects due to an abrupt step. This minimizes variations in S_b/S_{co} during the measurements of the growth α, thus improving accuracy and eliminating the need to calculate a variable area ratio during the time the growth α is measured. This simplifies data reduction and reduces both data scatter and uncertainty.[71]

The outside diameter of each grain was covered with a thin coating of silicon grease and the grains were press-fit into the sample holder. The positive lip of the propellant grain is inhibited with grease to restrict irregular burning of the leading edge. The effectiveness of the grease as an inhibitor in this situation has been verified through the use of high-speed movies.[71]

4. Air Driven Paddle

An air cylinder operated paddle was used as a suppression device to prevent pulsing the burner into oscillation during ignition and to allow multiple growth rates to be obtained during a single firing. Sequencing of the paddle into the burner was timed to give a growth rate measurement when the propellant was just flush with the T-burner wall and usually two additional growth rate measurements. An indication of the paddle position during the firing is provided through the use of a linear potentiometer which is attached to one end of the double acting piston rod. Through this measurement, it is possible to assure that the paddle is completely out of the burner at the time oscillations begin to grow and before measurement is made. The advantages of this system are given in more detail in Reference 74.

5. Ignition Technique

Standard bag igniters (as described in Reference 73) were used throughout the program. The bag igniter consists of an Atlas match, $BKNO_3$ powder, and Mg-Teflon pellets. Two bags were used, one in each end of the T-burner.

6. Pulsing Technique

For conditions where the T-burner is anticipated to be stable, a pressure pulse is imposed on the burner. Normally, three pulses are fired during a single test. The pulses are produced by igniting MKII Mod 0 squibs located in a special adapter in one end plate and protected from the combustion gases by a 0.200-in. thick layer of RTV rubber. The pressure transducer is located in the opposite end plate of the burner.

The pressure oscillations (with an initial amplitude of approximately 10 psi) can be introduced at any time sequence during the firing. The standard procedure is to pulse once at flush conditions and twice with small negative lips.

7. Standard Instrumentation

The standard instrumentation is shown in Figure 6-3 and consists of:

Kistler 701A Piezoelectric Pressure Transducer

Kistler Model 568 Charge Amplifiers

Krohn-Hite Model 310-AB Band-pass Filter

Ampex Model AR-200 FM Tape Recorder

Honeywell Model 1508 Visicorder

Tektronix Model 555 Oscilloscope (quick look record)

A complete description of the operational capabilities and limitations of the system can be found in References 71 and 73 and will not be repeated here.

To observe DC pressure rise during the firing and to permit measurement of harmonics, one channel of the FM and oscillograph is recorded with no filtering and with low amplification. Low signal to noise ratios and poor resolution, however, leave much to be desired as one attempts to obtain growth constants from data of this nature. By filtering the data with a band pass filter, both DC shifts and low and high frequency noise can be eliminated. Once the signal is properly filtered to pass the fundamental it is greatly amplified to improve resolution and accuracy of the exponential growth constant measurements.

The unfiltered trace is normally set for a maximum peak-to-peak deflection of approximately 1 in. while the filtered trace is set for 2 to 4 in. for deflection. Through this method, peak-to-peak amplitudes of less than 1 psi can be measured in determining the portion of the data over which the growth is linear.

When conducting tests in which oscillations do not grow spontaneously, it becomes difficult to determine total burn time for burning rate data. This problem is eliminated by placing a small orifice in the exhaust tube. A 0.25 in. diameter orifice was used and a mean pressure rise of 10 to 15 psi was typically observed. A side benefit to using the orifice is that it helps to damp out low frequency pressure surges which are stimulated by the pulses.

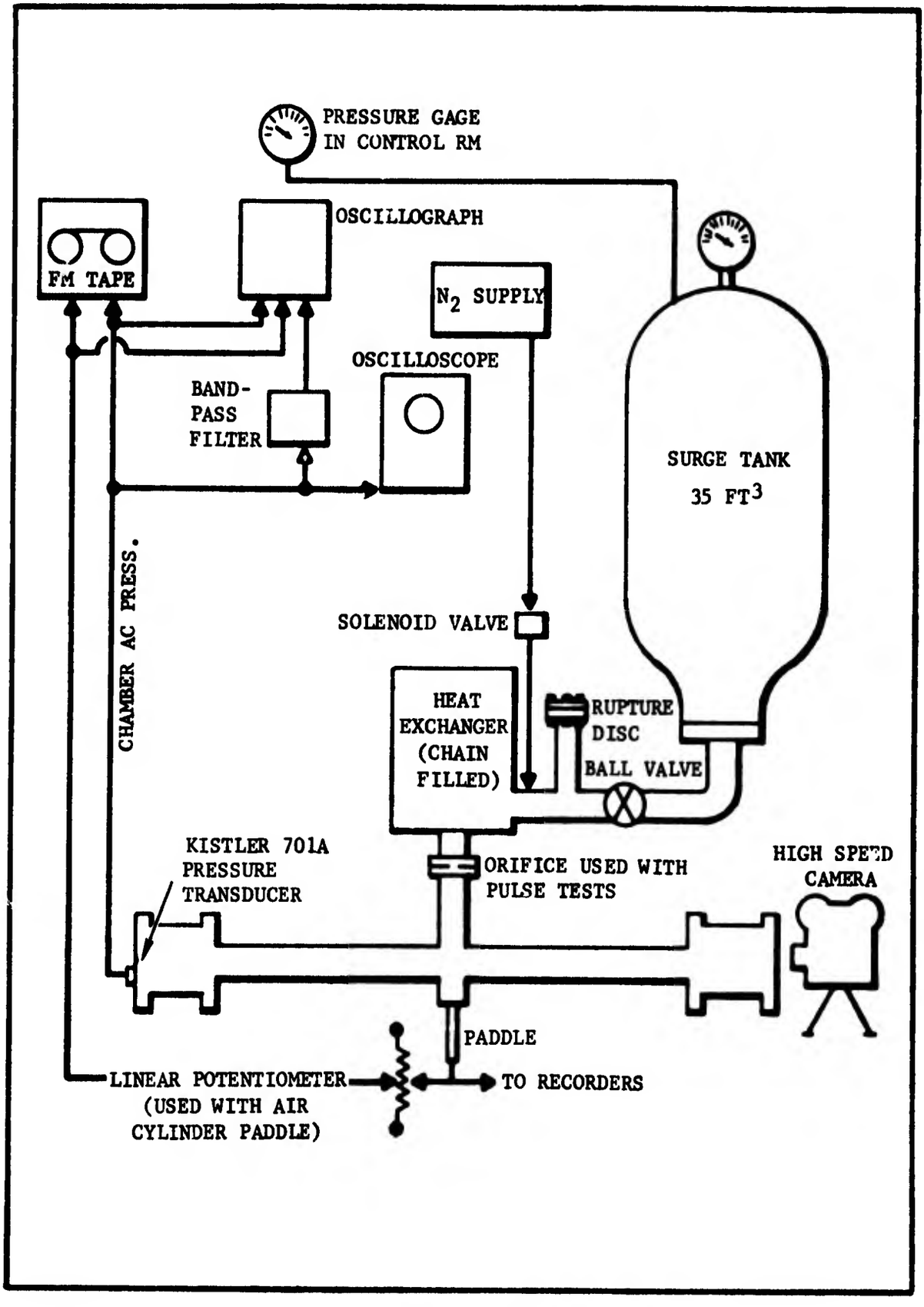

Figure 6-3. T-Burner Instrumentation

8. Preliminary Data Reduction/Reject Criteria

A preliminary check of the test results was performed with the purpose of identifying unacceptable tests, and to provide a quick-look α measurement to aid in determining the day-to-day direction of the program.

The oscillograph record of a test firing was examined for any indications which would render the test data invalid or unreducible. Criteria which were used to determine if the data were invalid included:

(a) Suppressor malfunction

(b) Pulse unit malfunction

(c) Growth starting before the suppressor paddle was fully withdrawn

(d) Burning behind the grains as indicated by an unusually rapid burnout

(e) Growths starting too close to burnout to allow for a full growth

(f) Growths starting from a finite amplitude (due to failure of the paddle to fully suppress oscillations)

The occurrence of any of these was considered sufficient justification for rejection of the data from that particular test. In pressure-coupled T-burner tests, paddle or pulse malfunction are the most frequent reasons for loss of data. However, in the velocity-coupled T-burner, the driving was sufficiently strong that occasionally the growth of oscillations began before the paddle was withdarwn, or the paddle did not fully suppress oscillations when activated. This resulted in the loss of several tests, particularly during the screening phase of the program where the test results were not fully anticipated. As experience was gained with velocity coupling, tests were planned so that lower growth rates occurred, and as a result, fewer tests were lost.

The second aspect of the quick-look data analysis was the measurement of the growth rate, α. Two pressures were measured between a low pressure and a higher pressure less than 50 percent of the limiting amplitude. The growth α was then calculated based on this rough measurement. As the different test series were fired, plots of this preliminary growth α versus area ratio were kept current to monitor and aid in directing the program. Later, these preliminary data were compared to the results of the final data analysis; gross differences between the two were investigated for possible errors.

9. Data Reduction Procedure

The methods used in the reduction of the velocity-coupled T-burner records obtained during this program were standard hand reduction techniques which have previously been used in the variable area T-burner and are reported in detail in References 71 and 73. These techniques are outlined briefly in the following paragraphs.

For a spontaneous growth measurement the peak-to-peak amplitude of a number of cycles was taken starting from the first cycle having an amplitude of 0.1 in. This starting amplitude was chosen to reduce the uncertainties of measurement errors. Measurements of the peak-to-peak amplitude were continued from the 0.1 in. displacement to the point where the limiting amplitude was reached as indicated in Figure 6-4. For a pulsed decay α the amplitude was measured from about the fifth cycle after pulsing to the point where the amplitude dropped below 0.1 in. The delay in starting the measurements was to allow the transient shocks and harmonics to die out leaving the undisturbed fundamental mode oscillation. The measured growth and decay alphas were taken from the linear portion of a semilog plot of the amplitude displacement as a function of the cycle number. The measurements and calculations were made according to those described in Reference 71.

The frequency was determined by dividing a given number of cycles by the time over which they occurred. Ten to thirty cycles, centered about the linear growth region, were used.

The burn rate was calculated by dividing the average web thickness of the propellant grain by the total burning time. The burning time was measured from the maximum pressure peak at ignition to the point where the oscillations began to drop from limiting amplitude on the last growth. (See Figure 6-4.) The burnout point was determined by drawing a line tangent to the peaks of the decay portion. The intersection of the two lines was taken as the burnout point. The drop in mean pressure as recorded on the unfiltered pressure transducer trace was used to determine burnout for cases where no oscillations were present at burnout (i.e., the pulse-decay tests). The intersection of two lines drawn in a manner similar to the oscillating case was taken as burnout. Comparisons of the oscillation decay and mean pressure drop methods were made on several firings and the results were identical for burnout calculations.

C. VELOCITY COUPLED T-BURNER

Based on the T-burner analyses described in Section IV, it was apparent that for a small discrete sample of propellant, the maximum velocity coupling occurs when the sample is placed half way between the vent and the end of the T-burner (i.e., the L/4 location). Because of the objective of developing a laboratory measuring device, using small propellant samples, it was decided to adapt the T-burner, placing a small test sample at the L/4 location. It was also recognized that propellant was needed in the end of

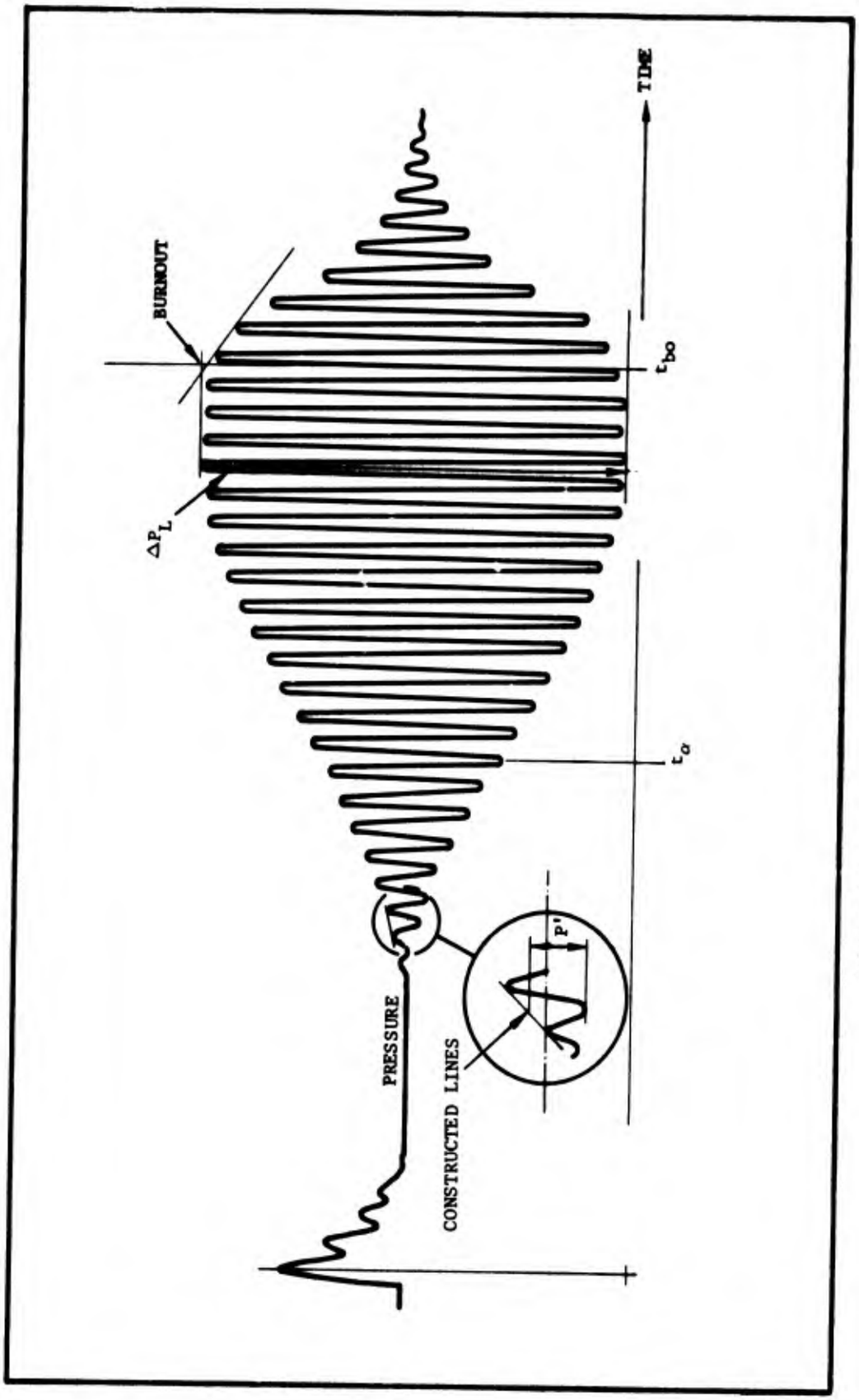

Figure 6-4. Data Reduction Examples

the T-burner to provide a continuous flow of hot gases throughout the T-burner and to provide some pressure-coupled driving. With the availability of the variable area T-burner described in Paragraph B, it has been possible to use the same propellant as both the driver and the test sample rather than use an unmetallized driver propellant as Stepp did.[12] Therefore, the standard configuration that has been adopted in this program is a T-burner with four propellant samples, two driver samples at the end of the burner, and two samples at the L/4 location. This configuration is referred to as the velocity-coupled T-burner.

Figure 6-5 is a schematic drawing of the velocity-coupled T-burner as has been used throughout the program. Hardware extensions were constructed to give frequencies of 450 and 800 Hz. Both the driver and test sample are tapered to give constant area ratios, and the test sample is tapered on both ends to minimize flow disturbances both upstream and downstream of the sample.

For a test series the size of the driver propellant was held constant and the area ratio of the test sample was varied. Calculations performed early in this phase of the work showed that a driver propellant area ratio between 1 and 2 would provide sufficient flow to maintain relatively uniform temperature throughout the burner and yet would not result in an excessive amount of pressure-coupled driving relative to the velocity-coupled test sample. Therefore, a driver area ratio size of 1-1/2 was established as standard. Test sample area ratios of 1-1/2, 3, 4-1/2, 6, and 7-1/2 have been used depending on the propellant and test conditions.

Other test procedures and hardware are essentially the same as used for the variable area T-burner as described in Paragraph B. The velocity-coupled T-burner is fired into the heat exchanger/surge tank system to control the mean pressure. The same propellant sample holders are used to hold the propellant grains in place as shown in Figure 6-2. The instrumentation is the same and the paddle suppression device is used to permit multiple growth constants to be obtained. Two standard bag igniters are used in each end of the T-burner. Separate igniters were not used in conjunction with the test samples, due to complications in the instrumentation and hardware. This resulted in an ignition delay time associated with the test sample, as it did not ignite until the hot gases from the driver sample reached it. This normally required 40 to 50 ms. In calculating propellant area ratios and diameter ratios, this ignition delay time had to be accounted for. Other than this slight difference in determining the ignition time, the data reduction techniques were the same as described for the variable area T-burner.

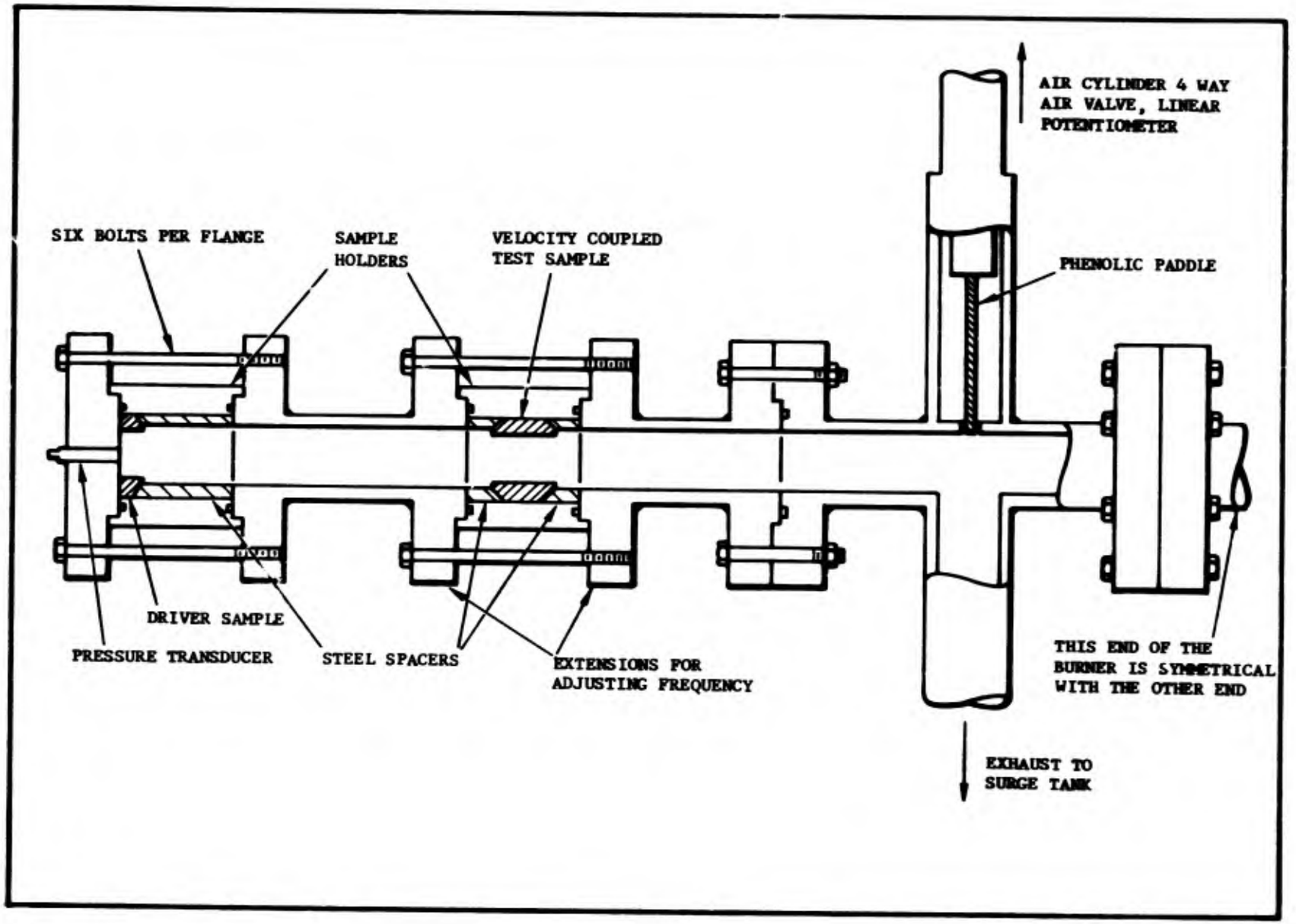

Figure 6-5. The Velocity Coupled T-Burner

D. END VENTED BURNER

The end vented burner utilized the same basic hardware as the VCTB. The difference being that the vent of the T-burner was blocked and an orifice was located in one end of the burner. During some of the screening tests the burner exhausted to a sufficiently low pressure to obtain sonic conditions at the orifice. However, problems were encountered in igniting the propellant samples at atmospheric pressures due to small propellant samples relative to large areas of metal walls. Apparently, the walls absorbed so much of the heat from the igniters that the propellant samples did not reach sustained combustion. Additional pyrotechnic material was used in the bag igniters for several tests but this did not solve the problem. The problem was finally resolved by pressurizing the burner with the T-burner surge tank and venting through a subsonic nozzle. The principle disadvantage of using the subsonic nozzle is that any shift in mean burning rate during oscillations is not as readily observed from a subsonic test as for a sonic test. However, the principle objectives of evaluating acoustics could still be determined from the subsonic test.

The tests that were fired used propellant located in the ends of the burner and at the L/4 position as in the VCTB. The test sample size was varied as in the VCTB technique. The size of the orifice was also varied dependent on the amount of propellant used.

E. TEST SUMMARY

As has been discussed, the final phase of the program was separated into two tasks. The first was a series of screening tests to determine whether the VCTB or the end vented burner was more practical as a laboratory device. The final task of the program was to evaluate the device selected from the screening tests (the VCTB) for a variety of typical test conditions.

Twenty-two screening tests were originally scheduled and 29 were actually fired. All tests were performed at 300 psi and 450 Hz with CYH oscillatory propellant based on the results of Phase II of the program (Section V) and to allow comparison with previously obtained T-burner data. Of the tests, six pressure coupled T-burner tests were planned at three area ratios* to establish the characteristics of CYH Lot 1-14 propellant. Six VCTB tests and 10 end vented tests were planned for evaluating the two techniques. Both symmetric and nonsymmetric tests were planned for the end vented tests.

Table 6-II summarizes the tests that were actually performed. Additional tests were performed in the VCTB because the initial tests at large area ratio oscillated so hard that the paddle did not suppress oscillations, and thus, a valid measurement of α was not obtained. The raw data from

*Two duplicate tests were planned at each test condition.

TABLE 6-II

COMPLETED SCREENING TESTS

Number of Tests	Test Configuration	Propellant Area Ratio									Test Purpose
		At Burner End				Test Sample					
		1.5	4.5	6.0	7.6	1.5	3	4.5	6.0	7.6	
8	Conventional Variable Area T-Burner	2	2	2	2	--	--	--	--	--	Verify Propellant Characteristics
8	Velocity Coupled T-Burner	*	--	--	--	1	2	2	2	1	Evaluate Test Technique
2	Symmetric End Burner	*	--	--	--	2	--	--	--	--	Check Nozzle Damping Calculations
11	Unsymmetric End Burner	*	--	--	--	--	--	4	6	1	Evaluate Test Technique
29	Total Number of Tests										

*Area ratio of driver propellant for test series.

all of the tests are tabulated in Appendix A. More end vented tests were performed than had been planned, because of a problem in getting all the propellant grains to ignite properly.

Because of the problems in obtaining data, the end-vented burner was not selected as the final technique for evaluation. However, the technique showed sufficient promise that a test series was included in the final test matrix to study the technique further and to provide an independent method for determining the velocity-coupled response.

The final test matrix consisted of seven test series with the overall objectives to determine the sensitivity of the velocity-coupled T-burner to typical variations in test conditions, and particularly to determine if the VCTB could differentiate between propellant formulations. These tests are summarized in Table 6-III. Several tests were fired at the standard baseline conditions at area ratios optimized to fill in data where the screening tests were lacking. A series of tests were fired with the objective of determining the magnitude of the vent term. Test series were fired with ANB-3066 and CYH SR-28 propellants to determine if the VCTB could differentiate between different classes of propellant (CMDB versus composite) and different lots of a given propellant. The tests with the CYH SR-28 propellant have particular significance because the SR-28 lot of propellant exhibits much lower amplitude oscillation in the Minuteman II, Stage III than does lot 1-14. The ANB-3066 was tested at 500 psi and 800 Hz to facilitate comparison with the data available from the RPL sponsored T-burner workshop contracts.[65,71,75-77] A test series was performed with CYH-1-14 at 800 Hz to determine if the test technique is sensitive to frequency variations. A test series was performed with a driver sample area ratio of 3 instead of 1-1/2 to determine an effect of acoustic pressure amplitude, driver sample size, or mean flow velocity. Varying the driver sample size results in a change in both the mean flow velocity and the pressure amplitude; tests were not performed to separate the effect of these variables. The final test series performed was with the end-vented configuration to evaluate that independent test technique.

TABLE 6-III

COMPLETED TEST MATRIX

Test Series	Propellant	Pressure	Frequency	No. of Tests	Driver Area Ratio				Test Area Ratio					Objective
					1-1/2	3	6	7-1/2	1-1/2	3	4-1/2	6	7-1/2	
Optimized Tests	CYH 1-14	300	450	5/6+	*	--	--	--	2/2+	1/1	2/3	--	--	Establish Baseline Condition
Vent Term Tests	CYH 1-14	300	450	6/9	--	--	*	--	2/2	--	2/2	0/2	2/3	Determine Vent Term Magnitude
ANB-3066	ANB-3066	500	800	4/4	2/2	--	2/2	--	--	--	--	--	--	Compare a Well Characterized
				6/13	*				2/2	2/5	2/5	--	--	Composite Propellant to CYH
Non-Oscillatory CYH	CYH SR-28	300	450	6/8	*	--	--	--	2/2	2/2	2/3	--	0/1	Determine if Technique can Differentiate Between Oscillatory and Non-oscillatory Lots of CYH
Frequency Variation	CYH 1-14	300	800	6/7	2/2	2/3(1)	2/1	0/1	--	--	--	--	--	Determine if Technique is
				6/9	*	--	--	--	2/2	2/2	2/1	0/2	0/2	Sensitive to Frequency
Driver Variation	CYH 1-14	300	450	4/5	--	*	--	--	2/3	2/2	--	--	--	Determine Effect of Amplitude and Driver Sample Size
End Vented Tests														
Symmetric	CYH 1-14	300	450	4/4	*	--	--	--	2/2	--	2/2	--	--	Evaluate Velocity Coupling by
Non-symmetric				4/6	*	--	--	--	2/2	--	2/4	--	--	Independent Technique

Total Number of Tests Planned - 51
Total Number of Tests Performed - 70

+ Number of tests planned/number of tests performed

(1) One test at an area ratio of 3 and two tests at 4-1/2.

SECTION VII

ANALYSIS OF VELOCITY COUPLED T-BURNER DATA

A. APPROACH

The data analysis is based on the equations developed and described in Section IV.C, using the same basic format and computer input as for the variable area T-burner. (See Reference 71.) The basic test conditions for each datum point, such as grain lengths and diameter, pressure, burner length and diameter, burn rate, measured frequency and α, etc., are input to the computer for a test series. The area ratios and required geometric factors are calculated internally. The computer uses the analysis of Section IV.C to calculate the theoretical value of α corresponding to the given test conditions. A nonlinear regression analysis is then used to compare the actual datum points to the calculated theoretical points. The difference between calculated and actual is minimized by varying floating variables. The variables that are allowed to float (or be fixed in varying combinations) are B_g, R_{vi}, VF, VFG, and τ (i.e., particle damping relaxation time). By optimizing on τ instead of α_d the variations in frequency due to volume change and propellant area ratio are more accurately accounted for[71]. A pressure and frequency dependent acoustic loss is also input to account for heat transfer. Thus, the value of α_d actually represents the sum of both a heat transfer loss as well as particle damping losses. It should also be noted that the α_d term will vary as the frequency varies from datum point to datum point. The α_d reported in the following paragraphs is an averaged value for the particular data set while the reported frequency is a nominal value.

The computer program also calculates 95 percent confidence limits for all floating parameters, a correlation coefficient and the percent variance explained for the data set. The correlation coefficient is calculated from the equation

$$CC = \left\{ \frac{\sum_{i=1}^{n} \frac{(\alpha_{ipred} - \bar{\alpha})^2}{SY_i}}{\sum_{i=1}^{n} \frac{(\alpha_i - \bar{\alpha})^2}{SY_i}} \right\}^{1/2} \qquad (7\text{-}1)$$

where SY_i is a weighting factor defined below. The percent variance explained is the correlation coefficient squared.

Due to the exploratory nature of the program, several different approaches were tried to determine a consistent method of analyzing the data. For example, an entire data set of both pressure coupled and velocity coupled data was input to the computer and all variables were allowed to float. However, it was felt that this allowed the computer too many degrees of freedom. A more restrictive approach was to fix the values of VF and VFG, floating the remaining three variables. This would be the logical approach if the values of VF and VFG were known accurately.

For reasons discussed in the following paragraphs, VF/VFG combinations of -1/+1, -1/+2 and -2/+1 were used in several instances with the -1/+1 taken as a standard combination. Even with this approach some inconsistencies were noted and it appeared that perhaps the computer still had too much freedom in fitting the data.

An examination of the basic equations led to the next approach. Considering flush conditions (i.e., $S_{co}/S_c = 1.$), the growth constant can be written as

$$\alpha^o = 4f\bar{M}_b^* \left\{ \frac{S_{bl}}{S_{co}} \left[B_s \mathcal{E}_{\ell 1} - \frac{R_{vi}}{2} P_{\ell 1} - \frac{VFG}{2} g_{\ell 1} + VF\, C_{\ell 1}^2 \right] + \frac{S_{bv}}{S_{co}} \left[\frac{R_{vi}}{2} (-P_{\ell v}) + B_s \mathcal{E}_{\ell v} - VFG \frac{g_{\ell v}}{2} + VF\, C_{\ell v}^2 \right] \right\} - \alpha_d \tag{7-2}$$

Consider first the driver sample. For short propellant grains, $\mathcal{E}_\ell \sim 1$, $P_\ell \simeq \frac{\pi}{2}\beta$, $g_{\ell 1} \sim 0$ and $C_{\ell 1}^2 = 1$. For the pressure coupled data

$$\alpha^o \simeq 4f\bar{M}_b \frac{S_{bl}}{S_{co}} \left[B_s + VF + R_{vi} \frac{\pi}{2}\beta \right] - \alpha_d \tag{7-3}$$

Thus, in fitting pressure coupled data (where only samples in the ends are used) the computer will fit to a value of $B_s + VF + R_{vi}$ (small number). The correction due to the velocity coupling is usually $\sim R_{vi}/7$ for $\beta \sim 0.1$ which has a significant value for $R_{vi} \sim 12$ as in the data considered here. However, it was found that the computer was apparently fitting the pressure coupled data to the sum of B_s + VF + constant.

Now consider the growth constant due to the velocity coupled sample. For propellant grains with $\beta_v < 0.2$, $P_{\ell v} \sim -1$, $g_{\ell v} \sim 1$, $C_{\ell v}^2 \sim 1$ and $\mathcal{E}_{\ell v}^2 \sim 1/2$. From equation (7-2) the growth constant can be written

$$\alpha^o = 2f\bar{M}_b (R_{vi} + B_s + 2VF - VFG) \frac{S_{bv}}{S_{co}} - \text{constant} \tag{7-4}$$

where the constant is the sum of the driving from the end samples plus the net damping of the system. From equation (7-3), it was concluded that $B_s + VF \sim$ constant. Therefore, from equation (7-4), it is apparent that $R_{vi} + VF - VFG \sim$ constant. From data varying the end sample area ratio, $B_s + VF$ is determined, while from varying the L/4 sample area ratio, $R_v + VF - VFG$ is determined.

---

* $\bar{M}_b = \frac{\rho_s r a_m}{\gamma \bar{p}}$ where a_m is the gas/particle speed of sound determined from the actual frequency of a firing.

Based on this logic the following approach at data analysis appears to be very consistent. Values of VF and VFG were fixed, and then the pressure coupled data was analyzed with a fixed value of the velocity coupling response, R_{vi}. The value of R_{vi} was estimated from the uncorrected velocity coupling α versus area ratio plots. From the pressure coupled data values for the pressure coupled response, B_s, and particle damping, α_d, terms were determined. The values of B_s and α_d, were then fixed in a run with both pressure coupled and velocity coupled data. In this manner, B_s and α_d were determined from the pressure coupled data with velocity coupling appropriately accounted for, and R_{vi} was determined from velocity coupling data with B_s and α_d properly accounted for.

An extensive study was also undertaken using what is termed the "baseline" set of data which includes the pressure coupled data (PC), the velocity coupled data (VC), the driver variation data (DV), and the vent test data, all at 300 psig and 450 Hz*with CYH 1-14 propellant. A total of 76 datum points comprized the set (35 PC., 7 vent, 15 DV and 19 VC). With the pressure coupled data giving B_s and α_d, the velocity coupled and driver variation data giving R_{vi}, and the vent test data to give VF and VFG, it was felt that much could be learned from such a set of data. Some of the results from analysis of the data set are summarized in Table 7-I. In the first case, all parameters were floating. In the second and third cases VFG was fixed at 0 and +1, respectively. In the next five cases, various values of B_s were fixed with α_d fixed at a predetermined value. In the last three cases, different values of VF/VFG were fixed and run in the computer.

There are several significant observations to be made from these analysis. First, the value of R_{vi} for such a wide variety of assumed and optimized values of B_s, VF and VFG is virtually a constant, 13 ± 0.8 except for Case No. 10. For the VF/VFG case (No. 10) of -1/+1 a low value of α_d resulted, along with low combinations of VF-VFG, B_s + VF and R_{vi} + VF-VFG. Also, that particular case had by far the lowest correlation coefficient, again indicating some inconsistency. With the exception of that one run it is significant that the sum of B_s + VF is a constant ($\sim$1.35), that R_{vi} + VF - VFG is a constant ($\sim$10), and that VF-VFG is a constant ($\sim$-3). Because of the form of the equations and the test setup, a value of R_{vi} of 13 can be determined, exclusive of the uncertainty in VF and VFG. However, the pressure coupled response, B_s, cannot be determined because it appears in the sum with VF.

A result of these tests is also shown in Figure 7-1 where VFG is plotted versus VF, showing the data fall on a line (except the -1/+1 case) which gives VF-VFG $\sim$ -3.

---

*The quoted frequency is a nominal value. The actual frequency corresponding to a given datum point typically varies $\pm$30 Hz of the nominal value. For data reduction purposes, the actual measured frequency is always used.

TABLE 7-I

ANALYSIS RESULTS FOR "BASELINE" SET OF DATA

Case No.	B_s	α_d Avg	R_{vi}	VF	VFG	VF-VFG	B_s + VF	R_{vi} + VF -VFG	Correlation Coefficient
1	2.7*	-51+	13.1**	-1.3	1.8	-3.1	1.4	10.0	0.960
2	4.9	-48	13.7	-3.6	0x	-3.6	1.3	10.1	0.953
3	3.4	-49	13.3	-2.3	1.0x	-3.3	1.3	10.1	0.958
4	0.56x	-49x	12.2	0.8	3.3	-2.5	1.4	9.7	0.955
5	1.4x	-49x	12.5	-0.03	2.7	-2.7	1.4	9.8	0.958
6	2.4x	-49x	12.9	-1.0	2.0	-3.0	1.4	9.9	0.959
7	3.4x	-49x	13.3	-2.0	1.2	-3.2	1.4	10.1	0.959
8	4.3x	-49x	13.7	2.9	0.6	-3.5	1.4	10.1	0.957
9	2.4	-51	12.9	-1.0x	2.0x	-3.0	1.4	9.9	0.959
10	2.1	-37	10.9	-1.0x	1.0x	-2.0	1.1	8.9	0.921
11	3.3	-46	12.8	-2.0x	1.0x	-3.0	1.3	9.8	0.954

* - Typical average deviation = $\pm$0.5

\+ - Typical average deviation = $\pm$13

** - Typical average deviation = $\pm$1

x - Denotes a fixed variable

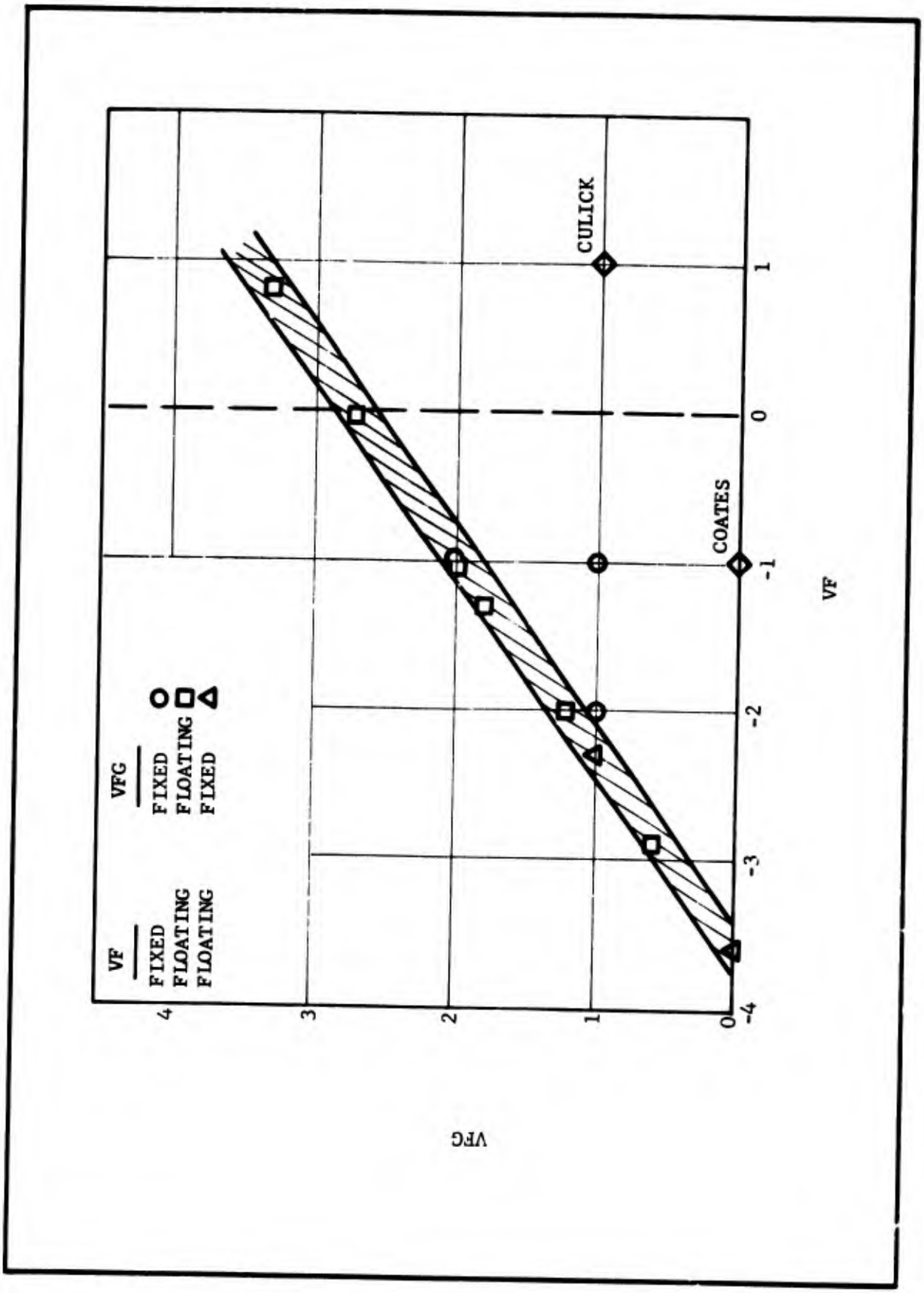

Figure 7-1. Comparison of VFG to VF for Baseline 1-14 Computer Analysis

Examining the correlation coefficient to determine which combination of VF/VFG gives the best fit of the data, the combinations with VF-VFG closest to 3.0 (i.e., -1/+2) seem to give a maximum correlation. (See Figure 7-2a.) In Figure 7-2b, the maximum correlation appears with a B_s value of $\sim$ 2.5 to 3 which would give a VF of $\sim$ -1. As should be expected, with all parameters floating a maximum correlation was achieved resulting in VF/VFG of -1.3/+1.8 and B_s of 2.5.

Based on this approach to analyzing the data it appears that the combination of VF/VFG which correlates the data best is $\sim$ -1/+2. The corresponding value of the pressure coupled response function is $\sim$ 2.5. The velocity coupled response function has a value of 13 independent of the values of VF and VFG chosen. Thus, the velocity coupled response is a factor of 5 greater than the pressure coupled response.

Typical data scatter at the 95 percent confidence level is $\pm$20 percent in B_s, $\pm$26 percent in α_d, and $\pm$10 percent in R_{vi}. Even after eliminating the uncertainty due to VF and VFG, the inherent data scatter in determining R_{vi} is half that of determining B_s.

The final topic considered here is that of weighting the data. The possibility of weighting the data was considered due to the uncertainty of the flow conditions over the velocity-coupled sample, particularly when the sample was recessed or protruding. With either a positive or negative lip there is an uncertainty in a datum point due to flow-related conditions. Also, experience with the pressure-coupled T-burner indicates that non-flush data are more suspect than flush data. Therefore, a weighting function was imposed on the data which allows the results to be weighted most heavily on the flush data.

Originally, arbitrary weights were assigned in steps depending on the degree of deviation from flush condition. Figure 7-3a shows this step weighting and the corresponding values of S_{co}/S_c. Full weighting was given for points with $0.9 < S_{co}/S_c < 1.1$; half weight was assigned points with $0.75 < S_{co}/S_c < 0.9$ and $1.1 < S_{co}/S_c < 1.25$; and one fourth weight was assigned points with $S_{co}/S_c < 0.75$ or > 1.25. However, since a datum point with a value of $S_{co}/S_c = 0.749$ should carry the same weight as a point with $S_{co}/S_c = 0.751$, assuming the step comes at 0.75 as in Figure 7-3a, a continuous weighting function was considered to be more correct than a step weighting function.

Figure 7-3a suggests a parabolic-type distribution of weights as a function of S_{co}/S_c. This type of a distribution gives relatively uniform weighting to the near flush condition data and drops off rapidly as the value of S_{co}/S_c increases or decreases beyond flush condition. Equation (7-5) describes the weighting function, SY_i, (see Equation 7-1) as a function of $(S_{co}/S_c)^2$ where 50 is the value of a weighting factor to position the curve properly within the limits of the step graph in Figure 7-3.

$$SY_i = 4.0 + \left|(1 - S_{co}/S_c)^2\right| 50 \qquad (7\text{-}5)$$

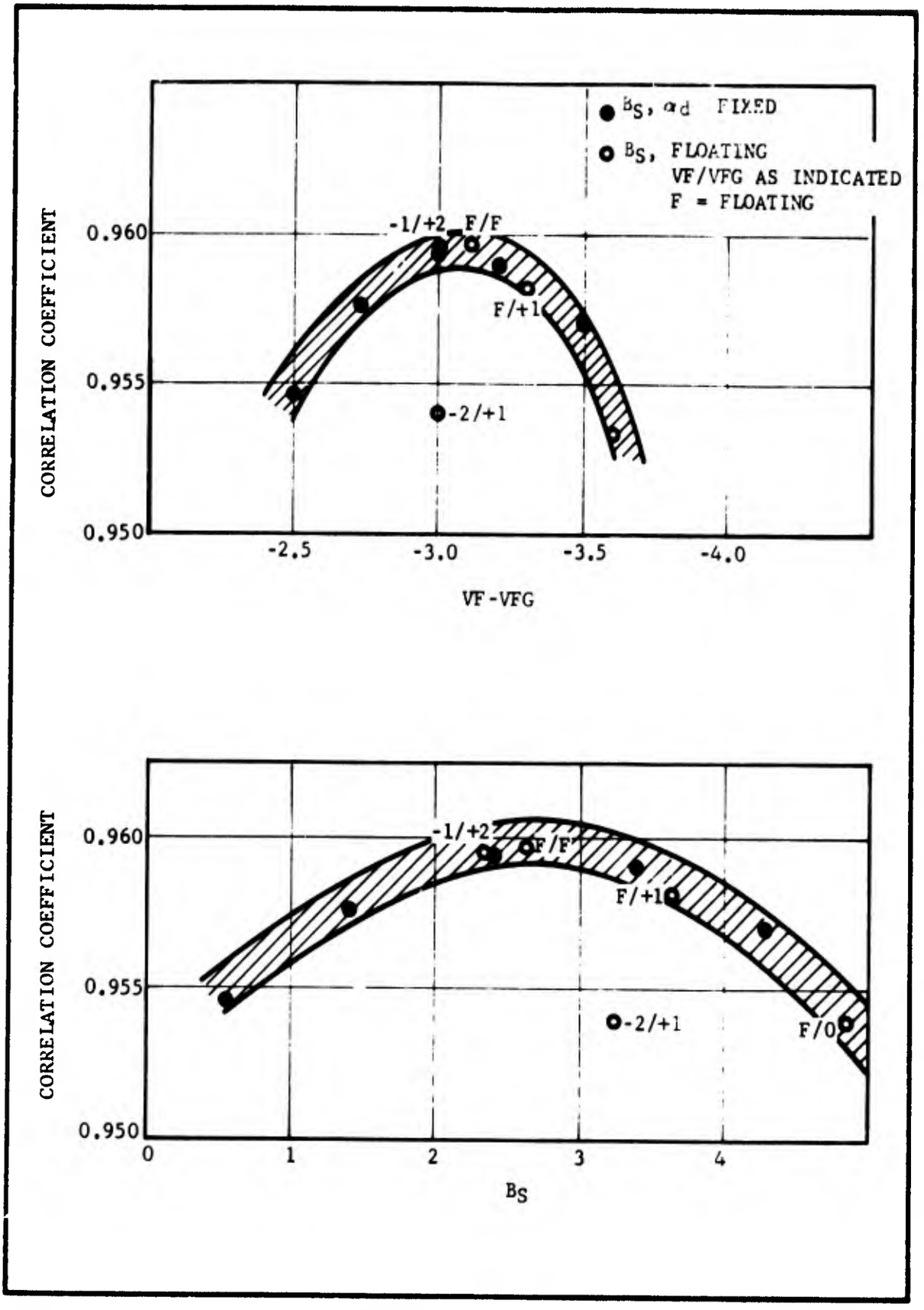

Figure 7-2. Data Correlation Resulting from Different Values of VF-VFG and B_S for Baseline Data

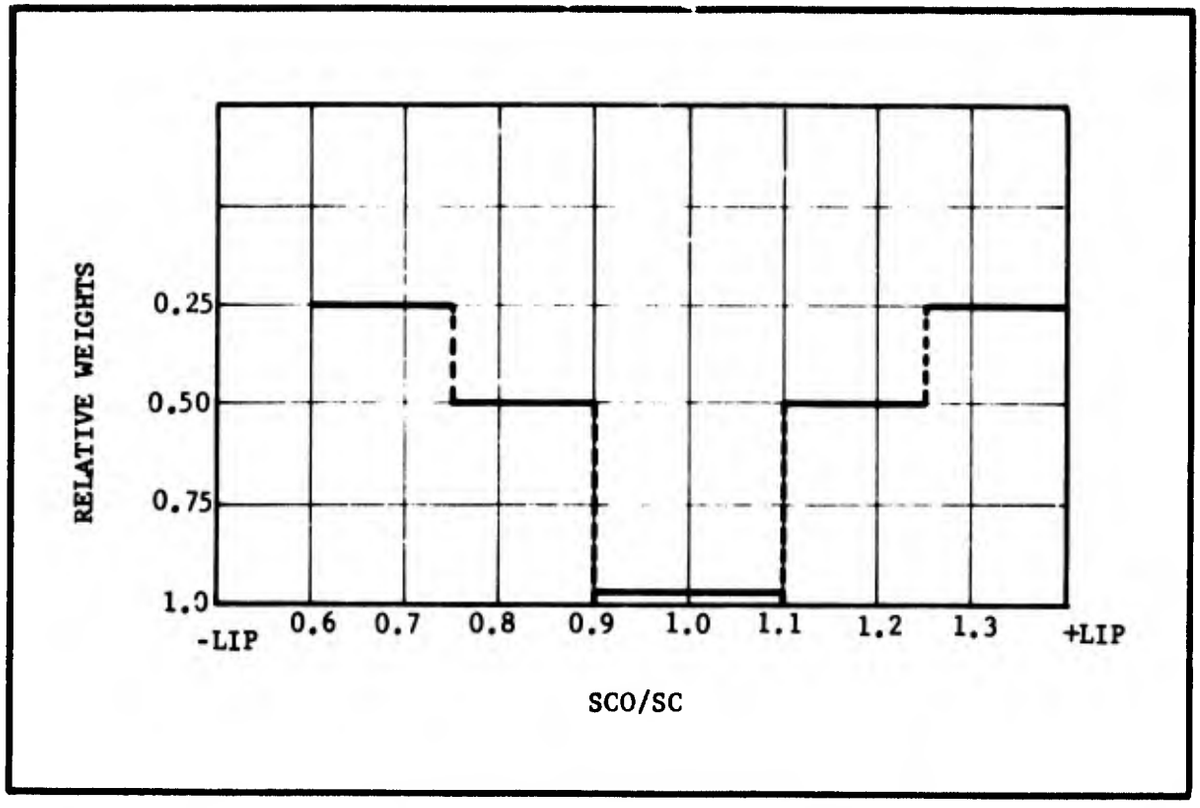

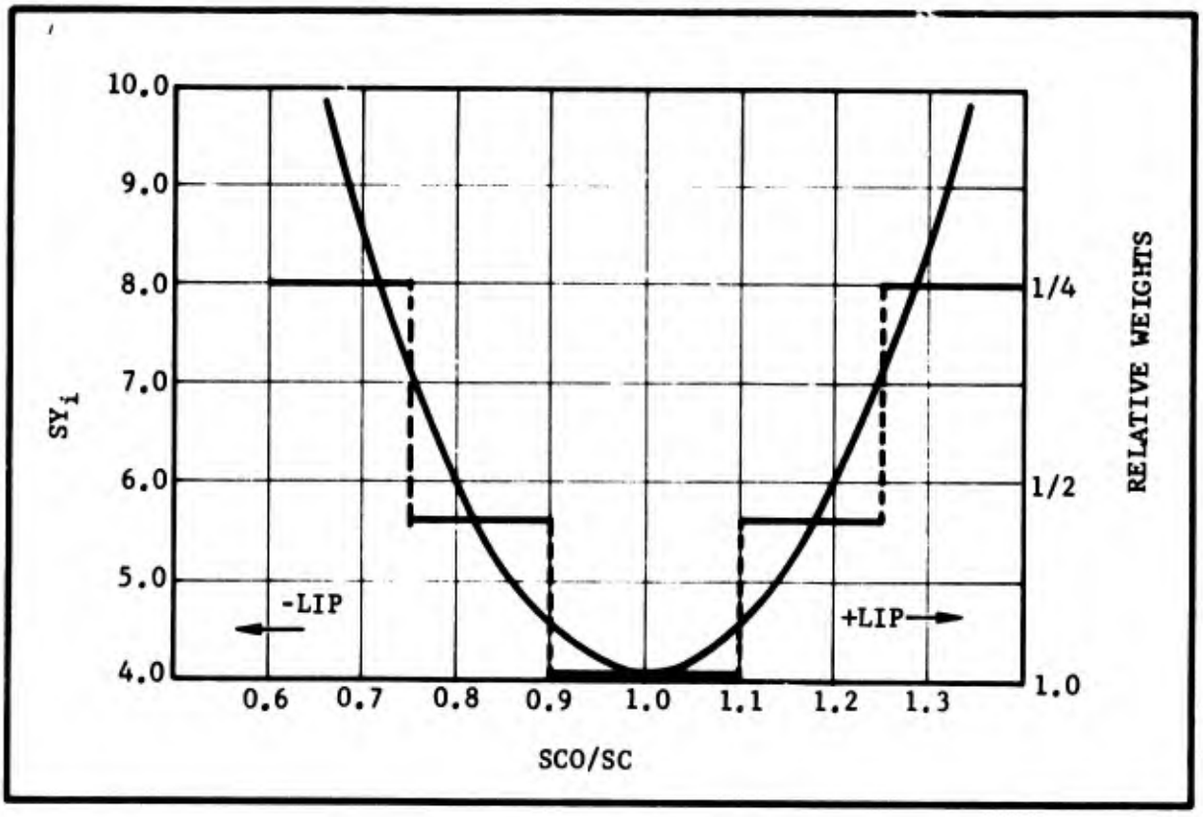

Figure 7-3. Preliminary Step Weighting and Continuous Weighting as a Function of S_{co}/S_c Used in the Computer Analysis

Therefore, a datum point with a small weighting function, SY_j, will cause greater adjustments in the parameters than one with a large weighting function.

Figure 7-3b is a plot of Equation (7-5) over the limits of S_{co}/S_c encountered in the variable area T-burner. The relative weighting of each point is shown on the right hand ordinate while the weighting function values form the left hand ordinate. These results have been incorporated into the data analysis computer program to provide a continuous weighting factor for each datum point based on the value of S_{co}/S_c for that point.

A comparison of the effect of weighting the data in this manner was performed with the baseline data set. The data were analyzed with the weighting described by Equation (7-5) and with no weighting at all for several combinations of VF and VFG. The values of the parameters determined by these two procedures are presented in Table 7-II. Three sets of conditions were considered with VFG floating and fixed at values of 0 and +1. The value of the velocity-coupled response function is ~ 13 for all cases; and the sum of B_s and and VF is also constant (~ 1.4). The differences in the values of B_s and R_{vi} are small but could well be significant. In addition, the percent variance explained is better with the weighted data than with the unweighted data.

Because of these differences in the values of both response functions and the concern for interpretation of nonflush data, the weighting was used as standard procedure in all computer data analysis.

TABLE 7-II

COMPARISON OF EFFECT OF WEIGHTING DATA

	Parameter Values*				Statistics	
	B_s	VF	R_{vi}	VFG	CC	Percent Variance Explained
VFG Floating						
No Weighting	3.8	-2.4	12.9	0.92	0.937	96.8
Weighting	2.7	-1.3	13.1	1.78	0.960	97.9
VFG = 0 (Fixed)						
No Weighting	5.0	-3.6	13.4	0x	0.935	96.7
Weighting	4.9	-3.6	13.8	0x	0.954	97.6
VFG = 1 (Fixed)						
No Weighting	3.7	-2.3	12.9	1x	0.937	96.8
Weighting	3.7	-2.3	13.4	1x	0.958	97.9

*α_d was fixed at -50 for all analyses

B. TECHNIQUE ANALYSIS

In this paragraph, the general characteristics of the VCTB technique are examined and compared with those of the pressure-coupled T-burner.

Figure 7-4 is a plot of α (corrected for volume changes) versus area ratio for the baseline pressure-coupled conditions and VF/VFG equal -1/+1. Plots for other combinations of VF/VFG are very similar as the correction is a weak function of VF/VFG. The upward curvature of the line is due to the effect of velocity coupling as shown in Paragraph IV.C. Figure 7-5 is the corresponding plot for the baseline velocity-coupled tests. The data were obtained by varying the velocity coupling sample area ratio holding the driver area ratio constant at a value of 1-1/2. The data appear to fit a straight line as predicted by theory.

It is convenient to examine the raw data as a function of lip (or diameter ratio). This is facilitated by use of the tapered samples which give essentially a constant area ratio (e.g., only one variable is changing with time). Figure 7-6 shows the pressure-coupled data plotted versus the diameter ratio with area ratio as a parameter. The growth constant decreases with decreasing diameter ratio; the effect being greater with larger area ratio. This trend is in general agreement with the theoretical predictions of Section IV. Figure 7-7 is the corresponding plot for the velocity coupling data. The trends of the data are the same but the magnitude of the change with S_{co}/S_c is much greater than for pressure coupled data. For the pressure coupled data at an area ratio of 4-1/2 there is a difference of $\sim$ 10 to 15 sec^{-1} between the flush data and a diameter ratio of 0.6. With the velocity-coupled data at an area ratio of 3, the corresponding difference is $\sim$ 50 sec^{-1}.

A comparison was made to see if velocity coupling influenced the steady state burn rate. Some of the theoretical analyses discussed in Section III indicate that the mean burn rate should increase under the influence of velocity coupling. However, there did not appear to be a significant difference in the burn rate of the propellant in the velocity-coupled T-burner compared to the pressure coupled T-burner data.

One test series was fired to determine if there was an effect of driver area ratio. These tests were fired at the baseline conditions, but with a driver area ratio of 3 instead of 1-1/2. Figure 7-8 shows the data plotted as α versus sample area ratio. The intercept is $\sim$ 0 in agreement with the pressure-coupled tests, and the data fall on a straight line like the standard velocity-coupled tests. There does not appear to be a significant difference in the data using the two different driver area ratios.

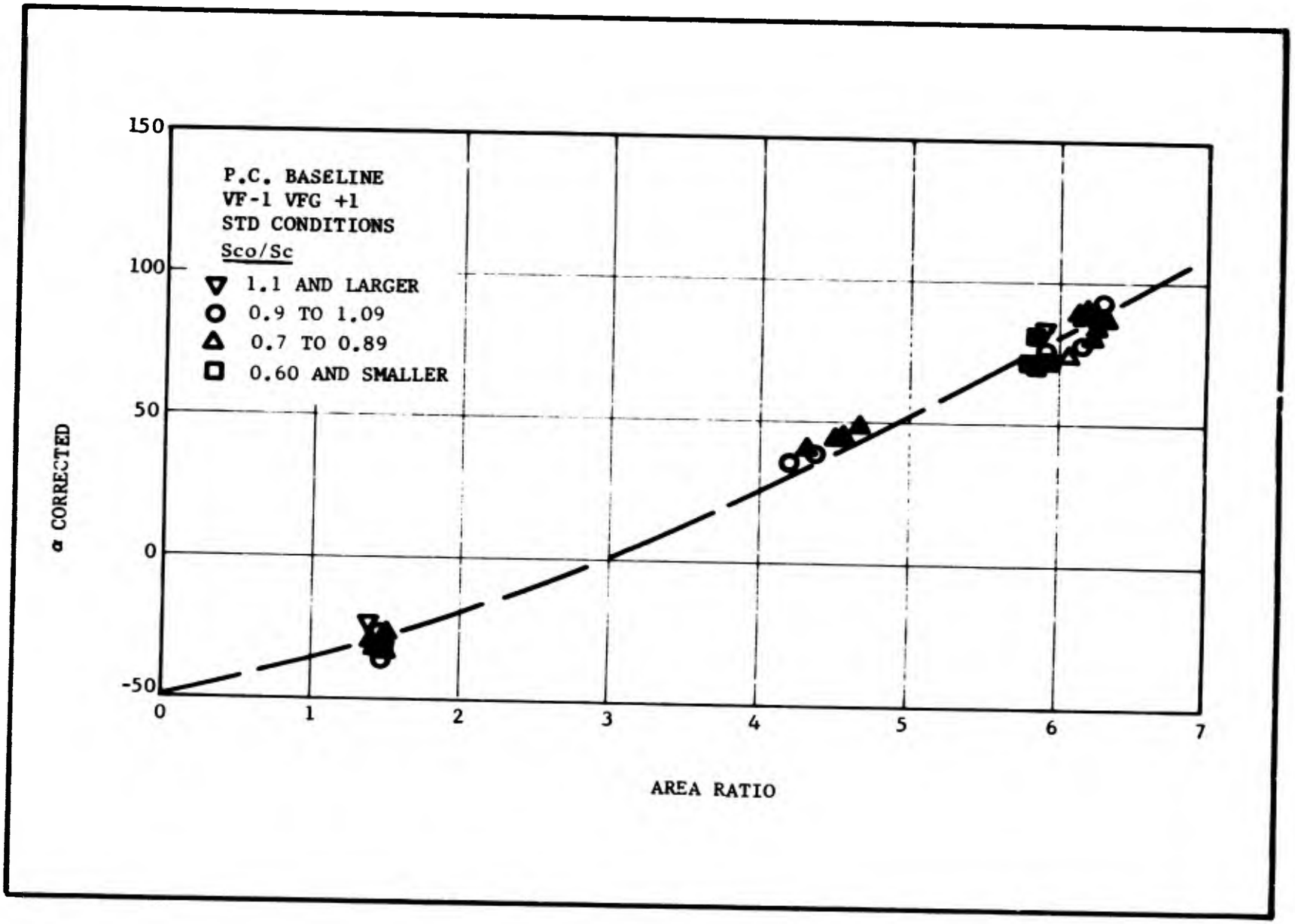

Figure 7-4. Corrected Baseline Pressure Coupled Growth α Versus Area Ratio

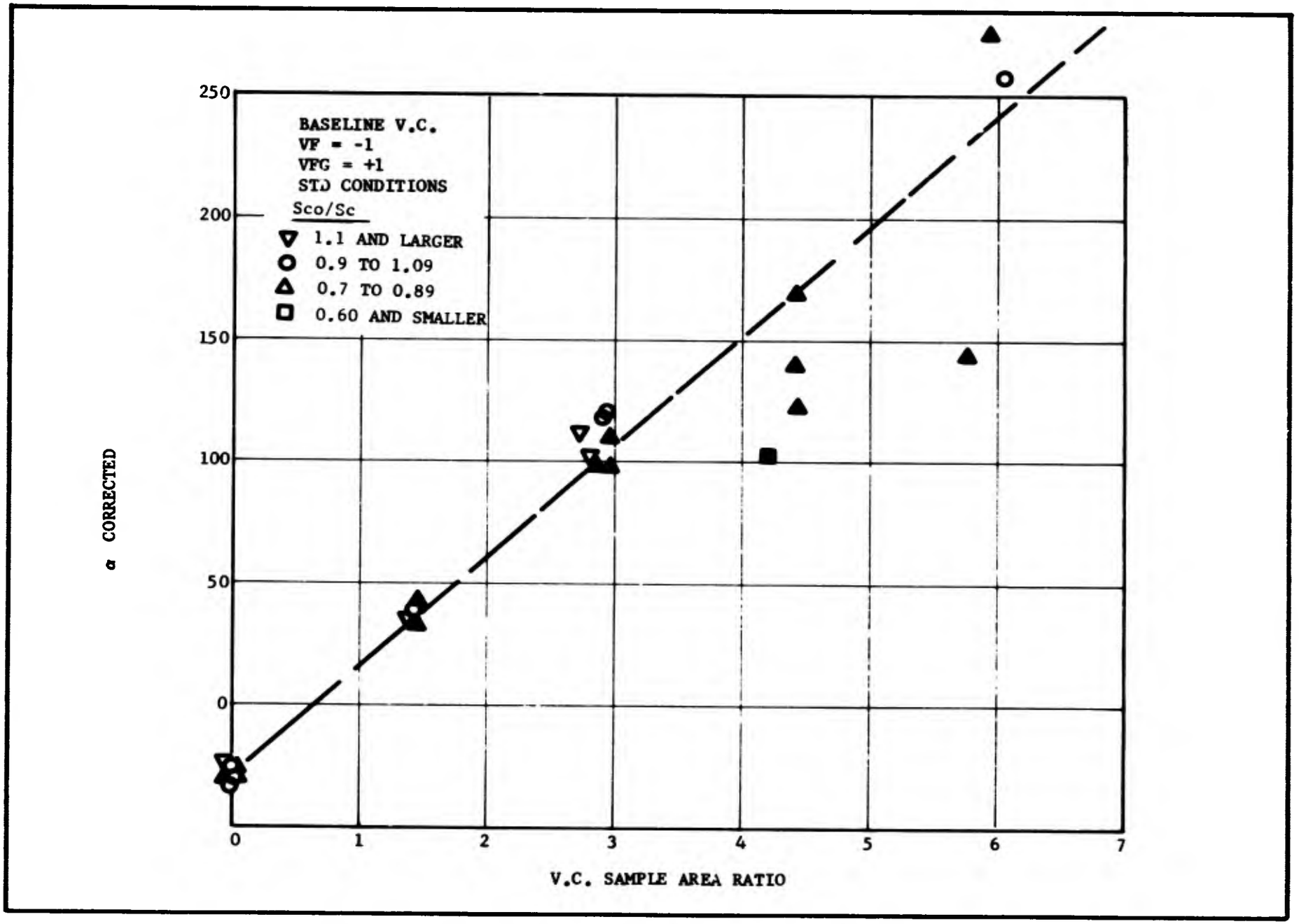

Figure 7-5. Corrected Baseline Velocity Coupling Growth α Versus Area Ratio

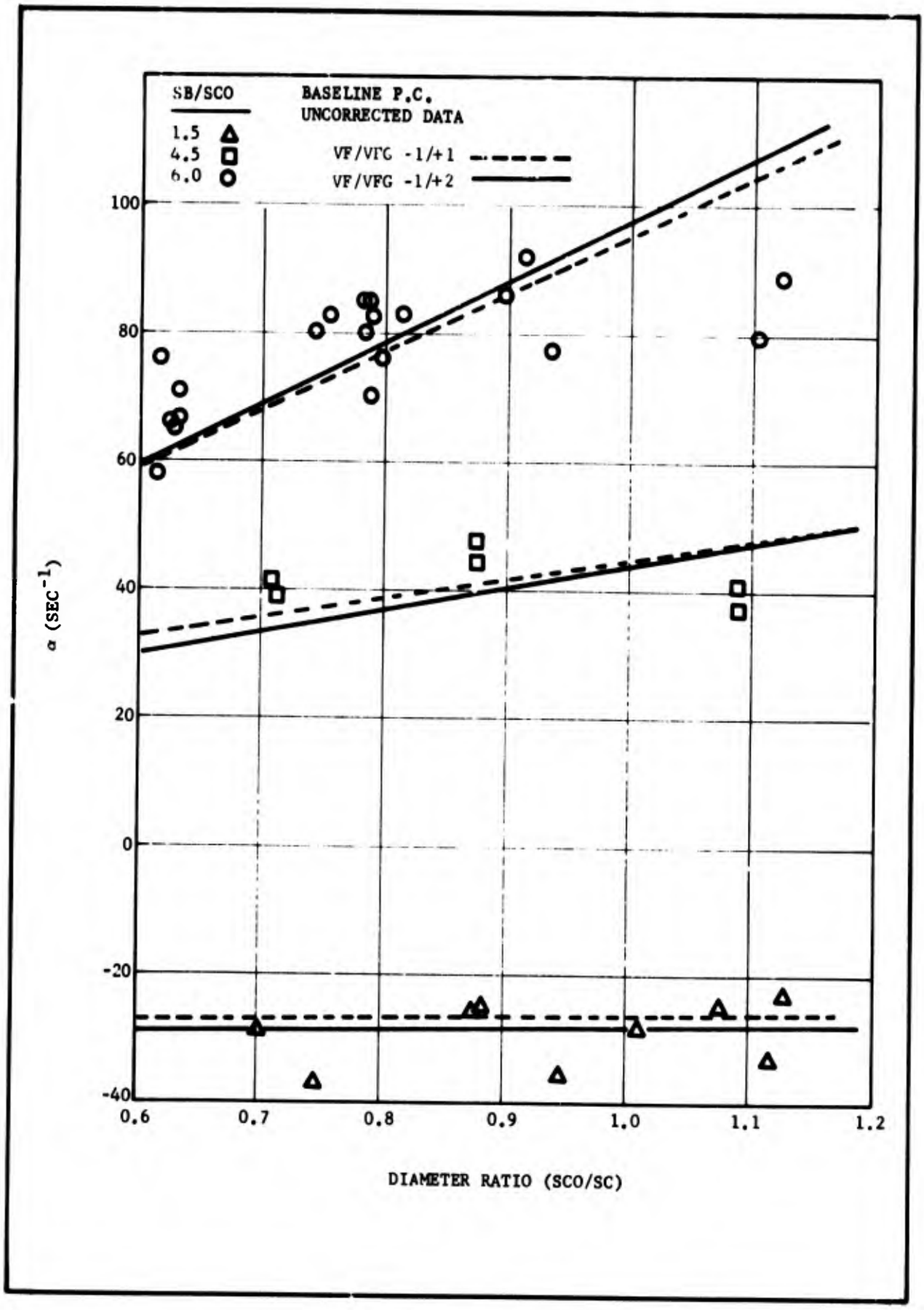

Figure 7-6. Baseline Pressure Coupled α Versus Diameter Ratio with Average Predicted Values for VF/VFG Combinations Listed

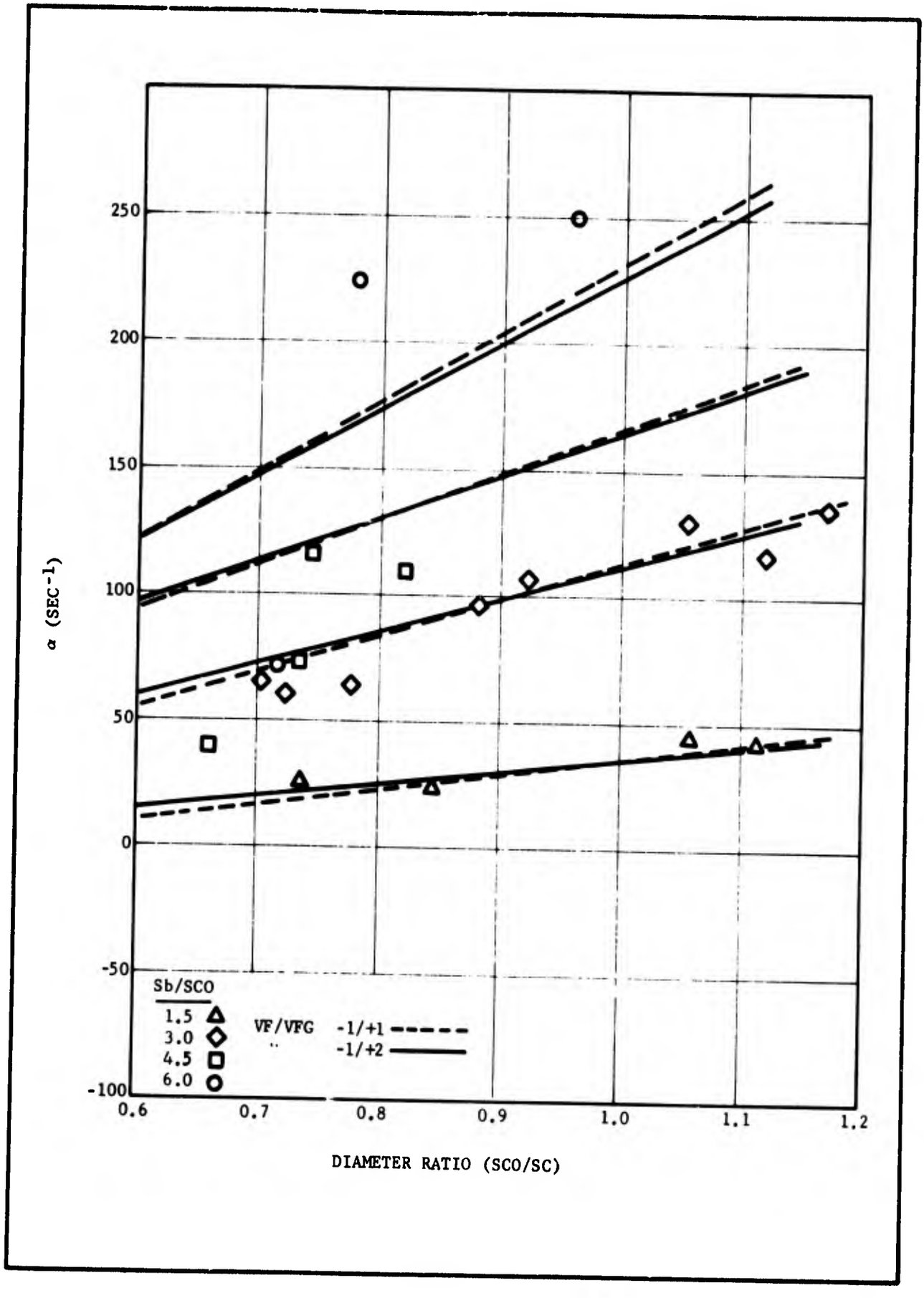

Figure 7-7. Baseline Velocity Coupled α Versus Diameter Ratio with Average Predicted Values for VF/VFG Combinations Listed

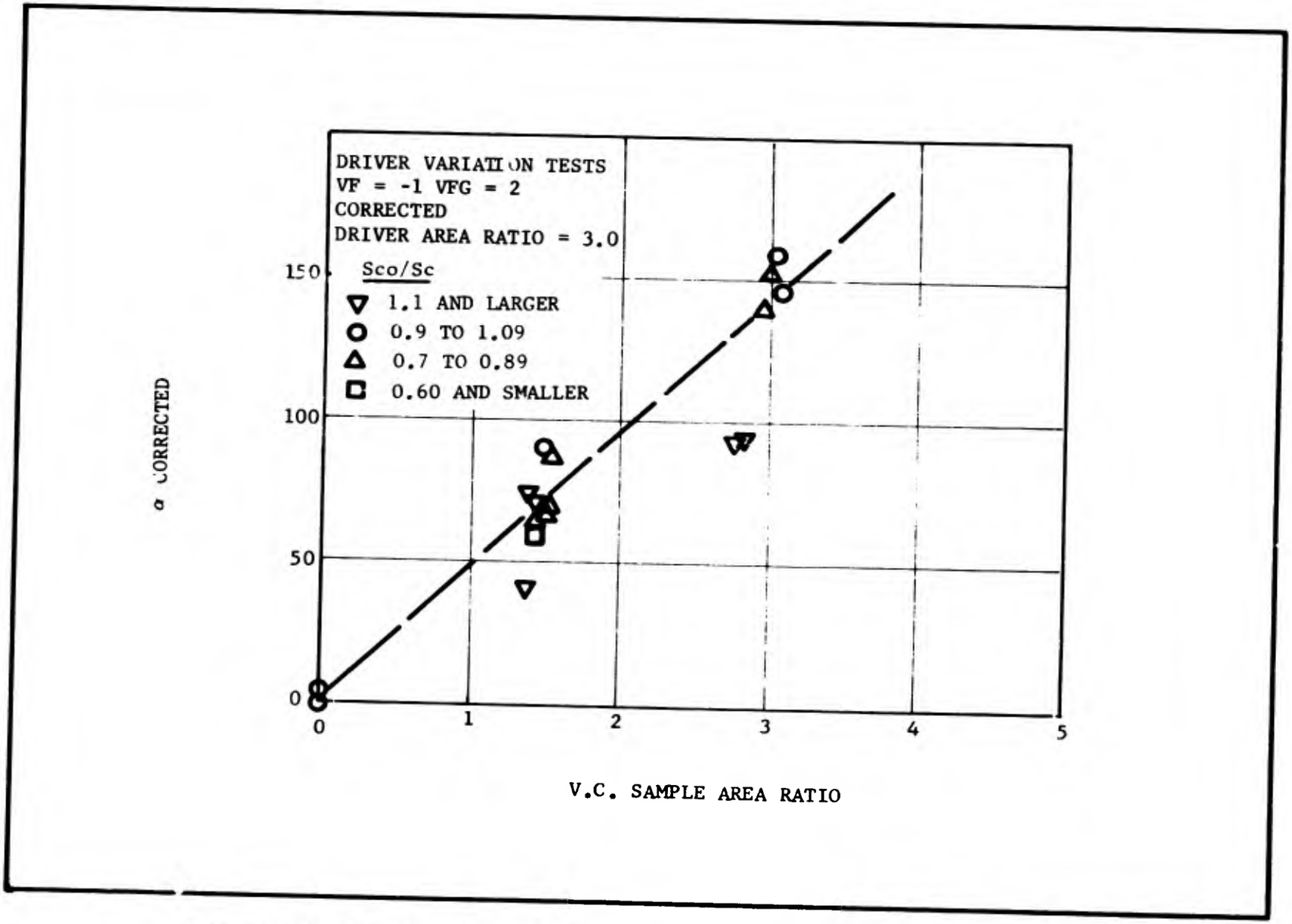

Figure 7-8. Corrected α Versus Area Ratio for Driver Area Ratio of 3

The pressure-coupled, velocity-coupled, and driver-variation data are compared further in Table 7-III. The pressure-coupled data were run with various combinations of VF/VFG fixed, and with a fixed value of R_{vi} (chosen so that R_{vi} + VF-VGF = 10). The value of B_s + VF is essentially a constant as with the baseline data set. The best correlation is obtained with VF/VFG of -1/+1, and the results are essentially independent of the value of VFG, as should be for pressure coupled data.

The pressure-coupled data were run with the velocity-coupled data, floating the three combustion parameters. The values of B_s + VF and R_{vi} + VF-VFG are constant for the three combinations of VF/VFG that were assumed, giving an R_{vi} of ~ 13. The best correlation was obtained with the -2/+1 case. The third combination of data considered was the pressure-coupled data plus the driver-variation data. The value of B_s was essentially the same as in the two previous data sets but both the R_{vi} and α_d are lower than determined by the standard data.

The conclusion reached from analyzing these sets of data is that R_{vi} can be determined from velocity-coupled tests with approximately the same confidence level as can the pressure-coupled response. However, R_{vi} is needed in evaluating pressure-coupled data and B_s is needed in evaluating velocity-coupled data; the two test techniques are by no means mutually exclusive. It appears that there may be a small effect due to the size of the driver sample, however, additional data and/or analysis would be required to verify this.

TABLE 7-III

SUMMARY OF COMPUTER ANALYSIS OF THE PRESSURE-COUPLED, VELOCITY-COUPLED, AND DRIVER-VARIATION TESTS

Data	B_s	α_d	R_{vi}	VF (Fixed Values)	VFG (Fixed Values)	B_s + VF	R_{vi} + VF-VFG	Correlation Coefficient
PC only*	0.6+	-50**	10	+1	+1	1.6	10	0.993
	1.4	-48	12	0	+2	1.4	10	0.992
	2.4	-49	12	-1	+1	1.4	10	0.992
	3.4	-49	12	-2	0	1.4	10	0.992
	3.3	-49	13.5	-2	+1	1.3	10	0.991
	4.3	-48	13.5	-3	0	1.3	10	0.992
PC + VC	2.5	-53	12.2++	-1	+1	1.5	10.2	0.969
	2.4	-52	13.2	-1	+2	1.4	10.2	0.968
	3.4	-52	13.4	-2	+1	1.4	10.4	0.970
PC + DV	2.4	-46	11.4	-1	+1	1.4	9.4	0.974
	2.3	-45	12.5	-1	+2	1.3	9.5	0.975
	3.4	-45	12.4	-2	+1	1.4	9.4	0.970

* Values of R_{vi} fixed on all PC only runs.

\+ Typical average deviation = ± 0.1

** Typical average deviation = ± 10

++ Typical average deviation = ± 1.0

C. TESTS TO DETERMINE THE VENT TERM

A series of tests were proposed and conducted in an attempt to evaluate the vent term, VF, and/or the flow turning term, VFG. The problem considered was to determine an experiment that would deemphasize the combustion terms, B_s and R_{vi}, and permit the isolation of the flow terms VF and VFG. It is apparent from the theoretical analysis that the geometry terms multiplied by the pressure-coupled and velocity-coupled response functions are proportional to the acoustic pressure and the product of acoustic pressure and acoustic velocity, respectively. Therefore, the contribution from the combustion will be zero at the pressure nodal point, the vent of the T-burner. Conversely, the flow terms are proportional to the acoustic velocity and both the g and C terms are maximum at the velocity antinode, the vent position. Thus, for a test sample located near the vent of the T-burner, $\mathcal{E}_{\ell_v}^{o} \longrightarrow 0$, $g_{\ell_v}^{o} \longrightarrow 2$, $C_{\ell_v}^{o} \longrightarrow 1.0$, and $P_{\ell_v}^{o} \longrightarrow 0$. In other words, the combustion contribution is essentially eliminated near the vent while the flow terms have significant contributions. Assuming short propellant grains near the T-burner vent, the equation for α becomes (See Equation (7-4):

$$\alpha^{o} = 4f\bar{M}_b \left\{ \left(\frac{S_b}{S_{co}} \right)_1 (B_s + VF) - \left(\frac{S_b}{S_{co}} \right)_v (VFG - VF) \right\} + \alpha_d \qquad (7\text{-}6)$$

Therefore, locating a test sample near the vent and systematically varying the area ratio of the vent sample results in a dependence on VF and VFG only. In other words,

$$\left[\frac{d\alpha^{o}}{d(S_b/S_{co})_v} \right]_{\substack{\text{Constant} \\ \text{driver}}} = 4f\bar{M}_b (VF - VFG) \qquad (7\text{-}7)$$

Based on the above logic, a series of tests were performed with the test samples located as near the vent as was physically possible. Figure 7-9 shows the configuration that was used. The hardware and instrumentation system that was used was the same that has been used in variable area T-burner testing[71] and for the velocity coupled T-burner testing described above. The tests were performed with CYH propellant at 300 psi and 450 Hz (i.e., standard conditions). Because of the proximity of the test sample to the vent, the normal propellant sample holder could not be used. Therefore, the test sample was machined to fit into the 1.5 in. ID of the T-burner wall (e.g., the sample has a 1.25 in. ID and 1.5 in. OD), resulting in the vent sample having a smaller web than the driver sample as shown in Figure 7-9. This resulted in the test sample burning out while the driver sample continued to burn, showing

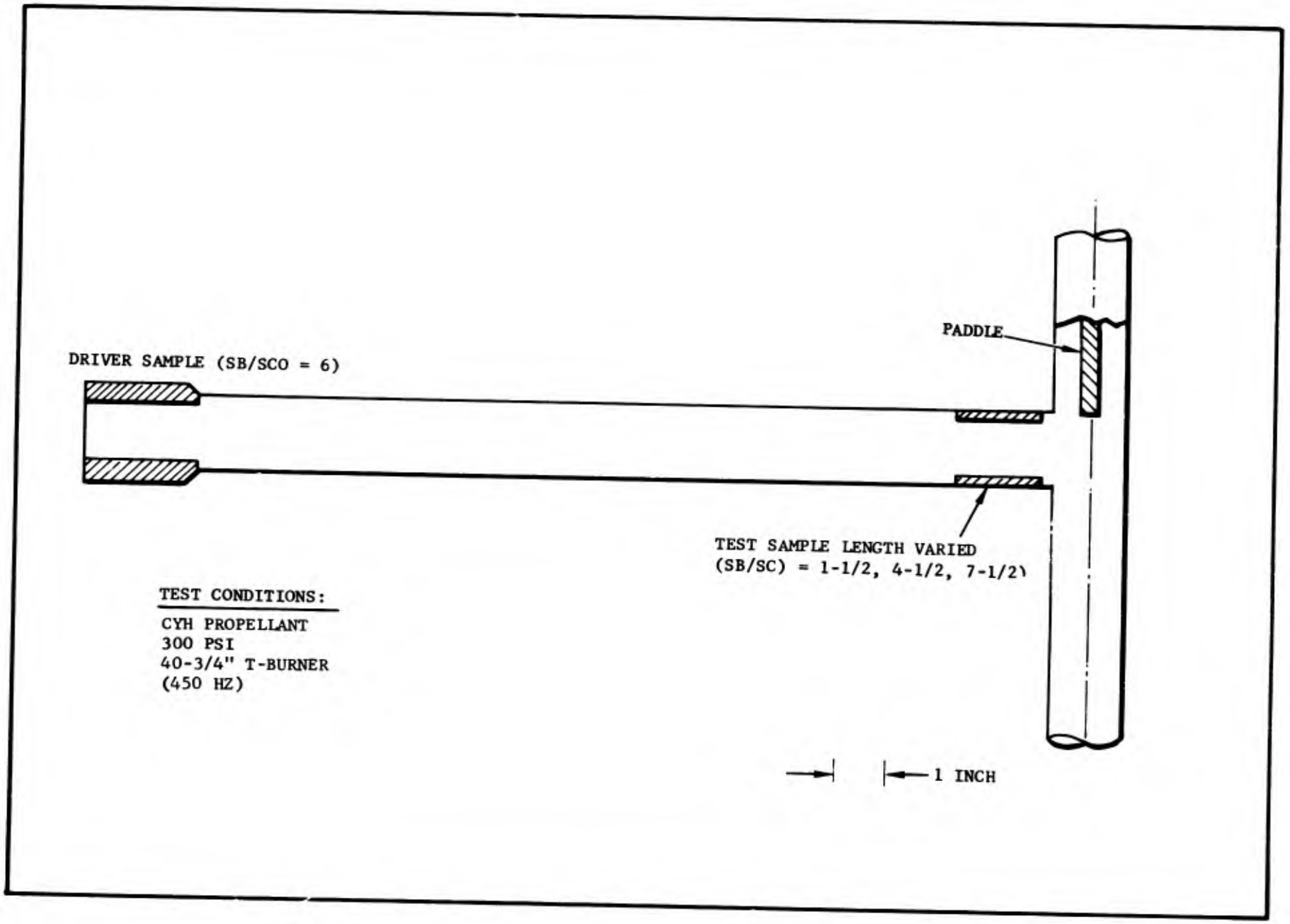

Figure 7-9. T-Burner Configuration to Determine the Flow Turning Terms in the T-Burner Analysis

an instantaneous effect of the test sample on the acoustic environment. The driver sample was chosen large enough ($S_{b1}/S_{co} = 6$) to drive the T-burner spontaneously unstable at an α of ~ 80 sec^{-1} and an amplitude of $\sim$ 80 psi peak to peak.

The results were rather dramatic. Figure 7-10 shows the oscillograph record of three of seven tests that were fired. Actual data from all of the tests fired are tabulated in Appendix A. The figure shows the AC pressure trace for the firings; the test conditions are noted. Test sample area ratios of 1-1/2, 4-1/2, and 7 were used. The test records show that both the limiting pressure amplitude and the measured growth constant were larger after the test sample burned out than while the test sample was burning, indicating that the test sample represented a loss to the system. The test records also show that the change in both α and amplitude becomes greater for larger test samples.

Figure 7-11 shows a plot of the corrected α versus the test sample area ratio (because the data were taken at very nearly flush conditions, the correction is negligible except at the area ratio of 6 where it is small). Calculated curves for various values of VF/VFG are superimposed using appropriate values of B_s, α_d, and R_{vi}. The result is rather emphatic. The only curves that fit the data are those with a net loss of 3 (i.e., VF-VFG = -3). It should be noted that there is considerable curvature in the predicted curves whereas Equations (7-6) and (7-7) indicate a straight line should result. The curvature comes about due to the fact that the samples were not located precisely at the center of the T-burner. As shown in Figure 7-9, the samples were located 1 in. from the centerline of the burner. Also, the large samples (S_b/S_{co} = 7) were 2.75 in. long, extending a significant distance into the mode shape. Therefore, the effects of combustion driving must be accounted for, which results in the deviation from the straight line. Referring back to Figure 7-1, the baseline set of data seemed to optimize on a value of VF-VFG $\sim$ -3. This was apparently due to the influence of these vent tests which virtually require such a result in order to agree with the data.

The results of these tests have considerable impact on interpretation of T-burner analysis. According to Culick's interpretation, VF/VFG have values of +1/+1 which would have no net effect acoustically for the present system. In other words, there would not have been any change in α or amplitude when the test sample burned out or when the area ratio was varied. Coates interpretation gives VF/VFG of -1/0 and a net loss of one which gives too little change in α with varying area ratio. Thus, neither is in agreement with the observed data.

While the results of these tests have not isolated the value of the vent term, VF, the net effect of the flow interactions terms has been shown to be a loss to the system of magnitude 3 (i.e., VF-VFG). Because the indicated loss is so large, the data could well be indicating

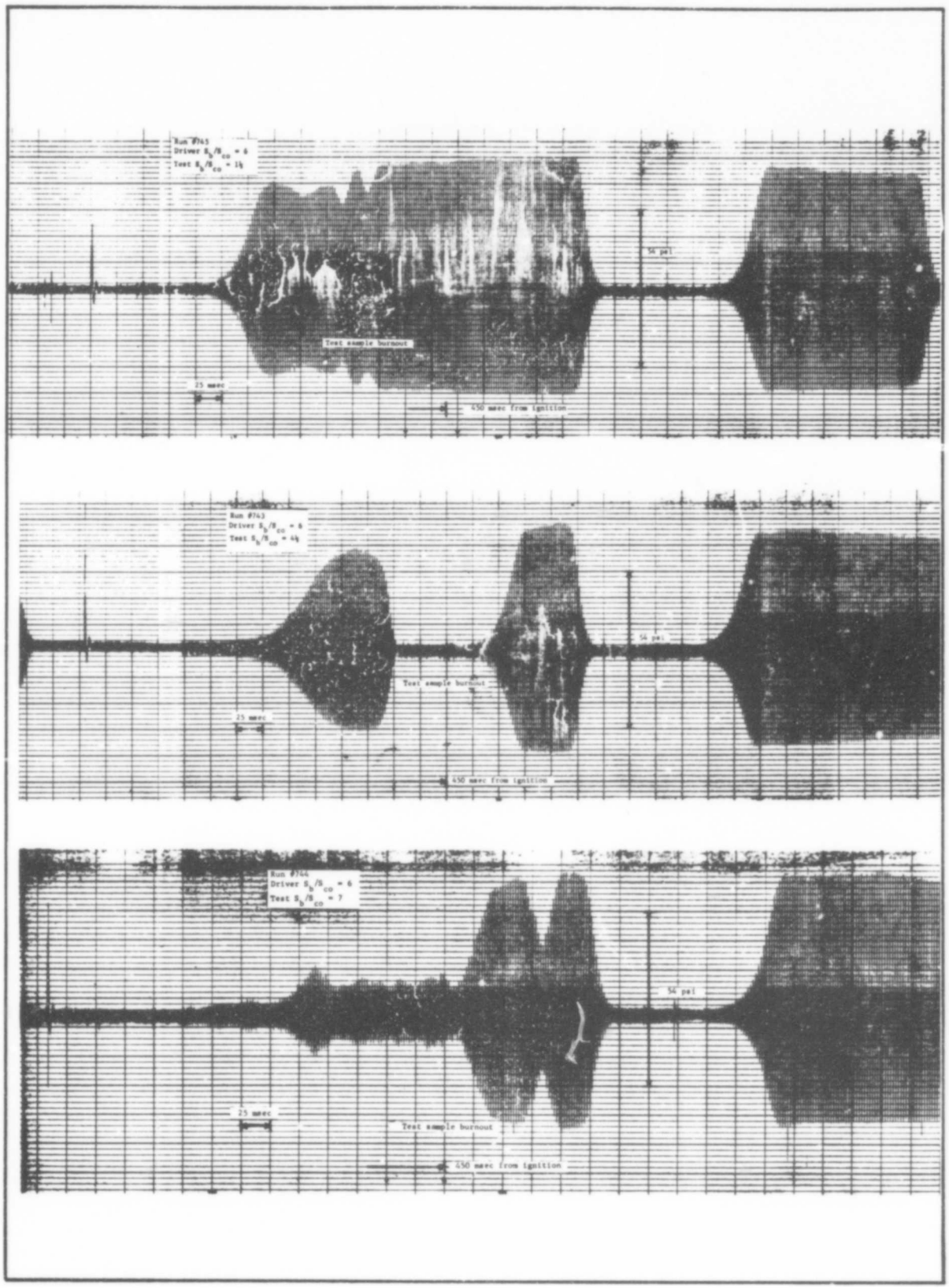

Figure 7-10. Vent Test Results for Firings with Three Different Test Sample Area Ratios

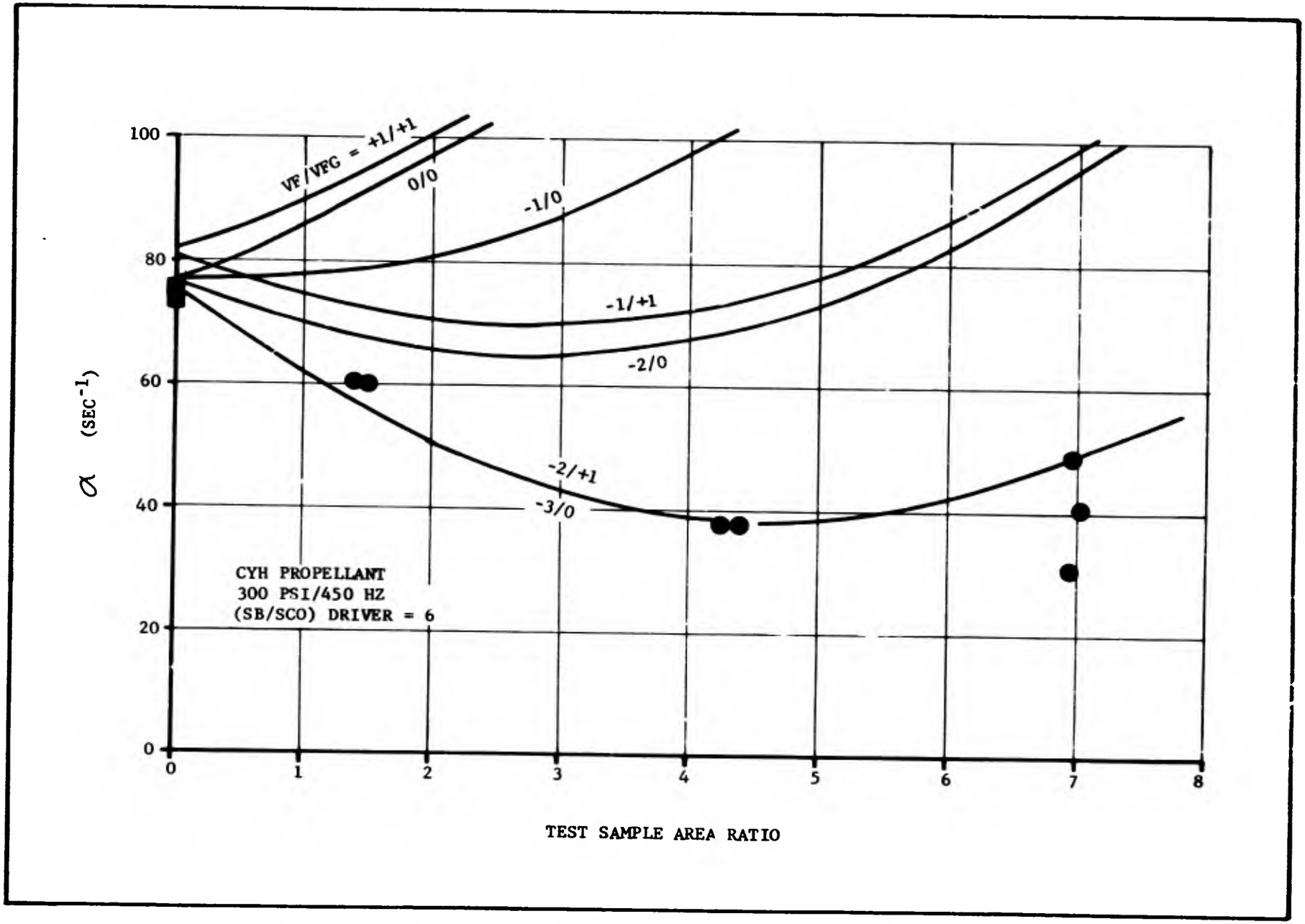

Figure 7-11. Comparison of Vent Test Data with Theoretical Calculations for Various Combinations of VF and VFG

that the formulation of the acoustic equations is not adequate to describe the T-burner; possibly a three-dimensional description will be required to obtain an accurate description of the T-burner.

D. EFFECT OF FREQUENCY

A test series was devoted to determine if the technique was sensitive to frequency. Both pressure-coupled tests and velocity-coupled tests were fired with CYH 1-14 propellant at 300 psig and 800 Hz. The 800 Hz was chosen because of available hardware and because of the possibility (discussed in Section III.B.2) of R_{vi} going from positive to negative with increasing frequency.

Figure 7-12 is the alpha versus area ratio plot for the pressure coupled 800 Hz data. Although the normal trend of α increasing with area ratio was observed, a very different trend was observed in that α tends to increase with decreasing diameter ratio. This is exactly opposite from the normally observed trend. At this time there is no explanation for such an occurrence. Figure 7-13 is the alpha versus area ratio for the velocity-coupled data. The system was stable (i.e., $\alpha < 0$) for area ratios of 1-1/2, and two initial paddle pulls at 4-1/2. Again, alpha was observed to increase significantly with decreasing diameter ratio. This is shown dramatically in Figure 7-14 where alpha is plotted versus the diameter ratio. Theoretical curves are superimposed for area ratios of 1-1/2, 6, and 7; the theory does not agree with the trend of the data.

The difference in pressure coupled data at 450 and 800 Hz is small but significant. The difference between the velocity coupled data at 450 and 800 Hz is very striking and grossly different than that observed with the pressure coupling. Quantitative analysis of the 800 Hz data was not accomplished. Table 7-IV summarizes several of the computer runs that were made. For the -1/+1 case, what appeared to be reasonable values of B_s, α_d, and R_{vi} were determined. However, for this case α was predicted to decrease with decreasing diameter ratio which is opposite to the observed trend of the data. Several runs were made with negative values of R_{vi} (fixed) to determine if this would give the correct trend with diameter ratio. This appeared to be the case, but the magnitude of the predicted changes were much smaller than those observed, and when R_{vi} was floated, the computer gave $R_{vi} > 0$. When all variables were floated, negative values of B_s were determined with VF/VFG becoming +4/+1 which is rather unreasonable.

A definite effect of frequency was observed in the VCTB; however, it was not possible to quantitize the data. Additional work is needed to quantitatively evaluate the effect of frequency.

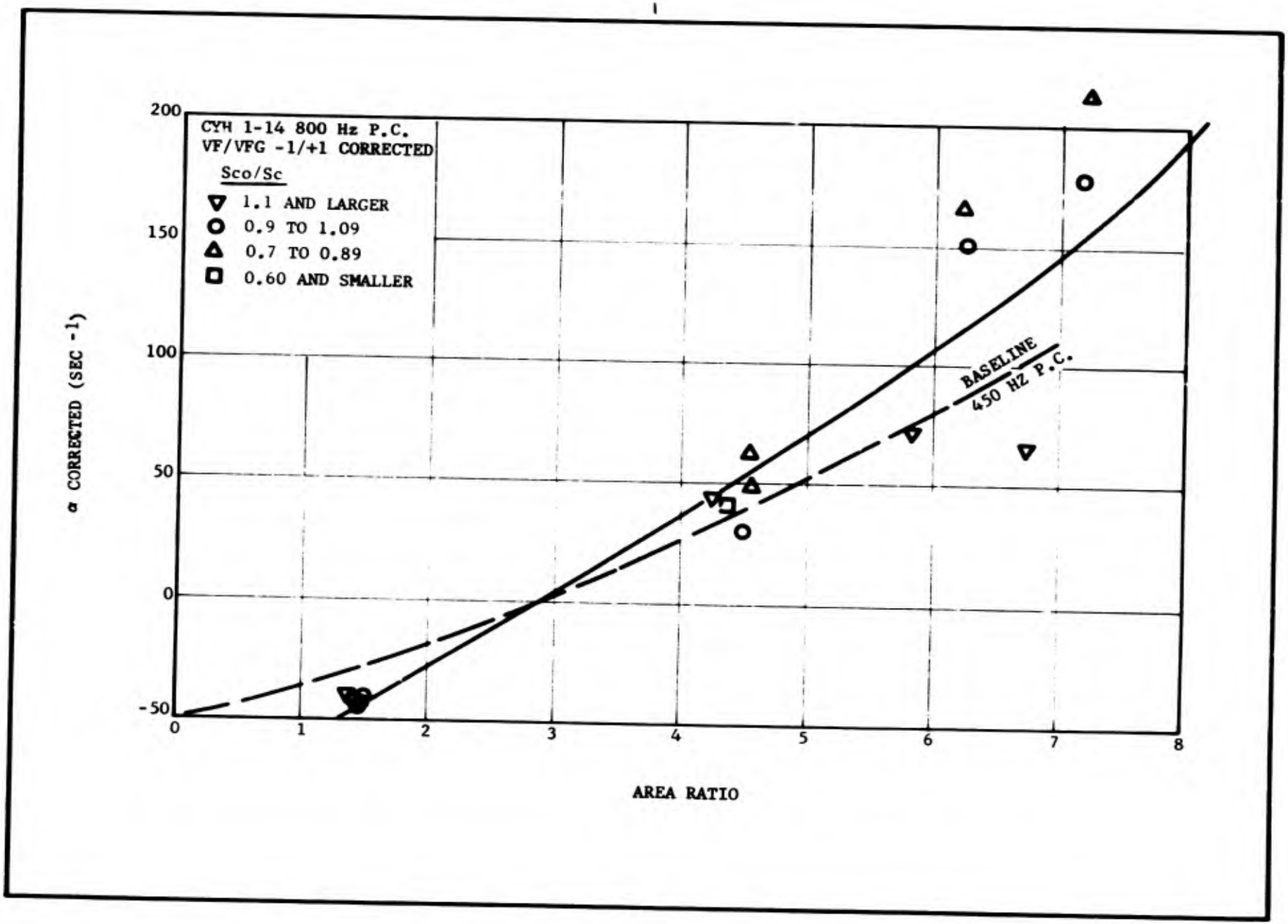

Figure 7-12. CYH 800 Hz Pressure Coupling Corrected α Versus Area Ratio with 450 Hz Baseline Prediction for Frequency Effects Comparison

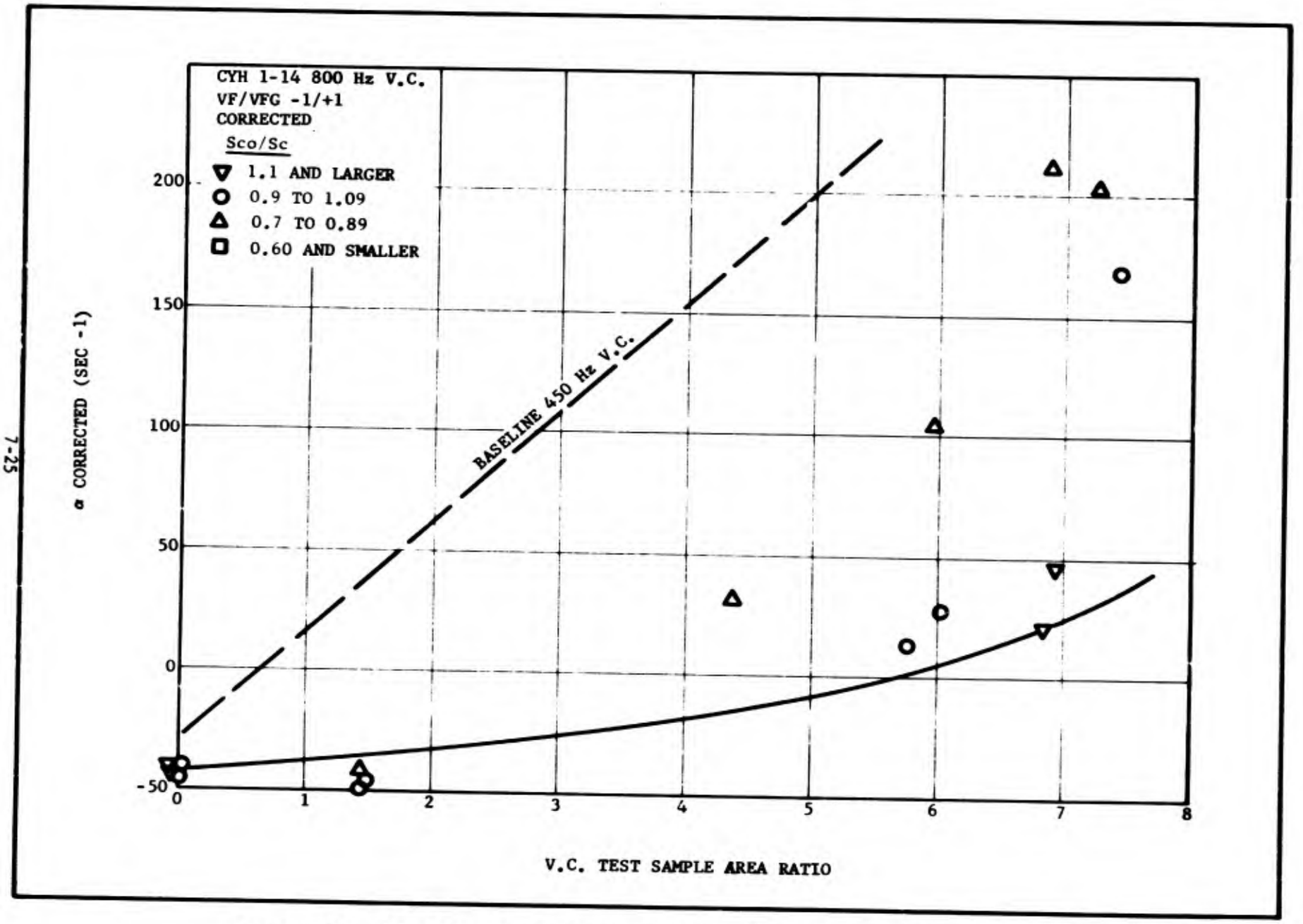

Figure 7-13. CYH 1-14 800 Hz Velocity Coupling Corrected α Versus Area Ratio with Baseline 450 Hz Prediction for Frequency Effects Comparison

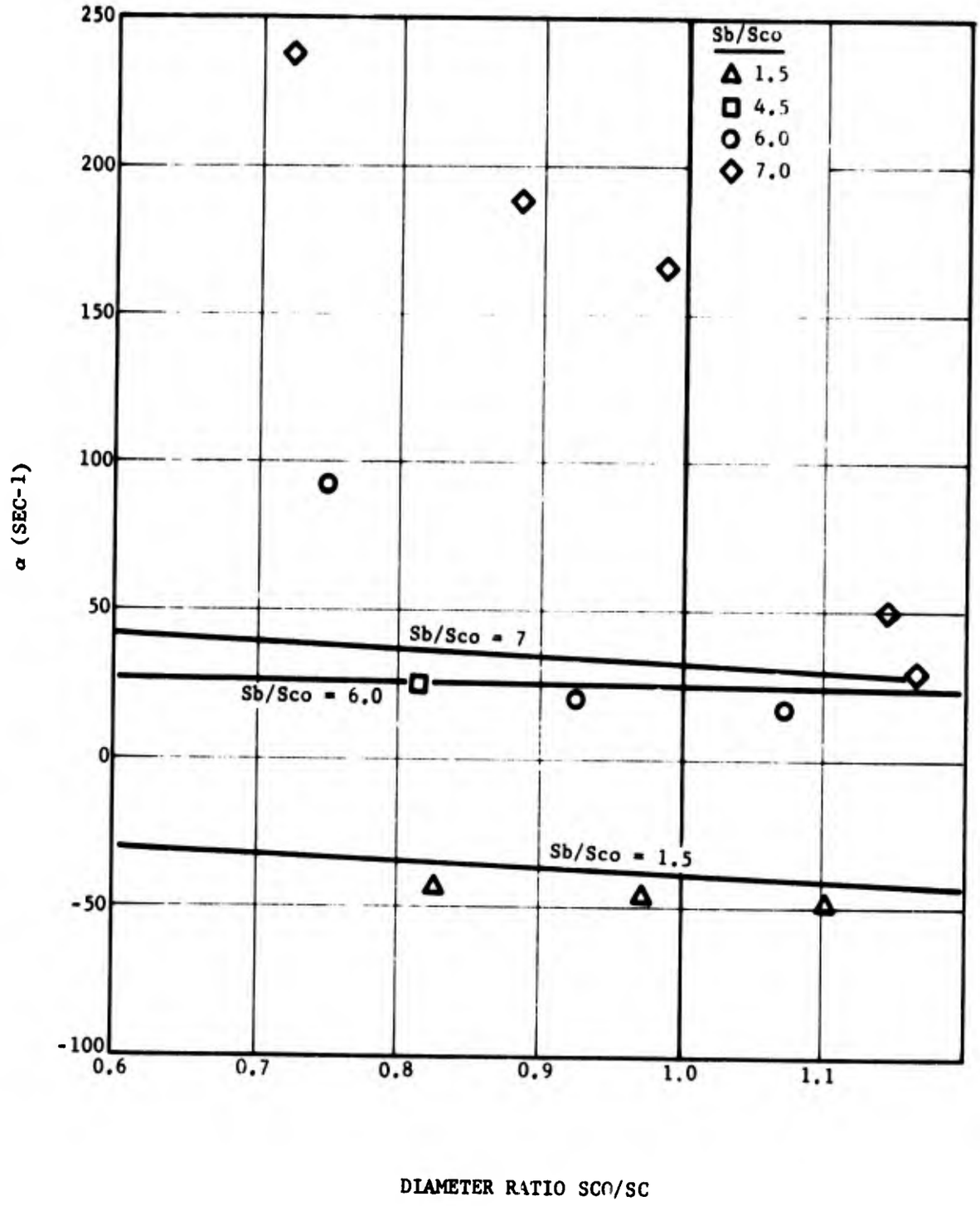

Figure 7-14. CYH 1-14 800 Hz Velocity Coupling α Versus Diameter Ratio with Average Predicted Value Line for VF/VFG = -1/+1

TABLE 7-IV

COMPUTER ANALYSIS OF 800 Hz DATA (CYH)

Case No.	Test Type	B_s	$\alpha_{d\ avg}$	R_{vi}	VF	VFG	B_s + VF	R_{vi} + VF - VFG	Correlation Coefficient
1	All data	3.1	- 96	3.4	-1^x	$+1^x$	2.1	1.4	0.832
2	All data	-1.4	- 93	-2.4	4.1	1.3	2.7	0.4	0.918
3	PC only	4.5	-112	-5^x	-1^x	$+1^x$	3.5	-7.0	0.928
4	PC only	4.1	-105	-3^x	-1^x	$+1^x$	3.1	-5.0	0.927
5	PC only	3.5	- 95	0^x	-1^x	$+1^x$	2.5	-2.0	0.925
6	All data less VC with $\frac{S_{bv}}{S_{co}} > 4.5$	3.3	- 93	1.7	-1^x	$+1^x$	2.3	-0.3	0.931
7	All data	3.3^x	-93^x	1.7^x	-1^x	$+1^x$	2.3	-0.3	0.787

x - Denotes fixed quantity

E. EFFECT OF PROPELLANT FORMULATION

A primary objective of the program was to develop a technique that could differentiate the velocity coupling characteristics of different propellants. Therefore, two test series were fired, one with ANB-3066 a composite propellant and the other with CYH SR-28, a nonoscillatory* lot of CYH propellant.

1. ANB-3066 Propellant

Testing with ANB-3066 was performed at 500 psi and 800 Hz, the standard conditions for extensive testing of this propellant.[65,71,75-77] The pressure-coupled data are shown in Figure 7-15; only four tests were fired at area ratios of 1-1/2 and 6 to verify that the data were consistent with previous ANB-3066 data. The Hercules-generated data from a previous program[71] are superimposed on the current data showing that the propellant used here is the same as that used on the previous program.

Figure 7-16 shows the velocity-coupled data. The same trends observed with CYH 1-14 at 450 Hz are observed with the ANB-3066 (i.e., the data fall on a straight line with a positive slope and α decreases as S_{co}/S_o decreases).

The data analysis is summarized in Table 7-V. The first three cases are those previously performed and reported on the Hercules variable-area T-burner program.[71] Cases 4-6 are the same data reanalyzed with velocity coupling included. It is significant that the sum of B_s + VF varies in the two different approaches. Based on cases 4-6 it is apparent that some of what has previously been considered pressure coupling is really velocity coupling. Cases 4-6 have improved correlation coefficients over cases 1-3 but this is expected because the computer has an extra degree of freedom with R_{vi} as a floating variable.

Cases 7 and 8 show an interesting factor that must be considered in the data analysis. As mentioned above, only four PC tests were run at two area ratios. When these were analyzed in Case 7 with all five variables floating, ridiculous values of the variables were determined. The computer simply had far too many degrees of freedom to fit such few data. In Case 8, where VF, VFG, and R_{vi} were fixed, the degrees of freedom were reduced sufficiently that reasonable results were obtained. Compare this to Case 9 where all the pressure coupled data from this program and the previous are analyzed (corresponding to area ratios of 1-1/2, 5-1/2, 6, and 7). The resulting numbers are much more reasonable even though a VFG of ~ 4 resulted. The conclusion reached here is that it is important to have more data at varying area ratios rather than numerous repetitive tests at few area ratios.

---

*Nonoscillatory as characterized by its performance in the Minuteman II, Stage III motor.

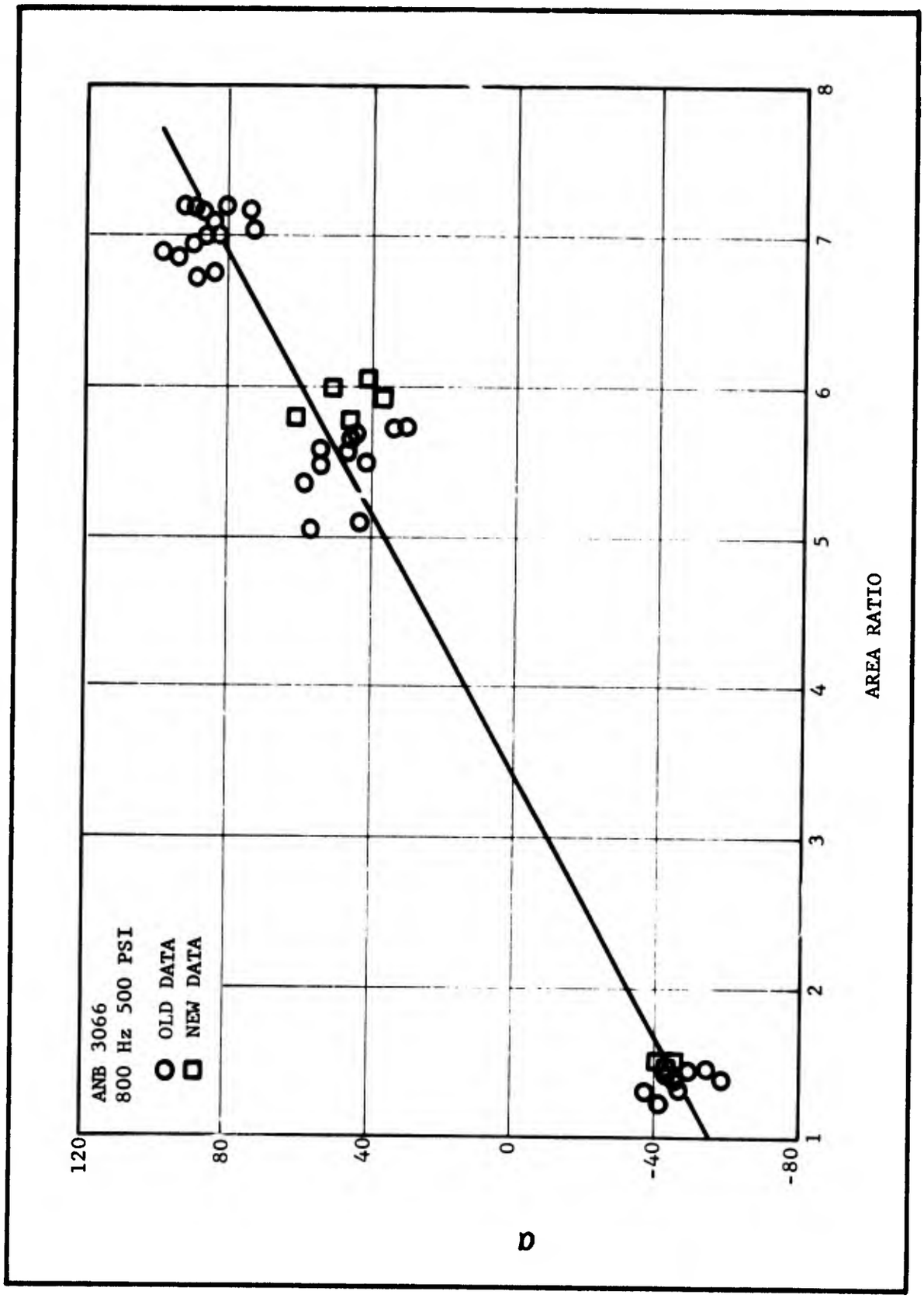

Figure 7-15. Comparison of ANB 3066 for Pressure Coupled Data from Reference 71 and New Test Data

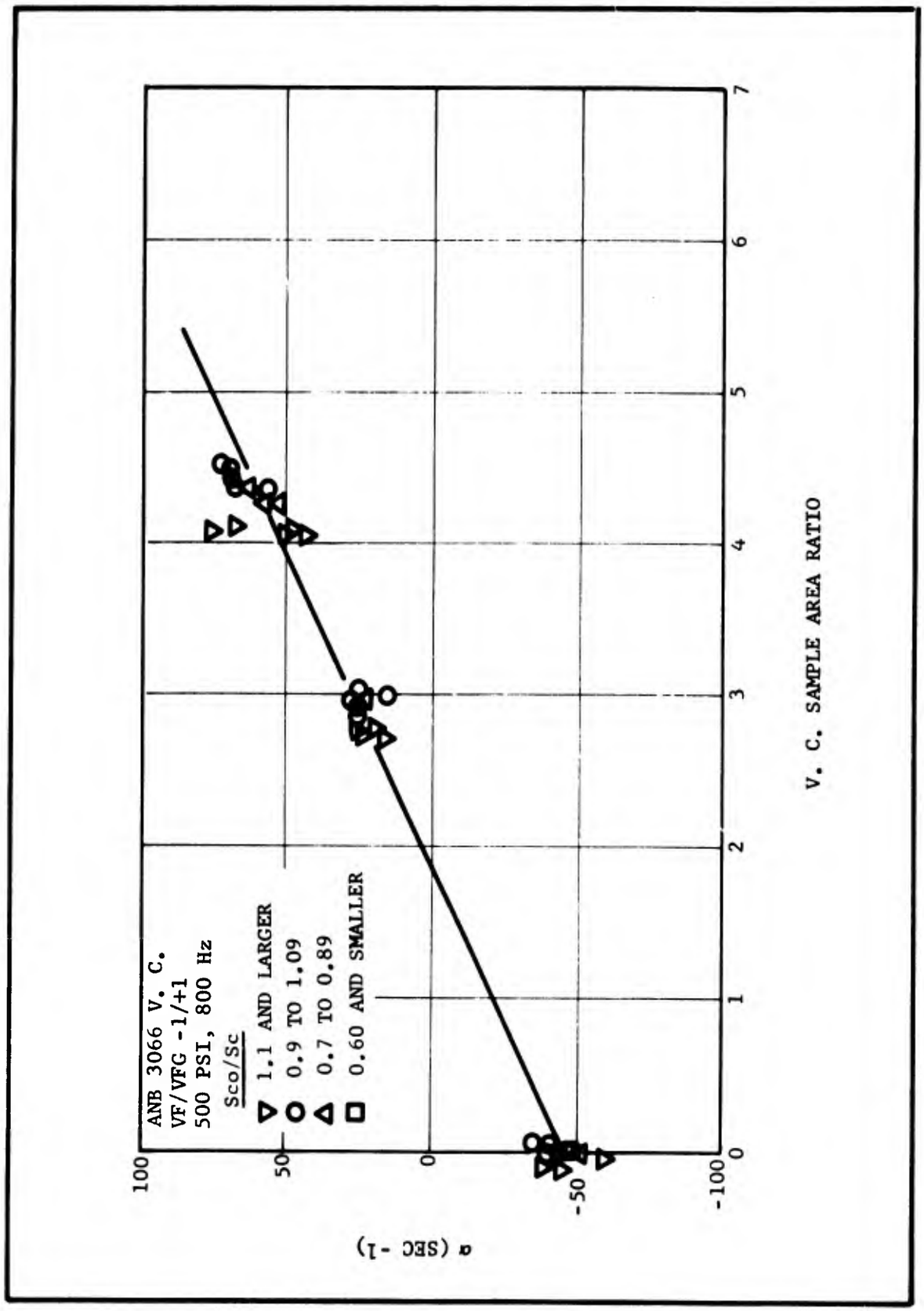

Figure 7-16. Corrected α Versus Area Ratio for ANB 3066 Velocity Coupled Data

TABLE 7-V

COMPUTER ANALYSES OF ANB 3066 DATA

Case No.	Test Type	B_s	α_d avg	R_{vi}	VF	VFG	B_s + VF	R_{vi} + VF - VFG	Correlation Coefficient
1	PC data analyzed in Ref 71	1.2	-75	0^x	$+1^x$	$+1^x$	2.2	0.0	0.965
2	PC data analyzed in Ref 71	2.2	-77	0^x	0^x	0^x	2.2	0.0	0.974
3	PC data analyzed in Ref 71	3.3	-79	0^x	-1	0	2.3	-1	0.979
4	PC Data from Ref (71)	2.3	-71	5.0^x	-1^x	$+1^x$	1.3	3.0	0.988
5	PC Data from Ref (71)	2.4	-68	4.5	-1^x	$+1^x$	1.4	2.5	0.988
6	PC Data from Ref (71)	3.5	-70	5.4	-2.2	1.0	1.2	2.2	0.989
7	PC Data tested during current work	-19	-26	-74.	19.6	-382	0.5	-	0.997
8	PC Data tested during current work	2.1	-69	5^x	-1^x	$+1^x$	1.1	3.0	0.995
9	All PC Data	2.9	-68	7.2	-1.9	4.2	1.0	1.2	0.988
10	All PC + VC Data	2.4	-70	5.0	-1.1	0.8	1.3	3.3	0.985
11	All PC + VC Data	2.2	-70	5.4	-1^x	$+1^x$	1.2	3.4	0.985

x - Denotes fixed quantity

It is significant to note that when the data from the two different programs were analyzed in the same way with VF, VFG, and R_{vi} fixed (Cases 4 and 8), the resultant values of B_s and α_d were the same.

Cases 10 and 11 are the results of analyzing all the pressure-coupled and velocity-coupled data together. Case 11 is the -1/+1 standard case while in Case 10 all the variables were floated. The results are almost the same. It should be noted again that the sum of B_s + VF and R_{vi} + VF - VFG are constants even though R_{vi} and B_s vary slightly between the two cases. Also, no tests were performed to verify the values of VF and VFG for these test conditions. It is assumed that VF and VFG should be constants, but this has not been verified. Assuming that VF-VFG = -3 holds for the current test conditions then B_s and R_{vi} can be inferred to be ~ 2.5 and ~ 6.5. For ANB-3066 R_{vi} is only about half that for CYH at 450 Hz.

The objective of this test series was to see if the VCTB technique could differentiate between different classes of propellants. The data indicate that there is a definite difference between the two propellants, R_{vi} differing by a factor of 2.

2. CYH SR-28 Propellant

A test series was performed with CYH-SR-28 propellant to determine if the VCTB technique could differentiate between oscillatory and nonoscillatory lots of CYH propellant. In the Minuteman II Stage III motor the oscillatory lots of propellant (lot 1-9 and upward) exhibit a high amplitude pressure oscillation at 550 Hz while earlier nonoscillatory lots (lot 1-8 and previous) were essentially stable. The chemical composition of the propellant did not vary outside of specification. Tests run with pressure-coupled T-burners (e.g., Ref 73) and other laboratory devices have shown some difference between the two categories of propellant. Window bomb movies show a rather extensive filigree structure to the oscillatory propellant lots, with the nonoscillatory lots burning significantly different.

Pressure-coupled data were obtained previously for SR-28[71] and are compared to the 1-14 data in Figure 7-17. The difference is statistically significant but small. The velocity-coupled data are shown in Figure 7-18. The difference between oscillatory and nonoscillatory propellant is dramatic. For example, at a test sample area ratio of 4-1/2, the oscillatory propellant oscillates so hard that it is difficult to make a quantitative measurement ($\alpha \geq 175$ sec^{-1}). At the same conditions, the nonoscillatory propellant oscillates weakly and only late in the firing. To be absolutely sure that something in the test procedures had not changed which would affect the results, three tests were fired in succession using identical hardware and procedures. These tests are No. 883, 884, and 885, listed in Appendix A. All were at 300 psi, 450 Hz, driver area ratio of 1-1/2, and test sample area ratio of 4-1/2. Tests 883 and 885 were with lot SR-28 and test 884 was with Lot 1-14. The lot 1-14 propellant oscillated before the paddle was

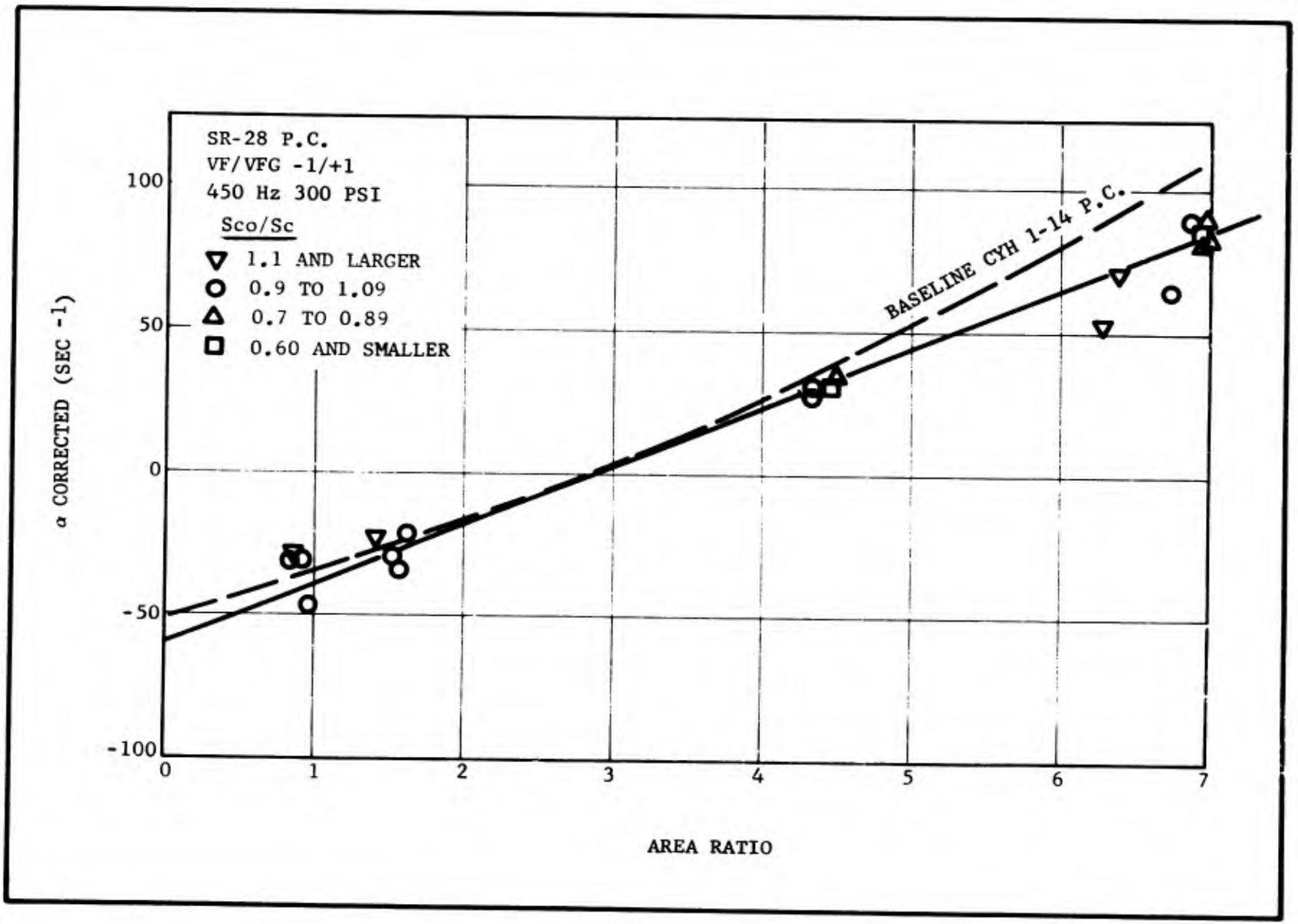

Figure 7-17. SR-28 Pressure Coupled Corrected α Versus Area Ratio with Comparison Line from Baseline 1-14

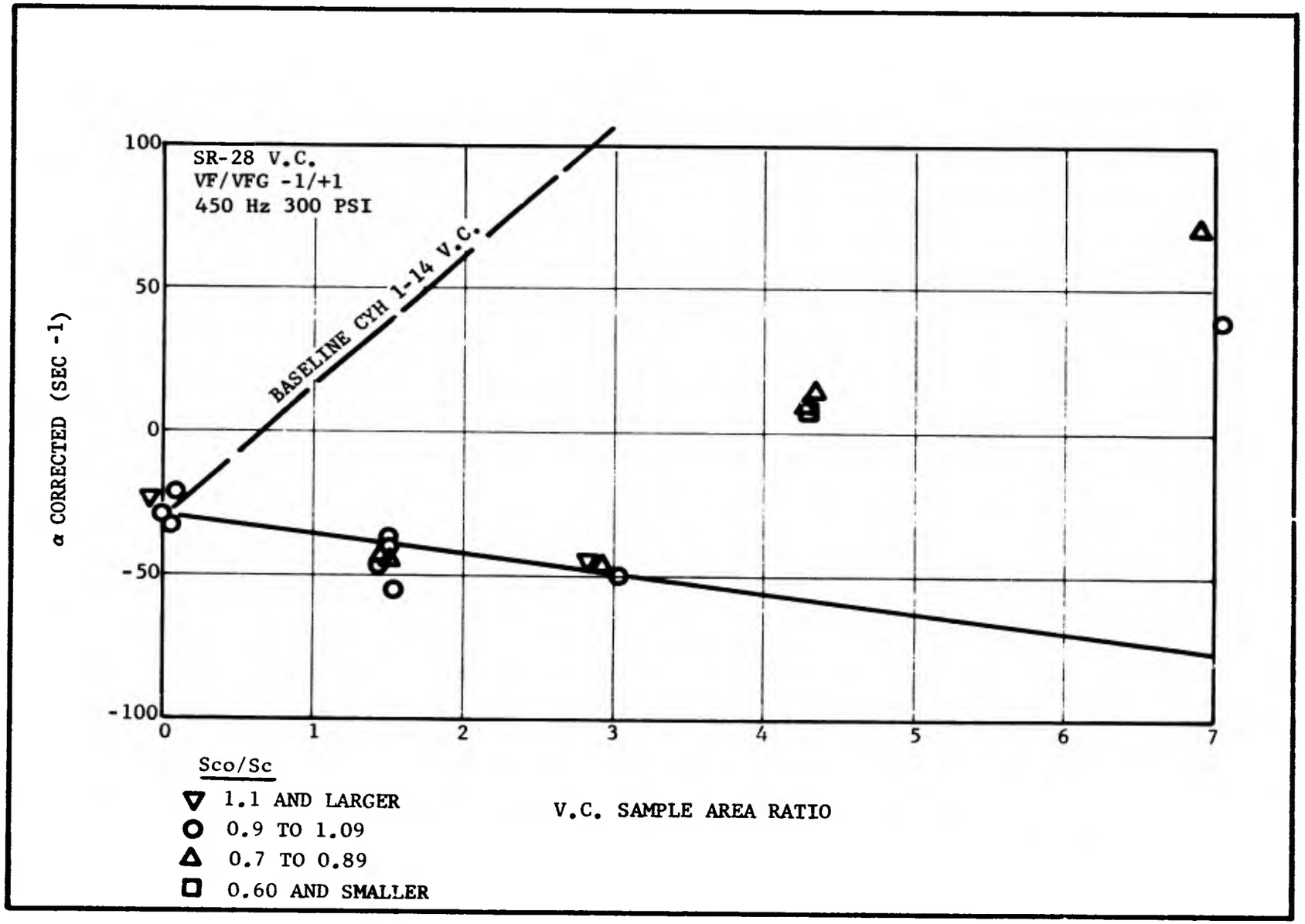

Figure 7-18. SR-28 Velocity Coupled Corrected α Versus Area Ratio with Comparison Line from Baseline 1-14 Velocity Coupled Data

withdrawn on the first two paddle pulls indicating an $\alpha \geq 150$, while the nonoscillatory propellant did not even oscillate. On the third paddle pull, lot 1-14 had an α of 109, lot SR-28 had α values of 23 and 25. The general result is that the propellants are conclusively different.

Figure 7-19 shows the data as a function of diameter ratio. The trend is the same as for the 800 Hz data; increasing α with decreasing diameter ratio, which is the opposite of the standard 1-14 data.

The data were sufficiently different that a quantitative analysis of the data was not totally successful. The computer runs are summarized in Table 7-VI. The data from Reference 71 are included as the first three cases. Cases 4 through 10 represent various attempts to fit the data (particularly to fit the trend of α with S_{co}/S_c). None were really successful. In Case 11 the tests with $S_{bv}/S_{co} > 3$ were excluded, and only the pulsed data were included. A very good fit of the data resulted ($cc \sim 0.99$) and a value of $R_{vi} \sim -2$ was obtained. However, the predicted trend with diameter ratio is not sufficient to give good agreement with the larger area ratio test points when they are added to the data set (see Case 12).

As with the 800 Hz data, it is apparent that the theory is not fully adequate to describe the results obtained.

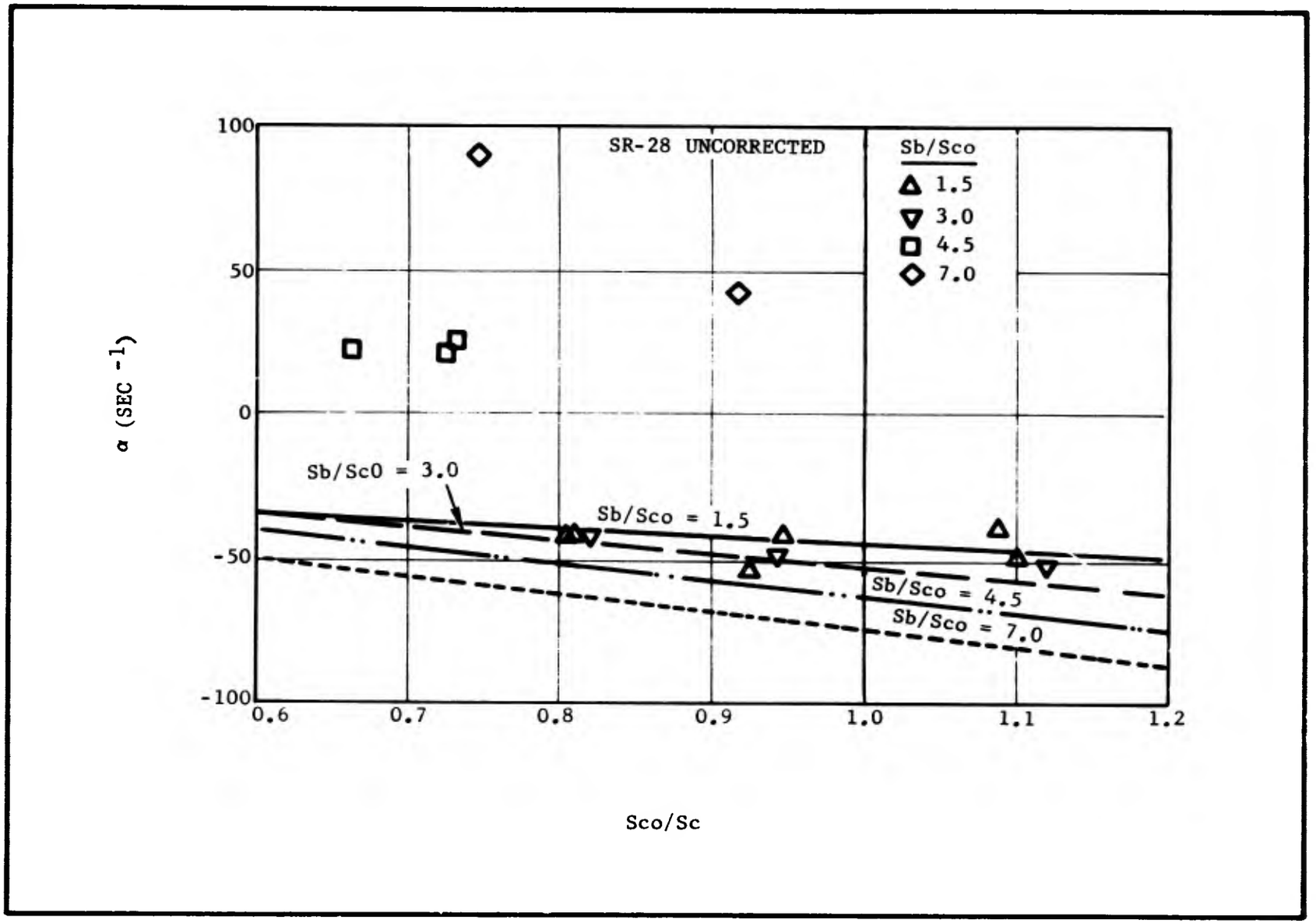

Figure 7-19. SR-28 α Versus Diameter Ratio with Predicted Line for VF/VFG = -1/+1

TABLE 7-VI

COMPUTER ANALYSIS OF SR-28 DATA

Case No.	Test Type	s	α_d avg	R_{vi}	VF	VFG	B_s + VF	R_{vi} + VF - VFG	Correlation Coefficient
1	PC only from Ref 71	1.4	-54	0^x	$+1^x$	$+1^x$	1.4	0	0.988
2	PC only from Ref 71	2.5	-56	0^x	0^x	0^x	2.5	0	0.986
3	PC only from Ref 71	3.6	-58	0^x	-1^x	0^x	2.6	-1	0.984
4	All data	3.0^x	-52^x	1.8	-1^x	1.5	2.0	-0.7	0.903
5	All data	2.0^x	-52^x	1.5	0^x	2.5	2.0	-1.0	0.915
6	All data	1.0^x	-52^x	1.3	$+1^x$	3.4	2.0	-1.1	0.925
7	All data	4.0^x	-52^x	2.1	-2^x	0.6	2.0	-0.5	0.891
8	All data	-2.5	-52^x	4.6	4.1	10.5	1.7	-1.8	0.952
9	All data	-4.2	-52^x	-5^x	6.5	4.0	2.3	-2.5	0.939
10	All data	3.2	-70	2.4	-1^x	$+1^x$	2.2	-0.4	0.935
11	All data less VC with $\frac{S_{bv}}{S_{co}} > 3.0$	3.4	-60	-2.3	-1^x	$+1^x$	2.4	-4.3	0.990
12	All data	3.4^x	-60^x	-2.3^x	-1^x	$+1^x$	2.4	-4.3	0.855

x - Denotes fixed quantity

F. END-VENTED TEST RESULTS

One test series of the final test matrix was to employ the end-vented burner to see if consistent data were obtained relative to the VCTB technique. Considerable difficulty was experienced with the original end-vented screening tests due to faulty ignition, etc. (See Section VI.D.) Therefore, the final end-vented test series was fired into the prepressurized surge tank system used for T-burner tests. In this manner the ignition problem was circumvented. A series of 10 tests were fired with varying symmetrical and nonsymmetrical configurations. All tests were at standard test conditions (CYH 1-14, 300 psi and 450 Hz). The data from the tests are tabulated in Appendix A.

Tests were fired in the end-vented burner with the propellant located symmetrically as in the VCTB. The results are plotted in Figure 7-20, with the data from the VCTB tests included for comparison. The basic differences between the two tests are that in the end-vented configuration, velocity coupling is eliminated due to symmetry; there is no "vent term" because the mean flow does not turn at the acoustic velocity antinode; and losses are introduced due to the end vent (i.e., nozzle losses). Equation (7-2) describing the VCTB can be modified to describe the end-vented burner, recognizing that $P_{\ell} \rightarrow 0$ and $C_{\ell}^2 \rightarrow 0$.

$$\alpha^o = 4f\bar{M}_b \left\{ \frac{S_{bl}}{S_{co}} \left(B_s C_{\ell_i} - \frac{VFG}{2} g_{\ell_i}\right) + \frac{S_{bv}}{S_{co}} \left(B_s C_{\ell_v} - VFG \frac{g_{\ell_v}}{2}\right) \right\}$$

$$- \alpha_d - \alpha_{NOZ} \left(S_b/S_{co}\right) \qquad (7\text{-}8)$$

where α_{NOZ} represents the losses due to the end vent and is some function of the mean velocity (i.e., the propellant area ratio). For the same assumptions that led to Equations (7-3) and (7-4), Equation (7-8) can be written as

$$\alpha^o = 4f\bar{M}_b \left[\frac{S_{bl}}{S_{co}} B_s + \frac{\frac{S_{bv}}{S_{co}}}{2} (B_s - VFG) \right] - \alpha_d - \alpha_{NOZ} \qquad (7\text{-}9)$$

The slope of an α versus area ratio plot is

$$\alpha^{o'} = 2f\bar{M}_b (B_s - VFG) - \frac{d\,\alpha_{NOZ}}{d(S_b/S_{co})_v} \qquad (7\text{-}10)$$

Calculating nozzle damping by

$$\alpha_{NOZ} = 0.65 \frac{aJ}{L} \qquad (7\text{-}11)$$

Values of α_{NOZ} of 23 and 48 sec^{-1} are calculated for the two sets of data in Figure 7-20, and the rate of change of α_{NOZ} is ~ -8. The slope of the data is approximately -17. Therefore,

$$2f\bar{M}_b (B_s - VFG) \sim -9 \qquad (7\text{-}12)$$

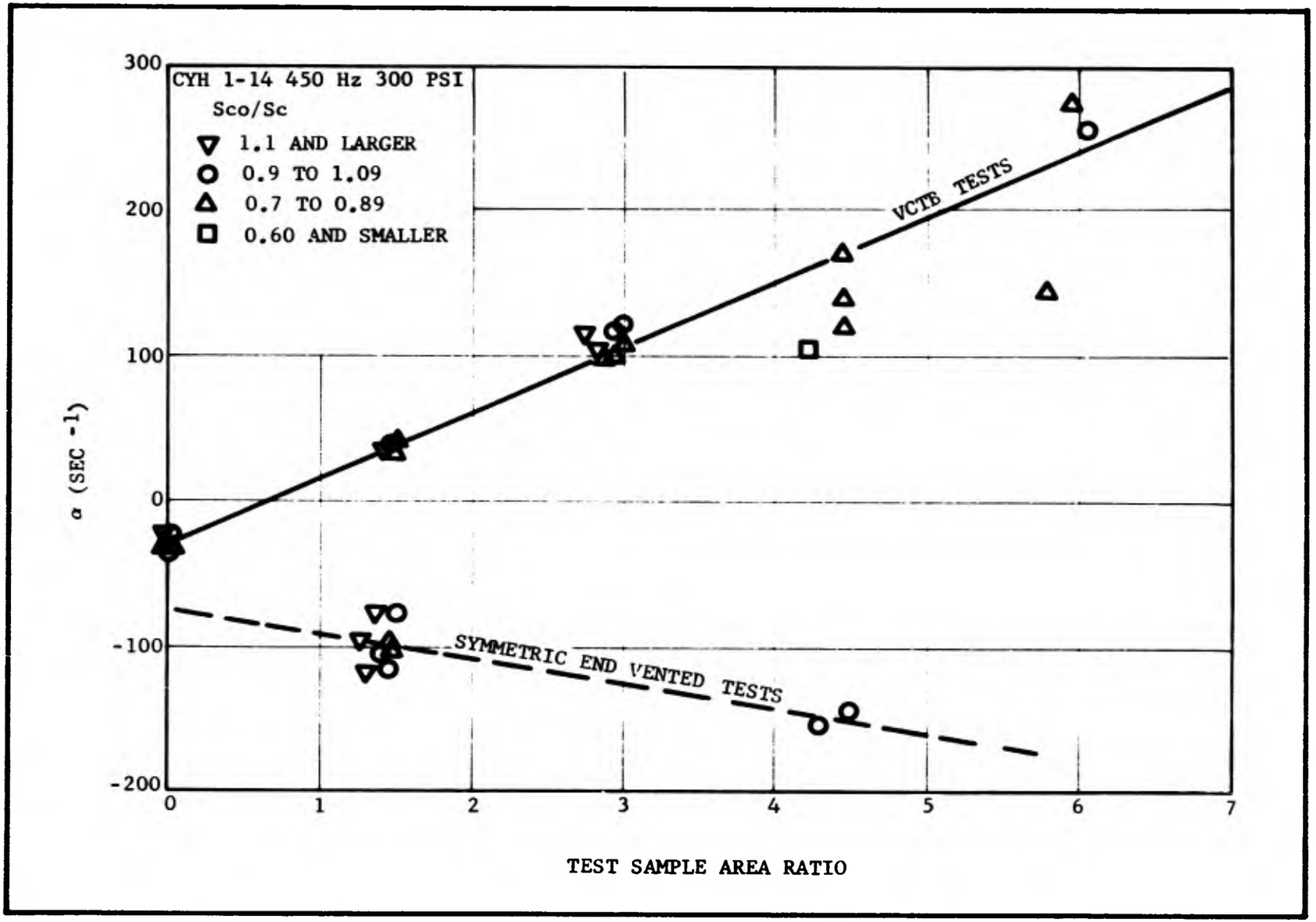

Figure 7-20. Comparison of Standard VCTB Tests to Symmetric End Vented Tests

For VFG of 0, +1 and +2, B_s would be 2.25, 1.25 and 0.25, respectively. The VCTB data indicated that values of $B_s \sim 2.5$ and VFG ~ 2 were optimum. Thus, there appears to be a discrepancy.

A second way of evaluating the data is to take the difference of the VCTB data and the end-vent data. Subtracting Equation (7-9) from (7-4) yields

$$\alpha_{VCTB} - \alpha_{EV} = 4f\bar{M}_b \; VF \; \frac{S_{bl}}{S_{co}} + 2f\bar{M}_b \; (R_{vi} + 2VF) \; \frac{S_{bv}}{S_{co}} + \alpha_{NOZ} \qquad (7\text{-}13)$$

At zero test sample area ratio, the observed α is 40 sec^{-1}. Equation (7-13) becomes

$$(\alpha_{VCTB} - \alpha_{EV}) = 4fM_b \; VF \; \frac{S_{bl}}{S_{co}} + \alpha_{NOZ} = 40 \qquad (7\text{-}14)$$

For the given test conditions and VF = 0, -1, or -2, α_{NOZ} should be 40, 54, or 67. The calculated nozzle damping is $\sim$23 or less which would give a value of VF > 0, which is inconsistent with the VCTB results. Equations (7-13) and (7-14) can be combined to give

$$\alpha_{VCTB} - \alpha_{EV} = 40 + \frac{\Delta \alpha_{NOZ}}{\Delta \frac{S_{bl}}{S_{co}}} + 2 \; f\bar{M}_b \; (R_{vi} + 2VF) \; \frac{S_{bv}}{S_{co}} \qquad (7\text{-}15)$$

At an area ratio of 1-1/2, $\alpha_{VCTB} - \alpha_{EV} \sim 140$; solving for $R_{vi} + 2VF$ yields

$$(R_{vi} + 2VF)1.5 \sim 15$$

At an area ratio of 4-1/2, $\alpha_{VCTB} - \alpha_{EV} \sim 325$, therefore

$$(R_{vi} + 2VF)4.5 \sim 13$$

For values of VF ≤ 0, $R_{vi} \geq 13$. Although the agreement between these data and the VCTB data alone is not quantitative, it is apparent that R_{vi} $\sim$ 10-15 which is in general agreement with the VCTB data.

Six tests were fired in the end-vented burner with propellant located nonsymmetrically in order to evaluate R_{vi} strictly from the end vent tests. During the phenomenological study (Section V) it was observed that using unequal amounts of propellant in a T-burner caused the mode shape to be significantly different from a simple cosine. This effect is not accounted for theoretically and, therefore, it was anticipated that quantitative interpretation of the data would not be possible with the nonsymmetric tests. The data are shown in Figure 7-21, and the raw data are tabulated in Appendix A. In these firings a single driver sample (S_b/S_{co} = 1-1/2) was used in the head end of the burner, and a test sample was located either a

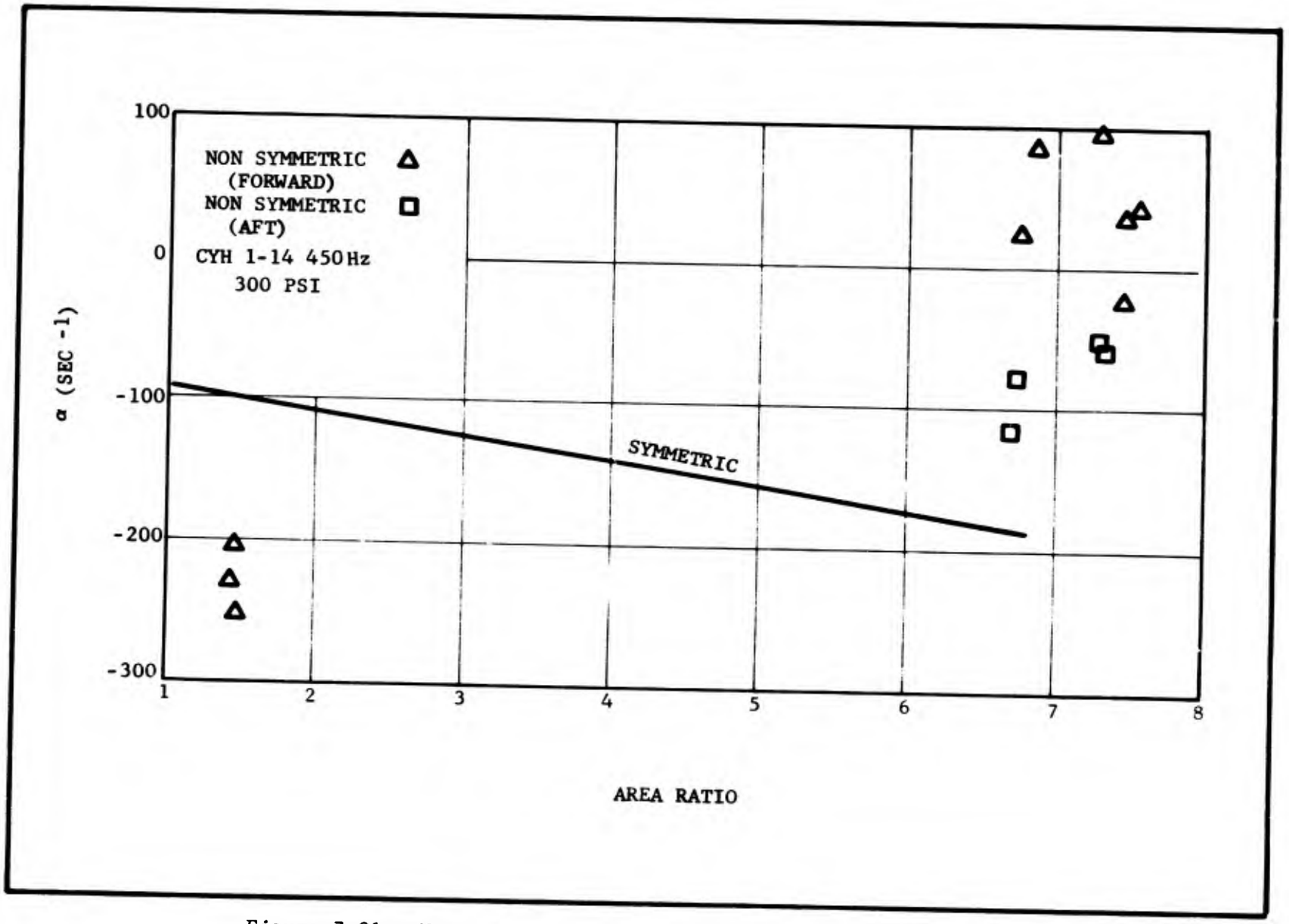

Figure 7-21. Nonsymmetric Forward and Aft Data as Compared to Average Symmetric Data

quarter length from the head end (nonsymmetrical forward) or a quarter length from the aft end (nonsymmetrical aft). The difference between the forward and aft tests should be directly proportional to R_{vi}. Because the forward tests gave a higher value of α than the aft test, R_{vi} must be greater than zero. However, the magnitude of R_{vi} calculated from the average difference of the two data sets is on the order of 3 which is much smaller than obtained from the VCTB. However considering the data scatter and the uncertainty in the actual acoustic mode shape, the agreement can be considered qualitatively correct.

A factor which tends to cast further doubt in the end vent data is the large disagreement between the nonsymmetric and symmetric tests at an area ratio of 1-1/2. Based on the VCTB data a difference of ~ 35 to 50 sec^{-1} should have been observed, while the actual value is ~ 125 sec^{-1} (which infers an $R_{vi} \sim 30$). There are two possible sources of error leading to this discrepancy. The first is the uncertainty in the mode shape and the applicability of the equations for a nonsymmetric burner. The second is related to measuring a correct value of α for a pulse test with large inherent nonlinearities. Based on the discussion in the following paragraph, the nonlinear coefficient, G is on the order of -15. Assuming an α of -100 sec^{-1}, Table 7-VII was constructed to show the errors that can be introduced in highly nonlinear pulse data.

TABLE 7-VII

ERRORS INTRODUCED IN PULSE DATA INTERPRETATION DUE TO NONLINEARITIES

Pressure Amplitude (0 to pk psi)	0	1	5	10
(sec^{-1})	-100	-100	-100	-100
Nonlinear contribution (sec^{-1})	0	- 15	- 75	-150
Observed rate of decay	-100	-115	-175	-250
Error due to nonlinearity	0	13%	43%	60%

For a 5 psi pulse and a measured α of -175, the actual linear α is -100, causing a very significant error in interpretation of such data. With the inherent scatter in the end vent data (due to high harmonic content) it was not possible to eliminate the nonlinear effects by reducing the data using techniques available to account for the nonlinear terms.

Although the end-vented burner appears attractive as a technique for evaluating velocity coupling, the results obtained were less than satisfactory. The basic data are much more noisy than typical T-burner data, and considerable harmonic content is apparent in the pulsed tests. Because of nonlinearities, the uncertainty in the measured value of α is excessive.

Uncertainty is also introduced via the calculation of acoustic losses due to the end vent. To determine velocity coupling in the end-vented configuration, a nonsymmetric propellant arrangement must be used which at present cannot be properly described theoretically. Further work (both experimental and theoretical) would be required to develop the capability to describe the nonsymmetry. Therefore, the end-vented burner is not recommended as a standard tool for future use unless the appropriate development of theory and experiment is performed. Even then it does not appear to be as practical as the VCTB.

G. NONLINEAR INTERPRETATION OF DATA

Nonlinear interpretation of the data obtained on this program is based on previously published work on analysis of nonlinear effects.[78, 79, 80] The expression for the envelope of acoustic oscillatory pressure is

$$\frac{\dot{R}}{R} = \alpha + GR + PR^2 \qquad (7\text{-}16)$$

where R is the oscillatory pressure amplitude, α is the linear coefficient of the pressure amplitude (i.e., the growth constant normally measured in a T-burner), G is the second order (or quadratic) coefficient, and P is the third order (or cubic) term. At the limiting amplitude, the derivative, $\dot{R}$, becomes zero, and Equation (7-16) can be rearranged to give

$$\frac{\alpha}{R_\infty} = -(G + P R_\infty) \qquad (7\text{-}17)$$

Therefore, the linear growth constant divided by the limiting pressure amplitude is a measure of the nonlinearities of the system. It should be noted that Equation (7-17) does not apply to a negative α or a decay constant because the value of $\dot{R}$ does not reach zero at a finite limiting amplitude.

Normalizing Equation (7-17) leads to a nondimensional parameter that has been used successfully in correlating instability data

$$\pi = \frac{\alpha}{R_\infty} \frac{\bar{P}}{f} \qquad (7\text{-}18)$$

Visualization of the nonlinearities of a system can be obtained by plotting α versus limiting amplitude. The slope of such a plot will be proportional to the π parameter. Figures 7-22 and 7-23 show both pressure-coupled and velocity-coupled data for CYH lot 1-14 and ANB-3066. The value of π for the velocity-coupled data is ~ 10 while for the pressure-coupled data it is ~ 1. This infers that the nonlinearities related to velocity coupling are an order of magnitude larger than pressure-coupled nonlinearities.

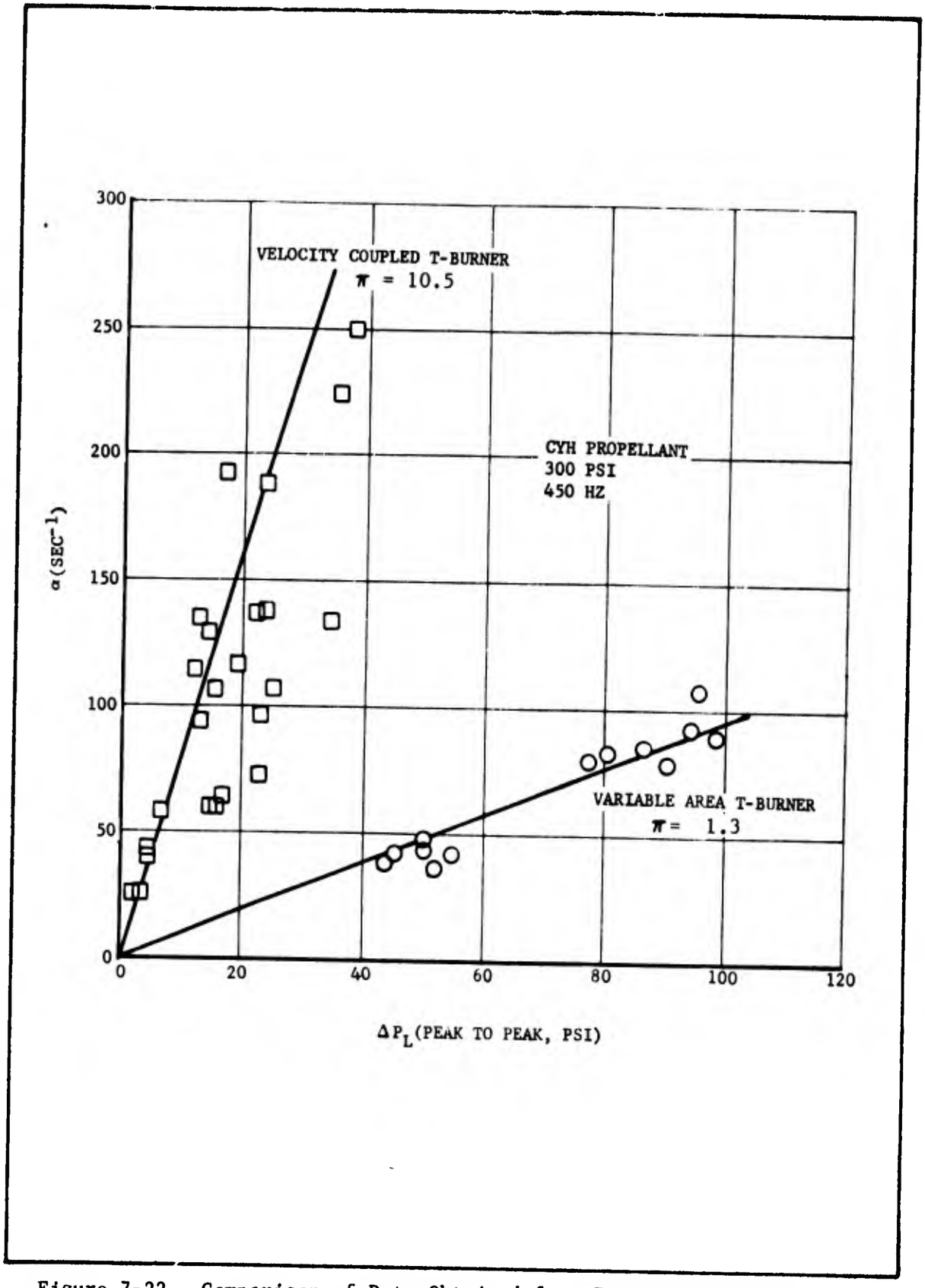

Figure 7-22. Comparison of Data Obtained from Pressure-Coupled and Velocity-Coupled T-Burner

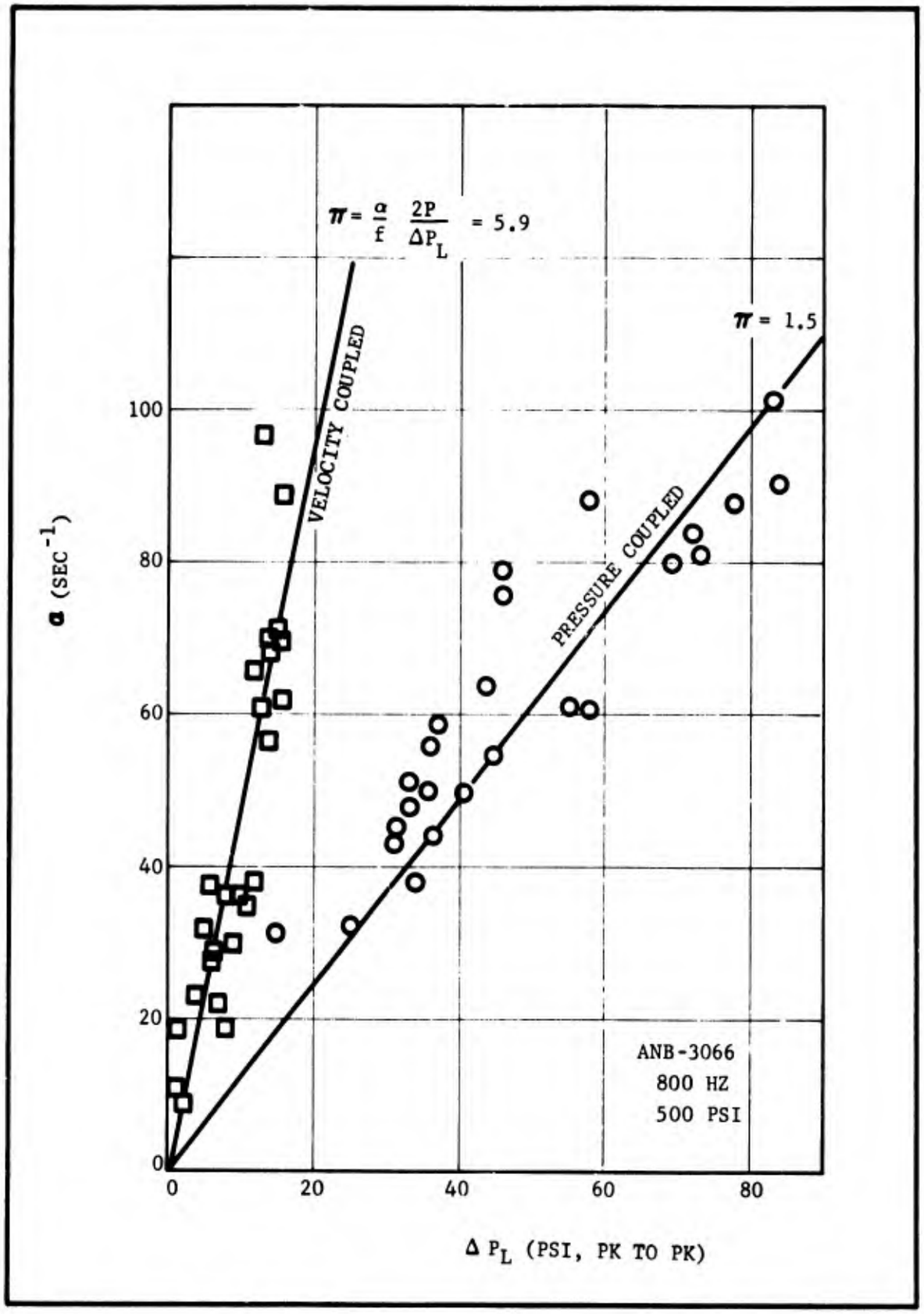

Figure 7-23. Plot of α Versus Limiting Amplitude to Evaluate the System Nonlinearities

An attempt was made to determine the G and P nonlinear parameters directly from oscillatory amplitude versus time data as described in Reference 78. However, typical firings reached a limiting amplitude so rapidly that there were insufficient data to perform the nonlinear data reduction. Based on Equation (7-17) it can be inferred that G is on the order of -15 for the CYH data and on the order of -5 for the ANB-3066 data. These compare to a G of ~-2 for ANB-3066 pressure coupled data[71].

H. FLOW REVERSAL

The effects of flow reversal have been explored to determine if the method of measuring the growth rate, α, should be modified or if effects of flow reversal can be seen in the data. Calculations were made to determine the flow reversal conditions in the T-burner for various values of S_b/S_{co}.

The flow reversal calculations were based on the following assumptions:

(1) Flow reversal occurs when the acoustic velocity U' exceeds the mean flow velocity $\bar{U}_g$. The onset of flow reversal is when $U' = \bar{U}_g$.

(2) The mean flow velocity $\bar{U}_g$ increases linearly over the propellant surface.

(3) There is no decrease in $\bar{U}_g$ as the gas travels through the burner*.

(4) U' has a sinusoidal distribution with no mode shape disturbance.

(5) Flush conditions were assumed, eliminating the influence of either a positive or negative lip, possible mode shape disturbances, and localized decelerations or accelerations due to changing volume.

Figure 7-24 shows the calculated mean flow and acoustic velocity profiles of the T-burner for CYH 1-14 propellant at 450 Hz, 300 psi, and a driver area ratio of 1-1/2. The solid lines in the figures represent the mean flow for different area ratios, while the dashed lines are for various acoustic pressure amplitudes (0 to peak). The final limiting amplitude, P_L, from the data is also indicated for each area ratio.

*Actually $\bar{U}_g$ will decrease as the temperature decreases due to heat losses along the T-burner length.

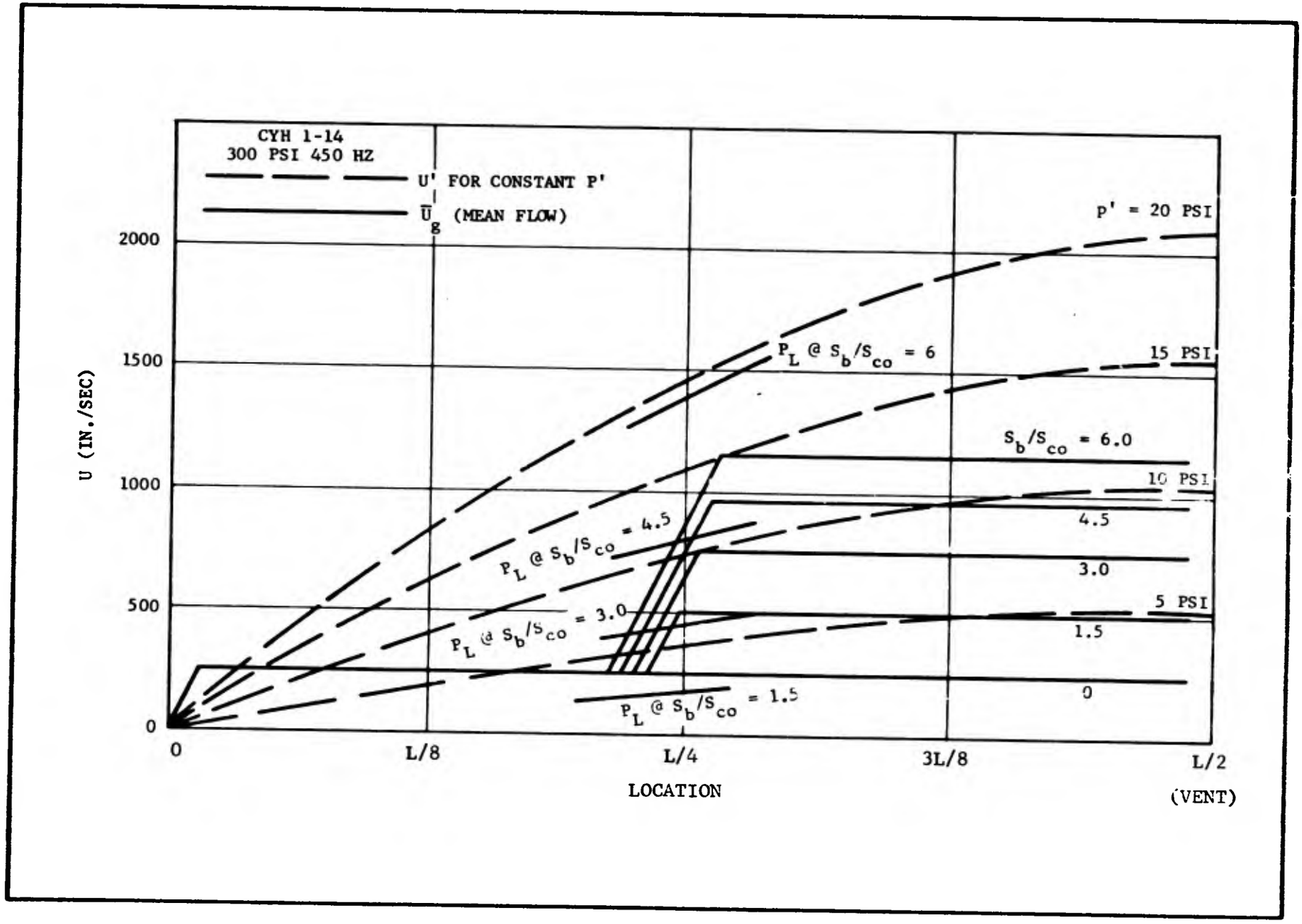

Figure 7-24. Flow Reversal Conditions for the VCTB. Experimentally Determined Limiting Amplitudes are Included for Area Ratios Tested

An initial observation is concerned with the limiting amplitude versus area ratio and the amount of the propellant sample subject to flow reversal. The amount of the sample subject to flow reversal decreases with decreasing area ratio. For an area ratio of 1-1/2, none of the test sample experiences flow reversal at limiting amplitude. Samples at area ratio of 3 and 4.5 are partially into the flow reversal regime before limiting amplitude is reached while at an area ratio of 6 the entire sample is in the flow reversal regime. An important correlation can also be seen which indicates that the greater the acoustic velocity (i.e., the sooner the condition of flow reversal is reached) the greater the data scatter.

A correlation between the onset of flow reversal and the end of the linear portion of the growth is also apparent where large flow reversal velocities are present. Figure 7-25 shows plots of ln P versus time for three growths at different area ratios. It can be seen that the onset of flow reversal corresponds very closely to the end of the linear growth for the two largest area ratio tests. For the area ratio 3.0 test, limiting amplitude was only slightly higher than that required for flow reversal and the linear growth was apparently terminated by some other nonlinear mechanism. This behavior corresponds to a much smaller data scatter than conditions where flow reversal occurs at low amplitudes. For example, pressure-coupled data result in less data scatter than velocity-coupled data. This may be linked to problems caused by flow reversal which are not experienced to the same degree by a pressure-coupled sample as by velocity-coupled samples. The conclusion is that increasing flow reversal causes erratic behavior. This would indicate that the greatest confidence should be placed in data where the test sample undergoes the least amount of flow reversal.

From the above analysis, the following conclusions can be made:

(1) By exercising caution, linear growth rate measurements can be obtained before the onset of flow reversal.

(2) The greater the acoustic velocity exceeds flow reversal, the greater the tendency for data scatter.

(3) The onset of flow reversal appears as an important factor in amplitude limiting for test area ratios where flow reversal occurs over 80 percent or more of the sample.

I. HARMONIC CONTENT

Velocity coupling is often associated with nonlinear wave form and generation of higher order harmonic modes.[4] However, it must be recognized that the wave form distortion comes about principally due to flow reversal effects. When the acoustic velocity exceeds the mean flow velocity (i.e., flow reversal), a rectification-type process occurs due to the fact that burning propellant responds to the magnitude of velocity, not the direction. To quote from Hart, et. al..."whenever flow reversal occurs,

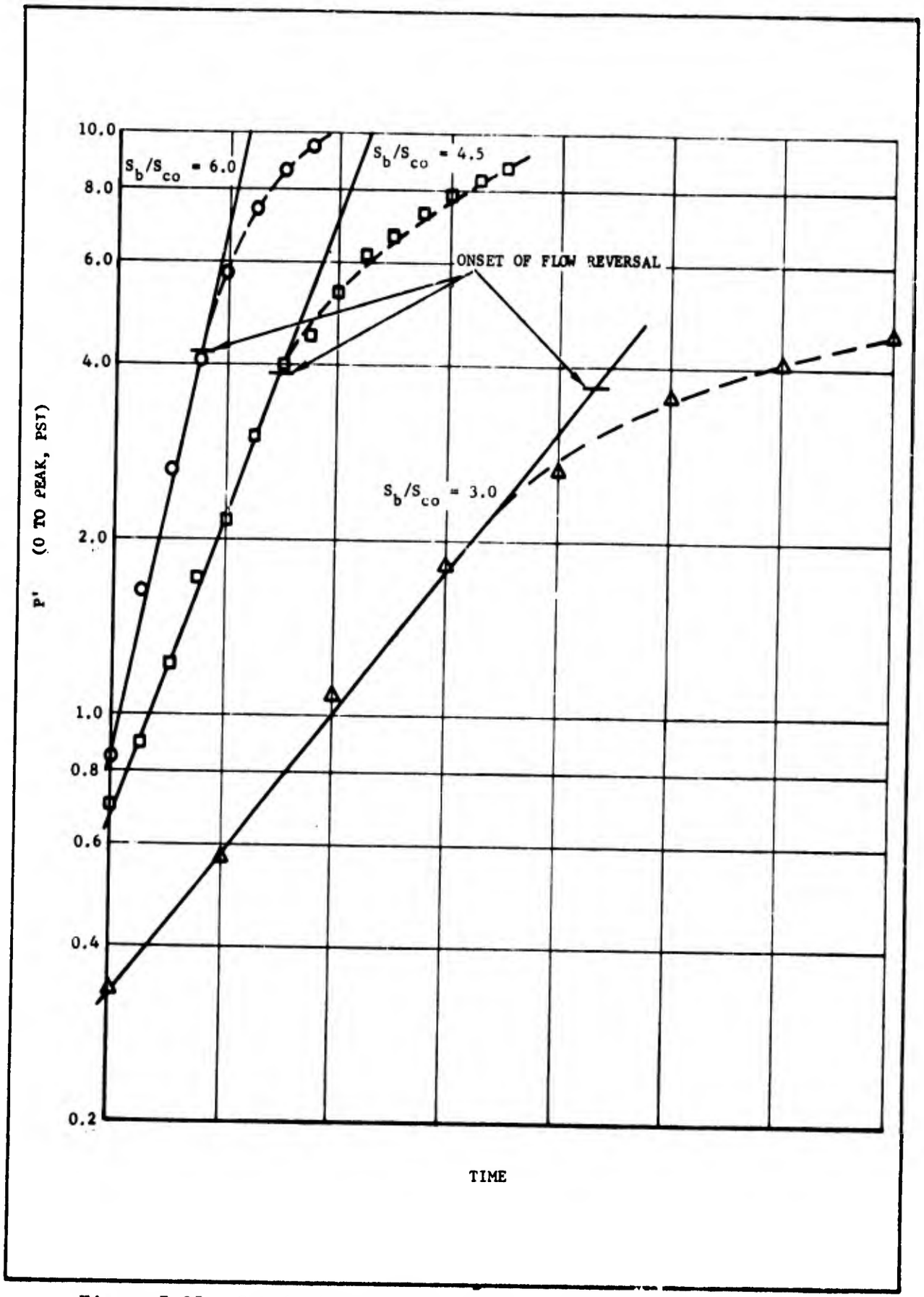

Figure 7-25. Standard VCTB Data Showing Onset of Flow Reversal Relative to the Termination of the Linear Growth Rate Regime

erosive response of propellants will lead to the generation of harmonics." Therefore, in analyzing nonlinear mechanisms that lead to amplitude limiting, nonlinear wave forms and harmonic coupling are very important. For linear analysis (the normal determination of growth rate and response function in the VCTB), harmonic coupling appears to be of secondary importance because growth rates are measured at amplitudes below where flow reversal occurs.

It was also very apparent that the wave form generated by the VCTB was very sinusoidal with minimal harmonic content. Data were obtained through Quantech analysis for the first five modes of the T-burner and are tabulated in Table 7-VIII. The data are recorded as a percentage of first mode amplitude. It is very evident that the relative magnitudes of higher modes are approximately the same for pressure-coupled tests as for velocity-coupled tests (comparing corresponding area ratios). Actually the second mode amplitude is lower in the VCTB than for the pressure coupled T-burner. This is probably true because the test sample is located at a pressure nodal point in the VCTB. It should be noted that the actual limiting amplitude did change drastically, from values ~100 psi for pressure coupling down to values ~ 25 psi. Although the limiting amplitude changed a factor of 4, the change in relative magnitudes of the harmonics were small. Based on these experimental data, the conclusions reached were:

(1) Harmonic coupling does not influence linear growth rate measurements.

(2) The limiting mechanism in the VCTB appears to be of such a nature that the amplitude limits while the harmonic content is very small.

TABLE 7-VIII

RELATIVE AMPLITUDE OF HARMONIC MODES IN T-BURNER AND VCTB

Type of Test	Area Ratios	Test Number	Percent Amplitude Relative to 1st Mode		
			2nd Mode	3rd Mode	4th Mode
Pressure Coupled Tests	4-1/2	(683)	10/14/9*	5/4/3	~ 1/2
	6	(682)	18/21/16	13/12/8	1.5/2/1
Velocity Coupled Tests	1-1/2	(732)	3/1	0	0
	3	(731)	5/4/5	8/12/10	~ 1/2
	4-1/2	(730)	5/6/6	12/14/7	~ 1/2
		(729)	5/7/7	13/11/8	~ 1/2
	6	(728)	7/10/8	14/12/8	~ 1/2

*The data are ordered as 1st/2nd/3rd paddle pull. Thus each paddle pull represents a larger negative lip.

Note: Quantech analyses were performed for 5th mode but there was not any discernable signal (no 5th mode).

SECTION VIII

CONCLUSIONS AND RECOMMENDATIONS

A. CONCLUSIONS

The principal objective of this program was to evaluate various methods for measuring the velocity-coupled response of solid propellants and to select the most appropriate method for future development. Based on the program results, the velocity-coupled T-burner was selected as the most promising technique for future evaluation. Data from tests performed indicate that the velocity-coupled T-burner can yield quantitative data. Therefore, it is recommended for future development as a standard test device.

In addition, it was an objective of the program to develop additional understanding of the role of velocity coupling in solid propellants. This was achieved in numerous observations, test results, calculations, etc. The most significant of these are listed.

During the phenomenological study portion of the program, a "dark mode combustion" was observed. When velocity oscillations exceeded about 70 ft/sec, an abrupt, reversible, order-of-magnitude change in flame luminosity would occur during which the propellant continued to burn with little or no visible flame. Ultimately, it was concluded that this mode of combustion was a localized phenomenon peculiar to certain test conditions.

Testing in the velocity-coupled T-burner resulted in quantitative data, with little evidence of wave distortion and larger than normal nonlinear limiting mechanisms. Harmonic content appeared to be equal to or less than that observed for the pressure coupled T-burner.

Testing in the end-venter burner resulted in much poorer quality data than the velocity-coupled T-burner. The data exhibited significant harmonic content, excessive data scatter, and quantitative results were not obtained.

A plot of the measured growth constant versus test sample area ratio is a straight line for the basic test technique in most cases, simplifying data interpretation. A very large effect due to either T-burner volume or sample/wall lip is observed (approximately three times as large as the corresponding effect in a pressure-coupled T-burner).

No significant difference in the response was observed in the data when the driver sample was varied (i.e., the mean flow and acoustic pressure amplitude).

The velocity-coupled response of CYH propellant was determined to be approximately 13 (at 300 psi and 450 Hz) which is almost an order of magnitude greater than the pressure-coupled response at these conditions. These data indicate that velocity coupling is a very significant mechanism relative to acoustics in solid propellant rocket motors.

Data were obtained with ANB-3066 propellant and with CYH lot SR-28 propellant both of which showed different characteristics than the CYH lot 1-14 propellant. Thus, the technique appears able to differentiate between different types of propellant (composite versus CMDB) and between different lots of propellant with differing motor characteristics.

Tests fired with the CYH 1-14 propellant at 800 Hz gave a lower response and differing test characteristics than the baseline data at 450 Hz. Thus, the technique appears to be sensitive to frequency changes.

Considerable uncertainty remains in quantitative interpretation of the data obtained due to the acoustic/flow interaction terms, VF and VFG. Until the magnitude of these terms has been defined there will be uncertainty in the value of the velocity-coupled response (the same holds true for pressure-coupled data also). The results of a series of tests fired with the purpose of evaluating the acoustic flow interaction terms indicate that the net sum of VF-VFG is an acoustic loss with a value of -3. Overall analysis of the data indicate that a combination of VF/VFG of -1/+2 correlates the data best. Actually, the data could be indicating that the formulation of the acoustic equations is inadequate to describe the T-burner.

The conclusion is reached that R_{vi} can be determined from velocity-coupled tests with approximately the same confidence level as can the pressure-coupled response, and that the two test techniques are by no means mutually exclusive (i.e., R_{vi} is needed in evaluating pressure-coupled data and B_s is needed in evaluating velocity-coupled data).

The net result from the current contract has shown that velocity coupling is significant and is quantitatively measurable.

B. FUTURE WORK

The current program can be considered successful, but the results have really only scratched the surface and considerable future work needs to be performed to develop the velocity-coupled T-burner technique and velocity-coupling technology in general.

The velocity-coupled T-burner technique needs to be completely developed and evaluated as a quantitative technique for measuring velocity coupling. It should be determined whether consistent data may be obtained for widely varying test conditions, if particular test conditions lead to inconsistent results, and what are optimum test conditions.

To expand the basic understanding of velocity coupling the magnitude and shape of the velocity-coupled response of typical propellants needs to be determined using the velocity-coupled T-burner. Tests should be performed to determine the velocity-coupled response of both smokeless and metalized propellants for a range of pressures and frequencies.

The current program has been directed specifically at linear velocity coupling with no attempt to explore or study acoustic erosivity. A

laboratory device is needed which will allow the characterization of acoustic erosivity. Also because of the manner that acoustic erosivity couples with motor ballistics, a theoretical interpretation of acoustic erosivity/ ballistic interactions needs to be performed.

REFERENCES

1. Price, E. W., Axial Mode Intermediate Frequency Combustion Instability in Solid Propellant Rocket Motors, AIAA Preprint 64-146, Solid Propellant Rocket Conference, Palo Alto, Calif., Jan. 29-31, 1964.

2. Hart, R. W., Bird, J. F., and McClure, F. T., "The Influence of Erosive Burning on Acoustic Instability in Solid Propellant Rocket Motors," Progress in Astronautics and Rocketry, Vol. 1, Academic Press Inc., New York 1960, pp 423-451.

3. McClure, F. T., Bird, J. F., and Hart, R. W., "Erosion Mechanism for Nonlinear Instability in the Axial Modes of Solid Propellant Rocket Motors," ARS. J., Vol. 32, March 1962, pp 374-378.

4. Hart, R. W., Bird, J. F., Cantrell, R. H., and McClure, F. T., "Nonlinear Effects in Instability of Solid Propellant Rocket Motors," AIAA J., Vol. 2, July 1964, pp 1270-1273.

5. Bird, J. F., Hart, R. W., and McClure, F. T., "Finite Acoustic Oscillations and Erosive Burning in Solid Fuel Rockets," AIAA J., Vol. 3, Dec. 1965, pp 2248-2256.

6. Price, E. W. and Dehority, G. L., Velocity Coupled Axial Mode Combustion Instability in Solid Propellant Rocket Motors, ICRPG/AIAA 2nd Solid Propulsion Conference, Anaheim, Calif, June 1967, pp 213-227.

7. Price, E. W., Review of Combustion Instability in Solid Propellant Rockets, First Technical Panel on Solid Propellant Combustion Instability, APL John Hopkins University TG-371-3, May 1961, p 7-48.

8. Price, E. W., "Review of Solid Rocket Combustion Instability in Development Programs 1960-1964," Technical Note 5008-16, June 1964, published in Johns Hopkins University, Applied Physics Lab., Report No. TG 371-8B, July 1964, Appendix III.

9. Price, E. W., Mathes, H. B., Sword, B. A., and Sprouse, H. J., Axial Mode Combustion Instability in Solid Propellant Rocket Motors, NAVWEPS Report 8658, NOTS TP 3700 U. S. Naval Ordnance Test Station, China Lake, Calif., December 1964.

10. Brownlee, W. G., "Nonlinear Axial Combustion Instability in Solid Propellant Motors," AIAA J., Vol. 2, Feb. 1964, pp 275-284.

11. Dickinson, L. A., "Command Initiation of Finite Wave Axial Instability in Solid Propellant Rocket Engines," ARS J., V. 32, No. 4, 1962, p. 643.

12. Stepp, E. E., "Effect of Pressure and Velocity Coupling on Low-Frequency Instability," AIAA J., Vol 5, No. 5, 1967, pp 945-948.

13. Culick, F. E. C., "Stability of Longitudinal Oscillations with Pressure and Velocity Coupling in a Solid Propellant Rocket," Combustion Science and Technology, Vol. 2, No. 2, 1970.

14. Hopkins, B. D., "Velocity Coupled Surface Response," The Investigation of Pressure Oscillations During Firing of the Minuteman II Stage III Motor, Final Report, Contract No. AF 04(694)-903, Vol. III, Appendix A, Hercules Incorporated, Magna, Utah, January 1971.

15. Flandro, G. A., Acoustic Combustion Instability in Flight Application Solid Propellant Rocket Motors, Final Report, Hercules Prime Contract AF 04(694)-903, Subcontract SC-259, University of Utah, Salt Lake City, Utah, 1969.

16. Hercules Incorporated, Velocity Coupling Analysis, AFRPL-TR-72-12, January 1972, Magna, Utah.

17. The Investigation of Pressure Oscillations During Firing of Minuteman II Stage III Motor, Final Report, Contract No. AF 04(694)-903, Vol. III, Hercules Incorporated, Magna, Utah, January 1971.

18. Povinelli, L. A., One-Dimensional Nonlinear Model for Determining Combustion Instability in Solid Propellant Rocket Motors, NASA Tech Note TN D-3410, April 1966.

19. Price, E. W. and Dehority, G. L., Velocity Coupled Axial Mode Combustion Instability in Solid Propellant Rocket Motors, Proc. of Second ICRPG/AIAA Solid Propulsion Meeting, Anaheim, Calif., June 1967, pp 213-227.

20. Marxman, G. A., and Wooldridge, C. E., "Finite Amplitude Axial Instability in Solid Rocket Combustion," Twelfth Symposium (International) on Combustion, The Combustion Institute, 1967, pp 115-127

21. Marxman, G. A., and Wooldridge, C. E., "Effect of Surface Reactions on the Solid Propellant Response Function," AIAA J, Vol 6, No. 3, 1968, pp 471-477.

22. Price, E. W., "Recent Advances in Solid Propellant Combustion Instability," Twelfth Symposium (International) on Combustion, The Combustion Institute, 1968, pp 115-127.

23. Beckstead, M. W., "Low Frequency Instability: A Comparison of Theory and Experiment," Combustion and Flame, Vol 12, No. 1, 1968, pp 417-426.

24. Roberts, A. K., Brownlee W. G., "Nonlinear Longitudinal Combustion Instability: Influence of Propellant Composition," AIAA J, Vol 9, No. 1, 1971, pp 140-147.

25. Roberts, A. K., Brownlee, W. G., and Jackson, F., "Combustion Instability and the Design of Solid Propellant Rocket Motors," Canadian Aeronautics and Space Journal, Vol 16, No. 1, Jan 1970, pp 21-27.

26. Brownlee, W. G. and Kimbell, G. H., "Shock Propagation in Solid-Propellant Rocket Combustors," AIAA J, Vol 4, No. 6, June 1966, pp 1132-1134.

27. Morris, E. P., "A Pulse Technique for the Evaluation of Combustion Instability in Solid Propellant Rocket Motors," Canadian Aeronautics and Space Journal, Vol II, No. 9, Nov 1965, pp 329-333.

28. Brownlee, W. G., "Nonlinear Axial Combustion Instability in Solid Propellant Motors," AIAA J, Vol 2, No. 2, Feb 1964, pp 275-284.

29. Dickinson, L. A., "Command Initiation of Finite Wave Axial Combustion Instability in Solid Propellant Rocket Motors," ARS J., Vol 32, April 1962, pp 643-644.

30. Roberts, A. K., et al "Longitudinal Combustion Instability: Behavior of Propellants with High Solids Content", 3rd ICRPG Combustion Conference, Oct 17-21, 1966, Cocoa Beach, Florida, CPIA No. 138, Vol 1, pp 335-340.

31. Roberts, A. K., et al, "Longitudinal Combustion Instability: Some Empirical Results and Related Design Considerations," 2nd ICRPG Combustion Conference, Nov 1-5, 1965, Los Angeles, Calif., CPIA No. 105, Vol 1, pp 769-788.

32. Roberts, A. K., and Brownlee, W. G., "Some Further Data on Nonlinear Axial-Mode Instability," 1st ICRPG Combustion Conference, Nov 16-20, 1964, Orlando Air Force Base, Florida, CPIA No. 68, Vol 1, pp 459-470.

33. Buffum, et al, "Acoustic Attenuation Experiments on Subscale, Cold-Flow Rocket Motors," AIAA J., Vol 5, No. 2, Feb 1967, pp 272-280.

34. Kimbell, G. H., and Brownlee, W. G., Flow Processes in a Solid Propellant Combustor During Unstable Operation, Carde Tech Note 1783/68, Project No. D46-47-60-02, Quebec, Canada, March 1968.

35. Kimbell, G. H., and Brownlee, W. G., Status Report on Optical Studies of Combustion Instabilities at Carde, Carde Tech Note 1784/68, Project No. D46-47-60-02, Quebec, Canada, March 1968.

36. Capener, E. L., et al, "Driving Processes of Finite-Amplitude Axial Mode Instability in Solid Propellant Rockets," AIAA J, Vol 5, No. 5 May 1967, pp 938-945.

37. Hercules, Incorporated, Poseidon Second Stage Vibration Report, Document No. SH015-B3A00HTJ-1 on LMSC Subcontract 17-10203, March 1971.

38. Povinelli, L. A., et al, Experimental Investigation of Transverse-Mode Solid Propellant Combustion Instability in a Vortex Burner, NASA Tech Note TN D-3708, Nov 1966.

39. Povinelli, L. A., "Additive Effects in Pressure and Velocity Coupled Solid Rocket Instability," 4th ICRPG Combustion Conference, 1967, SRI, Menlo Park, Calif., Vol I, CPIA No. 162, pp 347-352.

40. Eisel, J. L., and Dehority, G. L., "A Technique for Investigating Low Frequency Velocity Coupled Combustion Instability," 2nd ICRPG Combustion Conference, 1966, Los Angeles, Calif., CPIA No. 105, pp 703-712.

41. Price, E. W., et al, "Experimental Research in Combustion Instability of Solid Propellants," Combustion and Flame, Vol 5, No. 2, 1961, pp 149-162.

42. Lawhead, R. B., and Carlson, L. W., "Physical Processes of Solid Propellant Combustion," Proceedings 3rd Meeting, Technical Panel on Solid Propellant Combustion Instability, TG-371-5, May 1963, p 43.

43. Muller, G. M., "Acoustic Admittance Measurements: Reflected - Pulse Method," Proceedings 3rd Meeting, Technical Panel on Solid Propellant Combustion Instability, TG-371-5, May 1963, p 47.

44. Converse, A. O., and Klinzing, G. K., "Progress Report on Solid Propellant Combustion Instability Study," Proceedings 3rd Meeting, Technical Panel on Solid Propellant Combustion Instability, TG-371-5, p 81.

45. Calcote, H. F., "Acoustic Wave Burning Zone Interactions in Solid Propellants," Proceedings 3rd Meeting, Technical Panel on Solid Propellant Combustion Instability, TG-371-5, p 59.

46. Leader, G. R., "Experiments for the Measurement of the Acoustic Impedance of a Burning Solid Propellant," Proceedings 3rd Meeting, Technical Panel on Solid Propellant Combustion Instability, TG-371-5, p 51.

47. Foner, S. N., "APL Experimental Program," Proceedings 3rd Meeting, Technical Panel on Solid Propellant Combustion Instability, TG-371-5, p 11.

48. Dittus, F. W. and Boelter, L. M. K., Univ. Calif. Pubs. Eng., 2, 443 (1930).

49. Reed, R. G. and Sherwood, T. K., The Properties of Gases and Liquids, McGraw-Hill, New York, 1958, p 457.

50. Marxman, G. and Gilbert, M., "Turbulent Boundary Layer Combustion in the Hybrid Rocket," Ninth Symposium on Combustion (International), Academic Press, N. Y., 1963, p 371.

51. Smoot, L. D. and Price, C. F., "Pressure Dependence on Hybrid Fuel Regression Rates," AIAA J., 5, 1967, pp 102-106.

52. Wimpress, R. N., Internal Ballistics of Solid-Fuel Rockets, McGraw-Hill, New York, 1950, p 24.

53. Lenoir, J. M. and Robillard, G., "A Mathematical Method to Predict the Effects of Erosive Burning in Solid-Propellant Rockets," Sixth Symposium (International) on Combustion, Reinhold Pub. Corp., N. Y., 1957, pp 663-667.

54. Wormersley, J. R., "Method for the Calculation of Velocity, Rate of Flow and Viscous Drag in Arteries When the Pressure Gradient is Known," J. Physiol., 127, 1955, pp 553-563.

55. Linford, Robert, A Study of Pulsatile Flow Phenomenon, Ph.D. Thesis, University of Utah, 1961.

56. Flandro, G. A., Rotating Flows in Acoustically Unstable Rocket Motors, Ph.D. Thesis, C.I.T., 1967.

57. McClure, F. T., Hart, R. W., and Cantrell, R. H., "Interaction Between Sound and Flow: Stability of T-Burner," AIAA Journal, 1, 1963, pp 586-590.

58. Cantrell, R. H. and Hart, R. W., "Interaction Between Sound and Flow in Acoustic Cavities: Mass, Momentum, and Energy Considerations," J. Acoustic Soc. Am., 36, 1964, pp 697-706.

59. Coates, R. L., "Comment on Stability of Longitudinal Oscillations with Pressure and Velocity Coupling in a Solid Propellant Rocket," Comb. Science and Tech., 3, 1971, p 153.

60. McClure, F. T., and Hart, R. W., "Theory of Acoustic Instability in Solid-Propellant Rocket Combustion," Tenth Symposium (International) on Combustion, The Combustion Institute, 1965, pp 1047-1065.

61. Landau, L. D., and Lifshitz, E. M., Fluid Mechanics, Addison-Wesley Publishing Co., Reading, Mass., 1959, p 250.

62. Crocco, L. and Sirignano, W. A., "Effect of Transverse Velocity Component on the Non-Linear Behavior of Short Nozzles," AIAA Journal, 4, 1966, pp 1428-1430.

63. Culick, F. E. C., Interactions Between the Flow Field, Combustion, and Wave Motions in Rocket Motors, NWC TP 5349, China Lake, Calif., June 1972.

64. Sayer, L., Thiokol Chemical Corp., personal communication, 13 August 1971.

65. Derr, R. L., Evaluation of a Variable Area T-Burner for Metalized Propellants, AFRPL-TR-72-97, Lockheed Propulsion Co., Redlands, Calif., February 1973.

66. Liepmann, H. W., and Roshko, A., Elements of Gas Dynamics, Wiley, 1957.

67. Krashin, M., "Numerical Calculation of Velocity-Coupled Acoustic Instability with Allowance for Flow Reversal 2nd Threshold Velocity Effects," 9th JANNAF Combustion Meeting, Monterey, Calif., Sept. 11-15, 1972.

68. Horton, M. D., Testing the Dynamic Stability of Solid Propellants: Techniques and Data, U. S. Naval Weapons Test Station, NAVWEPS Report 8596, August 1964.

69. Horton, M. D., Oscillatory Burning of Propellants, Ph.D. Thesis, University of Utah, 1961.

70. Horton, M. D., Coates, R. L., and Beckstead, M. W., Velocity Coupling Analysis, AFRPL-TR-72-106, Hercules Incorporated, Magna, Utah, Oct 1972.

71. Beckstead, M. W., Bennion, D. U., Butcher, A. G., and Peterson, N. L., Variable Area T-Burner Investigation, Hercules Incorporated, Technical Report AFRPL-TR-72-85, December 1972, Magna, Utah.

72. Crump, J. R., and Price, E. W., AIAA J., Vol. 2, 1964, p 1274.

73. Bennion, D. U., Beckstead, M. W., Hopkins, B. D., and West, L. R., Final Report for Subtask 2 - T-Burner - of Task 5 - Pressure Oscillation Study, Report No. MTO-1124-50, Hercules Incorporated, Magna, Utah, August 1971.

74. Bennion, D. U., Beckstead, M. W., West, L. R., and Jessen, E. C., The Variable Area T-Burner as a Quality Assurance Tool, 8th JANNAF Combustion Meeting, CPIA No. 220, Vol. I, Nov. 1971, pp 425-441.

75. Micheli, P. L., and Lovine, R. L., Evaluation of a Pulse T-Burner for Metallized Propellants, Vol I: Experimental Procedures for the T-Burner, Vol II: Stability Analyses, Vol III: Piston Pulser Development, AFRPL-TR-72-54, Aerojet Solid Propulsion Company, Sacramento, Calif, Nov 1972.

76. Crump, James, Oscillatory Combustion Experimentation and Analysis, AFRPL-TR-72-99, Naval Weapons Center, China Lake, Calif, Dec 1972.

77. Peterson, John A., Mihlfeith, C. Max, and Sayer, L. H., Final Report Pressure Oscillation Investigation for Minuteman III, AFRPL-TR-72-98, Thiokol Chemical Corporation, Wasatch Division, Nov 1972.

78. Jensen, R. C., and Beckstead, M. W., "Limiting Amplitude Analysis," AFRPL-TR-73-61, Hercules Incorporated, Magna, Utah, July 1973.

79. Jensen, R. C., "A Mathematical Model for the Amplitude of Acoustic Pressure Oscillations in Solid Rocket Motors," 8th JANNAF Combustion Meeting, CPIA Publication No. 220, November 1971, pp 313-319.

80. Beckstead, M. W. and Jensen, R. C., "Nonlinear Interpretation of Linear T-Burner Data," 9th JANNAF Combustion Meeting, CPIA Publication No. 231, December 1971, pp 239-248.

APPENDIX A

TEST DATA

TABLE A-I

UNCORRECTED T-BURNER DATA
(Pressure Coupled Test Series)
(Baseline)

Run	L_b (in.)	$\frac{S_b}{S_{co}}$	$\frac{S_{co}}{S_c}$	β	t_α (sec)	f (Hz)	$\bar{P}$ (psig)	$\dot{r}$ (in./sec)	Pk-Pk Amp. (psi)	α (sec^{-1})	π_{NL}	Remarks
621												No Data
629	2.69	6.71	1.14	.133	.276	485	300	.28	91	123*	1.68	
	2.64	7.20	.95	.13	.514	478	300	.28	87	115*	1.66	Paddle in when growth started OK
	2.41	7.26	.78	.119	.802	460	300	.28	95	108*	1.48	
630	2.66	6.64	1.06	.132	.27	472	300	.27	87	127*	1.86	
	2.62	7.16	.98	.131	.50	467	300	.27	100	130*	1.66	Paddle in when growth started
	2.44	7.25	.89	.121	.783	456	300	.27	96	126*	1.72	½ linear growth while paddle in
631			Paddle did not operate									
632			Paddle did not operate									
662	.56	1.43	1.10	.028	.238	428	300	.28	---	-33	---	
	.542	1.49	.94	.027	.53	417	300	.28	---	-36	---	Osc. did not die completely Between pulses 1 and 2
	.47	1.44	.75	.023	.873	412	300	.28	---	-37	---	
663	.57	1.46	1.08	.028	.356	440	300	.27	---	-25	---	
	.53	1.51	.87	.026	.649	435	300	.27	---	-26	---	Osc. did not die completely Between pulses 1 and 2
	.45	1.44	.70	.022	.990	435	300	.27	---	-30	---	
681	2.34	5.94	1.10	.116	.30	460	300	.30	90	79	1.14	
	2.21	6.22	.90	.109	.56	448	300	---	86	86	1.34	
	1.96	6.06	.74	.097	.83	439	300	---	77	80	1.42	
682	2.36	5.93	1.13	.117	.276	483	300	.30	98	89	1.12	
	2.25	6.27	.92	.111	.532	464	300	.30	94	93	1.28	
	1.99	6.11	.76	.098	.796	448	300	.30	81	83	1.38	
683	1.71	4.38	1.09	.084	.324	459	300	.29	54	41	.98	
	1.58	4.51	.87	.087	.608	456	300	.29	49	48	1.28	
	1.36	4.32	.71	.067	.911	444	300	.29	44	41	1.26	
684	1.65	4.21	1.09	.081	.314	467	300	.29	52	37	.9	
	1.53	4.35	.88	.075	.603	475	300	.29	50	44	1.12	
	1.32	4.16	.71	.065	.901	457	300	.29	44	39	1.16	
909	.56	1.41	1.13	.028	.309	410	300	.25	--	-23	--	
	.56	1.49	1.01	.028	.478	416	300	.25	--	-28.5	--	
	.53	1.49	.88	.026	.690	401	300	.25	--	-29.1	--	

*Data eliminated from computer analysis by standard rejection criteria.

TABLE A-II

UNCORRECTED T-BURNER DATA
(Velocity Coupled Test Series)**
(Baseline)

Run	Driver L_b (in.)	Driver $\frac{S_b}{S_{co}}$	Driver β	Test Sample L_b (in.)	Test Sample $\frac{S_b}{S_{co}}$	Test Sample β	$\frac{S_{co}}{S_c}$	tα (sec)	f (Hz)	$\bar{P}$ (psig)	$\bar{t}$ (in./sec)	Pk-Pk Amp (psi)	α (sec^{-1})	π_{ML}	Remarks
633	.56	1.33	.028	2.78	6.62	.137	1.25	.190	480	300	.28	22	--	--	Paddle in when growth
	.55	1.48	.028	2.59	7.35	.132	1.02	.500	477	300	.28	27	--	--	started.
	.50	1.47	.024	2.45	7.29	.121	.80	.885	475	300	.28	35	191*	6.8	Paddle in most of growth.
634	.56	1.36	.028	2.27	5.53	.112	--	.26	461	300	.23	23	--	--	Paddle in when growth start
	.55	1.49	.027	2.22	6.04	.108	.96	.60	455	300	.23	38	249	8.66	ed Most of growth after
	.48	1.45	.024	1.95	5.89	.096	.78	.966	450	300	.23	36	225	8.44	paddle out.
635	.57	1.38	.028	1.69	4.05	.083	1.23	.206	474	300	.23	--	--	--	Osc. before paddle removed.
	.56	1.52	.027	1.65	4.52	.081	.95	.615	470	300	.23	22	135*	7.92	Paddle in most of growth.
	.49	1.48	.024	1.48	4.49	.073	.78	.965	475	300	.23	19	116	7.68	O.K.
659	.56	1.47	.028	.56	1.47	.028	1.04	.396	470	300	.24	4	43	13.7	Burn rate questionable.
	.45	1.44	.028	.45	1.44	.028	.70	.953	455	300	.24	2	25	17.4	
660	.57	1.51	.028	1.14	3.02	.056	1.02	.389	485	300	.30	14	128	11.3	
	.47	1.47	.023	.88	2.94	.047	.72	.827	470	300	.30	16	65	5.02	
661	.57	1.43	.028	1.11	2.79	.055	1.12	.264	485	300	.31	13	134	13.1	Paddle in when g owth
	.52	1.5	.026	1.02	2.95	.050	.85	.601	480	300	.31	15	107	8.76	started.
	.42	1.4	.021	.85	2.81	.042	.64	.992	478	300	.31	15	60	5.04	Burn rate questionable.
884	.56	1.34	.028	1.68	4.03	.083	1.24	.194	460	300	.26	18	--	--	Osc. before paddle removed.
	.54	1.50	.027	1.63	4.51	.080	.93	.596	453	300	26	16	--	--	Paddle in when growth
	.492	1.48	.024	1.50	4.42	.073	.82	.793	442	300	.26	25	109	5.94	started.
728	.56	1.37	.027	2.25	5.52	.110	1.18	.259	450	305	.25	27	--	--	Osc. before paddle removed.
	.533	1.49	.026	2.14	5.97	.105	.91	.634	457	305	.25	34	--	--	Growth started before
	.456	1.49	.022	1.82	5.73	.089	.72	1.037	459	305	.25	33	71	2.82	paddle was out.
729	.56	1.46	.027	1.70	4.38	.083	1.05	.399	446	305	.25	21	--	--	Osc. before paddle removed.
	.522	1.48	.026	1.62	4.54	.08	.90	.653	451	300	.25	24	138*	7.74	Some growth before paddle
	.442	1.41	.022	1.41	4.45	.069	.70	1.062	440	300	.25	21	39	2.54	was removed.
730	.56	1.39	.027	1.70	4.18	.083	1.12	.276	445	305	.24	18	--	--	Osc. before paddle removed.
	.536	1.49	.026	1.64	4.54	.081	.93	.624	441	305	.24	23	87*	5.16	Some growth before paddle
	.461	1.49	.023	1.44	4.49	.070	.73	1.028	452	305	.24	23	74	4.34	was removed.
731	.56	1.42	.027	1.12	2.81	.055	1.12	.312	440	300	.26	12	116	13.0	
	.523	1.49	.026	1.05	2.97	.051	.88	.656	442	305	.26	13	96	10.1	
	.454	1.45	.022	.90	2.86	.044	.70	1.022	429	296	.26	14	65	6.3	
732	.56	1.41	.027	.56	1.41	.027	1.13	.330	443	300	.25	4	42	13.5	
	.517	1.48	.025	.52	1.48	.025	.86	.731	435	300	.25	3	24	11.1	

*Data eliminated from computer analysis by standard rejection criteria.
**Velocity coupling sample centered 9.75 inches from burner end. Burner length = 40.75 inches.

TABLE A-III

UNCORRECTED T-BURNER DATA
(Driver Size Variation Test Series)**

Run	Driver L_b (in.)	Driver $\frac{S_b}{S_{co}}$	Driver β	Test Sample L_b (in.)	Test Sample $\frac{S_b}{S_{co}}$	Test Sample β	$\frac{S_{co}}{S_c}$	t_α (sec)	f (Hz)	$\bar{P}$ (psig)	$\dot{r}$ (in./sec)	Pk-Pk Amp (psi)	α (sec^{-1})	π_{HL}	Remarks
887	1.16	2.92	.057	.57	1.42	.028	1.14	.285	463	307	.27	32	80	---	ΔP_L not reached
	1.12	3.16	.055	.55	1.55	.027	.91	.596	452	312	.27	42	79	2.6	
	.97	3.04	.047	.49	1.53	.024	.75	.932	422	315	.27	35	47	2.01	
888	1.18	2.92	.058	.56	1.40	.027	1.14	.272	457	305	.26	29	86	3.96	
	1.15	3.20	.057	.54	1.53	.027	.91	.596	441	307	.26	34	85	3.46	
	1.03	3.14	.050	.49	1.49	.023	.75	.893	439	310	.26	33	49	2.1	
889	1.12	2.79	.055	1.12	2.79	.055	1.14	.273	464	307	.28	27	115	5.65	
	1.08	3.02	.053	1.08	3.02	.053	.92	.573	449	310	.28	43	147	4.62	
	0.95	2.94	.047	.95	2.94	.047	.76	.874	440	312	.28	43	104	3.43	
890	1.14	2.81	.056	1.14	2.81	.056	1.17	.258	455	307	.27	22	118	---	ΔP_L not reached
	1.12	3.10	.055	1.12	3.09	.055	.94	.56	456	312	.27	43	136	4.33	
	.99	3.01	.048	.98	3.00	.048	.77	.865	448	315	.27	46	118	3.61	
942	1.12	2.77	.055	.56	1.39	.027	1.16	.255	472	305	.28	16	53	4.35	ΔP_L not reached
	1.0	2.99	.049	.49	1.47	.024	.80	.772	457	307	.28	20	56	3.76	
	.88	2.9	.043	.43	1.41	.021	.65	1.092	443	310	.28	30	33	1.54	

**Velocity coupling sample centered 9.75 inches from burner end. Burner length = 40.75 inches.

TABLE A-IV

UNCORRECTED T-BURNER DATA
(Vent Location Test Series)**

Run	Driver L_b (in.)	Driver $\frac{S_b}{S_{co}}$	Driver β	Test Sample ℓ_v (in.)	Test Sample $\frac{S_b}{S_{co}}$	Test Sample β	$\frac{S_{co}}{S_c}$	t_α (sec)	f (Hz)	$\bar{P}$ (psig)	$\dot{r}$ (in./sec)	Pk-Pk Amp (psi)	α (sec^{-1})	π_{RL}	Remarks
743	2.31	5.99	.113	1.69	4.38	.083	1.06	.394	456	315	.30	60	38	.88	
	2.23	6.15	.109	--	--	--	.94	.501	448	310	.30	78	77	1.34	
	2.01	6.03	.099	--	--	--	.79	.729	440	308	.30	73	70	1.34	
744	2.32	6.02	.115	2.78	7.07	.136	1.09	.319	448	300	.29	24	42	2.36	
	2.09	6.18	.103	--	--	--	.81	.713	441	300	.29	76	83	1.48	
	1.69	5.74	.082	--	--	--	.62	1.157	426	300	.29	43	58	1.9	
745	2.35	5.90	.115	.58	1.47	.028	1.13	.264	461	300	29	67	60	1.18	
	2.04	6.14	.10	--	--	--	.79	.745	449	300	.29	76	85	1.48	
	1.70	5 76	.083	--	--	--	.62	1.115	430	300	.29	62	76	1.72	
746	2.34	5.94	.115	2.76	6.96	.135	1.11	.29	447	315	.29	80	30	.52	
	2.05	6.11	.101	--	--	--	.80	.72	441	310	.29	70	76	1.52	
	1.69	5.70	.083	--	--	--	.63	1.098	425	310	.29	62	66	1.56	
747	2.35	6.0	.115	2.75	6.97	.135	1.09	.307	435	310	.29	78	49	.88	
	2.04	6.16	.10	--	--	--	.78	.765	445	300	.29	78	85	1.46	
	1.74	5.85	.086	--	--	--	.63	1.101	430	300	.29	65	67	1.42	
748	2.33	5.91	.114	1.68	4.23	.082	1.10	.285	449	31.	.29	31	37	1.70	
	2.06	6.17	.101	--	--	--	.79	.728	444	320	.29	81	83	1.48	
	1.74	5.89	.085	--	--	--	.62	1.098	435	320	.29	68	71	1.54	
749	2.35	5.99	.115	.55	1.39	.027	1.10	.287	462	305	.29	73	61	1.12	
	2.03	6.11	.10	--	--	--	.78	.744	443	300	.29	81	80	1.34	
	1.68	5.68	.082	--	--	--	.62	1.116	430	305	.29	66	65	1.42	

**Vent sample located with edge ½ inch from vent opening. Burner length = 40.75 inches.
Second and third paddle pull points are included as pressure coupled baseline points in computer analysis.

TABLE A-V

UNCORRECTED T-BURNER DATA
(CYH 1-14 800 Hz Pressure Coupling Test Series)

Run	L_b (in.)	$\frac{S_b}{S_{co}}$	$\frac{S_{co}}{S_c}$	β	t_α (sec)	f (Hz)	$\bar{P}$ (psig)	$\dot{r}$ (in./sec)	Pk-Pk Amp. (psi)	α (sec^{-1})	ω_{HL}	Remarks
843	.56	1.37	1.19	.045	.247	715	307	.2[illegible]	---	-40	---	
	.56	1.43	1.10	.045	.356	716	310	.2[illegible]	---	-43	---	
	.56	1.49	1.00	.045	.479	710	310	.26	---	-40	---	
844	.56	1.37	1.18	.045	.246	707	310	.26	---	-42	---	
	.56	1.43	1.09	.045	.354	714	312	.26	---	-46	---	
	.56	1.49	1.0	.045	.477	711	312	.26	---	-41	---	
845	1.12	3.0	1.0	.091	---	---	---	---	---	---	---	Pulsed to steady osc.
880	2.33	5.82	1.14	.190	.276	773	312	.28	41	73	1.44	
	2.28	6.26	.94	.186	.526	756	315	.28	55	150	2.28	
	2.04	6.21	.77	.166	.822	722	317	.28	89	163	1.62	
881	2.68	6.75	1.12	.217	.292	766	310	.29	34	67	1.62	
	2.57	7.17	.91	.207	.561	740	315	.29	79	177	1.92	
	2.34	7.21	.74	.187	.871	739	320	.29	102	208	1.78	
938	1.68	4.25	1.11	.136	.31	---	305	.26	---	---	---	No osc.
	1.59	4.55	.87	.129	.66	752	307	.26	27	45	1.35	
	1.31	4.4	.63	.106	1.2	755	312	.26	27	49	1.55	
939	1.68	4.49	.99	.136	.442	756	305	.28	29	30	.84	
	1.54	4.54	.81	.124	.728	778	310	.28	33	62	1.5	
	1.29	4.38	.62	.104	1.172	775	312	.28	26	42	1.26	

TABLE A-VI

UNCORRECTED T-BURNER DATA
(CYH 1-14 800 Hz Velocity Coupling Test Series)**

Run	Driver L_b (in.)	Driver S_b/S_{co}	Driver β	Test Sample L_b (in.)	Test Sample S_b/S_{co}	Test Sample β	S_{co}/S_c	t_α (sec)	f (Hz)	$\bar{P}$ (psig)	$\dot{r}$ (in./sec)	Pk-Pk ΔP_{osc} (psi)	α (sec^{-1})	π_{HL}	Remarks
876	.56	1.35	.045	1.67	3.92	.135	1.29	.137	---	312	.26	---	---	---	---
	.56	1.48	.045	1.67	4.31	.135	1.07	.382	---	315	.26	---	---	---	---
	.49	1.46	.039	1.48	4.38	.120	.81	.787	700	315	.26	5	26	.47	
877	.56	1.41	.045	2.25	5.54	.182	1.17	.273	---	312	.26	---	---	---	No osc.
	.56	1.47	.045	2.25	5.78	.182	1.08	.371	795	312	.26	12	17	1.1	Close to burn out
878	.56	1.41	.045	2.25	5.54	.182	1.17	.269	---	310	.25	---	---	---	---
	.53	1.50	.043	2.18	6.04	.176	.93	.617	663	315	.25	---	21	---	ΔP not reached
	.47	1.46	.038	1.94	5.95	.156	.75	.956	687	315	.25	7	93	12.1	---
879	.56	1.43	.045	2.78	6.94	.225	1.14	.283	656	312	.27	7	51	7.32	---
	.51	1.48	.041	2.61	7.36	.211	.89	.623	---	320	.27	8	---	---	Paddle did not stop osc.
	.45	1.44	.036	2.29	7.20	.185	.72	.948	713	323	.27	14	239	15.4	---
882	.57	1.44	.048	2.78	6.87	.225	1.17	.247	670	312	.28	6	29	4.22	---
	.56	1.55	.045	2.77	7.46	.224	.98	.464	672	317	.28	8	167	19.6	---
	.49	1.50	.039	2.49	7.28	.195	.78	.790	734	330	.28	14	188	11.7	---
910	.56	1.42	.045	.56	1.42	.045	1.10	.30	723	347	.28	---	- 49	---	Over pressurized
	.55	1.49	.045	.55	1.49	.045	.97	.465	785	355	.28	---	- 45	---	---
	.51	1.48	.041	.51	1.48	.041	.83	.686	736	360	.28	---	- 44	---	---
911	.56	1.40	.045	.56	1.4	.045	1.14	.303	746	325	.24	---	-142*	---	---
	.56	1.48	.045	.56	1.48	.045	1.01	.489	749	330	.24	---	-118*	---	---
	.55	1.55	.044	.55	1.55	.044	.89	.701	765	332	.24	---	-140*	---	---
936	.56	---	---	1.12	---	---	---	---	---	---	---	---	---	---	Gas seal failure
937	.56	---	---	1.12	---	---	---	---	---	---	---	---	---	---	No results

*Data eliminated from computer analysis by standard rejection criteria.

**Velocity coupling sample centered 6.40 inches from burner end. Burner length = 24.75 inches.

TABLE A-VII

UNCORRECTED T-BURNER DATA
(ANB 3066 Pressure Coupling Test Series)

Run	L_b (in.)	$\frac{S_b}{S_{co}}$	$\frac{S_{co}}{S_c}$	β	f_α (sec)	f (Hz)	$\bar{P}$ (psig)	$\dot{r}$ (in./sec)	Pk-Pk Amp. (psi)	α (sec^{-1})	π_{NL}	Remarks
773	2.27	5.70	1.13	.183	.235	848	505	.35	41	50*	.86	
	2.02	6.64	.79	.163	.627	789	510	.35	33	38	.90	
774	2.30	5.78	1.13	.186	.233	832	507	.35	44	64	1.08	
	2.14	6.0	.90	.173	.468	781	507	.35	36	50	1.08	
	1.86	5.94	.70	.15	.778	779	510	.35	25	32	1.04	
781	.54	1.47	.96	.044	.429	765	512	.33	---	-40	---	
782	.56	1.38	1.18	.045	.199	747	537	33	---	-46	---	
	.56	1.48	1.0	.045	.373	747	512	33	---	-48	---	
	.51	1.47	.85	.041	.558	749	512	33	---	-47	---	
811	.56	1.5	1.0	---	---	---	---	---	---	---	---	Pulse units failed
812	.56	1.5	1.0	---	---	---	---	---	---	---	---	Ignition failure

*Data eliminated from computer analysis by standard rejection criteria.

TABLE A-VIII

UNCORRECTED T-BURNER DATA
(ANB 3066 Velocity Coupling Test Series)**

Run	Driver L_b (in.)	Driver $\frac{S_b}{S_{co}}$	Driver β	Test Sample L_b (in.)	Test Sample $\frac{S_b}{S_{co}}$	Test Sample β	$\frac{S_{co}}{S_c}$	t_α (sec)	f (Hz)	$\bar{P}$ (psig)	$\dot{r}$ (in./sec)	Pk-Pk Amp (psi)	α (sec^{-1})	π_{NL}	Remarks
775	.56	1.46	.045	1.13	2.88	.091	1.09	.267	800	512	.35	5	32	5.28	Growth started before paddle out
	.53	1.50	.043	1.07	2.98	.087	.92	.448	780	510	.35	4	23	4.4	Osc between puddle pulls
	.45	1.44	.037	.93	2.89	.075	.73	.726	---	510	.35	---	---	---	No osc
776	.56	1.42	.045	1.12	2.79	.091	1.15	.213	806	500	.35	8	36	3.56	---
	.51	1.47	.041	1.04	2.96	.084	.87	.521	781	500	.35	2	9	3.54	---
	.44	1.42	.036	.92	2.90	.074	.71	.767	---	505	.35	---	---	---	No osc
777	.56	1.38	.045	1.68	4.07	.136	1.23	.165	798	517	.34	13	97	6.16	Osc started before paddle out
	.53	1.49	.043	1.58	4.39	.128	.92	.458	792	517	.34	13	61	3.68	---
	.44	1.40	.036	1.33	4.23	.108	.70	.792	784	517	.34	7	22	2.7	---
778	.56	1.39	.045	1.68	4.1	.136	1.19	.182	811	523	.34	16	89	4.52	Osc started before paddle out
	.53	1.50	.043	1.62	4.5	.131	.93	.456	803	523	.34	16	62	3.12	All three growths this test
	.46	1.44	.037	1.41	4.38	.114	.74	.738	792	530	.34	11	35	2.68	---
779	.56	1.39	.045	1.11	2.71	.090	1.20	.174	787	520	.35	6	28	3.84	Osc started before paddle out on all growths
	.52	1.48	.042	1.06	2.94	.085	.92	.45	788	515	.35	8	19	2.04	---
	.45	1.44	.036	.92	2.88	.074	.72	.73	---	515	.35	---	---	---	No osc
780	.57	1.38	.045	1.68	4.07	.136	1.21	.161	814	535	.35	14	70	4.1	Osc started before paddle out on all growths
	.54	1.50	.044	1.58	4.34	.128	.95	.418	804	530	.35	14	57	3.30	---
	.46	1.46	.037	1.36	4.24	.110	.73	.725	778	535	.35	9	30	2.94	---
872	.55	1.41	.045	1.12	2.77	.091	1.16	.219	796	505	.33	6	29	3.92	---
	.52	1.48	.042	1.08	3.01	.087	.91	.492	670	512	.33	1	11	7.96	---
	.47	1.46	.038	.98	2.97	.079	.77	.707	---	512	.33	---	---	---	no osc.
873	.56	1.38	.045	1.14	2.75	.092	1.22	.158	798	505	.34	6	38	4.74	---
	.52	1.48	.042	1.09	3.03	.088	.92	.472	817	510	.34	1	19	12.9	---
874	.55	1.38	.045	1.68	4.06	.136	1.22	.153	734	510	.35	15	71	4.0	---
	.54	1.48	.043	1.66	4.51	.134	.96	.395	747	512	35	16	70	3.6	---
	.46	1.45	.037	1.44	4.44	.116	.74	.69	756	517	.35	10	36	2.92	---
875	.56	1.37	.045	1.68	4.02	.136	1.24	.135	771	512	.35	12	66	4.28	---
	.53	1.46	.043	1.66	4.49	.135	.98	.376	806	515	.35	14	68	3.74	---
	.46	1.44	.037	1.46	4.48	.118	.76	.673	805	517	.35	12	38	2.58	---

**Velocity coupling sample centered 6.40 inches from burner end. Burner length = 24.75 inches.

TABLE A-IX

UNCORRECTED T-BURNER DATA
(CYH SR-28 Propellant Test Series)**

	Driver			Test Sample											
Run	L_b (in.)	$\frac{S_b}{S_{co}}$	β	L_b (in.)	$\frac{S_b}{S_{co}}$	β	$\frac{S_{co}}{S_c}$	t_α (sec)	f (Hz)	$\bar{P}$ (psig)	$\dot{r}$ (in./sec)	Pk-Pk Amp (psi)	α (sec^{-1})	π_{NL}	Remarks
883	.57	1.42	.028	1.69	4.09	.083	1.21	.226	480	305	.25	--	--	--	Osc. No growth
	.56	1.56	.028	1.69	4.52	.083	.99	.520	440	310	.25	--	--	--	Osc No growth
	.44	1.46	.021	1.31	4.30	.064	.66	1.195	428	315	.25	14	23	2.4	
885	.56	1.42	.028	1.68	4.11	.082	1.19	.228	--	307	.26	--	--	--	No osc.
	.56	1.55	.028	1.65	4.53	.081	.95	.548	420	310	.26	--	--		Osc. No growth
	.47	1.5	.023	1.39	4.32	.068	.73	.964	417	315	.26	16	25	2.38	
886	.56	1.42	.027	2.63	6.49	.129	1.17	.232	433	312	.30	--	--	--	Osc. No growth
	.53	1.52	.028	2.53	7.05	.124	.92	.535	424	317	.30	27	44	2.42	
	.47	1.47	.023	2.34	6.91	.110	.75	.819	432	322	.30	37	89	3.52	
891	.57	1.43	.028	1.68	4.12	.082	1.19	.252	--	307	.25	--	--	--	No osc.
	.47	1.50	.023	1.37	4.28	.067	.73	1.008	427	315	.25	21	21	1.46	Very long growth
902	.56	1.43	.027	.56	1.43	.027	1.09	.359	434	320	.26	--	-39	--	
	.55	1.52	.027	.55	1.52	.027	.92	.592	447	317	.26	--	-54	--	
	.51	1.50	.025	.51	1.50	.025	.81	.806	424	320	.26	--	-41	--	
903	.56	1.42	.027	.56	1.42	.027	1.10	.353	445	302	.26	--	-49	--	
	.55	1.50	.027	.55	1.50	.027	.95	.570	429	302	.26	--	-41	--	
	.50	1.48	.025	.50	1.48	.025	.81	.822	415	305	.26	--	-41	--	
912	.56	--	--	.56	--	--	--	--	--	--	--	--	--	--	
913	.56	1.45	.027	.56	2.82	.055	1.120	.35	449	307	.23	--	-51	--	Estimated burn rate
	.53	1.48	.026	.53	3.01	.054	.94	.63	422	310	.23	--	-49	--	
	.48	1.46	.024	.48	2.98	.050	.82	.87	417	310	.23	--	-41	--	

**Velocity coupling sample centered 9.75 inches from burner end. Burner length = 40.75 inches.

TABLE A-X

UNCORRECTED T-BURNER DATA
(Screening End Vented Tests)

Run	Burner Orientation	Grain Placement	Nozzle Diameter (in.)	Back Pres. (psig)	Ignition Technique	Driver L_b	Driver S_b/S_{co}	Test Sample L_b	Test Sample S_b/S_{co}	$\bar{P}$	$\dot{r}$	α
651	Vertical	Unsym.	.325	Atm	Standard bag	0.56	1.5	1.68	4.5	≈45	---	No osc.
652	↓	↓	.325	↓	Standard bag	0.56	1.5	2.69	7.0	>300	---	Osc., α not measureable
653	↓	↓	↓	↓	1½ x standard bag nylon screen to hold bag near propellant	0.56	1.5	1.68	4.5	≈50	---	No osc.
654	↓	↓	↓	↓		0.56	1.5	1.68	4.5	---	---	No osc. Bad ignition
655	Horizontal	↓	↓	↓	2 x standard bag	0.56	1.5	1.68	4.5	---	---	No osc.
656	↓	↓	↓	↓	2 x std. bag. ¼ x ¼ x 1" Comp. prop. strips bonded to propellant	0.56	1.5	2.25	6.0	---	---	No osc.
657	↓	↓	↓	↓	2 x std. bag 2E prop. strips bonded to end plate	0.56	1.5	1.68	4.5	Low	---	No osc.
658	Vertical	↓	↓	↓	Std. bag. 300 psi in burner held by rupture disk	0.56	1.5	1.68	4.5	Low	---	No osc.
685	Horizontal	↓	.403	100	Same as #657	0.56	1.5	2.8	7.0	150	---	No osc.
686-1	↓	↓	.36	100	Same as #657	.58	1.42	2.8	6.84	340	.28	84 @ .225 sec
686-2	↓	↓	.36	100	Same as #657	.51	1.53	2.43	7.30	290	.28	94 @ .79 sec
687	↓	↓	.31	100	Same as #657 with igniter paste on grains	.51	1.5	1.69	4.5	200	---	Not measureable
688	↓	↓	↓	150	Same as #687	.56	1.5	1.67	4.5	200	---	Not measureable
689	↓	Sym.	.310	250	2 std. bags + 2 pellets + igniter paste	.56 .56 .48	1.31 1.44 1.47	.56 .56 .48	1.31 1.44 1.47	350 290 290	.26 .26 .26	-119 at .12 sec -103 at .38 sec -101 at .925 sec
690	↓	↓	.44	250	2 std. bags + 2 pellets + igniter paste	.56	1.5	1.68	4.5	290	--	Not measureable

Footnote: Burner length = 40.25"
Non-symmetric grain centered 9.75" from forward end.
Symmetric grains centered 9.25 and 31.0" from forward end.

TABLE A-XI

UNCORRECTED T-BURNER DATA
(Final End Vented Tests)

Run	Sample Location from Forward End (inches)	Pre-fire Pressure (psig)	Nozzle Diam. (in.)	Driver L_b	Driver $\frac{S_b}{S_{co}}$	Driver β	Test Sample L_b	Test Sample $\frac{S_b}{S_{co}}$	Test Sample β_1	$\frac{S_{co}}{S_c}$	t_α	F_q	$\bar{P}$	$\dot{r}$	α	
892	9.75, 31.0	260	.31	.56	1.29	.027	.56	1.29	.027	1.34	.098	366	287	.24	-94	
				.56	1.38	.027	.56	1.39	.027	1.17	.286	430	292	---	-58	
893	9.75, 31.0	266	.31	.56	1.46	.027	.56	1.46	.027	1.05	.445	422	307	.24	-11	
				.55	1.50	.027	.55	1.50	.027	.95	.604	430	307	---	-76	
				.52	1.49	.025	.52	1.49	.025	.86	.777	410	302	---	-98	
894	9.75, 31.0	260	.44	.56	1.44	.027	1.68	4.23	.082	1.12	.444	---	300	.22	---	Pulse unit
				.56	1.51	.027	1.68	4.45	.082	1.02	.603	---	300	---	---	failed
				.54	1.52	.027	1.62	4.43	.079	.95	.717	---	300	---	---	
895	9.75	260	.31	.56	1.42	.027	.56	1.42	.027	1.10	.418	456	270	.20	-232	
				.56	1.48	.027	.56	1.48	.027	1.02	.563	437	270	---	-202	
				.54	1.51	.027	.54	1.58	.027	.92	.745	---	270	---	---	No pulse
896	9.75	260	.31	.56	1.43	.027	.56	1.43	.027	1.08	.424	---	270	.23	---	Nc pulse
				.55	1.48	.027	.55	1.48	.027	.99	.572	---	270	---	---	No pulse
				.52	1.48	.027	.52	1.48	.026	.89	.757	400	267	---	-152	
897	31.0	260	.44	.54	1.48	.026	2.78	6.75	.136	1.21	.174	449	280	.22	-77	
				.50	1.47	.024	2.78	7.29	.136	1.04	.336	444	280	---	-50	
				.46	1.44	.022	2.59	7.34	.127	.88	.517	435	282	---	-59	
898	31.0	260	.44	.56	1.47	.027	2.8	6.69	.136	1.24	.19	416	282	.25	-115	
				.55	1.5	.027	2.8	7.04	.136	1.12	.331	---	282	---	---	No pulse
				.51	1.47	.025	2.8	7.48	.136	.99	.510	---	280	---	---	No pulse
899	9.75, 31.0	275	.44	.56	1.48	.027	1.66	4.29	.081	1.06	.402	388	335	.24	-153	
				.55	1.5	.027	1.66	4.48	.081	.97	.542	464	312	---	-142	
				.51	1.49	.025	1.55	4.43	.076	.87	.727	---	307	---	---	No pulse
900	9.75	275	.44	.56	1.37	.027	2.8	6.75	.137	1.22	.209	446	317	.25	22	Question-
				.50	1.47	.024	2.57	7.47	.126	.84	.760	465	317	---	34	able
				.47	1.45	.023	2.46	7.41	.120	.78	.872	424	345	---	-218	"
				.43	1.41	.021	2.25	7.24	.11	1.09	1.10	---	345	---	---	No pulse
901	9.75	275	.44	.56	1.38	.027	2.8	6.69	.136	1.24	.183	---	307	.26	---	Noisy
				.54	1.5	.026	2.76	7.52	.135	.96	.545	478	312	---	37	Osc.before
				.50	1.48	.024	2.56	7.47	.126	.84	.749	460	310	---	-22	paddle out
				.46	1.44	.023	2.39	7.36	.117	.75	.933	469	312	---	-106	

Footnote: Burner Length = 40.75"